

The Macroscopic Architecture of Covalent Organic Frameworks for Storage and Purification

Thesis Submitted to AcSIR

For the Award of the Degree of

DOCTOR OF PHILOSOPHY

In

CHEMICAL SCIENCES



(Academy of Scientific and Innovative Research)

By

Abdul Khayum M

(Registration Number: 10CC15A26030)

Under the guidance of

Dr. Ulhas K Kharul

&

Dr. Rahul Banerjee

Polymer Science and Engineering Division
CSIR-National Chemical Laboratory
Pune- 411008, Maharashtra, India

August 2019

**Dedicated to
My Family**

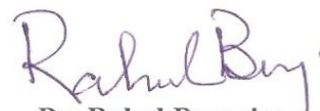
CERTIFICATE

This is to certify that work incorporated in this Ph.D. thesis entitled “The Macroscopic Architecture of Covalent Organic Frameworks for Storage and Purification” submitted by Abdul Khayum M to Academy of Scientific and Innovative Research (AcSIR) in fulfillment of the requirements for the awards of the Degree of Doctor of Philosophy, embodies original work under our supervision. We further certify that this work has not been submitted to any other University or Institution in part or full for the awards of any degree or diploma. Research material obtained from other sources has been duly acknowledged in the thesis. Any text, illustration, table etc. used in the thesis from other sources, have been duly cited and acknowledged.

It is also certified that this work done by the student, under our supervision, is plagiarism free.



Mr. Abdul Khayum M
(Student)



Dr. Rahul Banerjee
(Co-Supervisor)



Dr. Ulhas K Kharul
(Supervisor)

STATEMENT

I hereby declare that the matter embodied in this thesis entitled “The Macroscopic Architecture of Covalent Organic Frameworks for Storage and Purification” is the result of investigations carried out by me in the Polymer Science and Engineering Division, CSIR-National Chemical Laboratory, Pune, India under the guidance of Dr. Ulhas K Kharul and the co-guidance Dr. Rahul Banerjee, IISER Kolkata.

In keeping with the general practice of reporting scientific observations due acknowledgements have been made wherever the work described is based on the findings of other investigators.

Pune, August 2019


Abdul Khayum M

ACKNOWLEDGEMENT

*I would like to take this opportunity to express my sincere gratitude to my supervisor **Dr. Ulhas K Kharul**. I am thankful for his patience, motivation, timely advice and continuous support provided during every stages of my research work. My heartfelt thanks go to my co-supervisor **Dr. Rahul Banerjee** for introducing me to the wonders of scientific research, for his persistent guidance, encouragement, inspiration and support during my doctoral research work. Again I warmly thank him for his precious advice, analysis, criticism and discussions on my research work. I am very much thankful to him for his pursuance for improving me as a person as well as my scientific skills. I would also like to sincerely thank my DAC committee members **Dr. G. J. Sanjayan, Dr. R. Nandini Devi, Dr. C. P. Vinod and Dr. A. T. Biju** for their constructive, innovative suggestion and comments throughout my Ph.D. work period at CSIR-NCL, Pune.*

*I extend my sincere thanks to the Director of CSIR-NCL **Prof. Ashwini Kumar Nangia**, former Directors **Dr. Vijayamohanan K. Pillai and Dr. Sourav Pal**, Head of Physical and Materials Chemistry Division **Dr. P. A. Joy and Dr. Anil Kumar (Ex-HoD)** for their kind help and encouragement during the course of this work. I must earnestly acknowledge the collaborative assistance, valuable scientific discussions and suggestions that I received from **Dr. Sreekumar Kurungot**, NCL, Pune and **Dr. Rabibrata Mukherjee**, IIT Kharagpur. I also thank **Dr. Matthew Addicoat**, School of Science and Technology, Nottingham Trent University, Clifton Lane, NG11 8NS Nottingham, United Kingdom, for his help in theoretical calculations in a few projects. I am thankful to **Dr. Shatabdi Porel Mukherjee, Dr. Kumar Vanga and Dr. Jayaraj Nithyanandhan** for their constant support and guidance.*

*I am very grateful to UGC, New Delhi for fellowship support and CSIR for providing the platform carry out my research work. I thank all the non-teaching staff of CSIR-NCL for their assistance on various occasions. I wish to thank all my friendly and cooperative labmates **Tamas Da, Pradip Bhaya, Arijit Da, Chandan Da, Subhadeep Da, Tanay Da, Bishnu P Biswal, Harshitha, Suman, Bikash, Mohitosh, Saibal, Arjun, Suvendu, Jayshri Didi, Gobinda Da, Digambar Ji, Manas Da, Shouvik Da, Sujit Da, Kaushik, Himadri, Sharathettan, Shebeeb, Kanhu, Harshal, Amit Da, Arghya Da, Tapan Da, Sushil Bhaya,***

Srinu Anna, Kanhu da, Gargi Di, Kalipada, Biplab, Satyadip, Shouvik ans Sibani for creating a cheerful and enjoyable working atmosphere in the lab. They were extremely supportive as well as helpful during my tenure. I also thank project students Aswath and Nikhil, who helped in various projects.

*My stay on this campus has been pleasant with the association of all the research scholars at CSIR-NCL. I am thankful to **Bihag ettan, Unnikrishnan ettan, Anish ettan, Prajitha chechi, Leena chehci, Rajesh ettan, Jijil ettan, Eldo ettan, Vijayadas ettan, Sreekuttan ettan, Anumon ettan, Arun ettan, Sunil ettan, Vyshak ettan, Sreedala chechi, Kiran ettan, Anju, Lenin ettan, Manchunath, Jino ettan, Ramya chechi, Ram, Sudheesh, Suresh bayya, Munmun, Chaitanya, Manik, Dhanya Chechi, Prabhu, Loknath, Parashuram, Kiran, Manoj, Supriya, Jeyavani, Ambarish, Harshal, Varsha, Nishina, Sayantan, Subhrashish, Shailja, Siddarth, Moumitha, Sandeep, Shrikant, Navnath, Sarath, Jancy chechi, Raji, Roby, Maya, Naru, Bittu, Gouda, Kuyil and Punith** for their support, guidance, and advice.*

*I must thank to my collaborators **Vidhyanandh, Meena, Anuja, Sanoop, Maryam, Fayiz, Karthika, and Saurabh** for their extreme support, contributions, and suggestions towards my research work.*

*I would also like to thankful to all my friends **Vipin, Sandeep, Vinod, Mumthazir, Rajath, Junior, Shibin, Rashid, Zinoy, Tony, Aswathy, Ranjeesh, Ajith, Vipin, Munavvar, Rajith, Pranav, Sandeep, Emmanuel, Aswini, Betsy, Mariya, Kartika, Manik***

I am grateful to all my teachers and I expressed my gratitude for their encouragement in different part of my life. I thank the entire members of my family for their constant care and wishes. Last but not least, I would like to pay high regards to my parents for their constant encouragement and inspiration throughout my research work and lifting me uphill this phase of life. Dedicating this thesis to them is a minor recognition for their valuable support and encouragement.

Abdul Khayum M

PREFACE

The research on porous materials gain increasing attention due to their potential properties in various fields like gas storage; catalysis; energy storage; sensors; drug-delivery; optoelectronics etc. The recent research interest on porous materials mostly associated with the design of 2D or 3D symmetrical porous polymers, i.e., crystalline polymers like metal organic frameworks (MOFs); covalent organic frameworks (COFs); hydrogen bonded organic frameworks (HOFs) etc. Among these, COFs are very well known for their 2D/3D crystallinity; tunable porosity; low-density; and chemical and thermal stabilities. As a result of their exceptional structural features, COFs were well investigated for storage of valuable gases like H₂, NH₃, CO₂; heterogeneous catalysis; electrode material in energy storage devices; and water purification applications. However, the typical unprocessable granular form of COFs obstructs the leverage of material into the technologically relevant macroscopic forms like two-dimensional (2D) thin films, sheets and three-dimensional (3D) architectures. Meanwhile, the notable researches on the macroscopic architecture of alike materials such as graphene; carbon nanotubes; polymer gels etc delivered the outstanding output of the properties in various applications. In this regard, it is to be expected that the 2D or 3D macroscopic engineering of COFs can provide a new dimension of the scientific and commercial aspects of the material. Moreover, the advanced exploration of electrochemical energy storage demands flexible 2D- thin sheet with mechanical robustness and electrical conductivity. Additionally, scientist look forward to the development of 3D architecture aerogel of crystalline porous polymers which has paramount importance in adsorption based micro-pollutant purification of water.

In Chapter 2, we have developed an effective strategy for the fabrication nanometer level thin films of COFs derived covalent organic nanosheets. Herein, we have presented a chemical exfoliation strategy to delaminate the layers of COF into CONs. Interestingly, the chemical exfoliation method involves Diels-Alder cycloaddition reaction of anthracene stitched β -ketoenamine framework with an electron deficient *N*-hexylmaleimide as a dienophile. The obtained CONs exhibit high dispersion properties in organic solvents due to the presence of the long alkyl chains on the CON framework. As a result, we could fabricate the free-

standing thin film of CONs at air-water interphase through layer by layer assembly. Notably, the CON thin films display a controllable thickness ranging from ~1.5 nm to 1 μm .

Again, the significance of the fabrication of covalent organic frameworks into two dimensional thin films and sheets has been increased due to their potential features of macroscopic forms in various fields. In this regard, the development of mechanically robust 2D macro-architecture COFs requires scientific attention and has a pivotal role in the advanced applications like flexible energy storage systems. In the Chapter 3, we have developed mechanically strong and redox-active β -ketoenamine covalent organic framework thin sheets through a convergent synthetic strategy. In this method, we have integrated a Π -electron rich anthracene (**Da**) and redox-active anthraquinone (**Dq**) into a single framework through a solid-state synthesis. The obtained convergent COF thin sheet displays redox activity as well as mechanical strength, which has been further utilized as a flexible electrode in a quasi solid-state supercapacitor. In the convergent COF, the Π -electron rich anthracene boosts the mechanical strength of the thin sheets, whereas, the anthraquinones are responsible for the energy storage of the system.

However, the macroscopic two-dimensional (2D) form of covalent organic frameworks (COFs) face the challenge of modest performance in energy storage devices. It could be due to the indigent electrical conductivity of COFs in micro as well as macro levels. Taking in this to account, in Chapter 4, we have presented a novel COF-CNF hybrid materials in 2D macroscopic thin sheet form as an excellent energy storage platform. In these COF-CNF hybrids, the efficient interlayer interaction between COF and CNF provide a pure blended matrix with high electrical conductivity compared to the pristine COFs. Additionally, they possess inherent crystalline and porous nature. Notably, the excellent energy storage performance of COF-CNF hybrids in supercapacitor electrodes indicates the prospect of the macro-architecture of COFs in a futuristic direction. Moreover, we have fabricated a self-charging power-pack for light energy harvesting and consequent storage as electrical energy with a decent performance.

Moreover, the software controlled three dimensional (3D) macro-architecture of functional porous materials gains tremendous scientific and technological attention towards the molecular uptake. Meanwhile, the exceptional intrinsic porous features of covalent organic

frameworks (COFs) shows excellent molecular uptake through the adsorptive interactions. However, the molecular pollutant uptake from water requires a high exposure of the intrinsic pores towards the external environments for the lucid diffusion of water through the internal porous matrix. In this regard, in Chapter 5, we have demonstrated the integration of crystalline and porous COFs into template-free 3D printable objects with intrinsic micro- and extrinsic macro porosity. The interconnected 3D pores in these aerogels further enhances the rapid and efficient uptake of organic and inorganic pollutants from water (>95% of removal within 1 minute).

Finally, Chapter 6 deals about the conclusion of the overall thesis work. Again, it describes the future perspective of the fabrication of responsive smart-macroscopic COF thin films.

CONTENTS	PAGE
Certificate	iii
Statement	iv
Acknowledgement	v
Preface	vii

CHAPTER 1

The Significance of Macroscopic Engineering of Covalent Organic Frameworks for the Potential Applications **1-38**

1.1	A brief account on porous materials	2
1.2	Classification based on pore size.	3
1.3	Classification based on nature of linkers.	3
	1.3.1 Porous Inorganic framework materials	3
	1.3.2 Porous hybrid Inorganic-organic framework materials	5
	1.3.3 Porous organic framework materials	5
1.4	Covalent organic frameworks	7
1.5	The construction of COF	9
	1.5.1 Reversible chemical reaction	9
	1.5.2 Synthetic methods	11
	1.5.3 Nature of linkers	14
		11
1.6	Properties of COFs	17
1.7	Applications of COFs	19

1.7.1	Gas storage	19
1.7.2	Heterogeneous catalysis	21
1.7.3	Energy storage	22
1.7.4	Optoelectronics and semi conduction	24
1.7.5	Purification and separation	24
1.7.6	Drug storage and delivery	26
1.8	The significance of macro-architecture of the COFs	27
1.8.1	The attempts to fabricate macroscopic architecture of the functional materials	29
1.8.2	Macroscopic architecture of COFs	32
1.8.3	Applications of COF thin films	36
1.8.4	Macroscopic architecture of COFs in advanced level	38
CHAPTER 2		
Chemically Exfoliated Covalent Organic Nanosheets as Ultrathin Free-Standing Films		
		39-66
2.1	Introduction	40
2.2	Result and discussion	41
2.2.1	Synthesis and characterization	41
2.2.2	The structural characterizations	42
2.2.3	Chemical characterization	45
2.2.4	Properties of DaTp and DaTp CONs	48
2.2.5	Transformation of Morphology of COFs into CONs	50

2.2.6	The dispersion property of CONs in organic solvents	52
2.2.7	The fabrication ultrathin free-standing CON film at the air-water interface	55
2.2.8	The plausible mechanism for the thin film formation	59
2.3	Conclusion	60
2.4	Experimental procedures	60
2.4.1	Materials	60
2.4.2	Synthesis of <i>N</i> -hexylmaleimide	61
2.4.3	Synthesis of DaTp COF	62
2.4.4	Synthesis of 2,4,6-tris(anthracen-2-ylamino)methylene)cyclohexane-1,3,5-trione (DaTp monomer)	62
2.4.5	Synthesis of 2,6-diamino-13-ethyl-9,10-dihydro-9,10-[3,4]epipyrrroanthracene-12,14-dione (Reference compound 1)	63
2.4.6	Synthesis of 2-amino-13-ethyl-9, 10-dihydro-9,10-[3,4]epipyrrroanthracene-12,14-dione (Reference compound 2)	63
2.4.7	Synthesis of DaTp CONs	63
2.4.8	General methods for characterization	64

CHAPTER 3

Convergent Covalent Organic Framework Thin Sheet as Flexible Supercapacitor

67-99

3.1	Introduction	68
------------	---------------------	----

3.2	Result and discussion	74
3.2.1	Synthesis and characterization	74
3.2.2	Structural characterization	75
3.2.3	Chemical characterization	75
3.2.4	Properties of COF thin sheets	79
3.2.5	Morphology COF thin sheets	83
3.2.6	Electrochemical analysis of COF thin sheets	85
3.3	Conclusion	94
3.4	Experimental procedures	95
3.4.1	<i>Materials</i>	95
3.4.2	Synthesis of DqTp COF thin sheet	95
3.4.3	Synthesis of DaTp COF thin sheet	95
3.4.4	Synthesis of convergent COF thin sheets	96
3.4.5	General methods for characterization	96

CHAPTER 4

Weak Intermolecular Interactions in Covalent Organic Framework-Carbon Nanofiber Hybrids for the Efficient Energy Storage **100-133**

4.1	Introduction	101
4.2	Result and discussion	103
4.2.1	Synthesis and characterization	103
4.2.2	The structural characterizations	104

4.2.3	Chemical characterization	106
4.2.4	Properties of COF-CNF hybrid thin sheets	109
4.2.5	DFTB optimization of COF-CNF interactions	111
4.2.6	Morphology COF-CNF hybrid thin sheets	116
4.2.7	Electrochemical analysis of COF-CNF hybrid thin sheets	119
4.2.8	Supercapacitor studies	124
4.2.9	Self-charging power-pack	125
4.3	Conclusions	127
4.4	Experimental procedures	128
4.4.1	Materials	128
4.4.2	Synthesis of DqTp -CNF hybrid thin sheet	128
4.4.3	Synthesis of DqDaTp -CNF hybrid thin sheet	128
4.4.4	Three-electrode assembly	129
4.4.5	Device fabrication for two electrode experiment	130
4.4.6	General methods for characterization	131
 CHAPTER 5		
3D-Printable Covalent Organic Framework Aerogels for Water Purification		134-162
5.1	Introduction	135
5.2	Result and discussion	137
5.2.1	Synthesis and characterization	137
5.2.2	3D-Printing of COF aerogel	139
5.2.3	The structural characterizations	141

5.2.4	Properties of COF aerogels	144
5.2.5	The Morphology of COF aerogels	145
5.2.6	COF aerogel for micropollutants removal	154
5.3	Conclusions	158
5.4	Experimental procedures	158
5.4.1	Materials	158
5.4.2	Synthesis of COF aerogels	158
5.4.3	Water purification	159
5.4.4	General methods for characterization	160
CHAPTER 6		
Conclusions of All Chapters and Future Directive		164-167
6.1	Conclusions	164
6.2	Future directives	166
REFERENCES		168-185
About the Author		186
List of Publications and Conferences		187

LIST OF FIGURES

Figures	Page
1.1 <i>Classification of porous material based pore size; and framework structure.</i>	4
1.2 <i>The dynamic covalent chemistry of COFs.</i>	7
1.3 <i>The types of COFs formed from different reversible organic reactions</i>	8
1.4 <i>Different types of synthetic method of COFs [Room temperature synthesis: [Reprinted with permission from {D. D. Medina et al., J. Am. Chem. Soc.2015, 137, 3, 1016-1019} Copyright {2015} American Chemical Society] and Monolayer growth of template: Reproduced with the permission of AAAS [J. W. Colson et al., Science, 2011, 332, 228].</i>	12
1.5 <i>Symmetry of the linkers in COFs. The combination of different symmetric linkers decided the pore geometry of the COF.</i>	15
1.6 <i>The different types of linkers used for the construction of COFs.</i>	16
1.7 <i>Properties of COFs.</i>	17
1.8 <i>Different types of Applications of COFs.</i>	19
1.9 <i>a) Incorporation of Pd²⁺ into the interlayer of COF-LZU [Reprinted with permission from {S. Y. Ding et al., J. Am. Chem. Soc., 2011, 133, 19816} Copyright {2011} American Chemical Society]; b) In situ generation Pd nanoparticles in TpBpy COF [Reprinted with permission from {M. Bhadra et al., ACS Appl. Mater. Interfaces, 2017, 9, 13785–13792} Copyright {2017} American Chemical Society]; and c) Photocatalysis by using COF [Reprinted with permission from {M. Bhadra et al., J. Am. Chem. Soc. 2019, 141, 15, 6152-6156} Copyright {2019} American Chemical Society].</i>	21
1.10 <i>a) Hydroquinone stitched COF for supercapacitance [Reprinted with permission from {S.Chandra et al., Chem. Mater. 2017, 29, 5, 2074-2080} Copyright {2017} American Chemical Society]; b) Exfoliated COF for Li⁺ ion battery [Reprinted with permission from {S. Wang et al., J. Am. Chem. Soc. 2017, 139, 4258-4261}</i>	23

- Copyright {2017} American Chemical Society}; c) Anthraquinone stitched COF for Na⁺ ion battery [Reprinted with permission from {S. Gu et al., *J. Am. Chem. Soc.* 2019, 141, 24, 9623-9628} Copyright {2019} American Chemical Society].
- 1.11** a) COF membrane based water purification [Reprinted with permission from {S. Kandambeth et al., *Adv. Mater.* 2017, 29, 1603945} Copyright {2017} American Chemical Society]; b) COF foam based water purification [Reprinted with permission from {S. Karak et al., *J. Am. Chem. Soc.* 2019, 141, 18, 7572-7581} Copyright {2019} American Chemical Society]. **25**
- 1.12** The macroscopic architecture of functional materials and their possible applications. **27**
- 1.13** Thin film fabrication of a) MoS₂ [Y. Lee et al., *Nanoscale* 2014, 6, 2821 .Reproduced with permission. Copyright 2014, Royal Society of Chemistry]; b) MOF [Reprinted with permission from {T. Haraguchi et al., *Inorg. Chem.* 2015, 54, 11593–11595} Copyright {2015} American Chemical Society]; c) WSe₂ [X. Yu et al., *Nat. Commu.* 2015, 6, 7596. Copyright (2015) Nature Publishing Group]. **28**
- 1.14** Thin sheet fabrication of graphene oxide. a) [D. A. Dikin et al., *Nature* 2007,448, 457–460 Copyright (2007) Nature Publishing Group] & b) [Reprinted with permission from {K. Chen et al., *ACS Nano* 2018, 12, 54, 269-4279} Copyright {2018} American Chemical Society]. **29**
- 1.15** 3D architecture of different materials. a) [Reprinted with permission from {G. Zu et al., *ACS Nano*, 2018, 12, 1, 521-532} Copyright {2018} American Chemical Society]; b) [X. Zhu et al., *Nat.Commu*, 2015, 6, 6962. Copyright (2015) Nature Publishing Group]; c)[X. Gui et al., *Adv. Mater.*, 2010, 22, 617–621.Copyright (2010) Wiley VCH]; d) [J. Wang et al., *Angew. Chem. Int. Ed.* 2018, 57, 1 – 5. Copyright (2018) Wiley VCH]; e) [Reprinted with permission from {G.J. H. Lim et al., *ACS Materials Lett.* 2019, 1, 147–153} Copyright {2018} American Chemical Society]. **30**
- 1.16** COF-5 on graphene support [J. W. Colson et al., *Science*, 2011, 332, 228]. **33**
- 1.17** COF thin film growth on gold support [Reprinted with permission from {C. R. DeBlase et al., *ACS Nano* 2015, 9, 3178–3183} Copyright {2015} American Chemical Society]. **34**
- 1.18** Interfacial thin film fabrication of COF [Reprinted with permission from {K. Dey et al., *J. Am. Chem. Soc.* 2017,139,13083–13091} Copyright {2017} American Chemical Society]. **35**

1.19	<i>Solid-state synthesis of COF membranes [Reprinted with permission from S. Kandambeth et al., Adv. Mater. 2017, 29, 1603945] Copyright {2017} American Chemical Society].</i>	36
2.1	<i>a) The PXRD profiles of DaTp, DaTp CONs and simulated eclipsed form. b) The P63/m unit cell of DaTp. c) The crystal structure of the reference compound 1. d) The representation of the chemical exfoliation of DaTp into DaTp CONs.</i>	43
2.2	<i>a) Single Crystal X-Ray Diffraction of reference compound 1. In the ORTEP (with the 40 % probability level); Carbon (black), Oxygen (Red), Nitrogen (blue) and Hydrogen (small black circle) have been shown [CCDC No: 1497987]. b) Single Crystal X-Ray diffraction of reference compound 2. In the ORTEP (with the 40% probability level); Carbon (black), Oxygen (Red), Nitrogen (blue) and Hydrogen (small black circle) have been shown [CCDC No: 1497988].</i>	44
2.3	<i>FT IR spectra of a) comparison of the starting material with DaTp COF. b) Comparison of the monomer and DaTp. c)The comparison of DaTp, DaTp CONs and N-hexylmaleimide.</i>	46
2.4	<i>The comparison of ¹³C NMR spectra of a) Reference compound 1 and starting materials. b) Reference compound 2 and starting materials. The comparison of ¹³C CP MAS NMR spectra of c) DaTp and DaTp CONs (with N-hexylmaleimide). d) DaTp and DaTp CONs (with N-ethylmaleimide).</i>	47
2.5	<i>a) The quantitative integration of ¹³C solid-state NMR of DaTp CON. b) The reference unit of DaTp.</i>	48
2.6	<i>a) TGA of DaTp and DaTp CONs. b) N₂ gas adsorption analysis of DaTp and DaTp CONs. c) NLDFT pore size distribution of DaTp. d) NLDFT pore size distribution of DaTp CONs.</i>	49
2.7	<i>a) The SEM images of DaTp. It shows the aggregated ribbon-like morphology in 10 μm and 1 μm level focuses. b) The SEM images of DaTp CONs. It exhibits thins sheet-like morphology in different levels of focus (2, 3 and 5 μm) and also displays the aggregation of many CON layers into a single block of thin sheet.</i>	50
2.8	<i>a) The TEM images of DaTp. It shows the aggregated ribbon-like morphology in 200 nm and 100 nm levels focus. b) The TEM images of DaTp CONs. It exhibits thins sheet-like morphology in different levels of focus (100 and 50 nm) and also displays the aggregation of many CON layers into a single block of thin sheet.</i>	51
2.9	<i>The TEM images of partially exfoliated DaTp and the aggregation of small lateral sized CON layers</i>	51

2.10	a) The AFM image and b) height profile of DaTp CONs.	52
2.11	The dispersion of DaTp CONs in various organic solvents.	54
2.12	a) The Tyndall effect of DaTp CONs in DCM solvent. b) The DLS profile of DaTp CONs in DCM solvent [Inset: The TEM images of DaTp CONs]	54
2.13	a & b) The plausible self-assembly process of DaTp CONs into a thin film. c) The free-standing DaTp CON thin film in a copper loop. d) The graphical representation of the process of thin film making in a glass beaker.	55
2.14	The FT-IR spectroscopy of DaTp CON thin film.	56
2.15	a) The SEM image of DaTp CON thin film on a silicon wafer and a polysulfone membrane. b) The TEM images of DaTp CON thin films. It explains the large lateral sheets are formed by small lateral sized CONs.	56
2.16	The optical microscopic images of DaTp CON thin films.	57
2.17	The AFM images and corresponding height profiles of a) low; b) medium and c) high concentration of the DaTp CON-DCM suspension.	58
2.18	a) Drop casting of DaTp CON-DCM suspension on the water surface. b) The thin film formation at the air-water interface. c) The thin film on a glass surface. d & e) The mechanically grind CONs on water surface and f) on a glass surface.	59
2.19	Contact angle measurement DaTp pellet and DaTp CON thin film.	60
2.20	¹ H NMR (in CDCl ₃) of N-hexylmaleimide.	61
2.21	¹³ C NMR (in Acetone-d ₆) of N-hexylmaleimide.	62
3.1	The digital photographs of the fabrication of COF thin sheet through SSM method.	70
3.2	a) The diagrammatic representation of the fabrication of COF thin sheet. b) The digital photograph of 16 cm ² Dq₁D₁Tp COF thin sheet. c) The photograph shows the flexibility of Dq₁D₁Tp COF thin sheet. d) The cross-sectional SEM image of Dq₁D₁Tp COF thin sheet	71
3.3	The PXRD profiles of all COF thin sheets.	73
3.4	a) The PXRD profiles COFs, Tp and PTSA. b) The PXRD of all COFs after the treatment in 1M H ₂ SO ₄ for 24 hours.	74
3.5	a) The FT-IR spectra of a) DqTp ; b) DaTp ; and c) convergent COFs with starting materials. d) The FT-IR spectra comparison of all COFs with PTSA	76
3.6	¹³ C CP MAS Solid-state NMR of all COFs and the physical mixture of DqTp and DaTp COFs	77
3.7	¹³ C CP MAS Solid-state quantitative integrations of all COFs.	78
3.8	TGA of all COFs	80

3.9	<i>a) N₂ adsorption analysis of all COF thin sheets. b-e) NLDFT pore size distribution of COFs.</i>	80
3.10	<i>a) DMA of all COF thin sheets. b) The plot percentage of linker Vs percentage of breaking strain. c) Digital photographs of mechanical strength studies of all COFs.</i>	81
3.11	<i>a) Convergent nature of Dq₁Da₁Tp COF. b) Digital photographs of mechanical fluctuation of Dq₁Da₁Tp COF thin sheet.</i>	82
3.12	<i>TEM images of COF thin sheets.</i>	83
3.13	<i>SEM images of COF thin sheets.</i>	84
3.14	<i>a) The graphical representation and photographs of working electrode fabrication. b) The graphical representation of three-electrode assembly. c) The impedance analysis of all COF thin sheets.</i>	85
3.15	<i>The cyclic voltammetry of COF thin sheets in three-electrode assembly.</i>	87
3.16	<i>The galvanostatic charge-discharge curves of all COF electrodes.</i>	88
3.17	<i>a) The FT-IR spectra of COF thin sheet electrodes after the electrochemical analysis. b) The plot of Current density Vs Specific capacitance of all COFs.</i>	89
3.18	<i>a) The diagrammatic and photographic representation of device fabrication. b) The flexible COF supercapacitor has been used for power LEDs.</i>	90
3.19	<i>The impedance analysis of COF based supercapacitor devices</i>	90
3.20	<i>a) The CV; b) GCD; c) The long –term cyclic stability test of C.T-DqTp and C.T-Dq₁Da₁Tp supercapacitor devices.</i>	91
3.21	<i>a) The plot of Current density Vs Specific capacitance and b) the Ragone plot of COF based supercapacitors.</i>	92
4.1	<i>The diagrammatic representation of the COF-CNF hybrids.</i>	103
4.2	<i>a) The PXRD comparison of DqTp-CNF with DqTp COF, CNF and simulated PXRD in eclipsed form. b) The PXRD comparison of DqDaTp-CNF with DqDaTp COF, CNF and simulated PXRD in eclipsed form.</i>	104
4.3	<i>The PXRD of COF-CNF hybrids after the 3M HCl acid treatment for 24 hours.</i>	105
4.4	<i>The FT-IR profiles of DqTp-CNF and DqDaTp-CNF hybrids and their starting materials.</i>	105
4.5	<i>The ¹³C CP MAS solid-state NMR profiles of -CNF and DqDaTp-CNF hybrids.</i>	106
4.6	<i>The XPS profiles of all COF-CNF hybrids, COFs and CNF. b) The XPS profile of C1s. c) The XPS profile of O1s.</i>	107
4.7	<i>The XPS profiles of all hybrids and COFs after deconvolution.</i>	108
4.8	<i>The TGA curves of COF-CNF hybrids.</i>	109

4.9	<i>The N₂ gas adsorption of COF-CNF hybrids and CNF.</i>	110
4.10	<i>The NLDFT pore size distribution of COF-CNF hybrids.</i>	110
4.11	<i>The I-V plot of a) DqTp COF and DqTp-CNF hybrid and b) DqDaTp COF and DqDaTp-CNF hybrid.</i>	111
4.12	<i>The DFTB optimized unit cells of DqTp, DaTp, Dq₂Da₁Tp and Dq₁Da₂Tp COFs for the interlayer interaction studies.</i>	112
4.13	<i>The DFTB optimized monolayer COF-graphene systems.</i>	113
4.14	<i>The DFTB optimized 2-2-2 COF-graphene systems.</i>	114
4.15	<i>The DFTB optimized 3-3-3 COF-graphene systems.</i>	114
4.16	<i>The DFTB optimized models of vertically stacked COF on a slightly curved graphene.</i>	115
4.17	<i>The DFTB optimization of HOMO/LUMO of COFs.</i>	115
4.18	<i>The TEM images of COF-CNF hybrid thin sheets.</i>	117
4.19	<i>The TEM images of the physical mixture COF and CNF.</i>	117
4.20	<i>The TEM images of the COF-CNT hybrids. The scale bar represents a) 100 nm; b) 50 nm; c) 5 nm; and d) 20 nm.</i>	118
4.21	<i>The SEM images of COF-CNF hybrid thin sheets. a) (i)-(iv) DqTp-CNF hybrid and b) (i)-(iv) DqDaTp-CNF hybrid. It shows the surface and vertical cross-section of the thin sheet. Again, the CNFs are clearly visible in the zoomed image of vertical cross-section.</i>	118
4.22	<i>a) Free-standing and flexible DqDaTp-CNF hybrid. b) The graphical representation of COF on the surface of CNF. d) The DMA of both COF-CNF hybrids. e) The SEM images of DqDaTp-CNF hybrid thin sheet.</i>	119
4.23	<i>a) The CV profile of DqTp-CNF hybrid and DqTp COF at 50 mVsec⁻¹. b) a) The CV profile of DqDaTp-CNF hybrid and DqDaTp COF at 50 mVsec⁻¹. c) a) The CV profile of DqDaTp-CNF supercapacitor at 50 mVsec⁻¹. d) The GCD curves of DqTp-CNF hybrid and DqTp COF at 0.25 mA g⁻¹. e) The GCD curves of DqDaTp-CNF hybrid and DqDaTp COF at 0.25 mA g⁻¹. f) The GCD curves of DqDaTp-CNF supercapacitor at 0.50 mA g⁻¹.</i>	120
4.24	<i>a) CV and b) GCD profiles of DqTp-CNF & DqDaTp-CNF hybrids.</i>	120
4.25	<i>a) CV profile of CNF at 50 mVsec⁻¹; (ii) Comparison of CV profiles of DqTp-CNF hybrid with CNF at 50 mVsec⁻¹; (iii) The GCD curve of CNF at different current densities. b) a) CV profile of physical mixture COF and CNF at 50 mVsec⁻¹; (ii) Comparison of CV profiles of DqTp-CNF hybrid with physical mixture at 50</i>	121

	<i>mVsec⁻¹; (iii) The GCD curve of CNF at different current densities.</i>	
4.26	<i>a) The CV and b) GCD analysis of DqDaTp-CNF supercapacitor.</i>	122
4.27	<i>a) The plot of current density Vs areal capacitance. b) Ragone plot of power density Vs energy density. c) The long-term cyclic stability of DqDqTp-CNF supercapacitor.</i>	122
4.28	<i>a) The diagrammatic representation of self-charging power-pack. b) Digital photograph of the self power-pack device.</i>	126
4.29	<i>The X-ray tomography of self-charging power-pack device.</i>	126
4.30	<i>a) Voltage-current density curve of the perovskite solar cell. b-d) The discharging curves of supercapacitor in self-charging power-pack in different time photo charging.</i>	127
5.1	<i>The rheology analysis of COF aerogel precursor paste.</i>	137
5.2	<i>a) Rheology analysis of Time Vs Storage and Loss modulus; and b) COF precursor synthesis</i>	138
5.3	<i>The fabrication 3D-printed COF aerogel.</i>	138
5.4	<i>a) 3D printing of a nine numbered square grid; and b) 3D printing of 13 layers square object.</i>	139
5.5	<i>The COF aerogels are floating in water after the removal of PTSA.</i>	140
5.6	<i>The comparison of the experimental PXRD of COF aerogel with simulated AA eclipsed PXRD and their corresponding models.</i>	141
5.7	<i>The IR spectra of COF aerogels with the monomers.</i>	142
5.8	<i>The ¹³C CP MAS Solid-state NMR of COF aerogels.</i>	143
5.9	<i>The TGA curves of COF aerogels.</i>	144
5.10	<i>a) N₂ Gas adsorption analysis; and b) NLDFT pore size distribution of COF aerogels.</i>	144
5.11	<i>The SEM images of BDTp-GO aerogel.</i>	145
5.12	<i>The SEM images of DqTp-GO aerogel.</i>	146
5.13	<i>The SEM images of BDTp-GO before and after washing with water.</i>	146
5.14	<i>The TEM images of a) BDTp-GO; and DqTp-GO.</i>	147
5.15	<i>Fluorescent microscopic images of COF aerogels and pristine COFs: a) BDTp-GO; b) BDTp; c) DqTp-GO; and d) DqTp.</i>	148
5.16	<i>The X-ray tomographic 3D images of COF aerogel and pristine COFs.</i>	149
5.17	<i>The X-ray tomographic 3D images of macroporous structure of BDTp-GO aerogel.</i>	150
5.18	<i>The X-ray tomographic 3D images of macroporous structure of DqTp-GO aerogel.</i>	150

5.19	<i>The X-ray tomographic calculation of pore size distribution of COF aerogels in the μm range.</i>	151
5.20	<i>The X-ray tomographic 3D images of macroporous structure of pristine BDTp COF.</i>	151
5.21	<i>The macroscopic features COF aerogel and pristine COF.</i>	152
5.22	<i>The X-ray tomographic water flow analysis of BDTp-GO.</i>	152
5.23	<i>The X-ray tomographic water flow analysis of DqTp-GO.</i>	153
5.24	<i>The X-ray tomographic water flow analysis plot of 'Position Vs Pressure drop' of COF aerogels.</i>	153
5.25	<i>a) The organic and inorganic micropollutants; and b) The bar diagram of the efficiency of the removal each micropollutants by using COF aerogels.</i>	154
5.26	<i>The UV spectroscopic characterizations the adsorption properties of COF aerogels.</i>	155
5.27	<i>The Kinetic study of micropollutant removal from water.</i>	156
5.28	<i>The concentration study of micropollutant removal from water.</i>	156
5.29	<i>The pH study of micropollutant removal from water.</i>	157
5.30	<i>a) The UV spectra of COF aerogel adsorption; b) The digital photograph of COF aerogel adsorption of MB; and c) The diagrammatic representation of the interaction of micropollutant with the 3D tomographic images of COF aerogel and pristine.</i>	157
6.1	<i>a) The schematic representation of the post modification of COF into azobenzene decorated pores. b) The diagrammatic representation of COF aerogel activity towards molecular uptake under visible or UV light condition.</i>	167

LIST OF TABLES

Tables		Page
2.1	<i>Fractional atomic coordinates for the unit cell of DaTp</i>	44
2.2	<i>The dispersion stability of DaTp CONs in various organic solvents</i>	52
3.1	<i>The quantitative integration of ^{13}C CP MAS solid-state NMR for all COFs</i>	79

3.2	<i>The state-of-the-art-of the COF based supercapacitors.</i>	93
4.1	<i>DFTB data of COF-CNF hybrids (Perlayer stabilization in kcalmol⁻¹ and band gap in eV).</i>	116
4.2	<i>Areal capacitance of the supercapacitors reported previously. The areal capacitances from the three-electrode analysis were specified.</i>	123

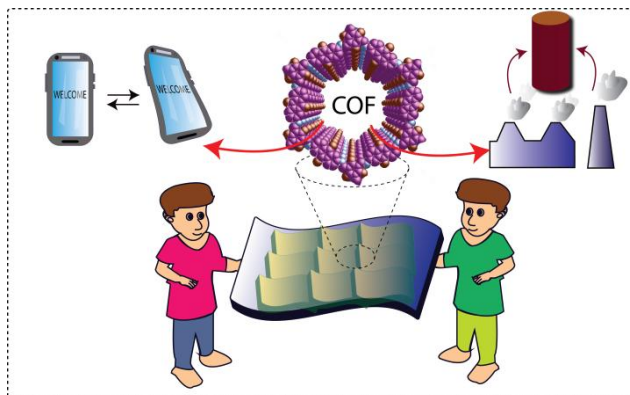
LIST OF SCHEMES

Scheme		Page
2.1	<i>The schematic representation of the synthesis of DaTp COF and CONs.</i>	42
3.1	<i>The schematic representation of the synthesis of all COFs.</i>	69
5.1	<i>The Chem-Draw image of synthetic scheme of COFs.</i>	136

CHAPTER 1

The Significance of Macroscopic Engineering of Covalent Organic Frameworks for the Potential Applications

Abstract: The research on porous materials gain increasing attention due to their potential properties in various fields like gas storage; catalysis; energy storage; sensors; drug-delivery; opto-electronics etc. The recent research interest on porous materials mostly associated with the



design of 2D or 3D symmetrical porous polymers, i.e., crystalline polymers like metal organic frameworks (MOFs); covalent organic frameworks (COFs); hydrogen bonded organic frameworks (HOFs) etc. Among these, COFs are very well known for their 2D/3D crystallinity; tunable porosity; low-density; and chemical and thermal stabilities. As a result of their exceptional structural features, COFs were well investigated for storage of valuable gases like H_2 , NH_3 , CO_2 ; heterogeneous catalysis; electrode material in energy storage devices; and water purification applications. However, the typical unprocessable granular form of COFs obstructs the leverage of material into the technologically relevant macroscopic forms like two-dimensional (2D) thin films, sheets and three-dimensional (3D) architectures. Meanwhile, the notable researches on the macroscopic architecture of alike materials such as graphene, carbon nanotubes, polymer gels etc delivered the outstanding output of the properties in various applications. In this regard, it is to be expected that the 2D or 3D macroscopic engineering of COFs can provide a new dimension of the scientific and commercial aspects of the material. Moreover, the advanced exploration of electrochemical energy storage demands flexible 2D- thin sheet with mechanical robustness and electrical conductivity. Additionally, scientist look forward to the development of 3D

architecture aerogel of crystalline porous polymers which has paramount importance in adsorption based micro-pollutant purification of water.

1.1 A brief account on porous materials

Porous materials are generally solids or fluids contain extrinsic or intrinsic pores in the solid or liquid matrix. The most of the materials in the nature can be classified in the porous category due to the presence micro or macro openings on the surface and the bulk. Wood; soil; bricks; plant leaf; honeycomb; sponges etc are some of those examples of porous material in nature [1.1]. The porous materials can be classified as three different types based on the size of the pore openings: 1) microporous (pore size < 2 nm); 2) mesoporous (pore size ~2-50 nm) and 3) macroporous (pore size > 50 nm) [Details are given in section 1.1] [1.2]. The earlier attempts to the synthesis of porous materials with high surface area mostly deal with the porous carbon or activated carbon by burning the precursors like woods or similar stuff. It has been used for applications like water purification and medicine and later developed for catalysis; gas separation; gas storage; and energy storage [1.1 & 1.3]. Although porous carbon exhibits excellent surface area, the structural irregularity of pores restricts them for the utilization in size-selective catalysis; separation; and adsorption like applications. Interestingly, a novel ordered porous material has been discovered in 1756, called zeolites which are composed of aluminosilicates ($[\text{SiO}_4]^{4-}$ and $[\text{AlO}_4]^{5-}$). The zeolites have been widely used in catalysis and molecular sieving applications due to their structural regularity and microporous nature [1.4]. However, the drawbacks such as lack of functional control and limited structural possibilities restrict them for the advanced level utilizations. Notably, Prof. Omar. M. Yaghi and his co-workers invented a pre-designed metal organic framework (MOF) from the reversible coordination bonds of metal ion and organic linkers [1.5]. Herein, the pre-design nature of MOFs allows the functional regulation and pore size control over the framework. Additionally, the reversible bond formation makes the material in a long-range order, and forms single crystal of MOFs. But they face the disadvantages like high weight-density; poor chemical stability; and the presence of toxic metals [1.6]. In 2005, the same group introduced a new material, called covalent organic framework (COF), in which the weak coordination bonds has been replaced by strong covalent linkages [1.7]. Unlike MOFs, COFs are composed of pure organic symmetric building units, hence displayed as a light-weight porous platform. It is noteworthy to mention that many other

porous materials have been investigated in the past decades along with the materials mentioned above. When we look at the structure and properties, it is difficult to classify the material into a particular category. However, in a general aspect, the porous materials can be classified based on the pore size and organic or inorganic nature of the structural framework.

1.2 Classification based on pore size.

Porosity of the materials is a measurement of the void fraction compared to the total volume of the matrix [1.2]. In this regard, the porous materials can be classified as three different types based on the size of the void openings (**Figure 1.1**): 1) microporous (pore size < 2 nm); 2) mesoporous (pore size ~2-50 nm) and 3) macroporous (pore size > 50 nm). Zeolites are typical microporous materials with the pore size distribution ranges from 0.1–2.0 nm [1.2]. Meanwhile, the activated carbons display the interconnected extrinsic pore diameter in the mesoporous range. Herein, the extrinsic porous nature of activated carbons is mainly due to the self-assembling of the carbon particles. Moreover, the general examples of macroporous materials are sponge; wood; honeycombs etc. It is difficult to classify the porous materials like MOF or COF into a particularly micro or mesoporous category. The pore size of these materials largely depends on the symmetric linkers used for the construction of the framework. Several examples of micro and mesoporous COFs are reported in the previous literatures [1.8]. Additionally, the recent development of COF into macroporous foams is indicating the significance of the material designing in the various class of porosity [1.9].

1.3 Classification based on nature of linkers.

The development of porous materials in the last few centuries contributes to the progress of the desired and significant structural evolution of the material. In the ancient time, people have used structurally amorphous carbon as a porous material for the different proposes. Later, the porous materials become more advanced and ordered inorganic metal framework like zeolites, and then shifted to organic-inorganic hybrid framework like MOFs. Recently, researchers developed pure organic ordered porous materials like COFs. In this regard, we can classify the porous materials into different categories based on the nature of linkers too (**Figure 1.1**): 1) Inorganic porous framework materials; 2) Inorganic-organic hybrid porous framework materials; 3) Organic porous framework materials.

1.3.1 Porous Inorganic framework materials:

The investigations on inorganic porous materials open a wide chemical diversity of the framework formation by using inorganic constituents like metals, aluminate, silicates,

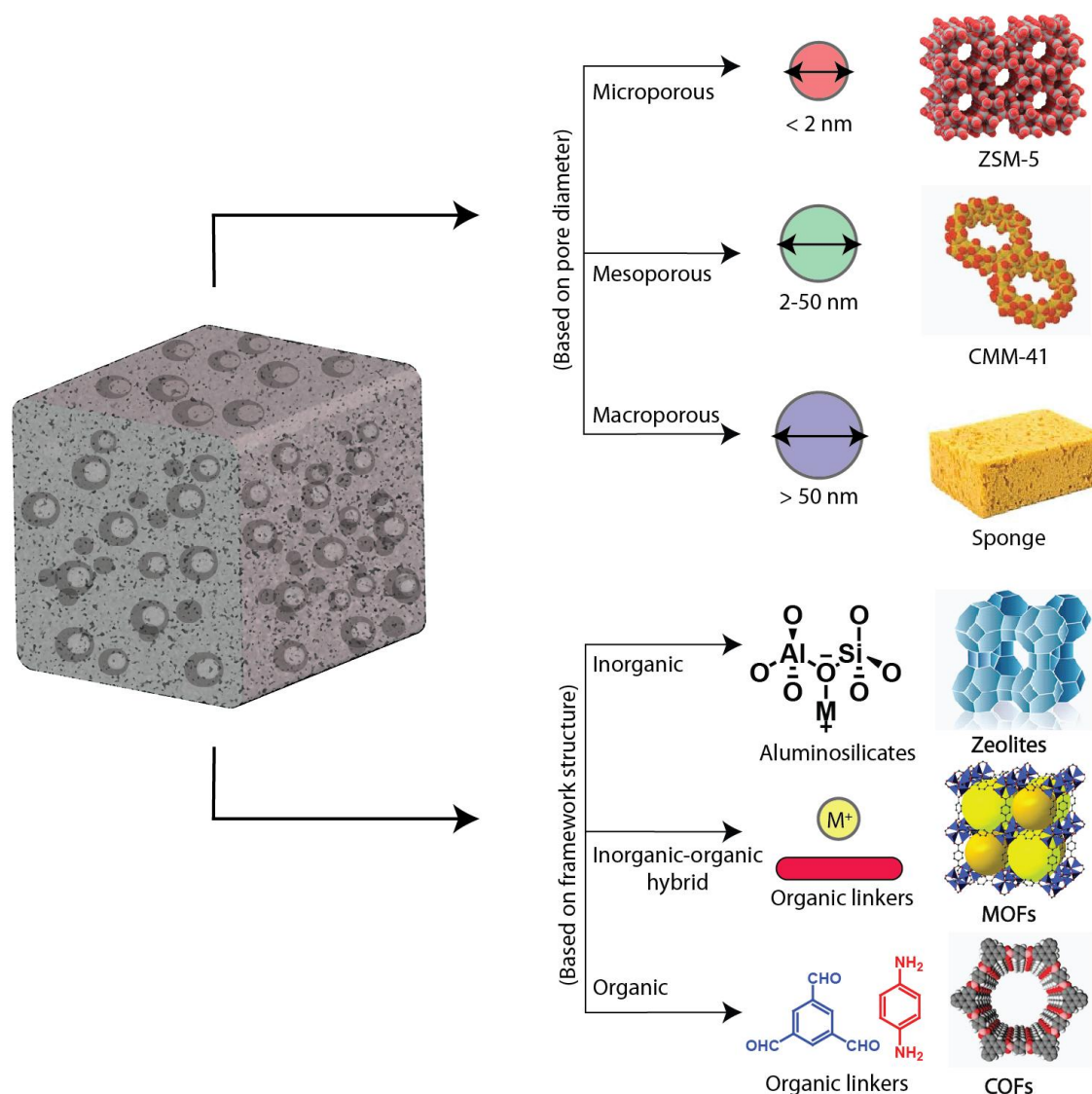


Figure 1.1: Classification of porous material based pore size; and framework structure.

phosphates, sulphides, oxides etc [1.10]. The aluminosilicates, also called zeolites ($A_{x/n}[\text{Si}_{1-x}\text{Al}_x\text{O}_2] \cdot n\text{H}_2\text{O}$) are one of the important materials belongs to this group. Generally, zeolites are formed by the corner sharing of tetrahedral silicate (SiO_4) and aluminates (AlO_4) [1.4]. The resulted ordered microporous nature allows the selective molecular sieving through the framework matrix and hence it is widely used in the heterogeneous catalysis, separation and purification applications. Similar 3D crystalline framework formation has been observed for the Aluminum phosphates (AlPO_4) and Gallium phosphates ($\text{GaPO}_4\text{-C}_n$ ($n = 1-12$)) which exhibits microporous features. The investigations on phosphates delivered a series of

microporous open frameworks such as methyl, indium, boron, beryllium, zinc and transition metal phosphates [1.10]. In addition to phosphate open framework, the researchers look forward to the development of more inorganic porous frameworks like binary metal oxides (eg: MnO_2); silicon nitrides (eg: Si_3N_4), and coordination polymers [1.10]. However, most of these materials in this category have only poor surface area due to the presence of metal atoms.

1.3.2 Porous hybrid Inorganic-organic framework materials:

The pure inorganic porous materials suffer the limitations like poor possibility pre or post functionalization; poor surface area; and lack of structural diversity. The researchers attempt to develop a porous material with structural diversity associated with high surface area lead towards the discovery of 2D or 3D hybrid organic-inorganic framework, called metal organic framework (MOFs) in 1996 [1.5]. The reticular chemistry allow the construction of several structures of MOFs with the desired form by tuning the metal nodes (eg: transition metal ions like Fe; Cu; Zn, p-block metal ions like In; Ga, alkaline metals, and actinides) and organic linkers (carboxylates, phosphate anions, bipyridines, pyridines, imidazolate etc). Furthermore, the manipulation over the MOF to more desired structure could possible through the post functionalization of the linkers [1.11]. Generally MOFs are classified into 1st; 2nd; and 3rd generations. In the 1st generation, MOFs are stable only in the mother liquor and the structure will be collapsed if it takes out from there. The 2nd generation MOFs contains robust framework and hence stable even after the removal of mother liquor. Again, in 3rd generation, the construction of the MOFs using flexible linkers made them more mechanically robust and exhibits changes in porosity by external stimuli [1.12]. The MOFs are extensively used for the storage of gas molecules like H_2 ; CO_2 ; and NH_3 due to the well built intrinsic microporosity and high surface area ($3000\text{-}5000\text{ m}^2\text{g}^{-1}$). The precise integration of the metal and organic units in the framework matrix further helps in catalysis; adsorption; energy storage; and chemical sensing. However, the poor chemical stability of MOFs in different chemical environments like acid or basic condition obstructs the potential utilization of the materials.

1.3.3 Porous organic framework materials:

At the earlier stage of human history, people have used porous carbon materials for the purification of water and medicinal propose. They burned wood; leaf; and different nuts to

produce the porous carbons with high surface area. Porous carbons or activated carbons contain sp^2 carbons network in an amorphous nature with a mesoporous surface area of 1000-1500 m^2g^{-1} [1.3]. Later, more ordered sp^2 carbon networks like graphene, carbon nanotube, carbon nanofiber, graphene oxides have been investigated with advanced properties [1.13]. The excellent electrical conductivity of the materials coupled with the good surface area exhibit potential electrochemical energy storage in supercapacitors and battery devices. Additionally, these materials show their potential utilities in heterogeneous catalysis; chemical sensing; drug delivery; opto-electronics; separation; and adsorption applications [1.13b].

Moreover, the most of intrinsic porous materials contains inorganic elements which cause the heavy density; highly expensive; and toxic towards the environment. Taking these into consideration, scientists tried to construct porous framework materials purely from organic building units. The reticular design approach porous organic framework is similar to the synthesis of MOFs, but may contain only light-weight atoms like H, B, C, N, O, F, S which could provide the low density of the material. The earlier developments of the construction of the porous organic frameworks mainly focused on the convergence of the symmetric organic building units into the framework through different chemical reactions like Suzuki cross-coupling, Sonogashira–Hagihara coupling, cyclotrimerization, Friedel–Crafts arylation, oxidative reactions etc [1.14]. The resulted intrinsic porous materials called porous organic polymers (POP) displayed wide applicability in gas storage; membrane separation; catalysis; energy conversions; adsorbents; sensors; and for nuclear energy capturing [1.23]. However, the irreversible interconnection of the organic linkers in POPs during the chemical reaction causes the amorphous nature of the material. Hence the desired precise integration of building units as well as long-range ordered nanopores are absent in the porous matrix of POPs. In contrast, a novel porous organic framework called hydrogen bonded organic frameworks (HOFs) exhibits long-range single crystal order of the framework [1.24]. The convergence of the organic linkers (eg: Hexakis[4-(2,4-diamino-1,3,5-triazin-6-yl)phenyl]benzene; 2,4-diaminotriazinyl; etc) through the intermolecular hydrogen bonding makes a long-range order organic framework with intrinsic porosity. However, the weak interconnection connected hydrogen bonds (~ 40 $kJmole^{-1}$) in the framework is not stable in high thermal, acidic or basic condition. In these aspects, a robust covalent linkage along with

chemical reversibility is required for the construction of chemically and thermally stable porous crystalline organic framework. In this regard, covalent organic frameworks are the

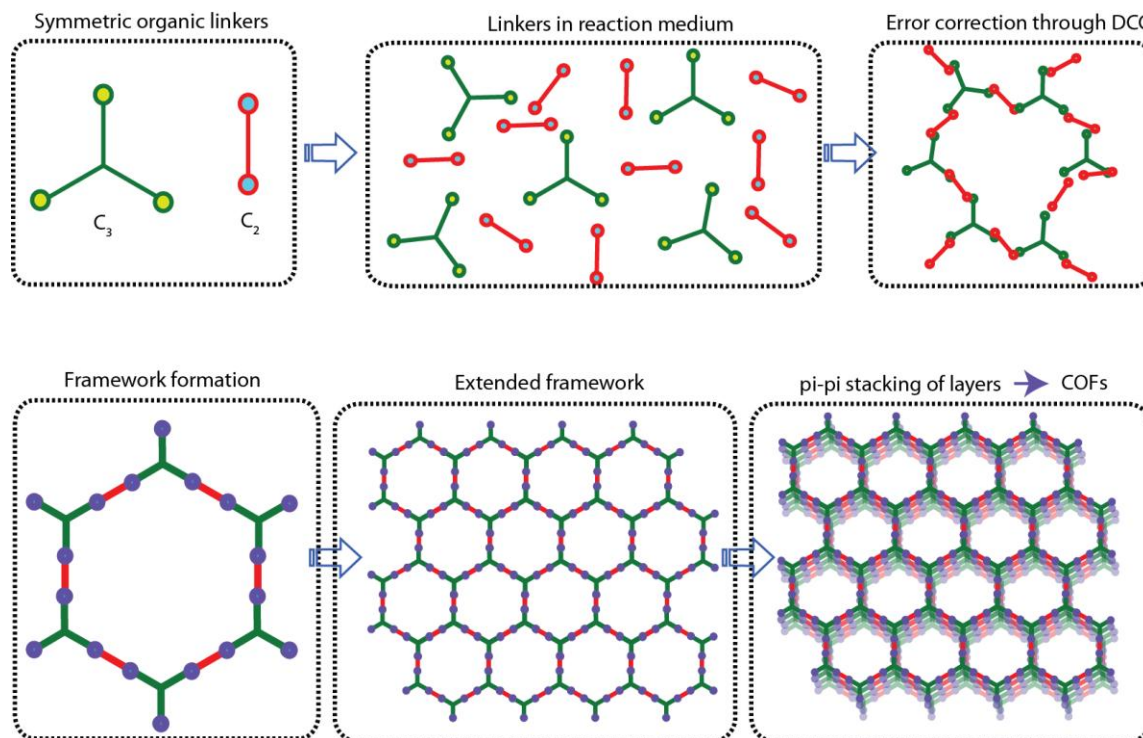


Figure 1.2: The dynamic covalent chemistry of COFs.

novel class of materials with porous-crystalline nature. The structural features and application of COFs have been discussed in the following section.

1.4 Covalent organic frameworks

The precise connection of molecules in an ordered arrangement through the intermolecular interactions results a crystalline material. However, it is difficult to fabricate a crystalline phase by the covalent stitching of molecules due to the strong interconnection ($\sim 340 \text{ kJ mole}^{-1}$) and the irreversible in nature of covalent reactions. In this regard, covalent organic framework, a crystalline porous polymer in which molecules are interconnected by strong covalent linkage brought a paradigm shift in the research of organic crystalline polymers. In 2005, Yaghi and coworkers discovered the first COF based on boronic ester linkage formation between symmetric organic building units. It should be noted that the major role in the formation of crystalline organic polymers is reversible dynamic covalent chemistry (DCC) [1.7 & 1.16]. In DCC, the bond formation between the functional groups has been

occurred in a reversible thermodynamic control rather than the kinetic mechanics, which results most stable thermodynamic product [1.17]. Herein, the reversible bond formation

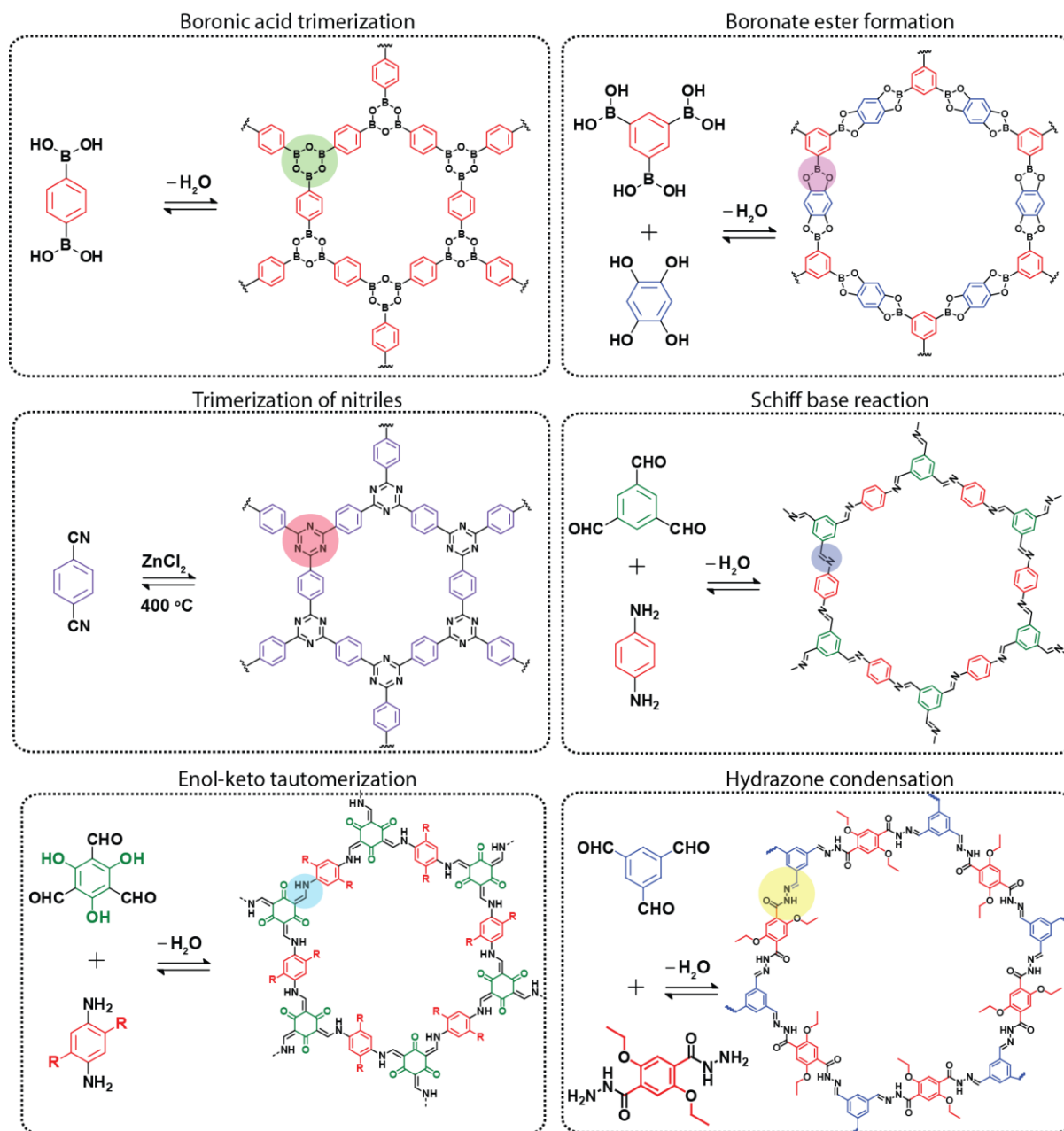


Figure 1.3: The types of COFs formed from different reversible organic reactions.

does the making and breaking of the covalent linkage in a suitable reversible thermodynamic condition which in turn produce maximum error corrections in the framework formation (**Figure 1.2**). The continuous error corrections in the framework formation avoid non-symmetric arrangement of the molecules and finally results an extended framework of the material. On the other hand, the kinetic control of the reaction generally yields the

amorphous material due to the haphazard connection of the building units. It is possible to synthesize 2D and 3D COFs by choosing the suitable symmetric linkers. In general, symmetric organic building units contain Π electron rich aromatic moieties, which help in the Π interaction among 2D layers of the material. Consequently, the extended 2D frameworks pi-pi stacks together in the crystalline matrix which further yields the precise build-up of nanopores. However, in 3D framework, such Π interactions are not available, herein; the structure is a diamond like 3D connection of the organic linkers [1.18]. Hence, the important criteria for the construction of crystalline and porous COFs are: 1) the reversible chemical reaction; 2) synthetic methods; and 3) the nature of the linkers.

1.5 The construction of COFs

1.5.1 Reversible chemical reaction:

The reversible dynamic covalent chemical reactions are the fundamental basis for the construction of the 2D or 3D COF (*Figure 1.3*). In this dynamic process, the reactant molecules are undergone in very slow kinetics and mostly on thermodynamic control help to reach in an equilibrium condition. At this stage, the functional group are reacting in a reversible way of bond making and breaking i.e., self error correction which yields a thermodynamically stable product. The mostly used dynamic covalent reactions for the synthesis of COFs are boronic acid trimerization; boronate ester formation; trimerization of nitriles; Schiff base reaction; aldol condensation; hydrazone reaction; azine reaction etc [1.19].

The first COF was made up of the trimerization of boronic acid aromatic groups into six-member boroxine ring which forms a framework (COF-1) with the pore size of 1.5 nm. In this self-condensation reaction, the two-fold symmetric boronic acid functionalized aromatic groups are undergone a reversible dynamic covalent assembly which yields water as a byproduct [1.7]. COF-102; 103; and Ppy-COF are some other examples of boronic acid trimerization COFs. In another DCC reaction, boronic acid groups were treated with the catechols (OH functionalized benzene) resulted a boronic ester linked COF-5 with pore size of 2.7 nm. Notably, Yaghi and co-workers demonstrated the change in pore size of the framework by the elongation and shortening of the boronic acid organic linkers into different sizes (COF-6: 0.86 nm; COF-8: 1.64 nm; COF-10: 3.2 nm etc) [1.19b]. A wide variety of COFs were demonstrated by changing the core of boronic acids (BTDADA; TPEBA, etc.)

and alcohol groups (1, 2, 4, 5-tetrahydroxybenzene; 2, 3, 6, 7, 10, 11-hexahydroxytriphenylene; etc.). Generally, the boroxine and boronic ester linked COFs are highly crystalline and exhibits excellent surface area. However, the stability of the framework is very poor towards even in a mild acidic or basic condition due to the chemical decomposition of boroxine and boronic ester linkage.

Interestingly, Schiff base is a well known dynamic covalent reaction which was used for the interconnection of organic linkers in COF in 2009 [1.20]. In Schiff base reaction, the aldehyde and amine are condensed to form imine bonds which were strategically used for the construction of the framework with symmetric aromatic organic moieties. The C=N bonds are chemically more stable than boronic esters, especially towards the moisture. Yaghi and co-workers reported the first imine linked COF in 3D structure by the condensation of tetra-(4-anilyl) methane and terephthalaldehyde (TA) in the presence of an acidic catalyst [1.20a]. The obtained 3D framework exhibits a tetrahedral connected ordered material with high porosity. Again, Wang *et al.* reported the first 2D imine linked COF from the assembling of the building units 1, 3, 5-triformylbenzene (TFB) and 1, 4-phenylenediamine (PDA) [1.20b]. Later, a series of novel imine linked COFs were synthesized by using the advantageous of reticular chemistry (eg: COF-LZU1, PI-2-COF, N₂-COF, NUS-14 etc.). Although the chemical stability of imine linked COFs is higher than boronic ester linked COFs, the decomposition of the connected linkers even at lower acidic or basic condition is the main drawback of such type of COFs. Recently, Kandambeth *et al.* demonstrated the synthesis of a series of chemically stable COFs towards lower *pH* [1.21]. They have used 1, 3, 5-triformylphloroglucinol (**Tp**) as a knot for the creation of the framework with different symmetric aromatic amines. The aldehyde groups in the **Tp** moieties react with amine and reversibly form imine bonds. The DCC allows the construction of the imine bonded framework in a symmetric long-range order. However, under thermal treatment, the imine bonds undergo the irreversible keto-enol tautomerism and create a β -ketoenamine framework which is chemically stable towards the acidic and mild basic condition.

Hydrazone bond formation is a different type of reversible chemical reaction which is constituted by the co-condensation of hydrazides and aldehydes. The first example of hydrazone linked COF has been demonstrated by Yaghi and co-workers in 2011 [1.22a]. They have selected 2, 5-diethoxyterephthalohydrazide and TFB are the linkers for the

construction of COF-43 through the hydrazone bond. At the same time, researchers investigated the possibility of azine linked COF formation by taking hydrazine as a linker [1.22b]. The first COF of this was established by Dalapati *et al.* by taking hydrazine and 1, 3, 5, 8-tetrakis(4-formylphenyl)pyrene as building units.

The triazine COFs are one of the most common types, which is composed of the reversible cyclotrimerization of the nitrile organic linkers ($-CN$) [1.23]. However, these cyclotrimerization reactions are carried out at high thermal condition with the presence of $ZnCl_2$ a Lewis acid catalyst which generally yields low crystalline polymers. The first triazine COF (CTF-1; by the condensation of 1, 4-dicyanobenzene) was demonstrated in 2008 by Prof. Arne Thomas and his coworkers. Although the triazine COFs are highly conjugated nitrogen rich framework which have been used catalysis and energy storage, the less possibility of functional diversity is a main disadvantage towards the extended applications.

Meanwhile, many other chemical linkages like borosilicate; squaraine; imide; spiroborate etc. reported for the synthesis of crystalline and porous COFs [1.19]. Notably, Zhuang *et al.* present an olefin linked COF by Knoevenagel condensation reaction of trigonal aldehyde 1, 3, 5-tris(4-formylphenyl)benzene (TFPB) and 1, 4-phenylene diacetonitrile [1.24].

1.4.2 Synthetic methods:

The synthesis of crystalline porous polymers has been carried through the thermodynamically controlled reactions. On the other hand, fast or kinetically controlled reactions lead to the formation of amorphous material due to the lack of continuous error checking. In this regard, it is really important to control the reaction conditions of COF synthesis (**Figure 1.4**) [1.8]. One of the most used and efficient synthetic methods for the construction of COF is solvothermal reactions [1.7]. In this method, the precursors of COFs were partially dissolved into a suitable polar solvent or mixture of solvents in a glass tube and then applied vacuum through freeze-thaw cycles. Afterwards, the sealed tube is undergone thermal treatment for optimum time and temperature. The solvents were usually organic and polar in nature by considering the solubility organic building units. The selection of solvents and the ratios of the mixture are pivotal and need to be optimized for the synthesis of each COF. However, the general solvent combinations are DMAc-toluene; DMAc; DMAc; DMAc; mesitylene-dioxane; DMAc-o-dichlorobenzene; tetrahydrofuran-

methanol-toluene etc. To maintain the reversibility of the reaction, the vacuum has been applied to the reaction vessel and then keeps for the thermal treatment. The obtained precipitate can be washed in different solvents like DMAc, acetone and water for removing oligomers, starting materials and other impurities. It has been noted that the high crystallinity and porosity for the obtained COF after solvothermal synthesis. It could be due to the well-maintained reversibility of the chemical reaction in the solvothermal condition.

Meanwhile, Andrew I Cooper and his coworkers developed a microwave-assisted synthesis of COF-5 and COF-102 [1.25]. In this technique, the COF precursors are mixed in organic solvents in a closed vessel which has been further allowed for the microwave assisted heating for 20 minutes. The main advantage of this fast method is the resulted product contains impurity free COFs and it could further avoid the tedious washing process. However, the fast reactions partially obstruct the self correction process in the reversible reaction hence yielded a less crystalline and porous material.

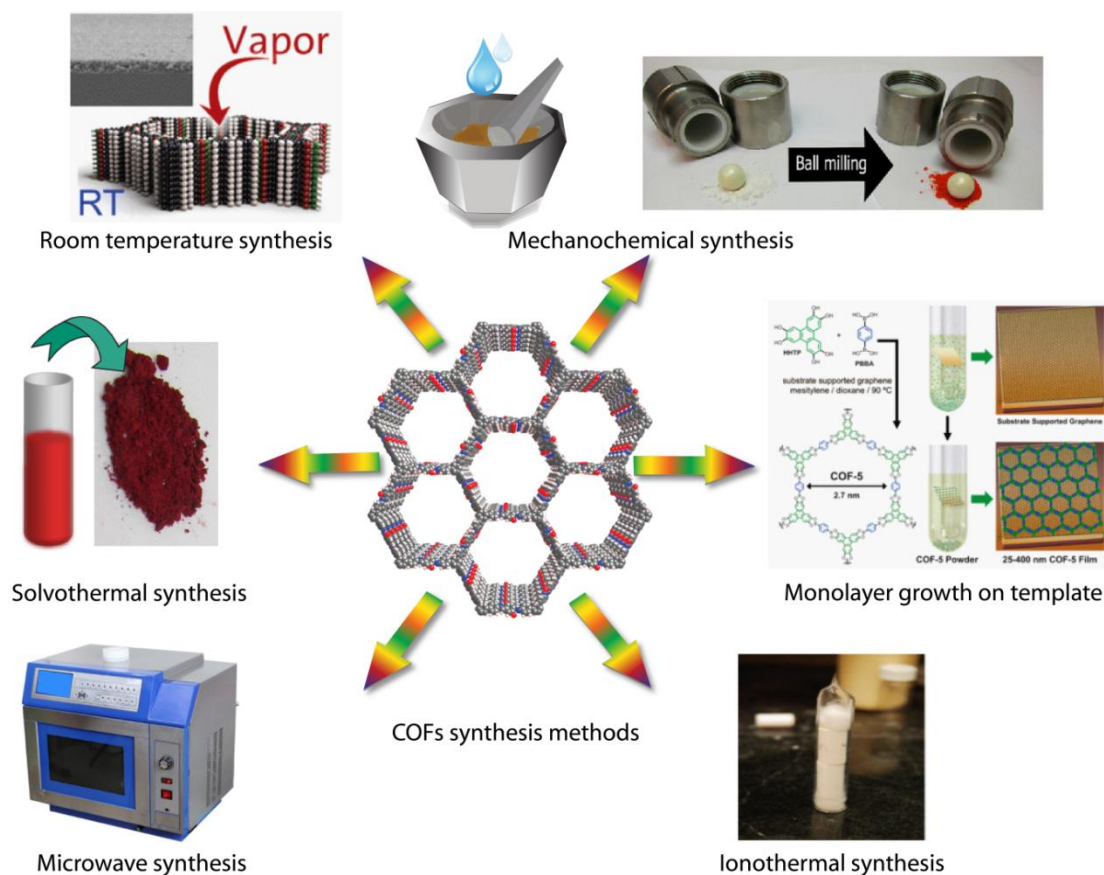


Figure 1.4: Different types of synthetic method of COFs [Room temperature synthesis: [Reprinted with permission from {D. D. Medina et al., *J. Am. Chem. Soc.* 2015, 137, 3, 1016-1019} Copyright

{2015} American Chemical Society] and Monolayer growth of template: Reproduced with the permission of AAAS [J. W. Colson *et al.*, *Science*, 2011, 332, 228].

Another method has been developed for the synthesis of COFs by Prof. Arne Thomas and his group in 2008 [1.23]. They have demonstrated the ionothermal based reaction for the synthesis of covalent triazine framework (CTFs) at a high temperature of 400° C with a presence of ZnCl₂ as a catalyst. The higher temperature causes the melting of ZnCl₂ and the reversible cyclotrimerization occur in the molten state. However, this reaction condition provides a poor crystallinity for the material. Additionally, the limited substrate scope due to the use of high temperature for this reaction inhibits the leverage of functional diversity of COFs.

Most of the reactions have been discussed above deal with the utility of higher energy conditions like temperature and microwave energy. Taking this into consideration, the investigation on the development of the synthesis of COFs at ambient condition is still on. One of the notable researches has been done by Prof. Thomas Bein and co-workers on the synthesis of BTDCOF and COF-5 on a glass surface at a closed chamber at room temperature [1.26]. In this technique, they have kept a solvent mixture mesitylene and dioxane (1:1 ratio) in a glass viol in a closed chamber. The reaction is started to happen when solvent mixture get evaporated and get contacted with precursors of the glass surface. The very slow kinetics allows the formation of an ordered COF thin on the glass surface.

However, the main drawbacks are the long reaction time (72 hours) for the completion of the reaction and large scalability. Recently, Kaushik Dey *et al.* reported an interfacial synthetic method for the fabrication of β -ketoenamine COF thin films at room temperature [1.26b]. They demonstrate the synthesis happens at the bilayer interface of water and DCM solvents. The water layer contains the salt of amine linkers and *p*-toluenesulphonic acid and aldehyde units are dissolved in DCM layer. Herein, very slow kinetics of the reaction allows the formation of crystalline and porous COF thin film at the water-DCM interface after 7 days. Again Prof. Josep Puigmartí-Luis and his team demonstrated a micro-fluid based synthesis of imine-linked COFs at room temperature [1.26c. In the micro-fluid instrument, the reactants and catalyst have been passed through two separate nozzles and then meet in a main channel.

After thorough mixing of the reactants and catalyst, COF was formed and collected from the outlet of the instrument.

Biswal *et al.* depicted the solvent-free green synthesis of series of β -ketoenamine COFs through the mechano-chemical synthesis [1.27a]. The precursor mixture with the presence of catalyst is thoroughly ground at room temperature and then undergone thermal treatment in a closed condition which finally yield COFs. Although this synthetic method is facile and cost-effective, the poor crystallinity and surface area of the obtained COFs are not favorable for the bulk synthesis of high-quality materials. Recently, Kandambeth *et al.* reported a novel strategy in the mechano-chemical grinding for improving the surface area and crystallinity of COFs. They have shown the mechanochemical grinding of precursors with *p*-toluenesulphonic acid as a solid catalyst yields high-quality material [1.27b]. Karak *et al.* proposed a mechanism for this synthetic method, and they observed the thoroughly mixed PTSA-amine results the formation of salts which reduce the reactivity of the amine linkers with the aldehyde [1.27c]. As a result, this slow kinetics promotes the efficient dynamic covalent chemistry in the reversible reaction of amine and aldehyde, and then finally yield a high crystalline and porous COFs. This method has several advantageous like ultra-fast synthesis (~ 1 min); bulk production of high-quality material; cost-effective; and environmentally benign.

1.4.3 Nature of linkers:

The physical and chemical properties of COF were strongly depended on the nature of the linkers used for the construction of the framework. In general, the linkers of COFs are symmetric; aromatic; planar; and rigid molecules for the construction of the crystalline framework [1.8]. The symmetry of the linkers is most important for the fabrication of the desired shape and size of the pores in COF (**Figure 1.5** & **Figure 1.6**). The investigations on several symmetric linkers lead to the use of two-fold (C_2), three-fold (C_3), four-fold (C_4) and six-fold (C_6) for the construction the 2D COF. Additionally, the tetrahedral (T_d) symmetric linker has been utilized for the synthesis of 3D COFs. Notably, the shape of the pore is determined by the symmetry of linkers. The usage of four-fold and two-fold symmetry linkers for the synthesis framework results a square shaped pores in COF. Meanwhile, the reaction of a three-fold knot with two-fold linkers yields a hexagonal pore. The detailed

analysis of the symmetry of the linkers is given below in the **figure 1.5**. It should be noted that the recent researches on the topology of COFs suggest the utility of various novel

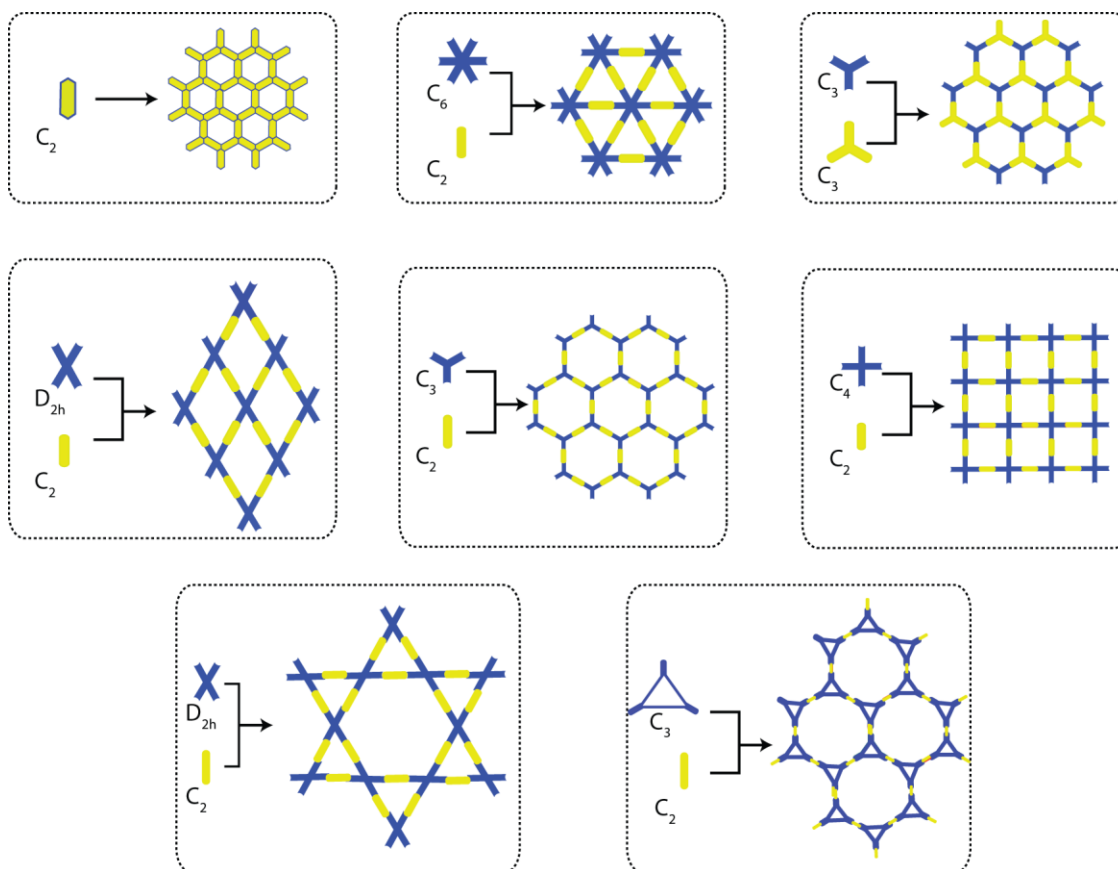


Figure 1.5: Symmetry of the linkers in COFs. The combination of different symmetric linkers decided the pore geometry of the COF.

symmetric and non-symmetric linkers for the construction of the symmetric framework [1.28]. The Π electron rich organic linkers can provide Π - Π interactions among the 2D layers of COF which result a high crystalline and ordered intrinsic pores. The lack of Π - Π interactions cause the inefficient self-assembly of the covalently stitched framework which further leads to the haphazard arrangement of layers. These kinds of materials generally will not exhibit any crystallinity and surface area due to the lack of ordered arrangement. In a thermodynamic concept, the self assembling of individual layers of COF by Π - Π stacking happen in the reaction condition for decreasing the entropy of the system, and gain a lower energy state. Moreover, the planarity and rigidity of the linkers enhance the efficiency of the Π - Π interaction of the COF layers in proper stacking mode. The control over the pore size is an important property of COFs which can be done by changing the size of the linkers. It is

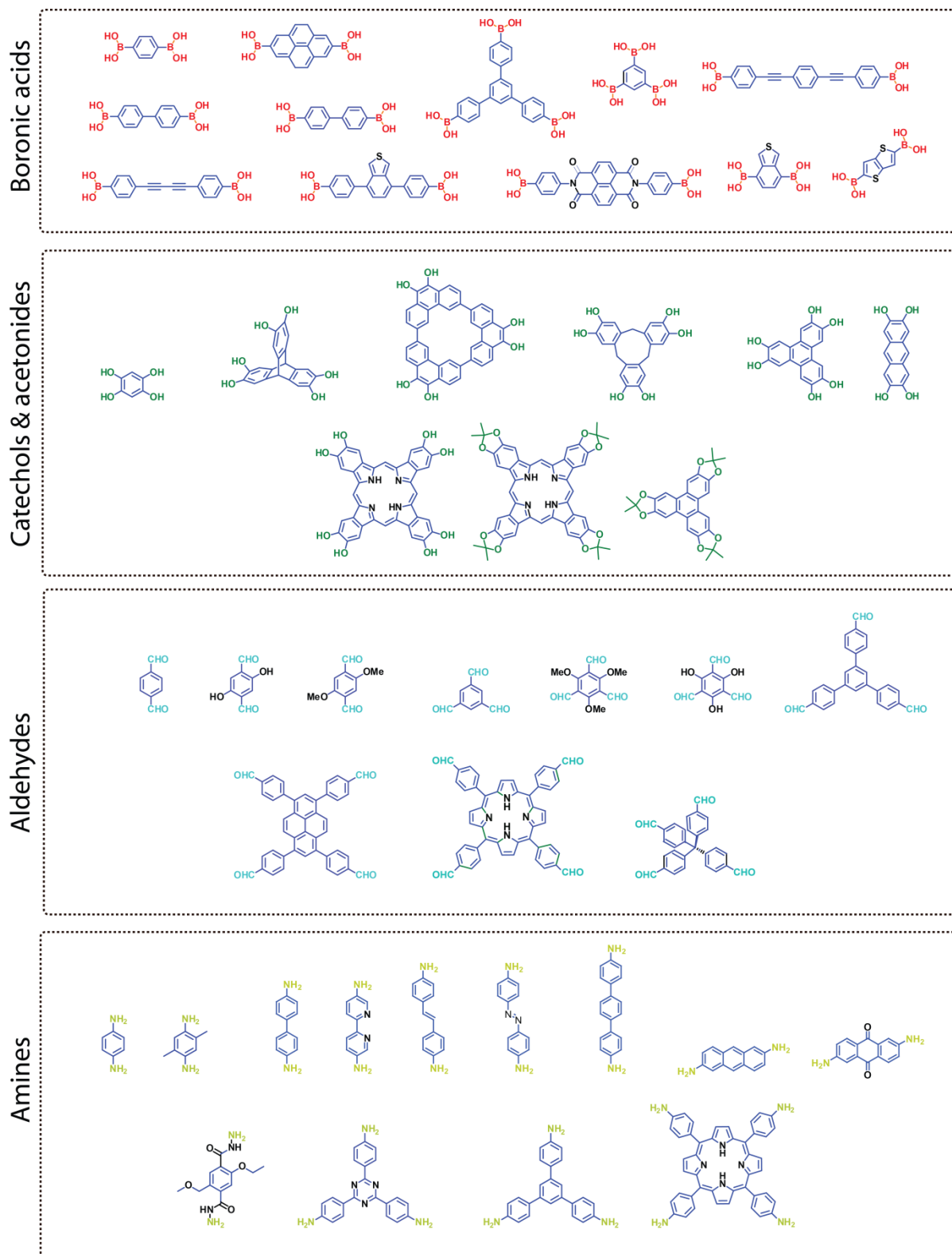


Figure 1.6: The different types of linkers used for the construction of COFs.

possible to tune the pore size from 0.5 nm (microporous) to 5 nm (mesoporous), considering the longer size of the linker result a larger pore size and vice versa [1.29].

1.6 Properties of COFs

The exceptional structural features of COFs provide many advantageous like crystallinity; tunable porosity; functional diversity; thermal and chemical stability; and low density (**Figure 1.7**). As mentioned previously, the crystallinity of COFs originated from the favorable slow reaction kinetics and then Π - Π interaction of the individual layers. A crystalline COF is an ordered structural material with many electron density planes (eg: 100; 110; 001 etc.). When it has been exposed to the X-ray energy, it could undergo the

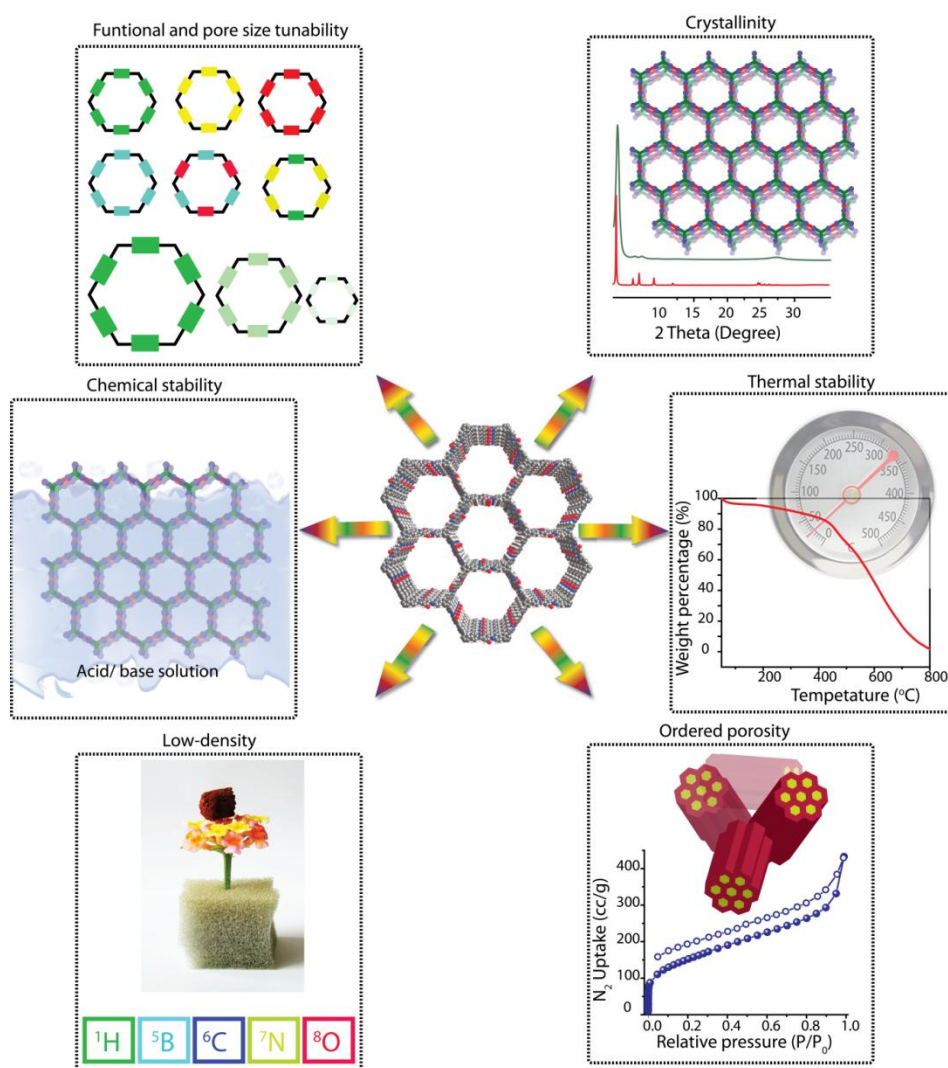


Figure 1.7: Properties of COFs.

diffraction process and display a well crystalline pattern in the PXRD profile. In 2D-COFs, the layer stacking could be occurred in eclipsed, near eclipsed and staggered mode which depends on the crystallization behavior of each COFs [1.7]. However, the single crystal formation of COF is a difficult task due to the strong covalent linkages allows the growth of ordered framework in a limited nanometer sized dimension. The recent research on the development of defect-free crystal growth of COFs result the micrometer sized crystals of 2D COFs by a seeded growth approach [1.30]. Interestingly, a modular strategy helps to the growth of single crystal of a series of imine-linked 3D COFs which has been reported by Omar Yaghi and Wei Wang [1.31].

Additionally, the design of COF with desired functional groups by the pre or post functionalization enhances the library of functionally diverse materials. The chemical properties such as pseudocapacitance; sensing; chemisorptions; catalysis; drug-delivery are largely depending on the functional moieties present in the COFs. The functional control over the COF allows the construction of the framework according to the specific desired applications. The functional groups can be attached on the top surface as well as on pore walls of COFs. The post-modification of COFs aids to bring unlimited functional varieties into the COFs without hampering the crystallinity and porosity of the materials. Moreover, COFs exhibit relatively higher thermal stability (400-500° C) compared to their monomer counterpart. It signifies potential utility of thermally unstable functional groups at high temperature without any thermal degradation when it has been stitched into a COF. The low weight density of COFs is due to their light-weight elemental compositions like C; N; O B; and H. It further helps in the easy carrying of the material and potential candidacy towards gravimetric basic applications like energy and gas storage. Again, the main advantage of COFs over other porous materials is the extraordinary chemical stability towards acidic or basic condition. Several strategies were developed for improving the chemical stabilities of covalent organic framework like pyridine doping; bulky group functionalization; incorporation of keto-enol tautomerism; and introducing OMe groups in the linkers [1.21, 1.31]. These latest researches suggest the chemical stability of COF surpasses even at 18M H₂SO₄ acid and 18M NaOH. It points out the potential utility of COFs in several commercial level applications without losing characteristic features of the material in harsh condition [1.31b].

1.7 Applications of COFs

1.7.1 Gas storage:

Covalent organic frameworks exhibit remarkable storage of gas molecules in their intrinsically built nano pores. The pore size of the COF matrix is suitable to accommodate

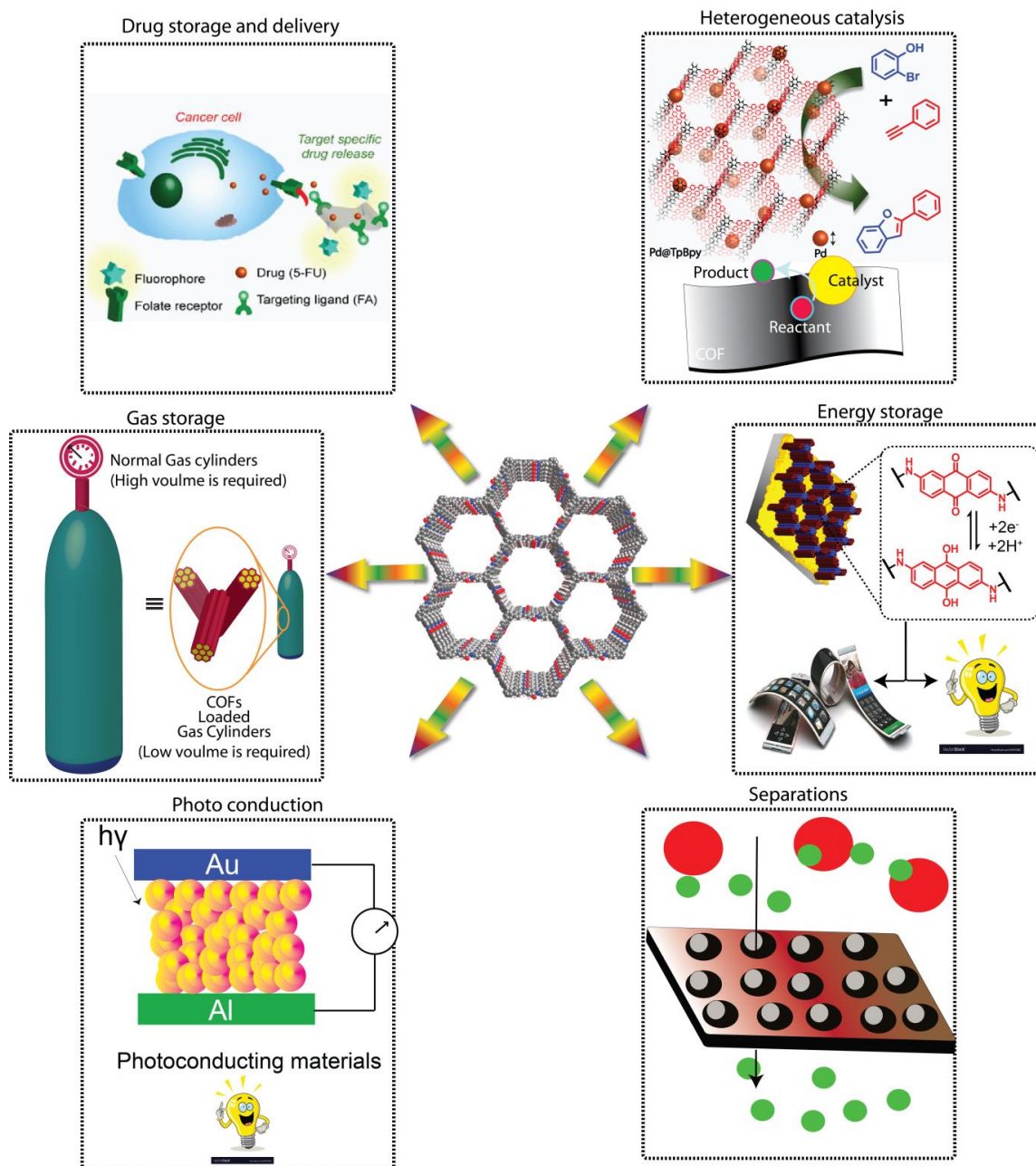


Figure 1.8: Different types of Applications of COFs.

gas molecules like H_2 ; CO_2 ; NH_3 ; and CH_4 which are potentially relevant to the commercial proposes. Considering to the high energy density performance of hydrogen, it has been

appraised as the most desirable energy fuel for the automotive industry. However, the low boiling point and explosive nature require safe storage of the hydrogen gas molecules for the energy-based applications. The dangerous situation of storing hydrogen at high pressure in cylinders is not recommendable due to the above concerns in automotive applications. In this regard, it requires an efficient adsorptive matrix for the occupation of these gas small molecules for avoiding such problems [1.32]. In this aspect, the microporous COFs have been successfully demonstrated as a hydrogen storage adsorptive material. A 3D COF known as COF-102 with 1.2 nm pore size has shown the hydrogen uptake capacity of 7.24 wt% at 77 K and 1 atm [1.18]. Although several COFs are reported as the adsorptive matrix for hydrogen fuel at 77 K, the most required room temperature condition for the adsorption is not yet satisfied.

Similarly, COFs have been used for the adsorption of another commercially important methane gas molecule which is widely accepted as an efficient fuel for the vehicles. In general, the need of high pressure (200 bar) for the storage methane at the room temperature in the regular storage tanks in vehicles create a high-risk environment. In this regard, the utilization of the microporous COFs could bring down the pressure for the storage methane up to 50 bar. Interestingly, COF-102 display the methane storage of 187 mgg^{-1} at 35 bar and 298 K [1.33].

Nowadays, the upraised ejection of greenhouse gas like carbon dioxide from automobiles and industries turns into important concerns of global warming and health issues. In this aspect, the ongoing research investigations introduce the potential applicability of microporous COFs for the removal CO_2 at the room temperature. COF-102 exhibits an excellent removal CO_2 (27 mmolg^{-1}) at 298K and 35 bar which is higher than most of the zeolites and MOF-5 [1.33]. Theoretical investigations suggest the doping of lithium in the porous matrix of the COF can enhance the adsorption carbon dioxide to a great extent [1.34].

Moreover, the exceptional uptake of industrially important precursor ammonia gas molecules by COF signifies the high standard of them among other porous materials [1.54]. The boronic ester linkage of the COF-10 enhances the interaction of the ammonia through Lewis acid-base interaction. The Lewis acid boron in COF could chemically interact with the Lewis base ammonia which amplifies the efficient storage of them at the ambient condition (1bar

pressure and 298K temperature). Moreover, desorption of ammonia has been noted at the higher temperature points out the recyclable use of the COFs [1.35].

1.7.2 Heterogeneous catalysis:

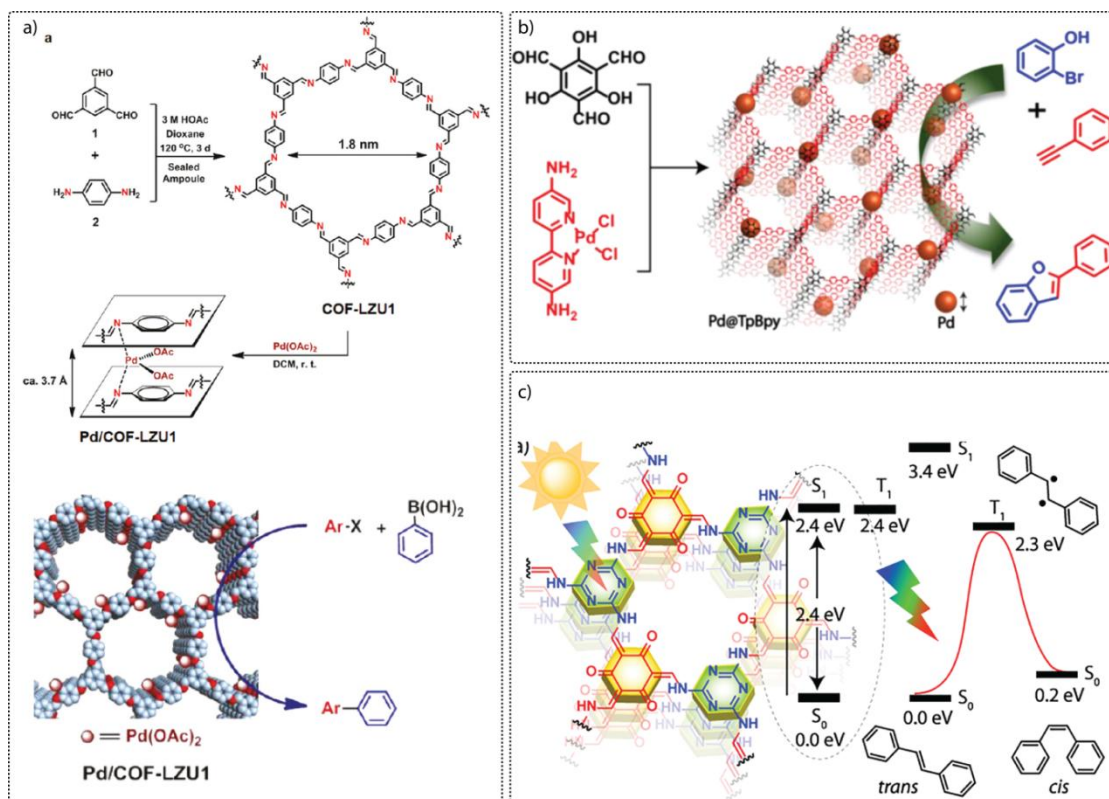


Figure 1.9: a) Incorporation of Pd²⁺ into the interlayer of COF-LZU1 [Reprinted with permission from {S. Y. Ding et al., *J. Am. Chem. Soc.*, 2011, 133, 19816} Copyright {2011} American Chemical Society]; b) In situ generation Pd nanoparticles in TpBpy COF [Reprinted with permission from {M. Bhadra et al., *ACS Appl. Mater. Interfaces*, 2017, 9, 13785–13792} Copyright {2017} American Chemical Society]; and c) Photocatalysis by using COF [Reprinted with permission from {M. Bhadra et al., *J. Am. Chem. Soc.* 2019, 141, 15, 6152-6156} Copyright {2019} American Chemical Society].

The COFs have been used for several catalytic reactions as a support and even as a catalyst itself [1.36]. Notably, the heterogeneity of COFs originated from the insolubility and the chemical stability in the reaction medium. The predesigned nature of COFs promotes the desired functional groups and linkage in the framework which can show the catalytic activity or act as the anchoring sites for the external catalyst. It is possible to functionalize a catalytic active site into the framework by post-modification reaction. Additionally, the pre-integrated nanopores enhance the lucid movement of the reactants through the entire porous matrix of

COF. The first report on the COF based heterogeneous catalysis by Wei Wang *et al.* demonstrate the incorporation of Pd²⁺ units into an imine linked COF (COF-LZU) exhibits an efficient Suzuki-Miyaura coupling reaction [1.36a] (**Figure 1.9a**). Rahul Banerjee and co-workers present the immobilization of catalytic Pd and Au nanoparticles on the porous β -ketoenamine based COF matrix (TpPa-1) which exhibits effective catalytic activities in C-H activations as well as C-C coupling reactions [1.36c]. Again, Bhadra *et al* introduce the utility of bipyridine linked COF for the *in situ* generation of Pd nanoparticles during the synthesis of COF. As a result, it displays excellent catalytic activity towards the synthesis of 2-substituted benzofurans from 2-bromophenols [1.36f] (**Figure 1.9b**). Recently, COFs were used as metal-free organo-catalyst by the post-modification reaction of achiral framework into chiral framework. The decoration of the chiral moiety on the pore-walls enhances the catalytic activity of chemically stable imine-linked COF [1.36g]. Additionally, the researchers developed the applicability of COFs in photocatalysis by controlling the HOMO-LUMO gap of the material (**Figure 1.9c**) [1.36e]. Notably, the utility of such frameworks in electrocatalysis gain tremendous scientific attention especially for hydrogen evolution; oxygen reduction; and CO₂ reduction reactions.

1.7.3 Energy storage:

The rapid consumption of non-renewable energy sources like fossil fuels have drawn major attention towards the requirement of sustainable energy resources and storages. Supercapacitors and batteries are the two devices undergone extensive research in past few decades as superior energy storage systems [1.37]. Supercapacitors also called ultracapacitors are viewed as outstanding devices in terms of greater power density, high charge-discharge and long-life than battery. However, the batteries are considered as high energy density source for the real-life and commercial applications. Both devices are structurally similar and contain two electrodes; electrolyte; and a separator. Notably, COFs could serve as excellent energy storage materials due to the inherent ordered & controlled nanoporous structure and pre-designed tunable redox functionality [1.38]. In contrast, those advantages are absent in the conventional amorphous carbon based materials used for the energy storage applications. The versatile properties such as tunable & ordered pore structure and the higher surface area of COFs offered to use as an electrode material in energy storage systems (**Figure 1.10**). Interestingly, COFs can accommodate 2 types of charge storage mechanisms: 1) electric

double layer capacitance which is mainly played by the surface area of the electrode, 2) redox capacitance due to the redox active functional groups present in the framework. Dichtel *et al.* demonstrate the use of anthraquinone stitched β -ketoenamine framework (DAAQ-TFP) for the electrochemical charge storage application [1.38a]. Herein, the redox-active anthraquinone linker is responsible for energy storage through the interaction with the H^+ ions in the electrochemical condition. Again, Bo Wang *et al.* introduce the exfoliation of

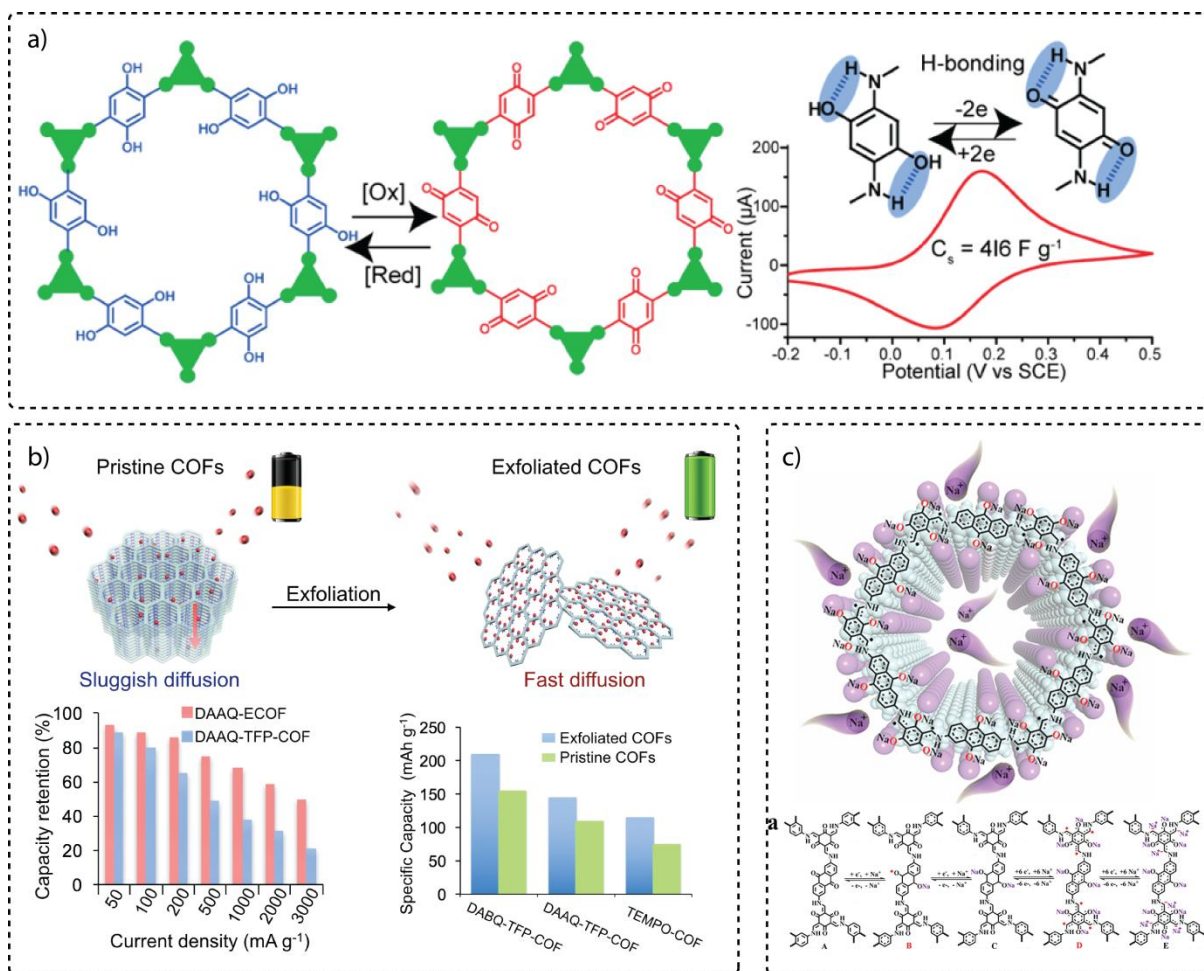


Figure 1.10: a) Hydroquinone stitched COF for supercapacitance [Reprinted with permission from {S.Chandra *et al.*, *Chem. Mater.* 2017, 29, 5, 2074-2080} Copyright {2017} American Chemical Society]; b) Exfoliated COF for Li^+ ion battery [Reprinted with permission from {S. Wang *et al.*, *J. Am. Chem. Soc.* 2017, 139, 4258-4261} Copyright {2017} American Chemical Society]; c) Anthraquinone stitched COF for Na^+ ion battery [Reprinted with permission from {S. Gu *et al.*, *J. Am. Chem. Soc.* 2019, 141, 24, 9623-9628} Copyright {2019} American Chemical Society].

DAAQ-TFP COF into CONs for the enhanced Li^+ ion uptake in battery [1.38e]. Herein, they have presented the exfoliation causes the increase in the diffusion of Li^+ ion through the COF

matrix and subsequent efficient charge storage (**Figure 1.10b**). The fabrication of DAAQ-TFP COF into nanometer thick film on gold support enhances the capacitance performance of the material. Donglin Jiang *et al.* reported a novel COF with a redox-active radical functional group ([TEMPO]_{100%}-NiP-COF) for the charge storage in supercapacitors [1.38c]. Interestingly, DAAQ-TFP COF has been utilized as the anode material in sodium ion batteries. The C=O of β -ketoenamine and anthraquinone participates the interaction with Na⁺ ion (**Figure 1.10c**)[1.38b].

1.7.4 Optoelectronics and semi conduction:

The 2D extended frameworks (XY plane) of COFs self-assembled into a 3D column (Z axis) by the Π - Π stacking of the organic building units present in the polymeric material. The regular fashion of Π - Π stacked column provide an environment of the overlapping the Π orbitals of the 3D arranged layers which faster the movement of electrons through it. In this aspect, the strategically selected suitable building units into the framework can make a HOMO-LMO gap, which is responsible for the electronic movement upon the irradiation of light or under an electric potential. The first example of the optoelectronic COF has been reported the group of Donglin Jiang and coworkers [1.39a]. They have designed a pyrene-2,7-diyldiboronic acids connected framework through boronic acid trimeriazation reaction (PPy COF). The Π electron rich pyrene moiety (Py) could bring the electrical generation in the matrix by carrying the charge in the vertical direction (Z axis) upon the visible light irradiation on COF (5 nA). They controlled the wavelength of the light radiation for the generation of electricity by tuning the conjugated functional group in the framework. They decorated the framework with porphyrines and phthalocyanine building molecules for increasing the wavelength maximum towards the infrared region [1.65]. Additionally, the latest reports point out the change in the metal ion center such as Cu²⁺; Zn²⁺; and Ni²⁺ could alter the hole or electron transport property of covalent organic framework [1.39c].

1.7.5 Purification and separation:

The functional porous matrix of COF displayed as an excellent adsorptive platform for the inorganic and organic chemicals. The efficient removal (169 wt%) of organic dye like

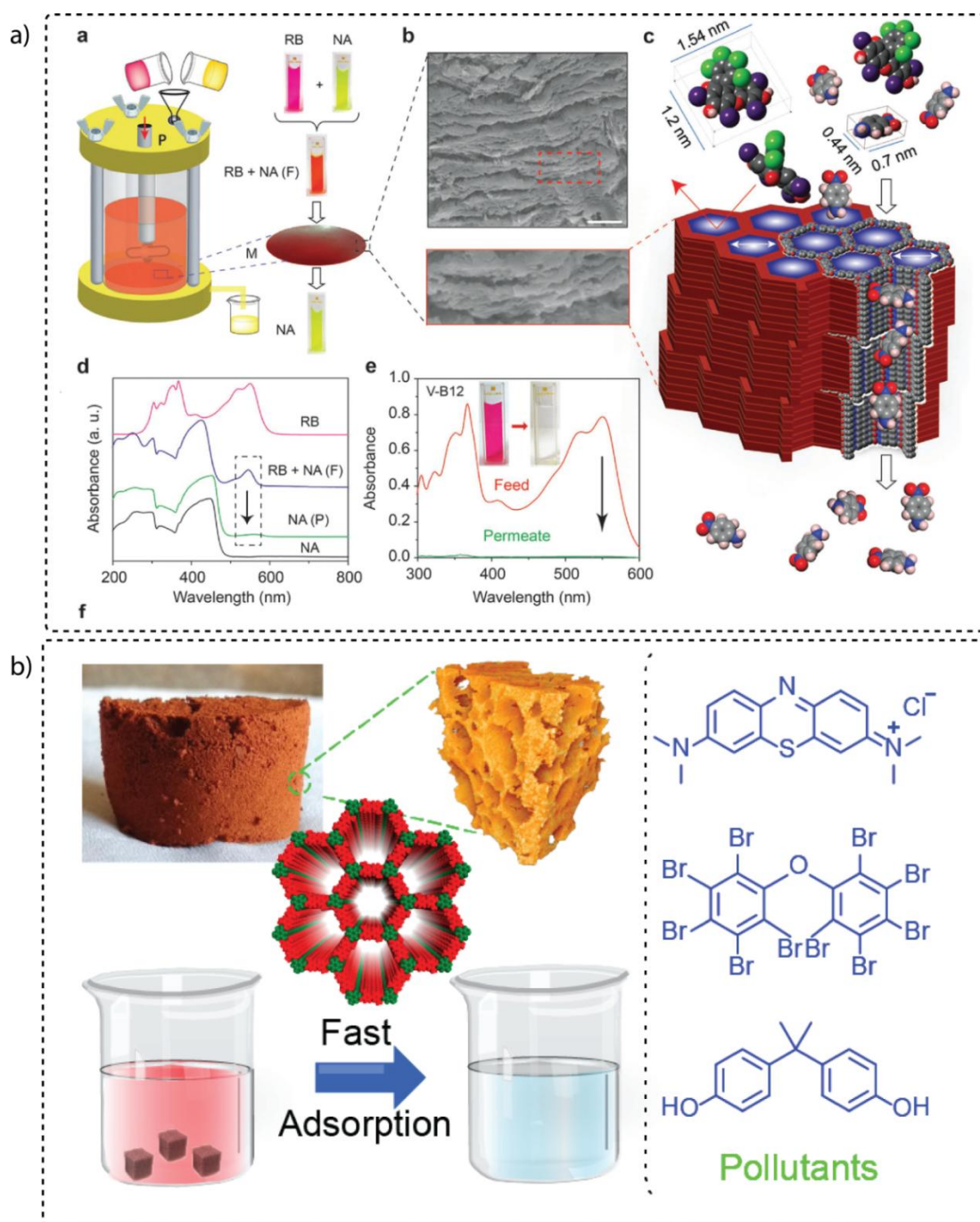


Figure 1.11: a) COF membrane based water purification [Reprinted with permission from {S. Kandambeth et al., *Adv. Mater.* 2017, 29, 1603945} Copyright {2017} American Chemical Society]; b) COF foam based water purification [Reprinted with permission from {S. Karak et al., *J. Am. Chem. Soc.* 2019, 141, 18, 7572-7581} Copyright {2019} American Chemical Society].

methylene blue has been done by imide-linked COF TS-COF-1 [1.40a]. Again, the presence of heavy metals like mercury in drinking water is an important concern due to severe health risk. In this regard, researchers developed an imine linked COF which is constructed from the

building units 1, 3, 5-tris(4-aminophenyl) benzene and *p*-phenylenediamine functionalized with a methyl thio group for the mercury adsorption from water [1.40b]. The adsorption capacity studies suggest the remarkable uptake of Hg by the COFs through the interaction of the Hg with 76% of methyl sulfur moieties (734 mg g^{-1}). Again, a post-modification of COF-V (constructed from 2, 5-divinylterephthalaldehyde and 1, 3, 5-tris(4-aminophenyl) by 1, 2-ethanedithiol through 'thio-ene' click reaction leads to the excellent Hg uptake of 1350 mg g^{-1} [1.40c]. Also it exhibits a high selectivity towards different metal ions like Pb^{2+} , Cu^{2+} etc. Again Karak et al. reported the rapid removal of organic and inorganic micropollutants from water by using COF foams [1.9] (**Figure 1.11b**). Additionally, the COFs are also used for the separation of industrially relevant separation of gas molecules. Prof. Yanan Gao and coworkers reported H_2/CH_4 and N_2/H_2 separation by using COF-320 on a porous alumina support [1.40d]. The further advancement COF as a membrane-based purification has been successfully shown by Knadambeth *et al* by the fabrication of self-standing covalent organic framework membrane (COMs) for the separation of micropollutants in water (**Figure 1.11a**). In this strategy, they have explored the advantage of intrinsic microporosity of the COFs for the size-dependent molecular sieving of the organic micropollutants (methylene blue; rose Bengal; congo red etc) [1.27b].

1.7.6 Drug storage and delivery:

The tunable porosities of COFs with the high surface area make them a good platform for the occupancy of drug molecules. Researchers utilized the COFs for various drug delivery applications by taking the opportunities ease of loading and the functional interaction advantages. Notably, PI-COF-4, a 3D polyimide COF, has been reported as ibuprofen (IBU) drug carrying COF with a maximum loading of 20 wt% [1.41a]. Similarly, an imine linked hollow sphere COF with an excellent surface area has been successfully performed as a storage carrier for trypsin enzyme [1.41b]. The mesoporous hollow sphere could uptake the trypsin molecules into sphere cores with a maximum loading of $15.5 \text{ } \mu\text{mol g}^{-1}$.

1.8 The significance of macro-architecture of the covalent organic framework

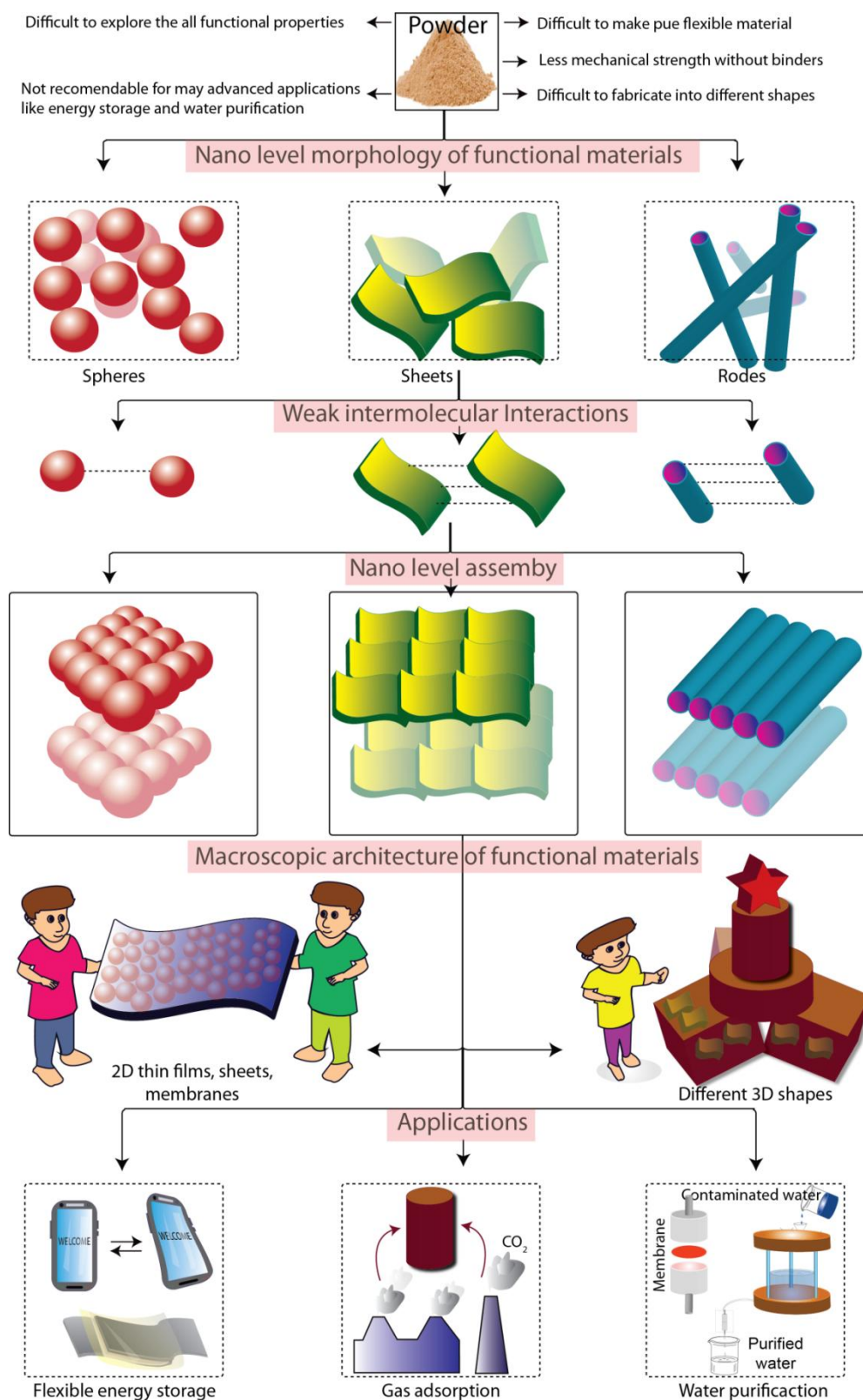


Figure 1.12: The macroscopic architecture of functional materials and their possible applications.

The judicious manipulation of atoms or molecules in a particular material is an important aspect for bringing excellent properties and applications. In the earlier section of the introduction, we have discussed diverse functional porous materials and porous framework materials. Importantly, the properties of the bulk form of these materials strongly correlate with the distribution of atoms or molecules in the nano and micro level of the materials. However, most of the cases the bulk form of the materials featured as powder or granular in nature. It could be due to the lack of interaction between the particles in the nano or micro level of the material. For example, porous carbons are generally exhibited as granular nature due to the lack of interaction of carbon particles in the nano form. However, the advanced technologies in electronic devices; separation; and purification required the macroscopic architecture of the materials in 1D wire forms; 2D thin films; membranes; and different types of 3D architectures [1.42] (**Figure 1.12**). Taking these into

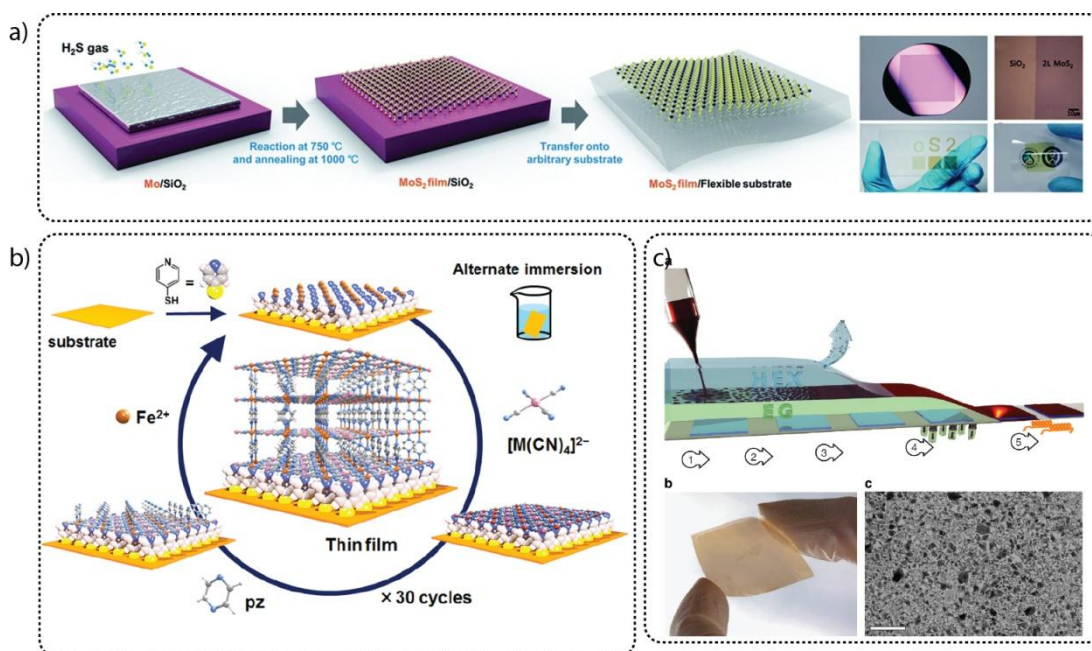


Figure 1.13: Thin film fabrication of a) MoS₂ [Y. Lee et al., *Nanoscale* 2014, 6, 2821 .Reproduced with permission. Copyright 2014, Royal Society of Chemistry]; b) MOF [Reprinted with permission from {T. Haraguchi et al., *Inorg. Chem.* 2015, 54, 11593–11595} Copyright {2015} American Chemical Society]; c) WSe₂ [X. Yu et al., *Nat. Commu.* 2015, 6, 7596. Copyright (2015) Nature Publishing Group].

consideration, scientists tried to develop the macroscopic architecture of different functional materials in to various dimensions. The macroscopic assembling of amorphous polymers like plastics; nylon; and rubber is well established and they are applied in commercial applications by taking their greater possibilities of the fabrication of different shapes and low-cost. However, these materials have limited utilities in the advanced applications like catalysis; sensing; photonics; energy storage; energy conversions etc.

1.8.1 The attempts to fabricate macroscopic architecture of the functional materials:

Nanoparticles:

Keeping these in perspective, the research interests turn to the macroscopic assembling of novel functional materials like nanoparticles which have only the particle size less than 100 nm. Notably, the robust thin films of nanoparticles like TiO_2 ; SiO_2 etc were successfully fabricated for photonic; superhydrophilic coating; energy conversion applications [1.43]. It is

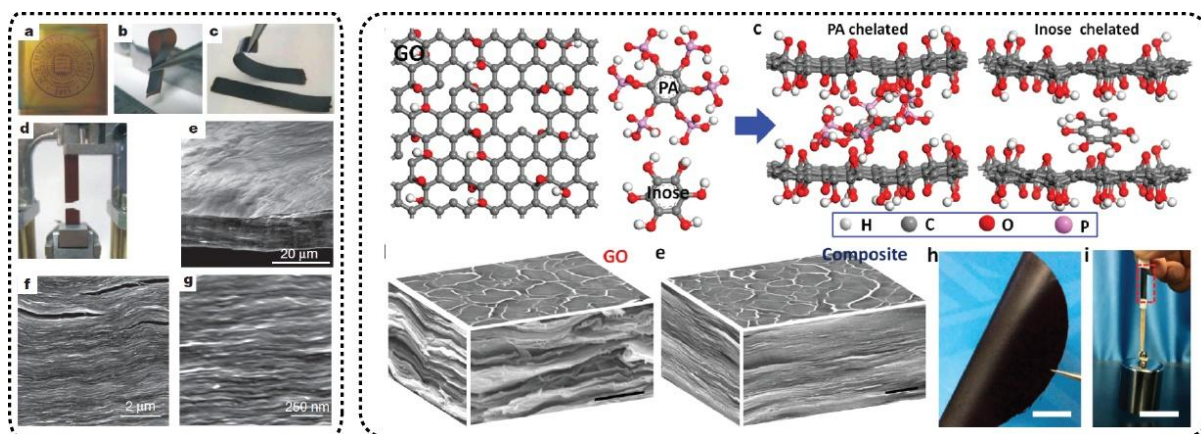


Figure 1.14: Thin sheet fabrication of graphene oxide. a) [D. A. Dikin et al., *Nature* 2007,448, 457–460 Copyright (2007) Nature Publishing Group] & b) [Reprinted with permission from {K. Chen et al., *ACS Nano* 2018, 12, 54, 269-4279} Copyright {2018} American Chemical Society].

to be noted that fine tuning of the morphology of the nanoparticles can affect the physical and chemical properties of the macroscopic thin film forms. Although nanoparticles properties can vary with size, the limited functional opportunities made them not suitable for wide range of relevant application.

Supramolecules:

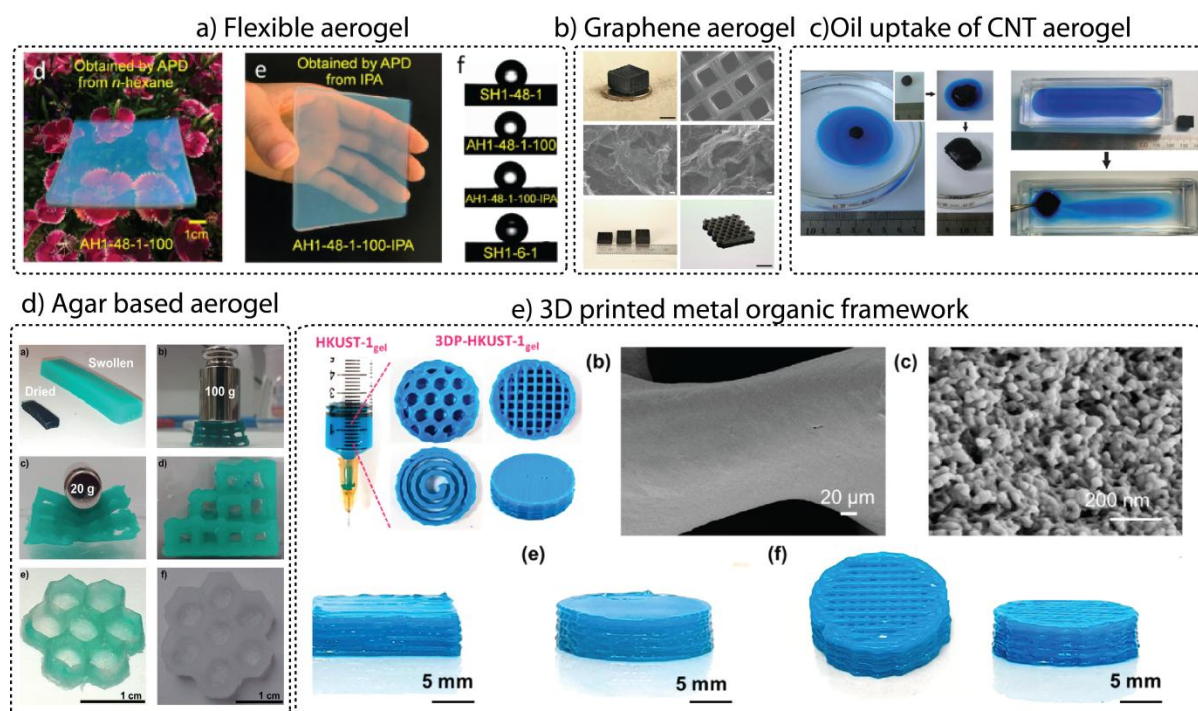


Figure 1.15: 3D architecture of different materials. a) [Reprinted with permission from {G. Zu et al., *ACS Nano*, 2018, 12, 1, 521-532} Copyright {2018} American Chemical Society]; b) [X. Zhu et al., *Nat. Commu*, 2015, 6, 6962. Copyright (2015) Nature Publishing Group]; c)[X. Gui et al., *Adv. Mater.*, 2010, 22, 617–621. Copyright (2010) Wiley VCH]; d) [J. Wang et al., *Angew. Chem. Int. Ed.* 2018, 57, 1 – 5. Copyright (2018) Wiley VCH]; e) [Reprinted with permission from {G.J. H. Lim et al., *ACS Materials Lett.* 2019, 1, 147–153} Copyright {2018} American Chemical Society].

Whereas, the judicious synthesis of desired organic molecules can offer diverse functional opportunities, however, the macro assembling of simple molecules into a large size object would be difficult due to the lack of enough interactions. In this regard, supramolecular chemistry offers the organization of the functional molecules into a macroscopic object through inter organic and inorganic molecule weak interactions [1.44a]. The availabilities of a large number of inter and intramolecular weak forces between the molecules promote self-assembling of the material into 2D and 3D forms [1.44]. The manipulation of the shapes and dimensions of the supramolecular assembly can be controlled by the rich non-covalent interaction among the molecules. Supramolecular thin films are often fabricated on supports or at the solvent-solvent or solvent-air interfaces. The 3D architectures of supramolecular gels were constructed by the cross-linking functional molecules by non-covalent interactions like hydrogen bonding; electrostatic interaction; metal-ligand interactions; and host-guest interactions. Particularly, supramolecular gels are considered as a novel class of smart

functional soft materials considering to their unique physicochemical properties such as self-healing nature; stimuli-responsive; bioactivity; and biodegradability [1.44c & d]. Furthermore, due to the weak non-covalent interaction of functional moieties helps the material to form a smart responsive behavior towards different external stimuli such as heat; light; and sound. However, the lack of intrinsic permanent porosity; and poor chemical and thermal stabilities of supramolecular assembled structures hinder the utility of the material in real life condition at high temperature; varying pressure; and at different acidic and basic environments. It could be due to the weak organized structure of the supramolecules, in which small external disturbances can rupture the weak bonds which leads to the collapse the bulk material happen and property won't be regain.

Porous carbons:

In this regard, the porous carbon materials are known for their chemical and thermal stability for applications like energy storage and physicochemical adsorptions. Additionally, the research of the macroscopic architecture of porous carbon-based material extended to 2D thin films; thick sheets; membranes; and 3D aerogels. The invention of atomic level thick 2D graphene layers further has been assembled to large scale thin film on different supports and also in free-standing sheets [1.42 & 1.45] (**Figure 1.13**). The exceptional features like semiconductivity; catalytic activity; and energy storage properties of these materials successfully have been applied in many fields. Meanwhile, the hetero group functionalized graphene oxides (GO) are developed as thin films and thin sheets through layer by layer assembly at the water-air interface [1.46]. Again, the reinforcement of the mechanical strength of the GO membrane has been achieved after the incorporation of strong interactive functional groups [1.46c] (**Figure 1.14**). Interestingly, the reduction of the GO into reduced graphene oxide (rGO) regains the potential electrical conductivity property and has been applied in many electrochemical applications. The graphene membranes were successfully utilized for the gas separation; water purification; and solvents separation applications. Similarly, thin sheets of graphene have been used for the flexible energy storage devices like supercapacitors and battery. Interestingly, researchers could develop the 3D architecture of such porous carbon material in the macroscopic form, and are called as aerogels. Graphene aerogels are gaining increasing attention due to the special porous features with high electrical conductivity and till now it is the lowest density material found in the history

(**Figure 1.15b**). Importantly, the graphene oxide aerogels are 3D printable due to the matching viscosity and shear stress [1.46d] (**Figure 1.15c**). Due to low density and ease of accessibilities of electrolyte, graphene aerogel is widely used as the supercapacitor and battery electrodes for energy storage applications with high volumetric capacitance [1.46e]. The aerogels possess the blended mesoporous materials in a macroporous matrix which could help the lucid diffusion of solvent molecules and which further been utilized in the separation; and water purification applications [1.42]. Moreover, many porous carbon varieties like graphene; graphene oxide; carbon nanotubes; and carbon nanofiber were explored as aerogels. However, the lack of intrinsic functional opportunities of these materials needs synthetically challenge and comparatively less efficient post-modification reaction for bringing more special activities.

MOFs:

Again, the introduction MOFs for the macroscopic construction into thin films; membranes; and 3D forms opens a new window of opportunities for applying reticular chemistry [1.47a]. Particularly, it helps the construction of macroscopic object with the desired ordered pore size and tunable functionality. Generally, MOF thin films can be fabricated by the interfacial self-assembling; and drop caring methods, which has been further used for the catalysis; molecular sieving; chemicals sensing; and energy storage applications (**Figure 1.13b**). Notably, the MOFs are carried out for technologically relevant 3D printing into different geometry [1.47b] (**Figure 1.15e**). But MOFs posses high gravimetric density; and contains toxic metals. Furthermore, the poor chemical stability of MOFs obstructs the utility of the respective macroscopic objects in moisture; acid; and base environments.

1.8.2 Macroscopic architecture of COFs

In the earlier section of the introduction, we have dealt with the properties of COFs. Taking the exceptional properties of COFs into consideration, the macroscopic assembling of the material has scientific and technological importance. Specifically, the macroscopic forms of COFs can hold these advantages: 1) reticular approach from the nano scale, which will provide the precise integration of the functional molecules; 2) thermal and chemical stability; 3) low weight density; and 4) ordered and tunable intrinsic pores. In this regard, people have

demonstrated the macroscopic architecture of COF into different forms like 2D thin film; sheets; and bulk forms.

COF thin films:

Synthesis of COF thin films on a support through the bottom up strategy is widely used for the fabrication oriented growth of the material. This method allows us to coat the functional COFs on desired substrates for various applications. The oriented growth of COF provides structurally defined material by avoiding the formation of random polymerization. Herein, we have detailed the attempts made on the fabrication of COF thin films on support as well as the in free-standing nature.

COF on graphene layers: One of important attempt among these was the growth of COF on graphene layers in the solvothermal synthesis [1.48a] (**Figure 1.16a**). In this approach,

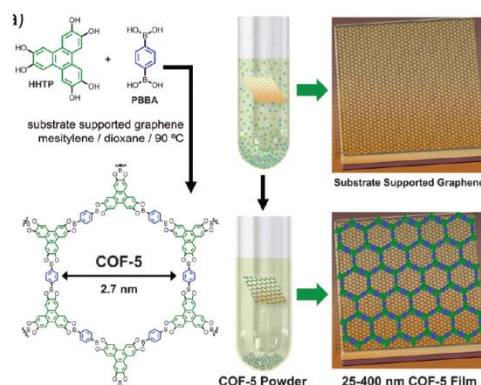


Figure 1.16: COF-5 on graphene support [J. W. Colson et al., *Science*, 2011, 332, 228].

Dichtel and coworkers demonstrate the oriented growth of boronic ester linked COF-5 (Constructed from HHTP and PBBA) on a single layer graphene (SLG) on different substrates like silica, silicon carbide and copper. They have found the COF is crystalline in nature and the aromatic building units are vertically stacked on the graphene support. The parallel growth of COF layers on the graphene layers was further analyzed by powder X-ray diffraction and grazing incidence diffraction. The thickness of the fabricated COF thin film was found to be 132 ± 18 nm.

COF on gold thin film: The effort on the synthesis of COF thin film with desired functionality is necessary for the advanced level applications. The successful attempt to fabricate an anthraquinone stitched β -ketoenamine COF thin film (DAAQ-TFP COF) on a

gold support has been reported by DeBlaze *et al* from the group of Dichtel [1.50]. In this work, they have synthesized DAAQ-TFP COF on the top of gold surface by the slow addition TFP into DAAQ monomer solution in the presence of gold surface. They could control the thickness of the COF thin film by adjusting the concentration of the monomer solution (200-1000 nm) (**Figure 1.17**). The oriented growth of COF on the gold electrode helps the well organization of the redox-active anthraquinone groups. Interestingly, the charge storage efficiency of the prepared COF thin film has been enhanced by 400% compared to the insoluble powder form of the same.

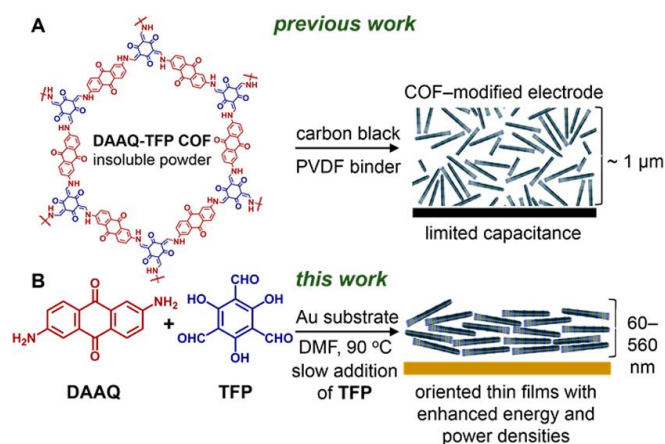


Figure 1.17: COF thin film growth on gold support [Reprinted with permission from {C. R. DeBlaze *et al.*, ACS Nano 2015, 9, 3178–3183} Copyright {2015} American Chemical Society].

COF on ITO surface: Notably, researchers have tried to develop novel functional COF for the optoelectronic applications. In this regard, one of the excellent research has been done by Bein *et al.* for developing thiophene linked COF with electron donor units [1.51a]. In this approach, they have used only lower concentration of monomer units for more ordered COF growth. Herein, they have fabricated the COF thin films with 150 nm thickness on the inorganic surfaces like ITO and NiO/ITO. Again, Lu *et al.* synthesized a DAB TFP COF (constructed from p-phenylenediamine and 1, 3, 5-triformylphloroglucinol) on the surface ITO; silicon; and FTO by using autoclave [1.51b].

Interfacial synthesis:

Most of the COF thin film synthesis on support is restricted due to their expensiveness and limited scalability. Although it has been realized the growth of COF on support in centimeter scale, the fabrication of free standing COF thin sheets is scientific and technological

challenge. Notably, the production of nanosheets by the exfoliation of COFs into a few layers was an important step towards the control over the morphology in nanometer scale. However, the lateral sizes of nanosheets are limited to 100-200 nm only [1.49]. In this regard, scientists seek for a new alternative to synthesize COF thin film in a large scale and reduce the cost. They found interfacial synthesis of COF could be a better alternative to produce bulk amount of thin films. Basically, there are two types of interfacial synthesis is possible: 1) air-liquid; and 2) liquid-liquid. Interestingly, Bao *et al.* reported an air-liquid interfacial synthesis of polyTB COF [1.52]. They could control the nucleation as well as the thickness of the COF thin films by adjusting the time. Again, Zhang *et al.* presented the monolayer fabrication of imine linked COF by using air-water interfacial synthetic strategy [1.53].

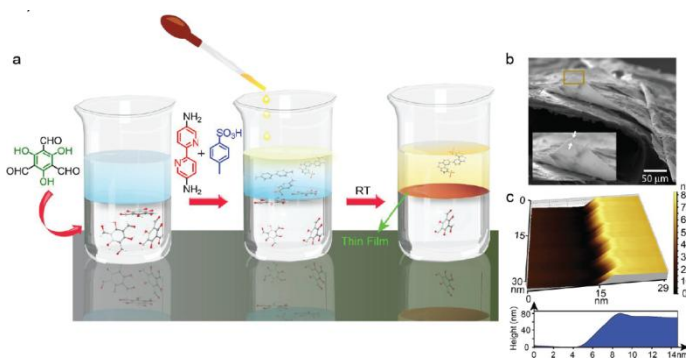


Figure 1.18: Interfacial thin film fabrication of COF [Reprinted with permission from {K. Dey *et al.*, *J. Am.Chem.Soc.* 2017,139,13083–13091} Copyright {2017} American Chemical Society].

Herein, they have taken terephthalaldehyde and 1, 3, 5-trihexyl-2, 4, 6-tris(4-aminophenyl)benzene linkers for the construction of the framework. The hexyl groups present in the polymer oriented to the air due to the hydrophobic nature and amine group contained phenyl rings placed on the interface. However, the limited porosity and crystallinity of these techniques discourage for their potential application. In this aspect, a novel COF thin film synthetic strategy has been developed by Dey *et al.* by the employment liquid-liquid interfacial technique [1.26b] (**Figure 1.16b**). Here, they have developed porous and crystalline β -ketoenamine based COF thin films at the interface of water and DCM with the presence of *p*-Toulenesulphonic acid as a catalyst. The prepared COF thin films could be carried on different supports and further have been used for organic micropollutant removal

from water by using separation method. The main advantages of this method are room temperature synthesis and large scalability of crystalline and porous materials.

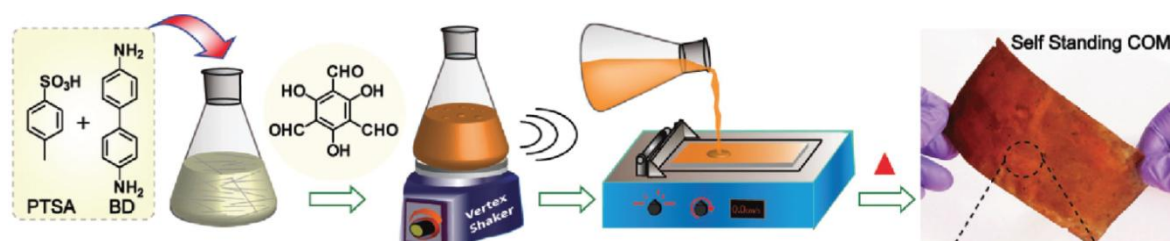


Figure 1.19: Solid-state synthesis of COF membranes [Reprinted with permission from S. Kandambeth *et al.*, *Adv. Mater.* 2017, 29, 1603945] Copyright {2017} American Chemical Society].

Additionally, Kandmabeth *et al.* developed a strategy to fabricate membranes of COF through the solid-state synthesis and further been applied the material for water purification [1.27b] (**Figure 1.16c**). In this mechanochemical solid-state synthesis, they have used PTSA as a catalyst for the formation imine bonds. They could develop the micrometer thick (200-300 μm) porous crystalline COF sheets for the separation molecular pollutants from water. The direct use of COF membrane for the water purification applications provides an efficient molecular sieving through the porous matrix.

1.8.3 Applications of COF thin films

Due to the insoluble granular nature of the bulk COF, the possibility of the applications in many advanced fields is limited. The recent development of the production of COF thin film by different methods leads to the exploration of the potential application of them.

Energy storage: The anthraquinone stitched β -ketoenamine COF thin films on gold support were successfully utilized for the supercapacitance applications. It should be noted that the performance of COF thin films as charge storage platform is very higher than the powder nature of the same. Again, the charge storage performance of DAAQ TFP COF thin film has been enhanced by inducing *in situ* polymerization of EDOT into electrically conductive PDEOT [1.54a]. Again, the exfoliated COF layers of DAAQ TFP are used as Li^+ ion storage platform in lithium ion battery [1.54b]. In these exfoliated ECOFs, the lucid diffusion Li^+ ion through the porous matrix of the COF increases the efficiency of charge storage compared to bulk COF.

Fuel cells: COF thin films were used as proton exchange membranes in fuel cells. In one important study, Montoro *et al.* reported two different COFs (RT-COF-1Ac & RT-COF-1AcB) and further post synthetically modified into lithium incorporated COF matrix [1.55a]. These COF films were strategically used as solid electrolytes in the proton exchange membrane of fuels. Furthermore, Himadri *et al.* demonstrated the PTSA loaded COF membranes with excellent proton conductivity ($7.8 \times 10^{-2} \text{ Scm}^{-1}$). The COF membranes are flexible and free-standing in nature [1.55b]. They have utilized these COFs as proton exchange membranes in fuel cells with a high power density 24 mWcm^{-2} .

Semiconductors: The COFs could be used as semiconductors considering to their tunable functional Π frameworks. However, the granular bulk form of them restricted to use in the advanced device applications. The recent development of the COF thin films bring out the important properties of the COFs into the device level. Cai *et al.* could fabricate a tetrathiofulvalene (TTF) linked COF thin film as a charge-carrier platform [1.56a]. In this work, they doped electron acceptors like I_2 into the porous COF thin film for the charge transfer from the electron donor TTF. Recently, Bao *et al.* presented an imine linked polyTB COF as a semiconductor layer in the field effective transistor (FET) [1.52].

Separations: The presence intrinsic micro and mesopores; and functional groups in COF aid the separations of molecules based on their size and properties. In this regard, several notable researchers have been done for the separations of molecular pollutants and more important gas molecules. As mentioned previously, Kandambeth *et al.* demonstrated COF membranes for the nano filtration of molecular pollutants. Similar studies have been done by Matsumoto *et al.* in COF supported with a polymer membrane called poly(ethersulfone) for the efficient rejection of rhodamine WT [1.57]. Again, in another interesting study, Fan *et al.* reported the growth COF LZU1 thin film on the support of alumina tube for the excellent removal of water soluble dyes [1.58]. COF thin films were used for the potential gas separation application by mixing the material with a porous support. In an important study, Li *et al.* demonstrated the fabrication of COF-1 membrane on a porous ceramic support [1.58]. Herein, the COF-1 membrane is composed from the nanosheets and it exhibits excellent H_2 permeance compared to MOF or graphene thin films. Furthermore, the mixed matrix membranes of COFs were reported as composite COF and polymers. These membranes exhibit high mechanical strength as well as good separation of gas molecules. One of the

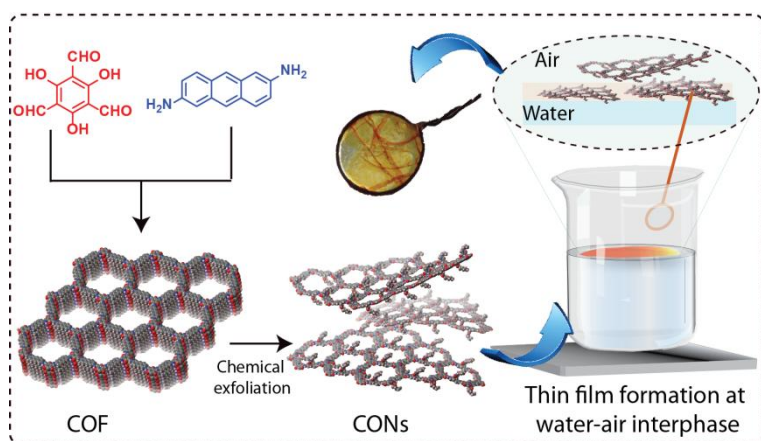
notable research has been carried out by Zhao et al. in COF nanosheets based (NUS-2 & NUS-3) mixed matrix membranes. They found that the permselectivity of 31.4 for H₂/CO₂ gas mixture with 20 wt% of the COF in polymer.

1.8.4 Macroscopic architecture of COFs in advanced level

It is really important to note that, the scientific challenges like fabrication of ultra-thin and free-standing COF films from the granular form is needed to overcome. Moreover, the further progress of the macroscopic architecture of COF should be in the level of functional exploration and direct applications like advanced energy storage and socio-economic water purification. Notably, modern energy storage devices required capacitive free-standing electrodes with mechanical robustness and flexible in nature. Additionally, the electrical conductivity of such electrode is a necessary factor for the enhancement of the capacitive performance. In this regard, we believe, bringing mechanical robustness as well as electrical conductivity in the macroscopic 2D forms of COFs may open commercial opportunities of the material. Furthermore, the 3D architecture of COF can be suitable for the industrial level water purification due to the intrinsic microporosity of the material. Keeping these in perspective, herein, we have tried to integrate the reticular chemistry of COFs into the macroscopic building of the material for advanced energy storage and water purification.

Chemically Exfoliated Covalent Organic Nanosheets as Ultrathin Free-Standing Films

Abstract: In this chapter, Covalent organic nanosheets (CONs) are a novel category of two-dimensional nanomaterial which is derived from crystalline and porous covalent organic frameworks. In this chapter, we have demonstrated an efficient chemical



exfoliation strategy to delaminate the layers of COF into CONs. Herein, the chemical exfoliation method involves Diels-Alder cycloaddition reaction of anthracene stitched β -ketoenamine framework with an electron deficient N-hexylmaleimide as a dienophile. The obtained CONs exhibit high dispersion properties in organic solvents due to the presence of the long alkyl chains on the CON framework. As a result, we could fabricate the free-standing thin film of CONs at air-water interphase through layer by layer assembly. Notably, the CON thin films display a controllable thickness ranging from ~ 1.5 nm to $1 \mu\text{m}$.

2.1 Introduction

Covalent organic frameworks (COFs) are emerged as potential porous polymers with the intrinsic ordered nature [2.1]. The fabrication of a COF consists of symmetric organic building units which are connected through strong covalent linkage in a two-dimensional (2D) or three-dimensional (3D) architecture. Notably, 2D COFs have been well explored due to their potential application towards gas storage, energy storage, heterogeneous catalysis, sensors, and purifications [2.2]. In general, the Π electron rich 2D layers in COF appeared as a columnar self-assembled mode by Π - Π interaction of the planar building units which in turn increase the crystallinity and porosity. However, in such cases, the adjacent stacked layers diminished the exposure of the functional moieties toward the reactive environments for many applications. Taking this into consideration, the research on the development of non-stacked layers of COF gains increased attention among the scientific community. In this way, the attempts to fabricate the COF thin films on different supports like graphene, HOPG, silicon wafer aid to understand the alterations in the properties of few-layer stacked COFs [2.3]. Although this bottom-up strategy is well known for the fabrication of ultrapure COF thin film in nanometer thickness, it is limited for the large scalability and its non free-standing nature further needs a support.

To overcome these issues, the novel developments arise for the synthesis of a few-layer COFs or better known as covalent organic nanosheets (CONs). It suggests the production of CONs is more feasible by means of efficiency and cost through top-down methods like exfoliations [2.4]. The exfoliation strategy involves the peeling of COF layers, i.e. breaking of the stacked 2D layers, into to CONs by applying various energies. More specifically, the 2D layers in COF are stacked together by the Π interaction self-assembly which is needed to be disturbed for the exfoliation of the individual layers. In this regard, S. Chandra *et al.*, reported an exfoliation strategy by using mechanical energy to break the Π interaction between the COF layers into CONs [2.5]. Furthermore, solvent assisted ultrasound energy has been used for the exfoliation of COF layers into CONs by W. Dichtel and co-workers. In this method, they have dispersed COFs in different solvents and then ultrasound frequency has been applied for breaking pi-pi stacking of the COF layers [2.6]. Recently, a novel self exfoliation technique has been demonstrated by S. Mitra *et al.*, for the delamination of a guanidinium stitched ionic covalent organic framework (i-CONs). When i-CONs are

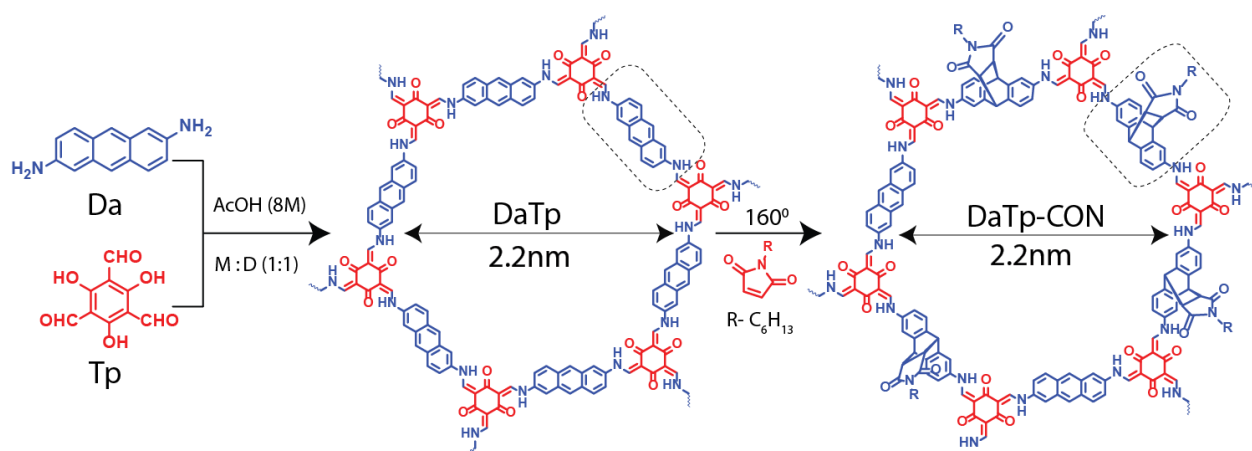
surrounded by water, the halide ions present in the inert layers of COF get into hydrated and causes the self exfoliation of individual layers [2.7]. Although these exfoliation strategies yield a few layer COFs, the lateral size of nanosheets are ended up within a few nanometers only. Moreover, the poor dispersion of the CONs in different organic solvents restricts the fabrication of ultrathin free-standing COF films.

Keeping these in perspective, we decided to strategize a novel technique for the exfoliation of COF into CONs and finally which can form free-standing CON thin film. Herein, we have chemically exfoliated an anthracene stitched 2D β -ketoenamine COF by using *N*-hexylmaleimide as an exfoliation agent. It is well known in the literature, the 9, 10 position of electron rich anthracene is highly reactive to the electron deficient dienophiles like maleimides through 4+2 Diels-Alder cycloaddition process [2.8]. During the course of reaction, the *N*-hexylmaleimides are stitched on the anthracene rich framework. Subsequently, the planar anthracenes get into the bend form which causes the breaking of the pi-pi stacking among the COF layers. The resulted maleimide functionalized CONs exhibit a high dispersion in organic solvents due to the presence of long alkyl chains. Moreover, it further carried for the fabrication ultra thin free-standing thin film by using layer-by-layer assembly at air- water interphase [2.9].

2.2 Result and Discussion

2.2.1 Synthesis and characterization

The anthracene linked β -ketoenamine 2D COF [2.10] has been solvothermally synthesized by using the building units 2, 6-diaminoanthracene (**Da**; 0.3 mmol) and 1, 3, 5-triformylphloroglucinol (**Tp**; 0.2 mmol) with the presence of 8 M acetic acid as a catalyst. The brown colour precipitate of **DaTp** is thoroughly washed and then used for the cycloaddition (4+2) reaction with *N*-hexylmaleimide at 160° C for 24 hours in mesitylene solvent. The obtained dark yellow product (**DaTp CONs**) is thoroughly washed with petether solvent and then used for further analysis.



Scheme 2.2: The schematic representation of the synthesis of **DaTp COF** and **CONs**.

2.2.2 The structural characterizations

The ordered nature of COFs has been inspected through the powder X-ray diffraction (PXRD) analysis. The PXRD profile displays the crystalline features of the **DaTp** (Figure 2.1a). The pre-designable advantages of COF allowed us to model the possible structures of the material in the Material Studio-6 software. In this regard, we have modeled the **DaTp** COF formed from C_3 symmetric **Tp** and C_2 symmetric **Da** in a hexagonal unit cell. The modeled unit cell exhibits a highly symmetric space group of $P6_3/m$ in an eclipsed (AA) stacked mode. Notably, the experimental PXRD profile of the **DaTp** has been matched with the simulated PXRD of the modeled structure of the same. It indicates the agreement of the modeled structure in the eclipsed form with the experimental PXRD profile. In the experimental PXRD profile, we could observe a sharp peak at the angle 2θ 3.5° corresponds to the 100 planes. Similarly, the weak peaks at the angle 2θ 6.3° and 26.7° indicate the presence of 110 and 001 planes in the crystalline material. Furthermore, we have calculated the d-spacing of the **DaTp** COF from the 001 planes of PXRD is 3.4 Å. It has been noted that the constructed hexagonal unit cell consists of the parameters $a = b = 29.0$ Å and $c = 3.4$ Å. Interestingly, the distinct changes in the PXRD profile of **DaTp CONs** suggest alterations in the ordered behavior of COFs after the chemical exfoliation. The drastic mitigation in the intensity of the first peak (100) in the PXRD profile of the **DaTp-CONs** signifies the exfoliation of the planar 2D layers of COF. The decrement of the electron density of the 100 planes is mainly due to the peeling of the layers from the bulk column,

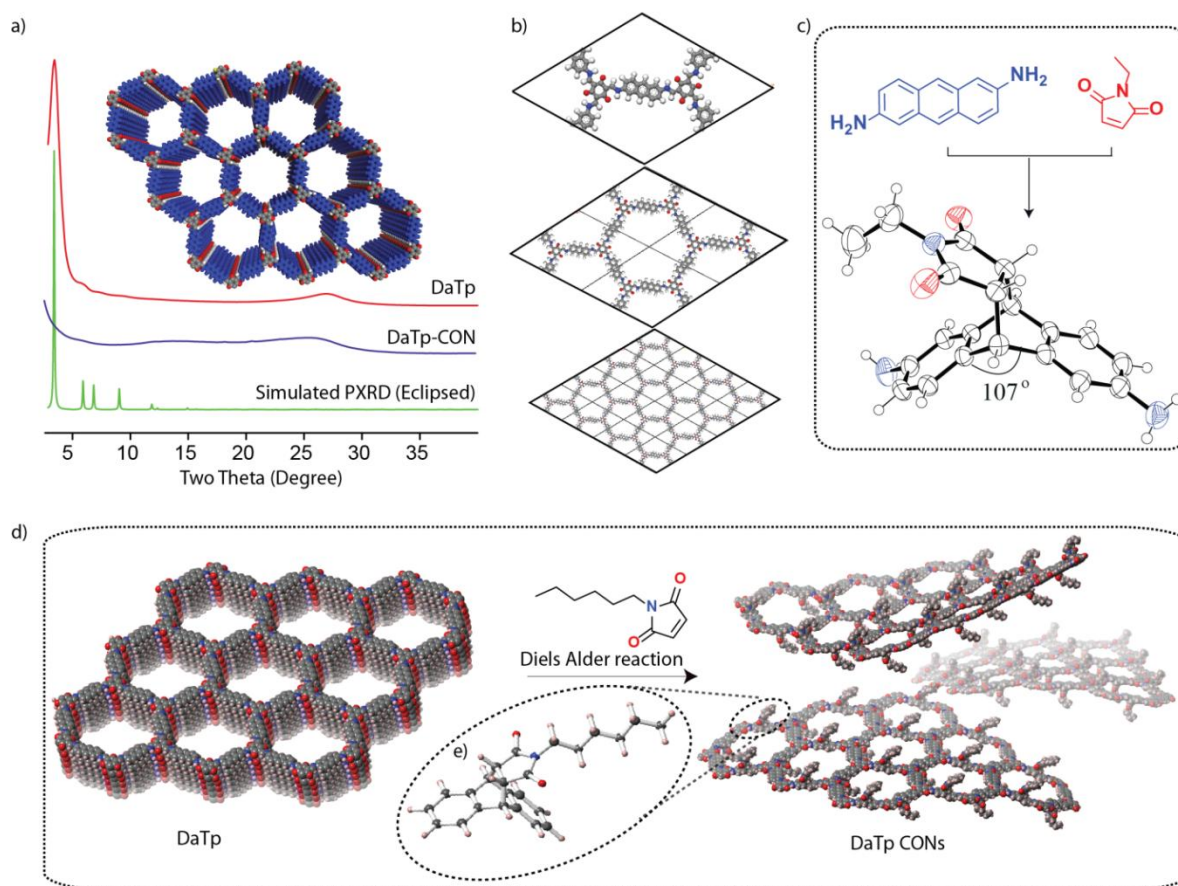


Figure 2.1: a) The PXR profiles of **DaTp**, **DaTp CONs** and simulated eclipsed form. b) The $P6_3/m$ unit cell of **DaTp**. c) The crystal structure of the reference compound 1. d) The representation of the chemical exfoliation of **DaTp** into **DaTp CONs**.

and which affects the intensity of the corresponding diffraction peaks (100) in the PXR profile. Additionally, the weak broadening of 001 peak at the 2θ of $\sim 27^\circ$ in the PXR of **DaTp-CONs** could be due to the incorporation of the *N*-hexylmaleimide units on the top of the COF layers. To get more insight about the exfoliation process, we have synthesized two reference compounds (1 & 2) from cycloaddition of 2, 6-diaminoanthracene/2-aminoanthracene with a strong dienophile *N*-ethylmaleimide [Figure 2.1c & Figure 2.3]. The single crystal X-ray diffraction (SCXRD) of the reference compounds provides the information of structural aspects of anthracene after the cycloaddition. Both reference compounds exhibit the bending anthracene from 180° to 107° after the Diels-Alder reaction. We surmise the bending of anthracene could break the effective Π interaction between the

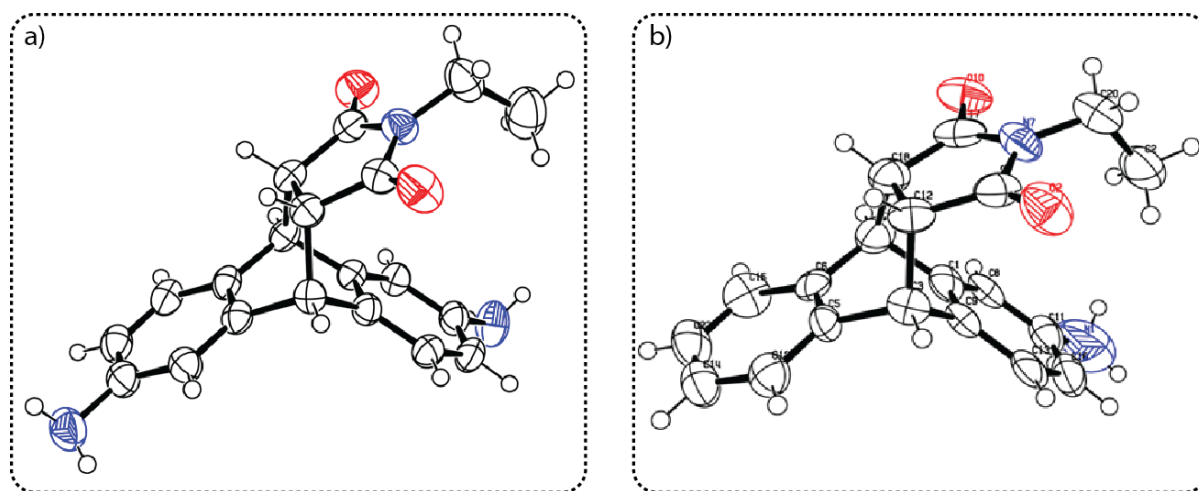


Figure 3.2: a) Single Crystal X-Ray Diffraction of **reference compound 1**. In the ORTEP (with the 40 % probability level); Carbon (black), Oxygen (Red), Nitrogen (blue) and Hydrogen (small black circle) have been shown [CCDC No: 1497987]. b) Single Crystal X-Ray diffraction of **reference compound 2**. In the ORTEP (with the 40% probability level); Carbon (black), Oxygen (Red), Nitrogen (blue) and Hydrogen (small black circle) have been shown [CCDC No: 1497988].

DaTp-COF

Space Group P6₃/m

a = b = 29.8330Å, c = 3.6214Å; α = 90.0000, β = 90.0000, γ = 120.0000

Atom No	X	Y	Z
C1	0.37066	0.6498	0
C2	0.40691	0.6376	0
N3	0.39996	0.58837	0
C4	0.43921	0.57682	0
C5	0.48947	0.61317	0
C6	0.55006	0.5368	0
C7	0.5133	0.55016	0

C8	0.46305	0.51325	0
C9	0.52591	0.59995	0
C10	0.42668	0.5271	0
C11	0.38629	0.70312	0
O12	0.43014	0.73254	0

Table 2.1: Fractional atomic coordinates for the unit cell of **DaTp**.

COF layers, hence the exfoliation happens due to the cycloaddition reaction [2.11]. Additionally, it is believed that the long hexyl chains hinder the possible layer restacking after the chemical exfoliation of the COF.

2.2.3 Chemical characterization

The FT-IR spectroscopy has been used for the investigations on the chemical linkage of the frameworks. The absence of N-H and aldehyde C=O peaks in the FT-IR spectra of **DaTp** rules out the possibility of the presence of starting materials (**Figure 2.3a**). The stretching vibration at 1590 and 1270 cm^{-1} correspond to the characteristic peaks of β -ketoenamine C=O and C-N bonds. Furthermore, we have synthesized a discrete monomer compound from **Tp** and 2-aminoanthracene for the comparison of the chemical linkage of the β -ketoenamine molecule with polymeric framework. Notably, the peak positions in the FT-IR profile of the **DaTp** matches with the IR profile of **DaTp** monomer (**Figure 2.3b**). Interestingly, after the functionalization with *N*-hexylmaleimides, **DaTp** **CONS** exhibit the characteristic C-H vibration peaks at the stretching frequency of 2937 and 2857 cm^{-1} . Additionally, a vibrational peak has been observed at the stretching frequency of 1695 cm^{-1} indicates the presence of imide C=O from the *N*-hexylmaleimide moiety.

The constructed **DaTp** COF and functionalized **DaTp** **CONS** have been further scrutinized for ^{13}C CP MAS solid-state NMR spectroscopy to understand the atomic level information of the frameworks (**Figure 2.4a**). The ^{13}C solid-state NMR of **DaTp** displays a resonance signal at 182.3 ppm indicates the presence of the keto (C=O) functional group in a β -ketoenamine

framework. However, after the functionalization with the *N*-hexylmaleimide, we could observe a new resonance peak at 178 ppm in the ^{13}C solid-state NMR spectra of **DaTp** **CONs**. Furthermore, the resonance signals at 14, 21, 30, 38 ppm correspond to the chemical shift of the sp^3 carbons of the alkyl chain in the *N*-hexylmaleimide unit. Importantly, the peaks at the chemical shift of 44-47 ppm signify the formation of new cyclic sp^3 carbons at the center of anthracene and maleimide after the cycloaddition reaction. This observation is

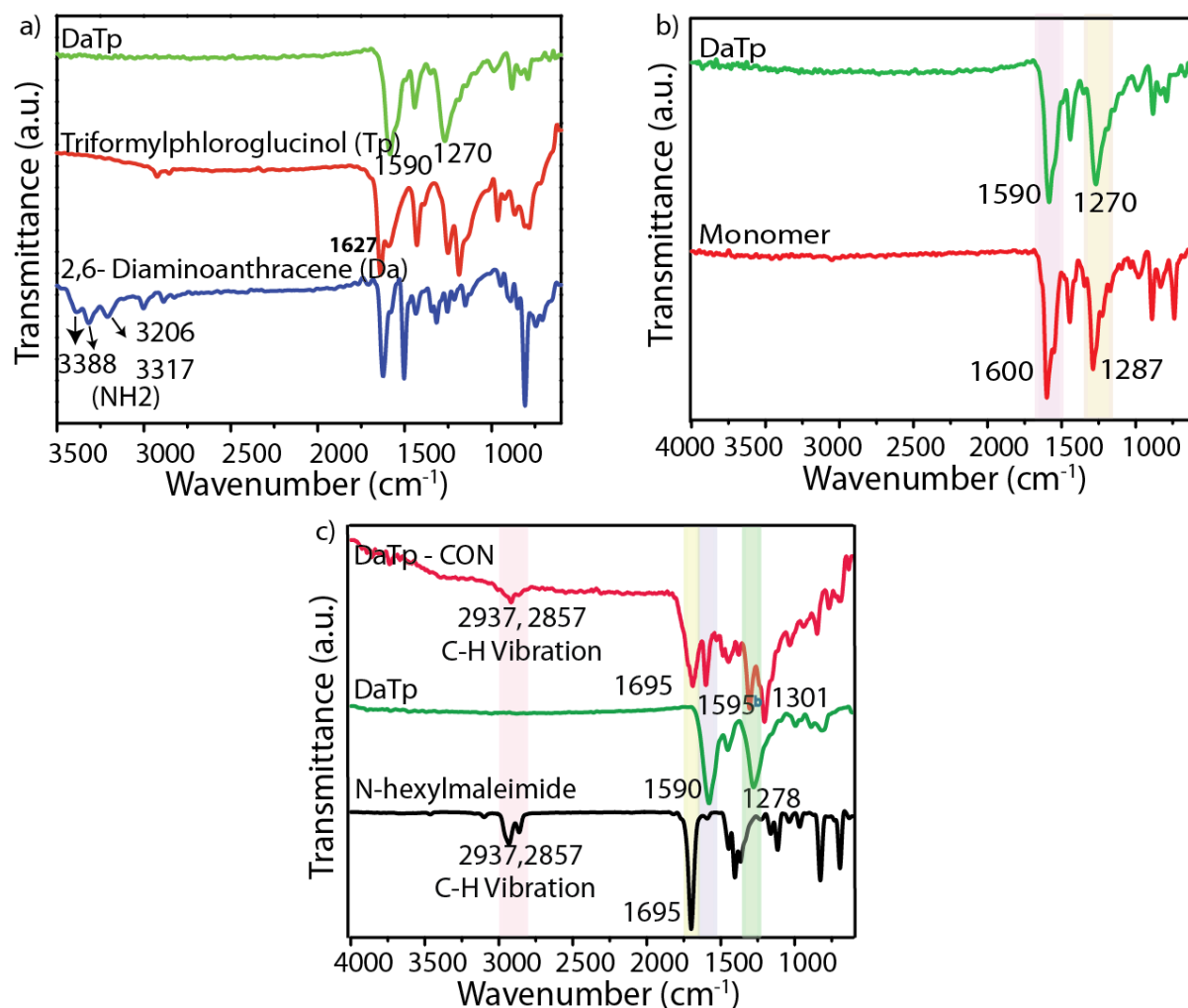


Figure 2.4: FT IR spectra of a) comparison of the starting material with **DaTp** COF. b) Comparison of the monomer and **DaTp**. c) The comparison of **DaTp**, **DaTp** **CONs** and *N*-hexylmaleimide.

further supported by the analysis of ^{13}C NMR of the reference compounds formed from the anthracene and *N*-ethylmaleimide (**Figure 2.4c & d**). Herein, we have synthesized two different reference compounds (**Reference compound 1**: 2-aminoanthracene + *N*-ethylmaleimide and **Reference compound 2**: 2,6-diaminoanthracene + *N*-ethylmaleimide)

for the conclusive explanation of the ^{13}C NMR spectra. Notably, spectra of both reference compounds clearly exhibit new sp^3 carbon peaks resonance at the chemical shift of 44-47 ppm. Meanwhile, the disappearance of the sp^2 carbons at the 9, 10 position of anthracene and C=C carbons of *N*-ethylmaleimide further indicates the cycloaddition of the corresponding carbons. In order to get more insight about the cycloaddition of *N*-alkylmaleimide with

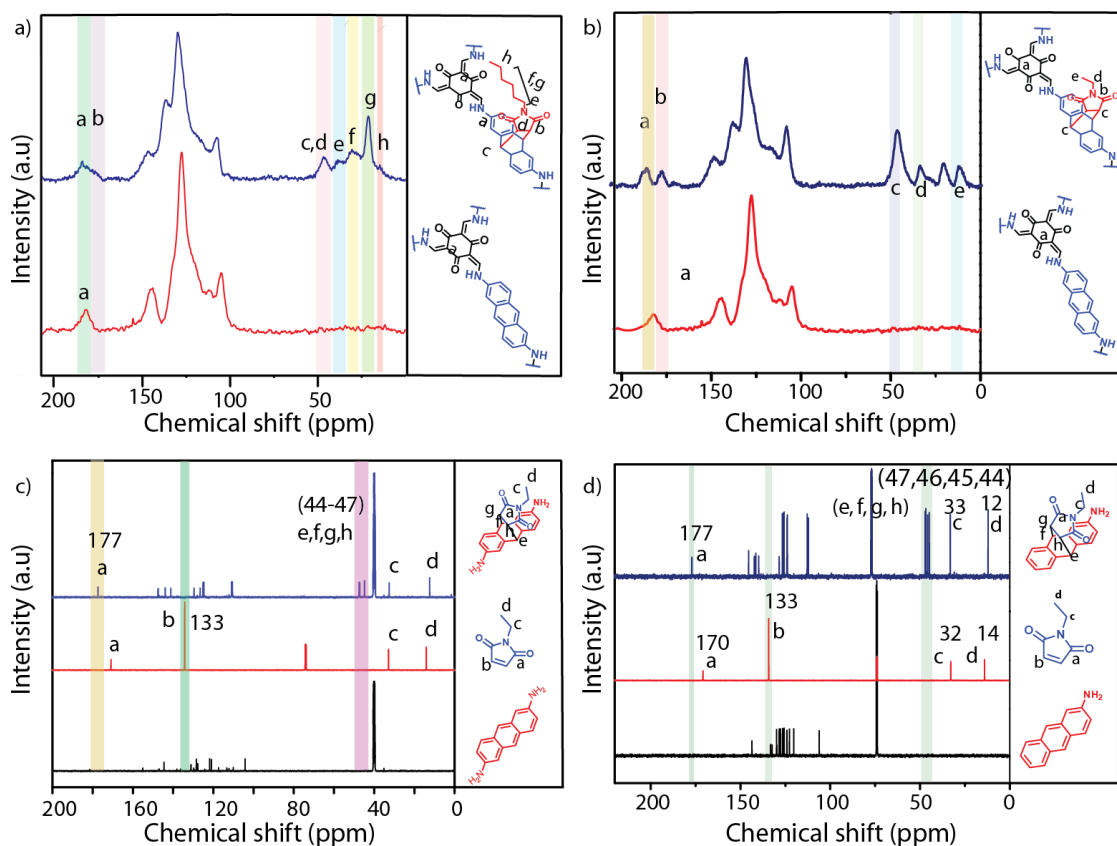


Figure 2.5: The comparison of ^{13}C NMR spectra of a) **Reference compound 1** and starting materials. b) **Reference compound 2** and starting materials. The comparison of ^{13}C CP MAS NMR spectra of c) **DaTp** and **DaTp CONs** (with *N*-hexylmaleimide). d) **DaTp** and **DaTp CONs** (with *N*-ethylmaleimide).

DaTp, we have performed Diels-Alder reaction between **DaTp** and *N*-ethylmaleimide which possess a short alkyl chain. Again, the ^{13}C solid-state NMR of the **DaTp**-*N*-ethylmaleimide cyclo adduct clearly shows the newly formed cyclic sp^3 carbons peak at 44-48 with all other characteristic peaks (**Figure 2.4b**). It indicates the general feasibility of **DaTp** COF towards the 4+2 cycloaddition reaction.

Again, to calculate the quantitative inclusion of the *N*-hexylmaleimides, we have performed quantitative solid-state NMR analysis at high scanning rate for the peak integration. Herein, a

single layer of **DaTp** unit cell has been considered as a reference to integrate the peaks in NMR. Particularly, a single layer of **DaTp** unit cell contains 3 anthracene moieties. It should be noted that three number of anthracene is calculated from one full length anthracene and four half length anthracenes present in the unit cell. It is to be expected that 100% of the cycloaddition reaction leads to the addition of three *N*-hexylmaleimides in the final unit cell.

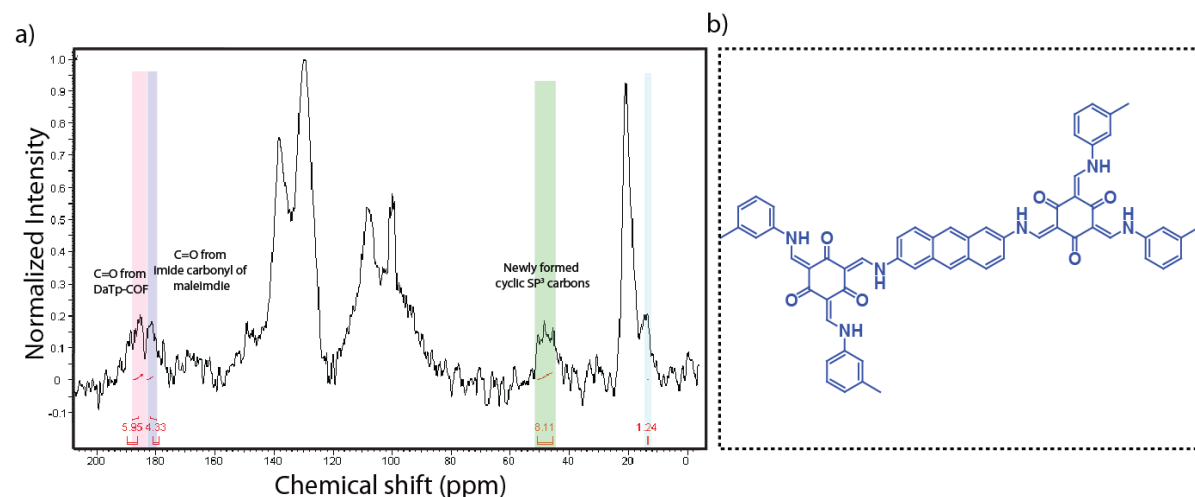


Figure 2.5: a) The quantitative integration of ^{13}C solid-state NMR of **DaTp CON**. b) The reference unit of **DaTp**.

In this regard, six (3×2) β -ketoenamine carbonyl carbon ($\text{C}=\text{O}$); six (2×3) imide carbonyl carbon ($\text{N}-\text{C}=\text{O}$) from maleimide moieties and twelve (4×3) newly formed cyclic carbons are supposed to appear at the final structure after 100% reaction. Based on these presumptions and considering the β -ketoenamine carbonyl carbon ($\text{C}=\text{O}$) signal as standard, we have integrated the ^{13}C NMR spectra of the **DaTp CONs**. As a result, we could notice that ~ 4 number as imide carbonyl carbons ($\text{N}-\text{C}=\text{O}$) and ~ 8 numbers of newly formed sp^3 carbons after the integration process (Figure S13). We have obtained $\sim 66\%$ of cycloaddition in one reference unit of **DaTp** and believed that this could be the same for bulk **DaTp CONs**.

2.2.4 Properties of **DaTp** and **DaTp CONs**

Both **DaTp** and **DaTp CONs** were subjected to the thermogravimetric analysis (TGA) for the measurement of the thermal stability (**Figure 2.6a**). Notably, the thermal stability of functionalized **DaTp CONs** (190°C) is less than compared to the pristine **DaTp COF** (320°C). It could be due to the retro Diels-Alder reaction [2.13] as well as the thermal

decomposition of the *N*-hexylmaleimide functionalized CONs. Furthermore, the N₂ gas adsorption analysis has been carried out at 77K after the vacuum drying of both **DaTp** and **DaTp** CONs (**Figure 2.6b**). It should be noted that a large mitigation in the surface area of the DaTp CONs (53 m²g⁻¹) has been observed compared to the pristine **DaTp** (631 m²g⁻¹). The reduction in the surface area of CONs could be due to the chemical exfoliation of the 2D layers results the destruction of the ordered intrinsic pores in the COF matrix. The pore size

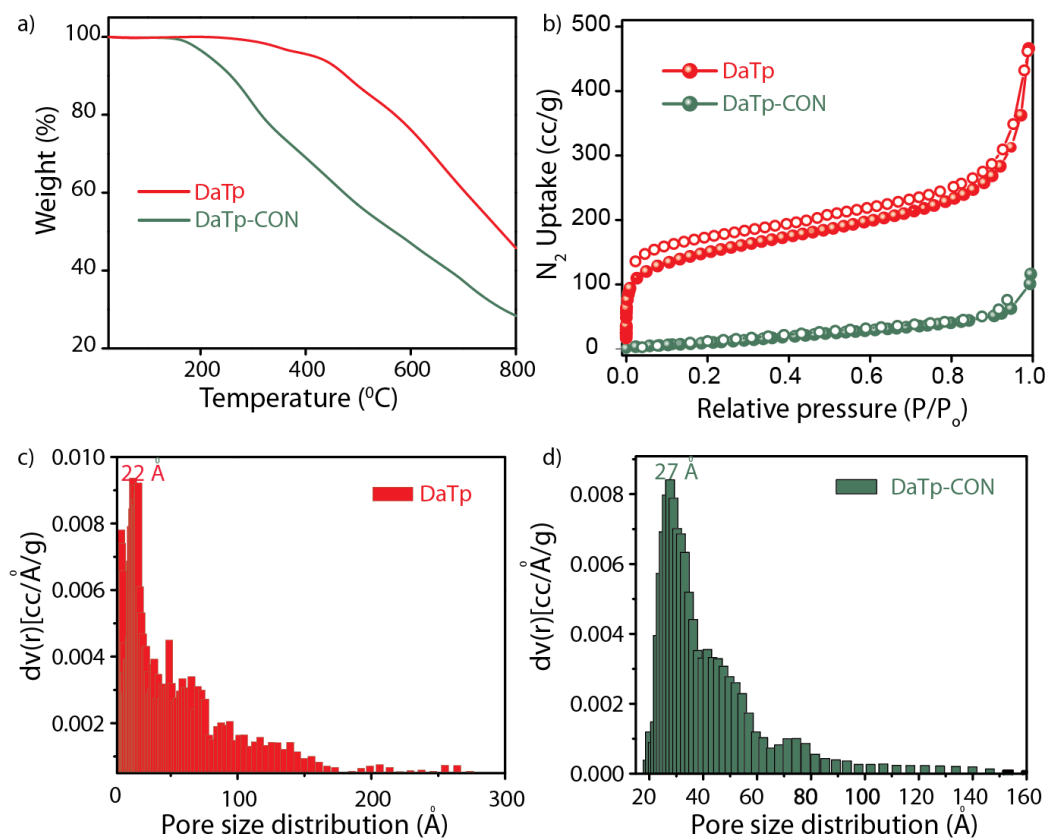


Figure 2.6: a) TGA of **DaTp** and **DaTp** CONs. b) N₂ gas adsorption analysis of **DaTp** and **DaTp** CONs. c) NLDFT pore size distribution of **DaTp**. d) NLDFT pore size distribution of **DaTp** CONs.

distribution of **DaTp** has been calculated from non-local density functional theory (NLDFT). It features the pore diameter of 2.2 nm for **DaTp** COF (**Figure 2.6c**). The slightly small pore size distribution compared to the model could be due to slipped stacking arrangement of anthracene rich 2D layers into a long column. Notably, after functionalization, the pore size distribution analysis displays the pore diameter of ~2.7 nm which could be the indication of low-depth pores after the exfoliation (**Figure 2.6d**).

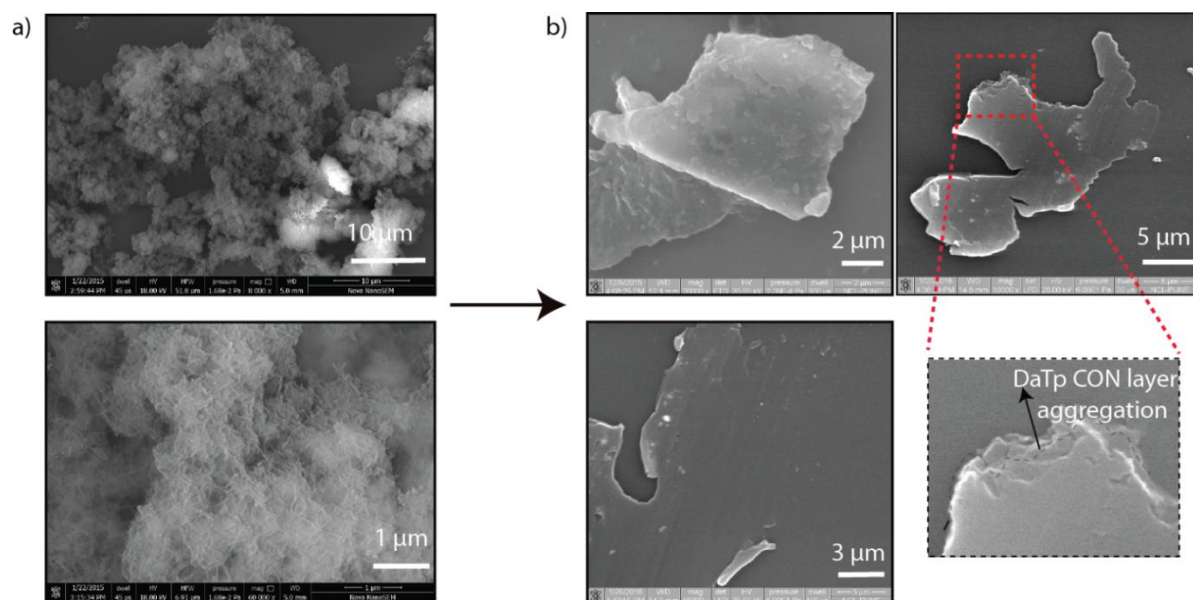


Figure 2.7: a) The SEM images of **DaTp**. It shows the aggregated ribbon-like morphology in 10 μm and 1 μm level focuses. b) The SEM images of **DaTp CONs**. It exhibits thin sheet-like morphology in different levels of focus (2, 3 and 5 μm) and also displays the aggregation of many CON layers into a single block of thin sheet.

2.2.5 Transformation of Morphology of COFs into CONs

The morphological features **DaTp** and **DaTp CONs** were investigated by various imaging characterizations like scanning electron microscopy (SEM) and transmission electron microscopy (TEM) and atomic force microscopy (AFM). The transformation of the morphology of COF into CONs is clearly evident from the nano and micro level image analysis. Importantly, a drastic change in the morphology of **DaTp** is observed after the chemical exfoliation into CONs in the SEM images (**Figure 2.7**). The SEM images of pristine **DaTp** COF displays aggregated ribbon-like morphology of the material in the micro level scanning (**Figure 2.7a**). Whereas, the **DaTp CONs** exhibits a thin sheet-like morphology in the recorded SEM images (**Figure 2.7b**). Furthermore, the TEM images reveal the changes in the morphology of COFs into CONs in the nanometer scale (**Figure 2.8**). Again, a morphological transformation has is observed in the nano meter level of the material, i.e., the aggregated ribbon-like structure (length: 100-200 nm; width: 20-40 nm) of **DaTp** COF has been turned to a thin sheet morphology (length: \sim 500 nm; width: \sim 200 nm)

upon the chemical exfoliation of the CONs. To get more insight about the morphological transformation COF into CONs, we have recorded TEM images of the partially exfoliated **DaTp** CONs which shows the mixed ribbons and thin sheet-like morphology and also the

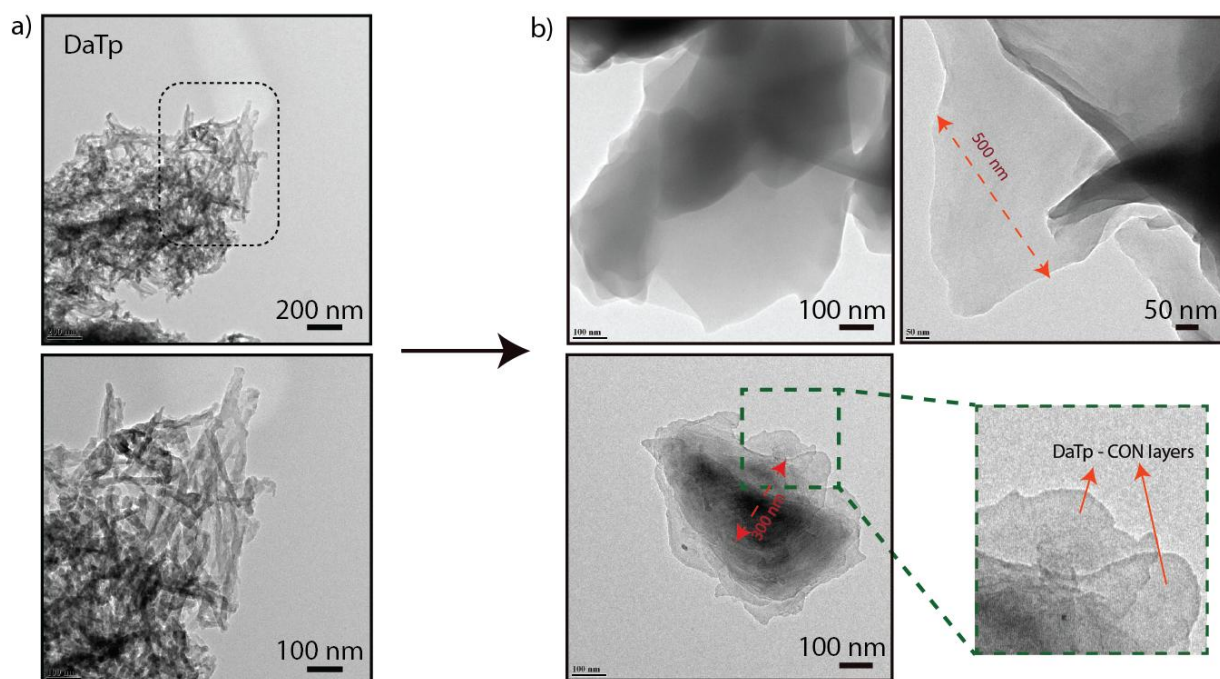


Figure 2.8: a) The TEM images of **DaTp**. It shows the aggregated ribbon-like morphology in 200 nm and 100 nm levels focus. b) The TEM images of **DaTp** CONs. It exhibits thin sheet-like morphology in different levels of focus (100 and 50 nm) and also displays the aggregation of many CON layers into a single block of thin sheet.

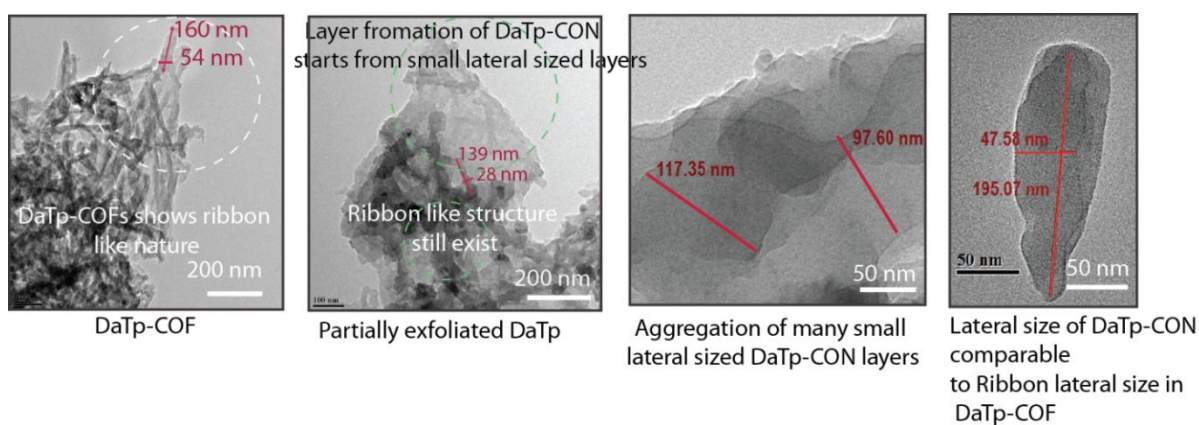


Figure 2.9: The TEM images of partially exfoliated **DaTp** and the aggregation of small lateral sized CON layers

transformation of ribbons into sheets (**Figure 2.9**). It is important to note the larger lateral dimension of CON thin sheets could be due to self-assembling of alkyl group functionalized smaller lateral size thin sheets. It is worth to mention that both SEM and TEM images clearly show the assembling of many layers into one single block which finally appeared as a large

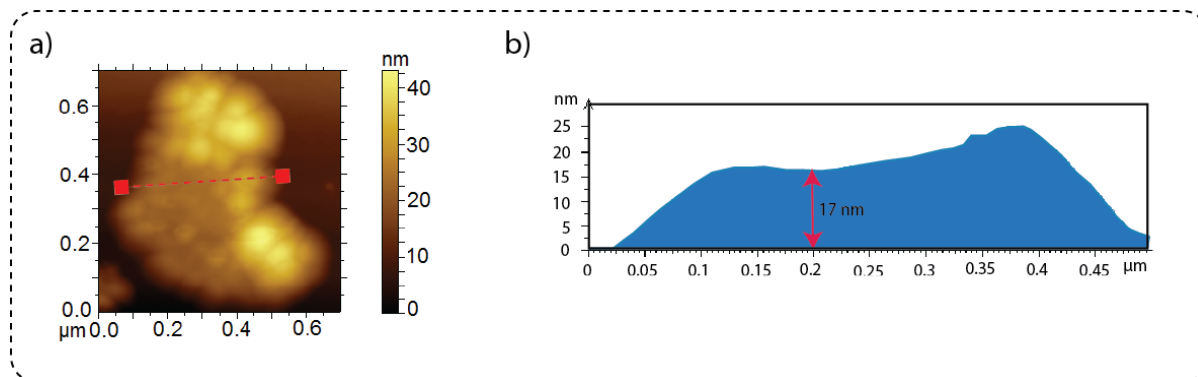


Figure 2.10: a) The AFM image and b) height profile of **DaTp** CONs.

lateral dimensional thin sheet. Again, we have analyzed AFM images of the **DaTp** CONs for understanding the thickness of the sheets. It was found to be the average thickness of 17 nm for the sheets in the AFM height profile. We surmise this higher thickness could be due to the self-assembling of the layers into a thick single sheet during the sample preparation time. Although these CONs are well dispersible in the organic solvents, it could self assemble together during the evaporation of the solvent molecules during drying the sample.

2.2.6 The dispersion property of CONs in organic solvents

The functionalization of anthracene with *N*-hexylmaleimide boosts the interaction of the CONs with the organic solvent molecules through the long alkyl chains [2.13], hence exhibits an excellent dispersion in many organic solvents with various polarity. In this regard, we decided to test the dispersion stability of **DaTp** CONs in different organic solvents. We have observed that a stable dispersion of **DaTp** CONs in high polar solvents

Solvent	Polarity Index	Dispersion (Stability)
N, N-dimethylacetamide (DMA)	6.5	Two months
N, N-dimethylformamide	6.4	Two months

(DMF)		
N, N-dimethylsulphoxide (DMSO)	7.2	Two months
N-methylpyrrolidone (NMP)	6.7	Two months
Acetonitrile	5.8	One month
Methanol	5.1	One month
Acetone	5.1	One month
Ethyl acetate	4.4	One month
Chloroform	4.1	One month
Dichloromethane (DCM)	3.1	One month
Isopropyl alcohol	3.9	One week
Hexane	0.1	One week

*Table 2.2: The dispersion stability of **DaTp** CONs in various organic solvents*

like DMA, DMF, NMP, chloroform, acetonitrile for more than a month (*Table 2.1 & Figure 2.11*). Meanwhile, low polar solvent like hexane exhibits a moderate dispersion for the **DaTp** CONs. Moreover, when we irradiate a red laser (650 nm) through the suspension of **DaTp** CONs-DCM mixture displays a strong Tyndall effects shows the well dispersion of nanometer-sized thin sheets in an organic solvent (*Figure 2.12*). The good suspension character of **DaTp** CONs allow us to carry out the dynamic light scattering (DLS) analysis for measuring the size of the nanosheets in a dispersed state in the solvent (*Figure 2.13*). Herein, in the DLS measurement of **DaTp** CONs-CHCl₃, the hydro dynamic radius analysis is correlated with lateral size of the nanosheets displayed in the TEM images. The DLS profiles suggest the CONs have 100-200 nm hydrodynamic radii with a relative number of 100 (inset: TEM image of 47-192 nm lateral sized **DaTp**-CONs). The DLS profile also

exhibits the nanosheets size with 400-500 nm hydrodynamic radii with a Relative number 41. This could be due to the aggregation of CONs into a relatively larger lateral dimension in the suspension (TEM images of 350 nm lateral sized **DaTp**-CON layers).

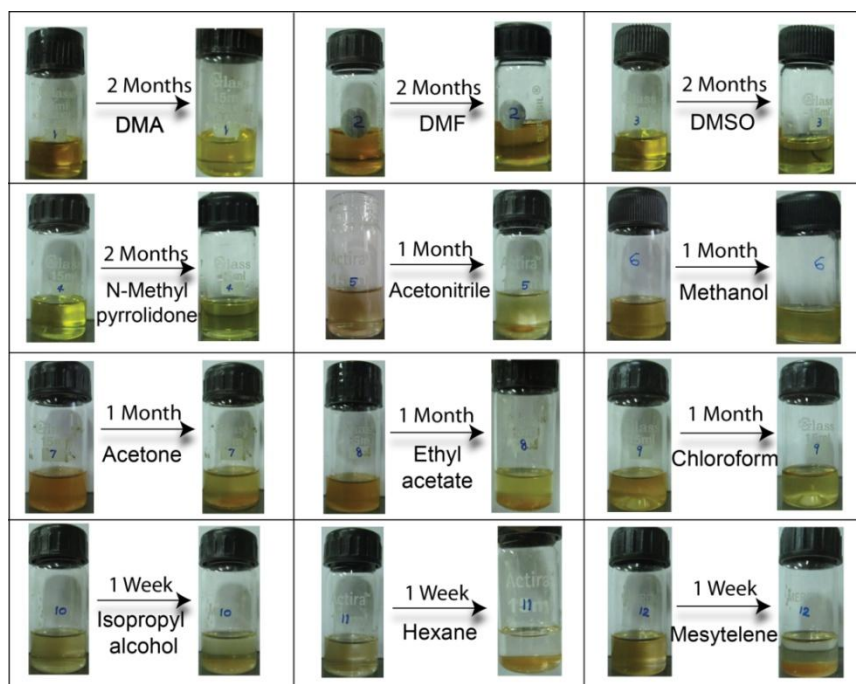


Figure 2.11: The dispersion of **DaTp** CONs in various organic solvents.

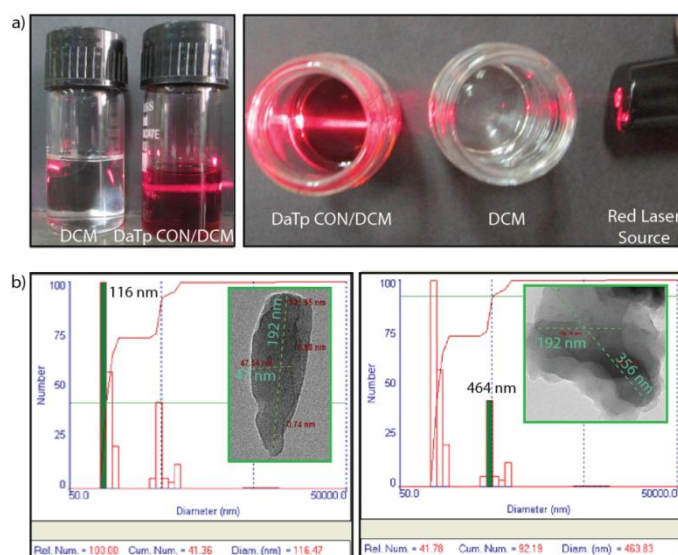


Figure 2.12: a) The Tyndall effect of **DaTp** CONs in DCM solvent. b) The DLS profile of **DaTp** CONs in DCM solvent [Inset: The TEM images of **DaTp** CONs]

2.2.7 The fabrication ultrathin free-standing CON film at the air-water interface

Considering to the good dispersion of **DaTp CONs** in organic solvents and hence the increased processability, we have strategized the fabrication of **DaTp CON** thin film through the interfacial layer by layer (LbL) assembly at the air-water interface [2.12]. We surmise the presence of hydrophobic alkyl chain on the framework of CONs may aid the self assembling process on the water surface. Furthermore, we have chosen the dispersion solvent as DCM due to the well-spreading nature owing to its high vapour pressure and low surface energy compared to the water. To fabricate the thin films, we have taken a well dispersed **DaTp CON-DCM** suspension and drop cast on the top surface of the water very slowly

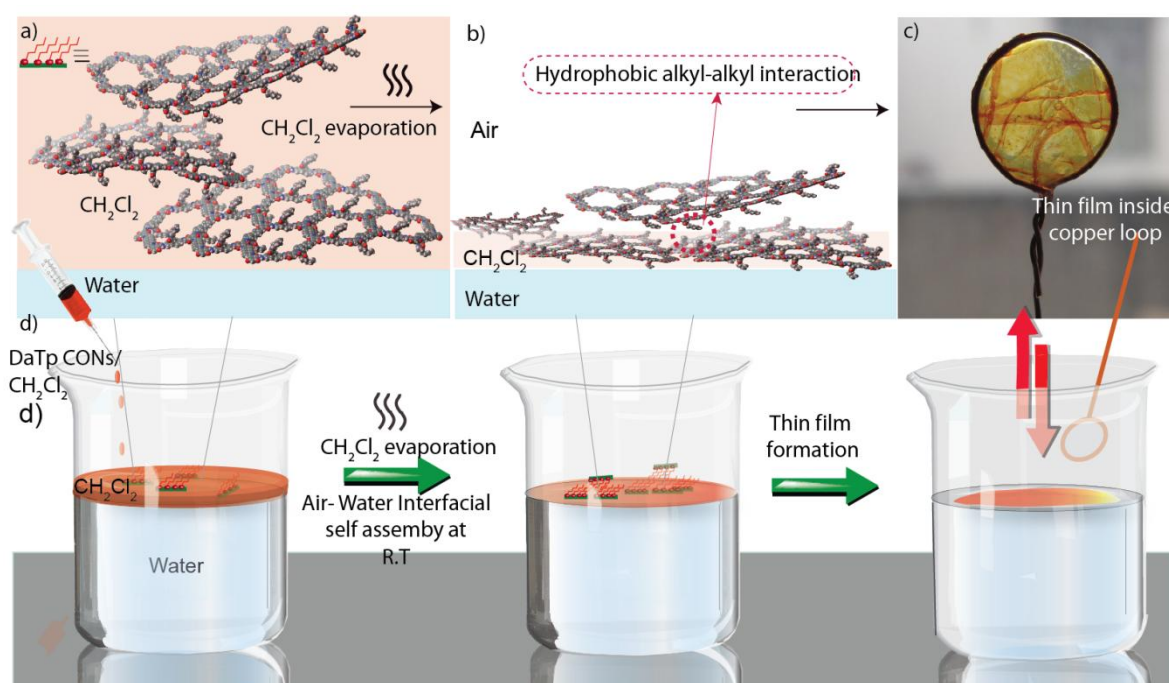


Figure 2.13: a & b) The plausible self-assembly process of **DaTp CONs** into a thin film. c) The free-standing **DaTp CON** thin film in a copper loop. d) The graphical representation of the process of thin film making in a glass beaker [M. A. Khayum et al., *Angew. Chem., Int. Ed.*, 2016, 55, 15604–15608 Copyright (2016) Wiley VCH].

DCM could spread on the whole water surface immediately and it also helps to spread the CONs on the same surface upon the addition each drop of suspension. After a transient bilayer formation of water and DCM, the low boiling DCM molecules starts to evaporate

quickly. As the evaporation occurs, the **DaTp CON** thin sheets can self-assemble to a thin film by the hydrophobic interaction of the alkyl groups grafted on the frameworks. After the

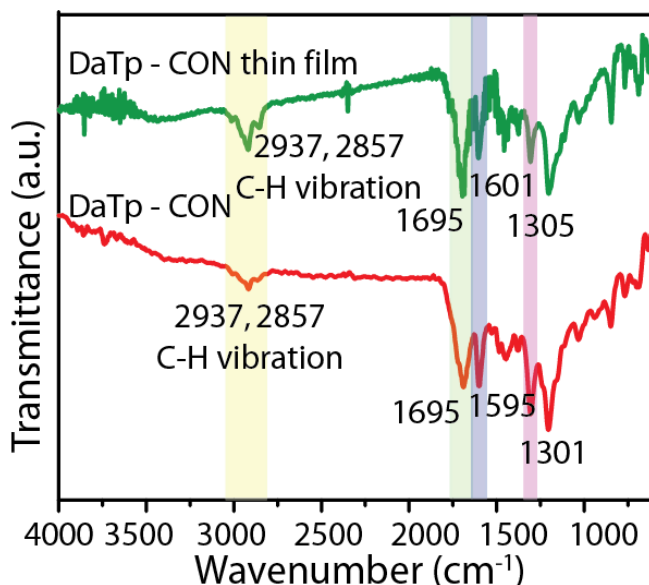


Figure 2.14: The FT-IR spectroscopy of **DaTp CON** thin film.

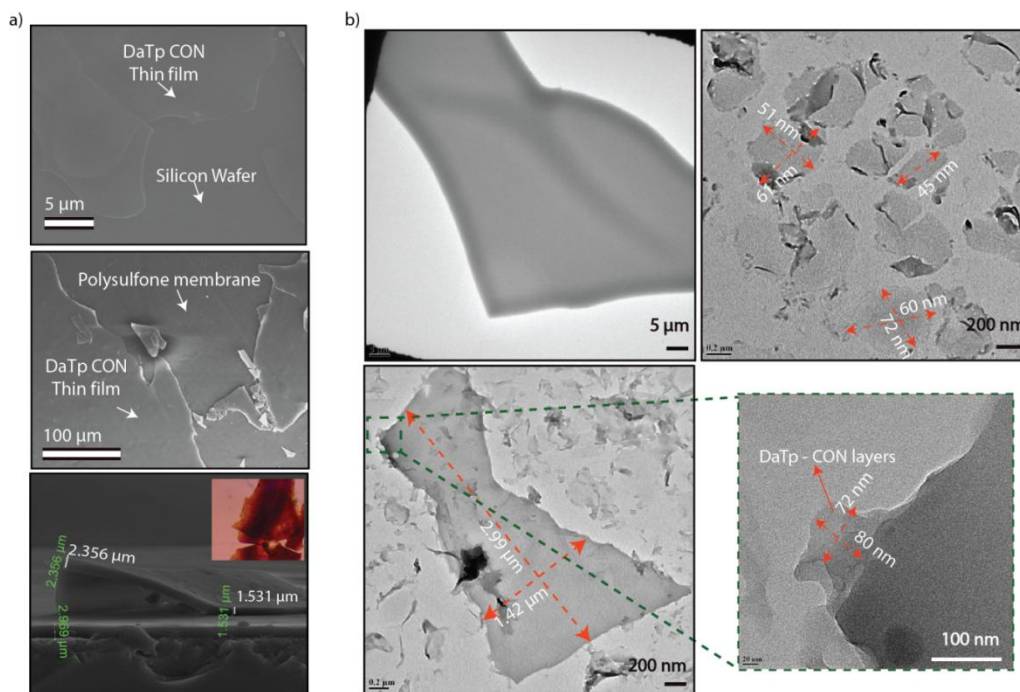


Figure 2.15: a) The SEM image of **DaTp CON** thin film on a silicon wafer and a polysulfone membrane. b) The TEM images of **DaTp CON** thin films. It explains the large lateral sheets are formed by small lateral sized CONs.

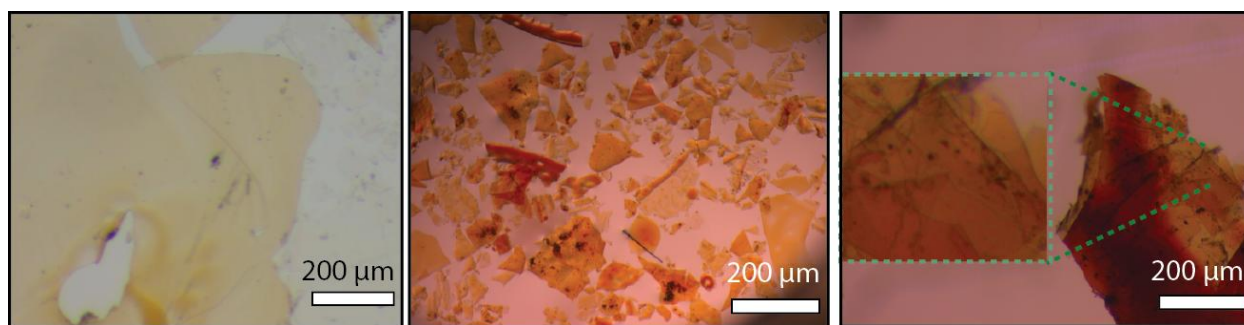


Figure 2.16: The optical microscopic images of **DaTp CON** thin films.

complete evaporation of the DCM, it is observed that a thin film has been formed at the air-water interface. Subsequently, this semi-transparent **DaTp CON** thin film could be transferred to various supports like glass, silicon wafer and even to a copper loop as a free-standing film. It is to be noted that, it could stand over a copper loop more than a month if undisturbed. This indicates the long-lasting free-standing nature and robustness of the **DaTp CON** thin film. The FT-IR spectra of the obtained CON thin film display a similar profile compared to the **DaTp CONs**, suggesting the intact chemical nature of the CONs even after the self-assembly process. The SEM image clearly shows the crack-free and continuous nature of the thin film on a silicon wafer and a polysulfone membrane. Furthermore, we have analyzed the nanometer-level self-assembly of the crushed thin film through the TEM. It displays that higher lateral size thin films are formed by the layer-by-layer self-assembly of small lateral size CON thin sheets. This further justifies the role of hydrophobic alkyl chains in the self-assembly of the thin film at the air-water interface. Additionally, the optical microscopic images display the aggregation of small thin films into a thick sheet. Moreover, to probe the control over the thickness of the fabricated free-standing thin film, we have carried out the AFM imaging and height profile mapping of the **DaTp CON** thin film sample on the silicon wafer. To control the thickness, we have used different concentrations (low: 1mg/5ml; medium: 4mg/5ml; and high: 8mg/5ml) of the **DaTp-CON** DCM solution for the fabrication of thin film in an 8 cm diameter glass beaker. At low concentration suspension, we could notice a comparatively very low sub-nanometer level thickness (1.2-1.6 nm) of the film

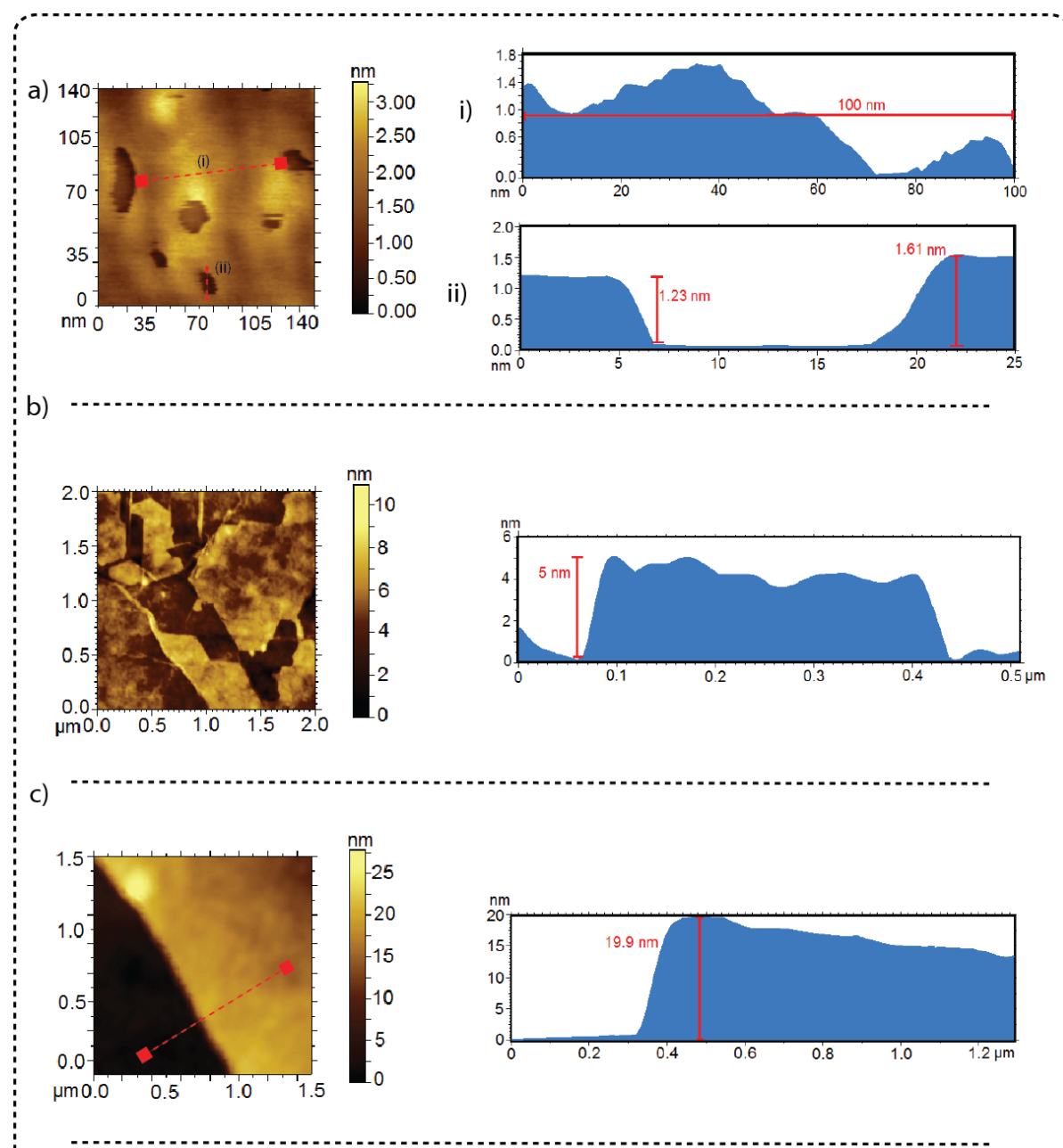


Figure 2.17: The AFM images and corresponding height profiles of a) low; b) medium and c) high concentration of the **DaTp** CON-DCM suspension.

from the height profile mapping of the AFM images. It worth mentioning that the length of the *N*-hexyl maleimide is ~ 1 nm, taking this into consideration, the thin film could be formed by the assembly mono or bilayer of the functionalized CONs. Similarly, the medium concentration of **DaTp** CONs delivered a thickness range of ~ 5 nm in the AFM height

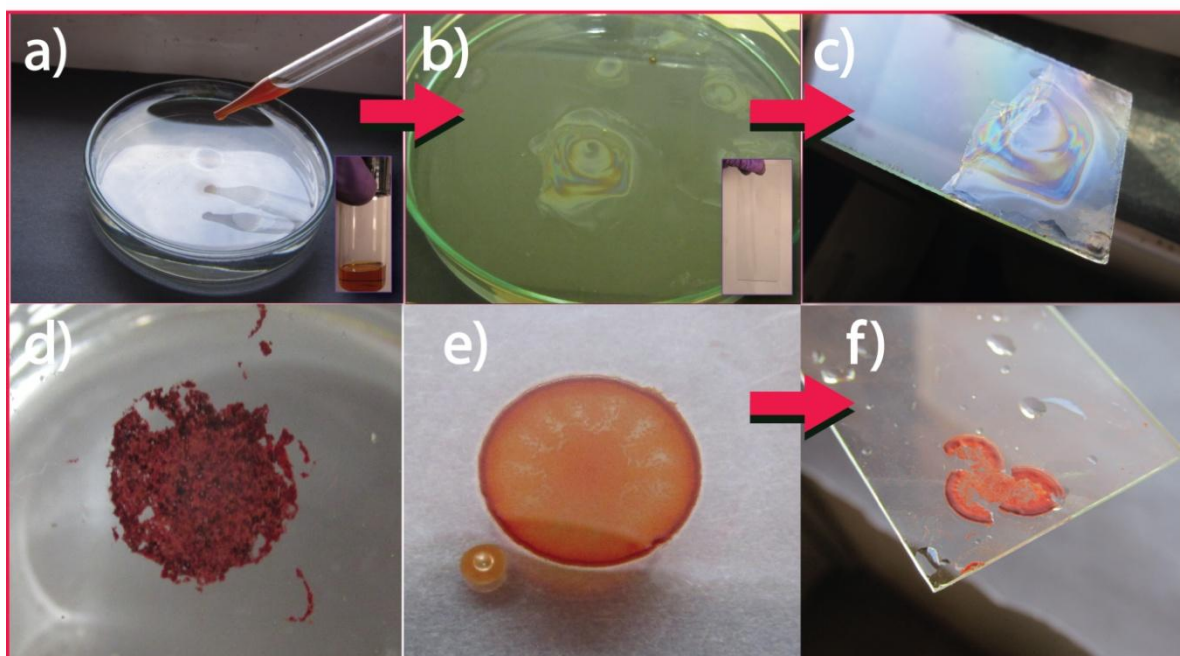


Figure 2.18: a) Drop casting of **DaTp CON-DCM** suspension on the water surface. b) The thin film formation at the air-water interface. c) The thin film on a glass surface. d & e) The mechanically grind CONs on water surface and f) on a glass surface.

profile. The AFM mapping of high concentration displays the thickness of 19 nm which shows the varying concentration leads to varying thickness. It is important to note that we could make the thin film with thickness up to 1 μm by controlling the concentration of the suspension.

2.2.8 The plausible mechanism for the thin film formation

We have performed the water contact angle analysis of the **DaTp CON** thin film to measure the hydrophobicity of the material. It displays good hydrophobic nature of the **DaTp CON** thin film (123°) compared to the pellet of pristine **DaTp COF** (73°). It could be attributed due to the presence of hydrophobic hexyl chain on the CONs. It further points out the possible mechanism of the thin film formation at the air-water interphase. The alkyl groups present in the CONs enhance the interaction with the solvent; hence a good separation of nanosheets is possible in the organic phase. When this suspension is added on the water surface, the alkyl group prevents the CONs to interact with the hydrophilic surface due to the presence of hydrophobic chains [2.13]. As the evaporation occurs, the CONs are self-

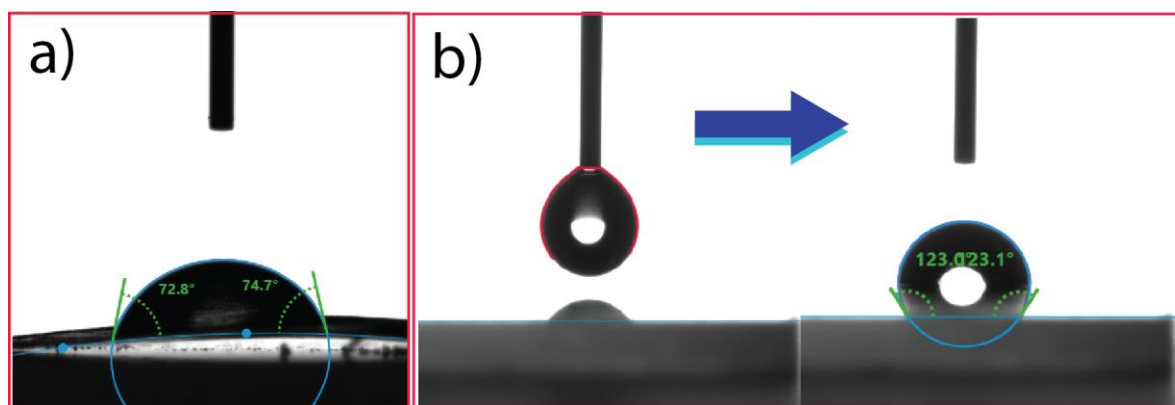


Figure 2.19: Contact angle measurement *DaTp* pellet and *DaTp* CON thin film.

assembled each other to reduce the entropy and the interlayer interaction has become more significant than the CON-solvent interaction which ultimately forms as self-assembled thin film on the water surface. Whereas, the attempts to make the self-assembled thin film from the mechanically exfoliated CONs has been failed due to the absence of such functional moieties in the framework.

2.3 Conclusion

In summary, we have synthesized an anthracene functionalized 2D- β -keoenamine framework by using solvothermal method. The obtained 2D-COF has been further subjected to the post modification at the 9, 10 position of anthracene by *N*-alkyl maleimide through 4+2 Diels Alder reaction. As a result of the cycloadduct formation, the planar anthracene is bent to 107° which causes the breaking Π - Π interaction between the interlayers of COF and ultimately results the chemical exfoliation of the COF layers. The resulted **DaTp** CONs exhibit good dispersion nature in the various organic solvents due to the presence of long alkyl chains. By taking this advantage, we have fabricated centimeter scale free-standing CON thin film through the layer by layer self-assembly at the air-water interface. The fabricated **DaTp** CON thin film showcases a defect-free and continuous nature with long last stability at the undisturbed condition.

2.4 Experimental procedures

2.4.1 Materials

1, 3, 5-triformylphloroglucinol (**Tp**) and 2, 6-diaminoanthracene were synthesized from phloroglucinol and 2,6-diaminianthraquinone respectively by the reference of reported articles [2.14 and 2.15].

2.4.2 Synthesis of *N*-hexylmaleimide

The 1-aminohexane (3.85 g, 0.038 mmol) was added in 30 ml acetic acid and then thoroughly stirred for 10 minutes at 0°C for dissolving the compound. Then the maleic anhydride (4.47 g; 0.0456 mmol) was added into the prepared solution. After the solution was stirred for 6 hours continuously, the reaction mixture was refluxed for another 24 hours under N₂ atmosphere. We observed the reaction mixture turned into a yellowish liquid indicates the completion of reaction. Consequently, we have added 100 ml of water to the obtained solution which in turn changed the yellowish colour to white. Then we have extracted the compound with 50 ml ethyl acetate and water (2 times), and again saturated NaHCO₃ (4 times) and water (2 times). The crude product was dried under NaSO₄ and then purified by the column chromatography (1:9-Ethylacetate: pet ether). The final product (*N*-hexylmaleimide) was obtained as a pale yellow liquid and confirmed through ¹H and ¹³C NMR. ¹H NMR (ppm, CDCl₃): 0.82 (t, 3H), 1.12-1.31 (q, 6H), 1.51 (t, 2H), 3.45 (t, 2H), 6.67 (s, 2H). ¹³C NMR (ppm, Acetone- d₆): 14.43 (1C), 23 (1C), 27 (2C), 32 (2C), 38 (1C), 135 (2C), 172 (2C).

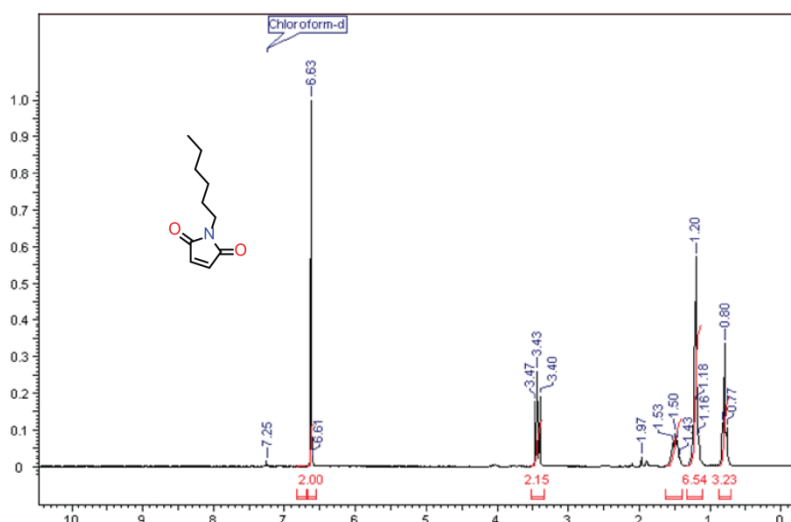


Figure 2.20: ¹H NMR (in CDCl₃) of *N*-hexylmaleimide

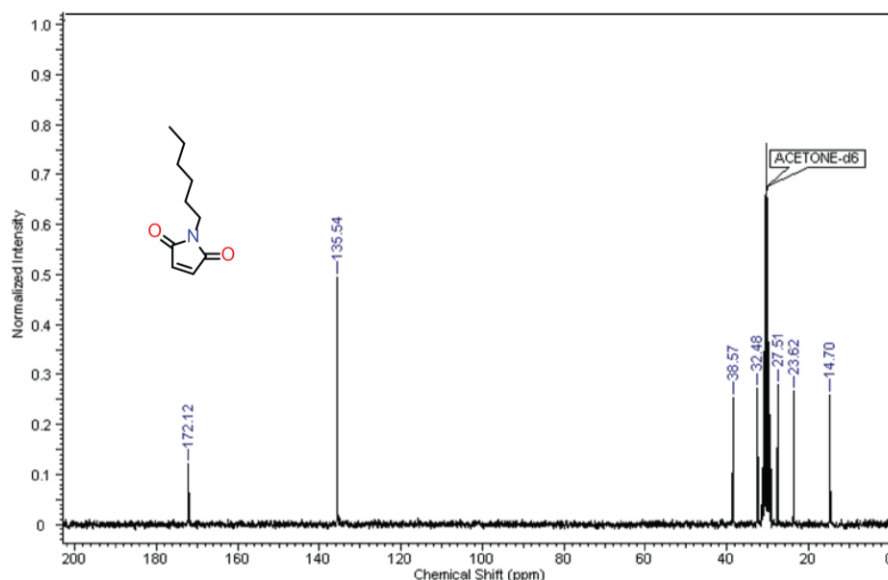


Figure 2.21: ^{13}C NMR (in Acetone- d_6) of *N*-hexylmaleimide.

2.4.3 Synthesis of *DaTp* COF

We have performed a solvothermal synthesis of reversible Schiff base condensation reaction between 2,6-diaminoanthracene (**Da**: 62.4 mg, 0.3 mmol) and 1, 3, 5-triformylphloroglucinol (**Tp**: 42 mg, 0.2 mmol) in Pyrex glass tube. The 2 ml solvent mixture of mesitylene–dioxane in 1:1 ratio has been taken for the partial solubility of the organic building units. Additionally, a catalytic amount of 8M acetic acid (0.2 ml) was added to above reaction mixture for the reversibility of Schiff base reaction. The whole reaction mixture was sonicated for 15 minutes and then followed by flash frozen (at 77K by using liquid N_2 bath) and degassed for three times freeze-thaw cycles. After the complete evacuation, the Pyrex tube was sealed and then kept at at 120°C for 72 hours. Then reddish brown precipitate was obtained by centrifugation and subjected for washing by DMA (three times), water (three times) and Acetone (three times). A dark reddish brown product was collected after the compound was dried at 150°C under vacuum for removing the trapped solvent molecules (yield 80%).

2.4.4 Synthesis of 2,4,6-tris(anthracen-2-ylamino)methylene)cyclohexane-1,3,5-trione (*DaTp* monomer)

The monomer compound was synthesized from **Tp** (0.05g; 0.23 mmol) and 2-aminoanthracene (0.27g; 1.428 mmol). Both reactants were taken in ethanol (25 ml) and then refluxed for 24 hours at N₂ atmosphere. After the completion of reaction, the crude product was collected by filtration, and then washed with ethanol for three times to remove the excess amount of reactants. The obtained product was dried under a vacuum oven to remove the solvent molecules which finally yielded 75% of the brownish yellow colored product. **IR (powder, cm⁻¹):** 1590 (s), 1448 (m), 1287 (s), 980 (m), 900(s), 755 (s).

2.4.5 Synthesis of 2,6-diamino-13-ethyl-9,10-dihydro-9,10-[3,4]epipyrroloanthracene-12,14-dione (Reference compound 1)

The reference compound 1 was synthesized by 4+2 Diels-Alder reaction of 2, 6 -diaminoanthracene (0.032 g; 0.55 mmol) and *N*-ethylmaleimide (0.019 g; 0.55 mmol). The reaction mixture was taken in 15 ml toluene solvent and then refluxed for 24 hours under N₂ atmosphere. The crude product was collected and then purified by Column chromatography (1:1 petether: ethylacetate) which finally yielded 75% pure cycloadduct. **¹³C NMR (ppm, DMSO-d₆):** 12.3 (1C), 32.5 (1C), 44 (2C), 47 (2C), 110 (4C), 124(2C), 126 (2C), 141 (1C), 143 (1C), 147 (2C), 177 (2C).

2.4.6 Synthesis of 2-amino-13-ethyl-9, 10-dihydro-9,10-[3,4]epipyrroloanthracene-12,14-dione (Reference compound 2)

The reference compound 2 was synthesized by 4+2 Diels-Alder reaction of 2-aminoanthracene (0.030 g; 0.155 mmol) and *N*-ethylmaleimide (0.019 g; 0.155 mmol). The reaction mixture was taken in 15 ml toluene solvent and then refluxed for 24 hours under N₂ atmosphere. The crude product was collected and then purified by Column chromatography (1:1 petether: ethylacetate) which finally yielded 80-85% pure cycloadduct. **¹³C NMR (ppm, CDCl₃):** 12.4 (1C), 32.9 (1C), 47-45 (4C), 112 (2C), 123 (2C), 126-128 (2C), 139 (2C), 141 (1C), 142 (1C), 145.7 (2C), 177 (2C).

2.4.7 Synthesis of DaTp CONs

The **DaTp CONs** was synthesized by 4+2 Diels-Alder reaction of 2 **DaTp** (15 mg; 0.015mmol) and *N*-hexylmaleimide (8.6 mg; 0.047mmol). The reaction mixture was taken in 20 ml mesitylene solvent and then refluxed for 24 hours at 160° C under N₂ atmosphere. The solution turned into a reddish color during the course of reaction. The mesitylene was removed by the vacuum drying and then DCM (2ml) and pet ether (20 ml) was added to the crude product. Again, the derived precipitate was washed with pet ether for 3-4 times and then dried 60° C under vacuum, which finally yielded as a dark yellow color product. **IR (powder, cm⁻¹):** 2857-2915 (w), 1695 (s), 1600 (s), 1446 (m), 1300 (s), 1200(s), 1034 (w), 935 (w), 853 (m), 776(m), 703 (m).

2.4.8 General methods for characterization

(a) Powder X-Ray Diffraction (PXRD): The PXRD data were investigated on a Phillips PANalytical diffractometer using a Cu K α radiation ($\lambda = 1.5406 \text{ \AA}$), with a scan rate of 2° min⁻¹. The tube current and voltage were optimized at 30 mA and 40 kV respectively. The COF powder was taken in an Aluminium holder and then scanned between 2 and 40° 2 θ (step size of 0.02°).

(b) Thermogravimetric Analysis (TGA): TGA was investigated on SDT Q 600 TG-DTA analyzer instrument. 2 mg of the COF sample was placed in an aluminium crucible and heated from 25 to 900 °C under N₂ atmosphere at heating rate of 20 °C min⁻¹.

(c) IR Spectroscopy: The Fourier transform infrared spectra (FTIR) of the COFs were recorded on a *PERKIN ELMER FT-IR SPECTRUM* (Nicolet) spectrometer in ATR mode.

The FTIR profiles were investigated within the range of 4000-600 cm⁻¹.

(d) Gas Adsorption: The N₂ gas adsorption experiments of COF samples were analyzed in an *Autosorb* automatic volumetric instrument (*Quantachrome*) (up to 1 bar). COFs were degassed under vacuum at 120°C for 12 hours prior to the gas adsorption analysis.

(e) SEM: SEM images were recorded with a Zeiss DSM 950 scanning electron microscope and FEI, QUANTA 200 3D Scanning Electron Microscope with tungsten filament as electron source operated at 10 kV. The COF samples were sputtered with Au (nano sized film) prior to imaging by a SCD 040 Balzers Union.

(f) **TEM:** TEM images were investigated by using FEI Tecnai G2 F20 X-TWIN TEM at an accelerating voltage of 200 kV. To preresare the TEM sample for the analysis, The COF Samples were dispersed in acetonitrile solvent and drop cast on copper grids TEM Window (TED PELLA, INC. 200 mesh).

(g) **^{13}C CP MAS Solid-state NMR:** We have used a Bruker 300 MHz NMR spectrometer, and for quantitative analysis ^{13}C CP MAS decoupled solid-state NMR was taken in Jeol 400 with scanning rate 849 and Ligand NMR data were taken in Bruker 200 MHz NMR spectrometer.

(h) **Optical microscopy:** Optical images of samples were investigated by Modular Routine Stereo Microscope with 8:1 Zoom Leica M80.

(i) **Dynamic Light Scattering:** The Brookhaven Instruments Corporation 90 plus Particle Size analyzer with scattering angle 90° and laser wavelength 632.8 nm has been used for the DLS.

(j) **Contact angle:** We have used Kruss Drop Shape Analyzer –DSA25S for the contact angle measurement.

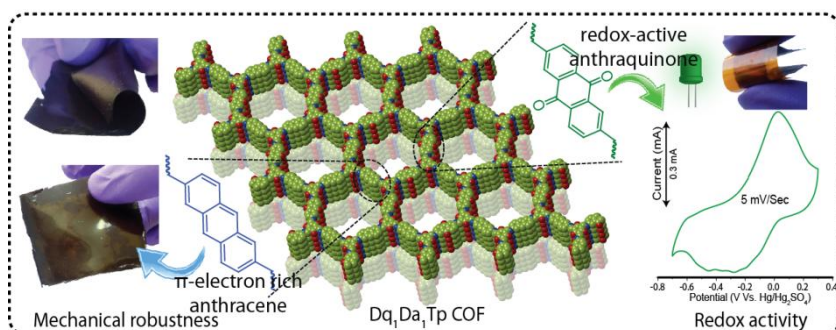
(k) **Atomic Force Microscopy (AFM):** We have investigated the surface morphology and thickness of thin sheets and films by using the AFM ‘Agilent Technologies, USA, Model 5100’. All scans were recorded in an air medium.

NOTE: The experimental observations and results in this chapter have been already published in *Angew. Chem. Int. Ed.* 2016, 55, 1 – 6; entitled: “Chemically Delaminated Free-Standing Ultrathin Covalent Organic Nanosheets”. The major contribution of this publication was done by the Dr. Rahul Banerjee and his student Abdul Khayum M from CSIR National Chemical Laboratory, Pune. The AFM images were investigated by the collaboration with Dr. Rabibrata Mukherjee and his student Anuja Das from *Indian Institute of Technology, Kharagpur*.

CHAPTER 3

Convergent Covalent Organic Framework Thin Sheet as Flexible Supercapacitor

Abstract: The significance of the fabrication of covalent organic frameworks into two dimensional thin films and sheets has been



increased due to their potential features of macroscopic forms in various fields. In this regard, the development of mechanically robust 2D macro-architecture COFs requires scientific attention and has a pivotal role in the advanced applications like flexible energy storage systems. Keeping this in perspective, herein, we have developed a mechanically strong and redox-active β -ketoenamine covalent organic framework through a convergent synthetic strategy. In this method, we have integrated a π -electron rich anthracene (**Da**) and redox-active anthraquinone (**Dq**) into a single framework through a solid-state synthesis. The obtained convergent COF thin sheet displays redox activity as well as mechanical strength, which has been further utilized as a flexible electrode in a quasi solid-state supercapacitor. In the convergent COF, the π -electron rich anthracene boosts the mechanical strength of the thin sheets, whereas, the anthraquinones are responsible for the energy storage of the system.

3.1 Introduction

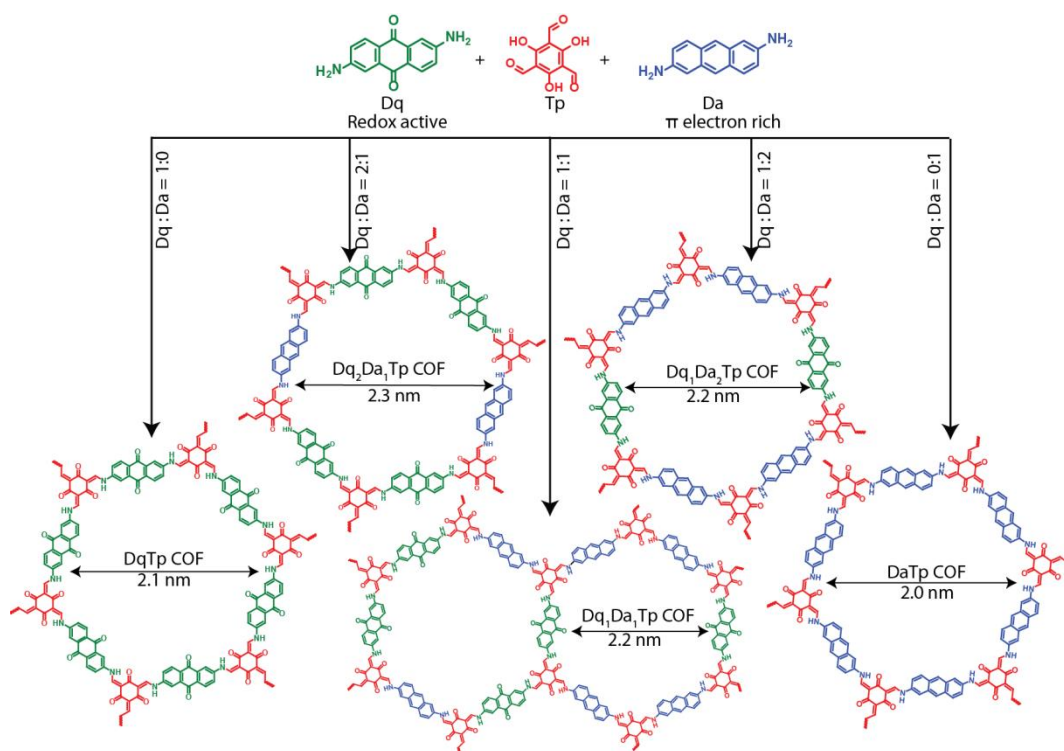
Owing to their promising features, the development of the macroscopic architecture of COFs into the two-dimensional (2D) form results novel advancements in several commercial level applications. Specifically, the various 2D macroscopic forms of COFs such as thin films; thin sheets; and porous membranes exhibit their excellent performance toward energy storage; sensors; gas and solvent separations; and water purification [3.1]. However, most of these 2D forms face the lack of enough mechanical strength towards the external physical disturbances and makes the COF as a fragile candidate for the commercial utilities. Although researchers have developed polymer-COF membranes for boosting the mechanical strength of the 2D forms, the mixing of the polymer reduces the intrinsic features like crystallinity and porosity of the COFs [3.2]. In this regard, boosting the mechanical strength of the 2D macroscopic forms of COFs without losing crystallinity and porosity is scientifically and technologically important for the next level advances of the material, especially in the flexible energy storage devices. Due to the presence of the well-ordered nano pores and precisely integrated redox functionalities in the COF matrix, it could serve as an excellent energy storage material in supercapacitors and batteries [3.4]. Meanwhile, such ordered porosity and well-connected redox functionalities are not available in the polymer or other carbon-based electrode materials [3.5].

COFs as energy storage platform:

The rapid consumption of non-renewable energy sources like fossil fuels has drawn a major attention towards the requirement of sustainable energy resources and storages. Supercapacitors and batteries are the two devices undergone extensive research in past few decades as the superior energy storage systems. Supercapacitors also called ultracapacitors are viewed as outstanding devices in terms of greater power density, high charge-discharge and long-life than battery [3.4]. The charge storage mechanism in a supercapacitor can occur through two ways: 1) Electric double layer capacitance (EDLC). In EDLC, the energy storage mechanism occurs through the physical adsorption of the charges on the surface of the electrode; 2) Pseudocapacitance: In this mechanism, the charge will be stored through the reversible chemical reactions of redox functional groups grafted on the electrode [3.6]. In the EDLC, the surface area of the electrode plays the major role for the adsorption of charges. Meanwhile, the reversible electrochemical reaction between electrode and electrolyte is

playing the important role in the pseudocapacitance mechanism. Interestingly, the versatile properties such as tunable & ordered pore structure and the higher surface area of COFs offered to use as an electrode material in energy storage systems. Moreover, the precise integration of redox-active functional moieties can enhance the charge storage performance of the COFs. The ordered intrinsic pores in the COF can aid the lucid diffusion electrolyte ions through the entire porous matrix of the COF, whereas the amorphous material lacks such properties. In this regard, it has been considered that the COFs are promising materials in energy storage applications.

The previous reports on COF based energy storage applications mostly described on the granular based electrode materials [3.3b & 3.4a]. It is important to note that, during the electrode fabrication process, the crystalline porous COFs are subjected to ultra-sonication or mechanical grinding to make uniform slurry with binders and conductive additives. However, during the course of grinding or sonication, there is a great chance of losing crystallinity as well as the surface area of the material which may affect on the overall performance in the capacitance. Moreover, the previous attempts of



Scheme 3.6: The schematic representation of the synthesis of all COFs.

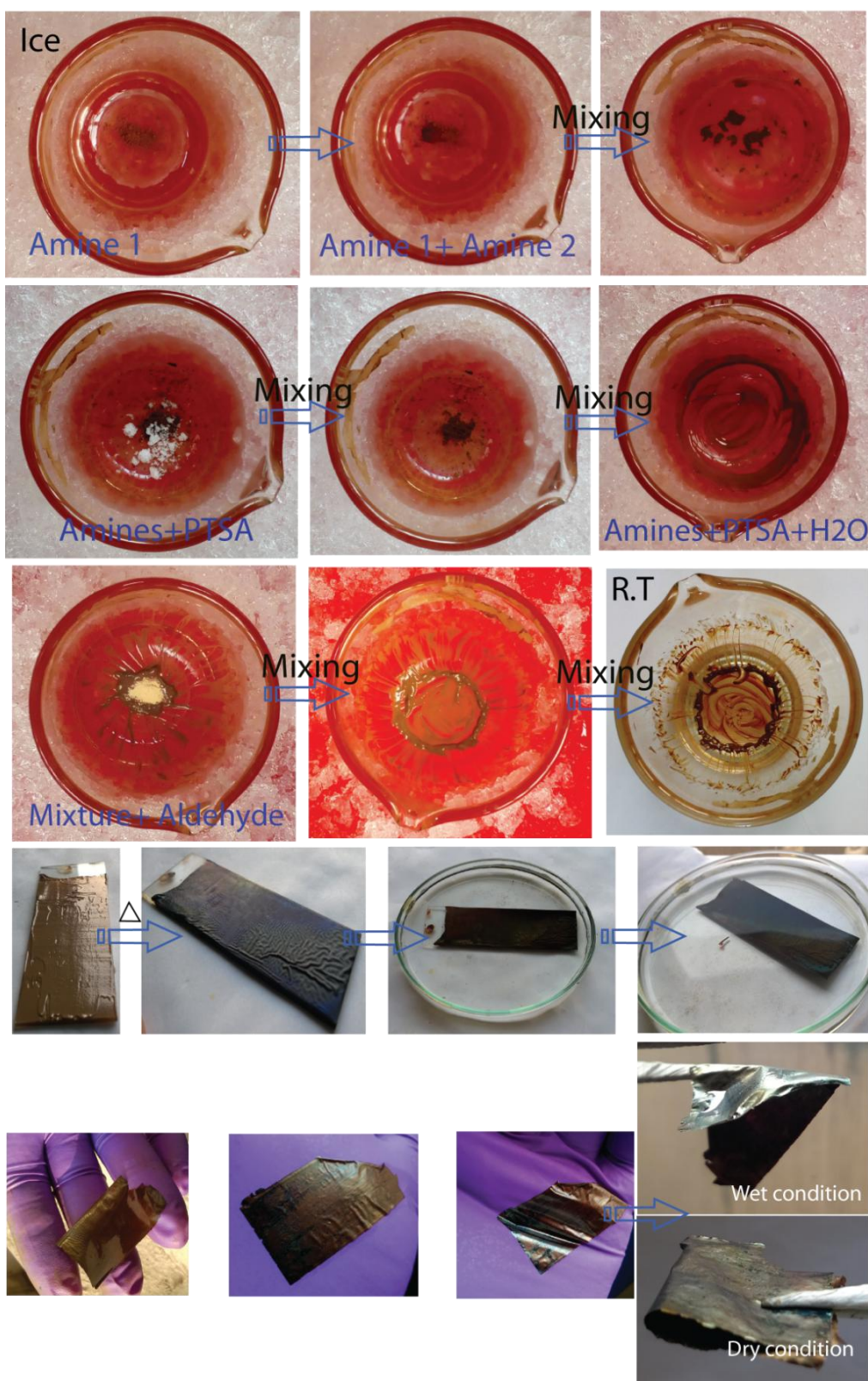


Figure 3.1: The digital photographs of the fabrication of COF thin sheet through SSM method.

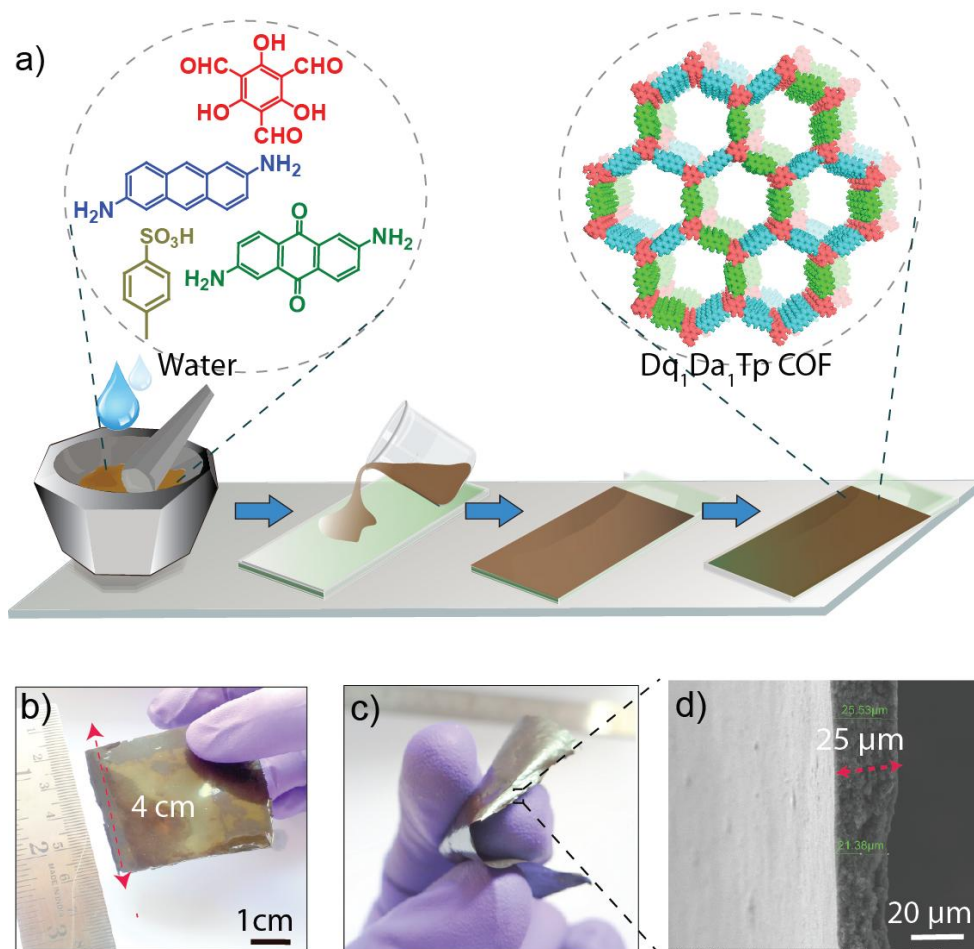


Figure 3.2: a) The diagrammatic representation of the fabrication of COF thin sheet. b) The digital photograph of 16 cm² Dq_1D_1Tp COF thin sheet. c) The photograph shows the flexibility of Dq_1D_1Tp COF thin sheet. d) The cross-sectional SEM image of Dq_1D_1Tp COF thin sheet

COF based energy storage applications were mostly executed in the conventional liquid electrolyte supercapacitor system [3.3a]. Herein, the major shortcomings are electrolyte leakage and rigid compact nature of the devices. Notably, electrolyte leakage is a major concern of liquid electrolyte based conventional supercapacitors, which end up with the requirement of highly expensive device package due to the corrosive and toxic nature of liquid electrolyte. In this regard, the investigation on COF thin film coating on a gold thin film current collector avoids the tedious electrode fabrication process for a conventional liquid electrolyte supercapacitor [3.1c]. However, the disadvantages like the scalability and the usage of a highly expensive gold thin film in such system is not favourable in the commercial aspects. The advanced wearable electrochemical energy devices such as foldable

phones and wearable electronics often demands flexible and mechanically robust solid state super capacitors as a flash power sources [3.5 & 3.7]. In this aspect, a novel design and fabrication strategy needs to be developed to transform fragile COF micro-crystallites into mechanically robust supercapacitor electrode thin sheets. Although the mechanical strength and the integrity of COF crystallites can be improved by the usage of binders or additives; pore blocking from such polymeric binders can cause a reduction in the active surface area and electrochemical capacitance performance.

Keeping all these in perspective, in this chapter, we have developed a novel convergent linker strategy to synthesize and fabricate redox-active COFs into flexible solid-state supercapacitors (SSC) with high mechanical strength. This convergent strategy involves in-situ insertion of two axial-linkers with distinct physicochemical properties into single COF matrix through solid-state molecular mixing procedure (SSM). It is noteworthy that the

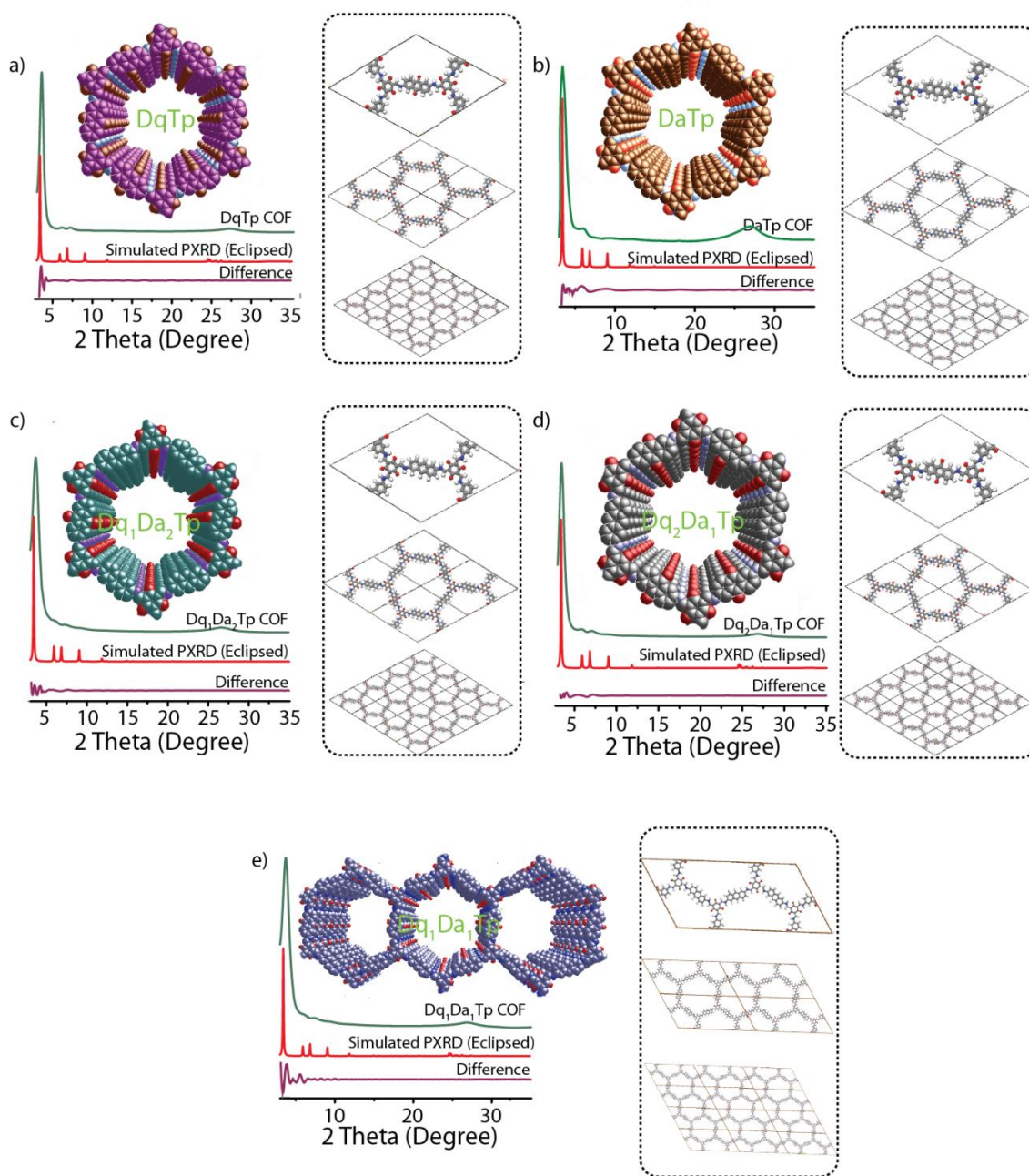


Figure 3.3: The PXRD profiles of all COF thin sheets.

researches on the non-covalent interactions suggest their pivotal role in the improvement of mechanical robustness of a macroscopic material [3.8]. Notably, the hetero-functional groups were present in the graphene oxide (GO) are found as a key to enhance the mechanical strength of the GO sheets by imparting the interlayer hydrogen bonding [3.9]. Taking these into consideration, in the convergent COF, we have strategically chosen the π -electron rich anthracene (**Da**) [3.10] as a linker which assists to improve the mechanical strength.

Whereas, the redox-active anthraquinone (**Dq**) moiety is responsible for the charge storage and hence the pseudo-capacitance of the material. The demonstrated convergent SSM method is very simple, scalable for the hetero-linked COFs [3.11]. Furthermore, it allows the facile fabrication of redox-active COF crystallites into defect-free uniform thin sheet electrodes without using any binders. Moreover, the functional regulation on the molecular level of the framework keeps the crystalline and porous nature of the material.

3.2 Result and Discussion

3.2.1 Synthesis and characterization

We have taken the various ratios of **Dq** and **Da** linkers in 1:0 (**DqTp**), 0:1 (**DaTp**), 1:2 (**Dq₁Da₂TP**), 1:1 (**Dq₁Da₁TP**) and 2:1 (**Dq₂Da₁TP**) to rationalize the importance of the quantitative inclusion of functional moieties (*Scheme 3.1*). The solid-state mixing (SSM) of the linkers (amines and aldehyde) with the presence of *p*-toluenesulphonic acid (PTSA) catalyst provides a precursor paste which has

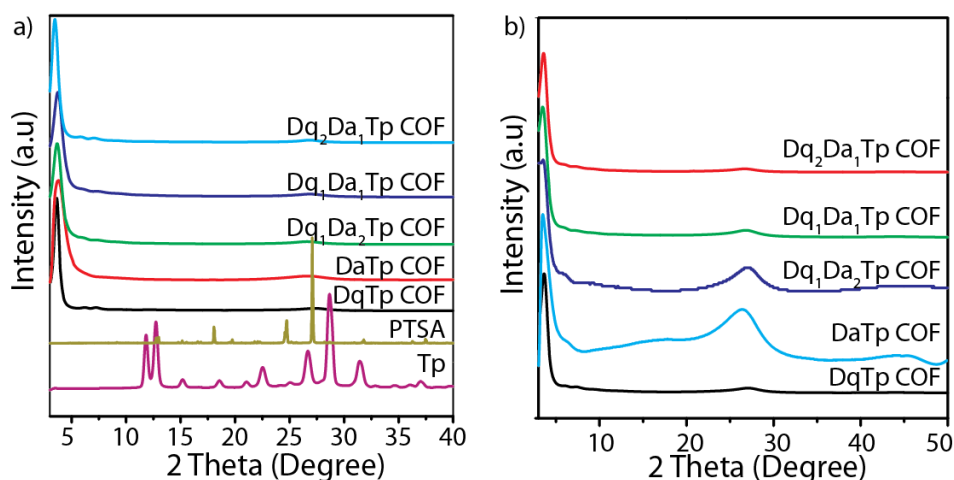


Figure 3.4: a) The XRD profiles COFs, **TP** and PTSA. b) The XRD of all COFs after the treatment in 1M H₂SO₄ for 24 hours.

been further fabricated as a thin sheet on a glass slide (*Figure 3.1 & 3.2*). The thermal treatment (90°C) in a closed condition allows the formation of β -ketoenamine framework [3.12] and obtained thin sheets were washed by DMA, water and acetone. The rationale variations of linkers in COFs have been reflected in their redox-active and mechanical properties. We have observed that the mechanical strength of the COF thin sheet was greatly

enhanced by the increment in the percentage of **Da** linker. Meanwhile the higher **Dq** loaded COF thin sheets (**DqTp**,

Dq₂Da₁Tp and **Dq₁Da₁Tp**) exhibit good redox activity as well as specific capacitance (154, 122 and 111 Fg⁻¹ respectively at 1.56 mAcm⁻²) in three-electrode assembly. The convergent **Dq₁Da₁Tp** COF supercapacitor displays high mechanical strength and maintains its capacitance under mechanical deformation such as bending (90% of the capacitance retention even after 2500 cycles).

2.2.2 The structural characterizations

The crystallinity of COFs is inspected through the powder X-ray diffraction analysis (PXRD). PXRD profile of each COF indicates the crystalline nature of the material (*Figure 3.3*). Moreover, the distinctive PXRD profiles of all COFs compared with the starting material PXRDs suggests that phase purity of all synthesized thin sheets (*Figure 3.4*). All COFs exhibit typical 2D layered hexagonal ordered nature with three major peaks in PXRD profiles which are assigned as 100, 110 and 001 planes. The first peak position of **DqTp**; **DaTp**; **Dq₁Da₂Tp**; **Dq₁Da₁Tp** and **Dq₂Da₁Tp** COFs have been appeared at the angle of 2θ 3.6°, 3.4°, 3.7°, 3.4° and 3.6° respectively. Likewise, the second peak position at the 2θ angle 6.1°, 6.2°, 6.0°, 5.8°, and 5.9° correspond to 110 planes for the above mentioned COFs. The peak which is diffracted from 001 planes are generally weak and broad and located around the angle of 2θ 26-27° range. Moreover, the possible structures of the COFs were modeled in Material Studio S-6. The experimental PXRD of the COFs are well matched with the simulated PXRD in the eclipsed molecular structure. In addition, the Pawley refinement has been done on all models with the experimental PXRD profiles [**DqTp** (Rp = 5.1%, Rwp= 6.5%); **DaTp** (Rp = 4.6%, Rwp= 2.9%); **Dq₁Da₂Tp** (Rp = 2.2%, Rwp= 2.8%); **Dq₁Da₁Tp** (Rp = 9.96%, Rwp= 12.62%); and **Dq₂Da₁Tp** (Rp = 7.45%, Rwp= 9.07%)]. It is noteworthy that all as synthesized COFs are chemically stable in acid as well as organic solvents due to the keto-enol tautomeric nature. The retained PXRD is a direct evidence of the intact structural regularity of each COFs even after the stability test in 1M H₂SO₄ for 24 hours (*Figure 3.4*).

3.2.3 Chemical characterization

The absence of N-H vibration peaks from amine linkers and the aldehyde carbonyl peak from **Tp** in FT-IR profile of the COFs ruled out the presence of the precursor impurity in the thin

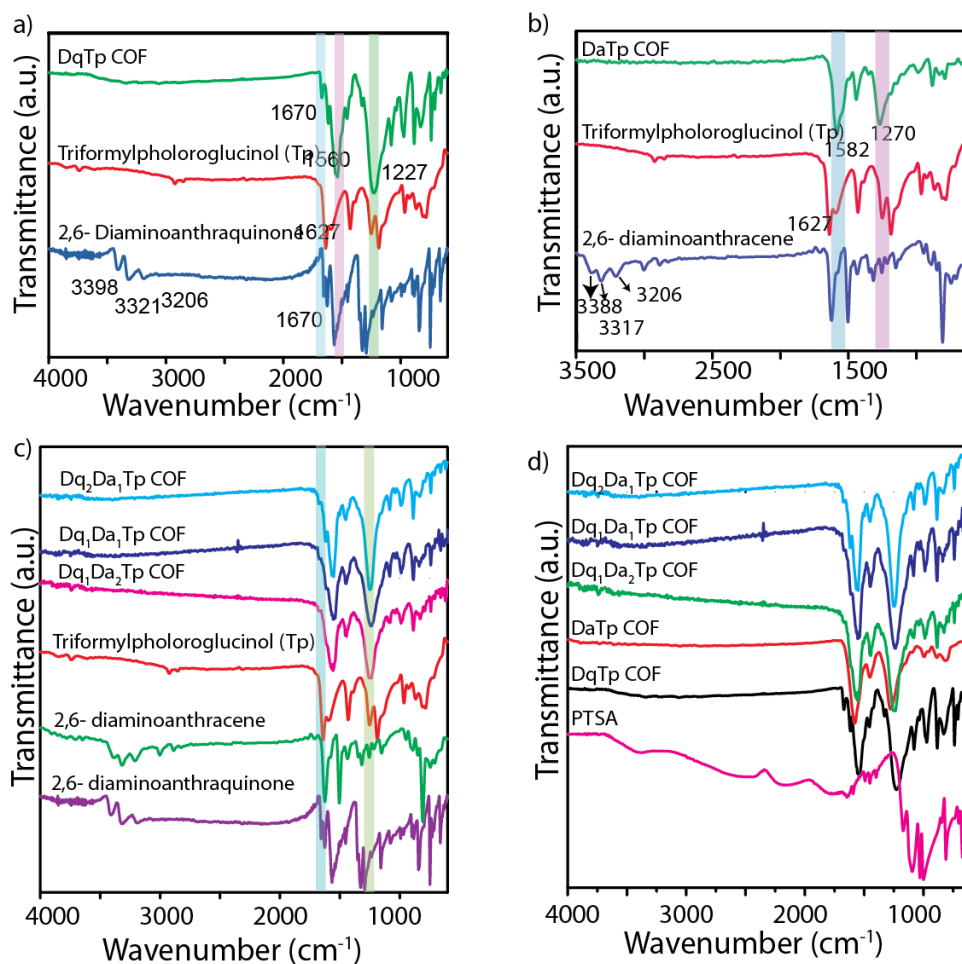


Figure 3.5: a) The FT-IR spectra of a) **DqTp**; b) **DaTp**; and c) convergent COFs with starting materials. d) The FT-IR spectra comparison of all COFs with PTSA

sheet matrix (**Figure 3.5**). Similarly, the absence of the intense and sharp peak at 1605 and 815 cm⁻¹ signifies the complete removal PTSA during washing time. The FT-IR spectra of **DqTp** shows the stretching vibrations at 1669, 1611, 1554, 1328 cm⁻¹ correspond to C=O of anthraquinone moiety, C=O from keto-enol tautomeric center, C=C and C-N functional groups respectively. Similarly, the anthracene linked **DaTp** exhibits the characteristics stretching peaks of C=O and C-N from the β -ketoenamine framework at 1580 and 1280 cm⁻¹ respectively. Whereas the hetero linked **Dq₁Da₂Tp**; **Dq₁Da₁Tp** and **Dq₂Da₁Tp** COFs displayed their characteristic peaks with a slight variation in stretching frequency from the single linker **DqTp** and **DaTp** COFs. Herein, the stretching frequency of anthraquinone C=O

group has been featured at 1674, 1674 and 1669 cm^{-1} for **Dq₁Da₁Tp** and **Dq₂Da₁Tp** COFs respectively. Additionally, the characteristic keto-enol tautomeric

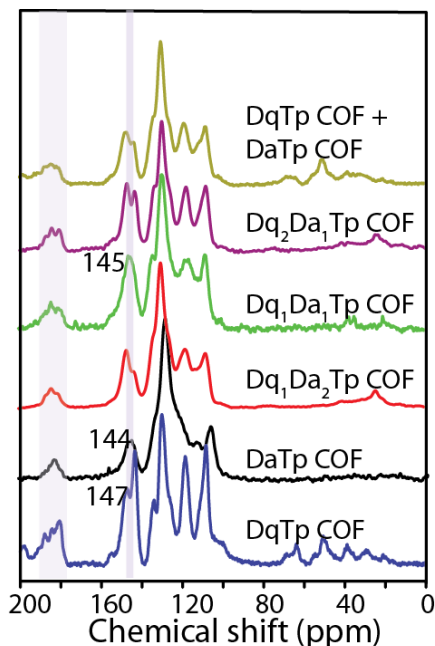


Figure 3.6: ^{13}C CP MAS Solid-state NMR of all COFs and the physical mixture of **DqTp** and **DaTp** COFs.

peaks of the above mentioned COFs have been displayed at 1660-1670 cm^{-1} and 1237-1242 cm^{-1} for C=O and C-N respectively.

The additional structural information of single-linker and hetero-linker COFs has been further supported by ^{13}C CP-MAS solid-state NMR spectra (**Figure 3.6**). **DqTp** displays **Dq** C=O resonance at the chemical shift of 180 ppm and the C=O group of typical β -ketoenamine framework at the chemical shift of 184 ppm. Moreover, the α -enamine and enamine carbon exhibit the peak shifts at 118 and 147 ppm respectively. Similarly, the **DaTp** features the ^{13}C peaks at 144 and 182 ppm correspond to the enamine and keto carbons. Notably, similar characteristic peaks have been observed in the ^{13}C NMR spectra of hetero-linked **Dq₁Da₁Tp** COF except a small chemical shift (145 ppm) in enamine (-C=N-H) carbon compared to the single-linker COFs, which could be a sign of the possible formation of the hetero-linked COF with anthracene (**Da**) and anthraquinone (**Dq**) as linkers (Figure 2a). Again, a slight chemical shift has been observed for the -C=N-H carbon of **Dq₁Da₂Tp**

(147.1 ppm) and **Dq₁Da₂Tp** (146.8 ppm). Moreover, we have calculated the monomer ratio (**Dq:Da**) in the hetero-linked COFs by the integration of ¹³C NMR peaks of

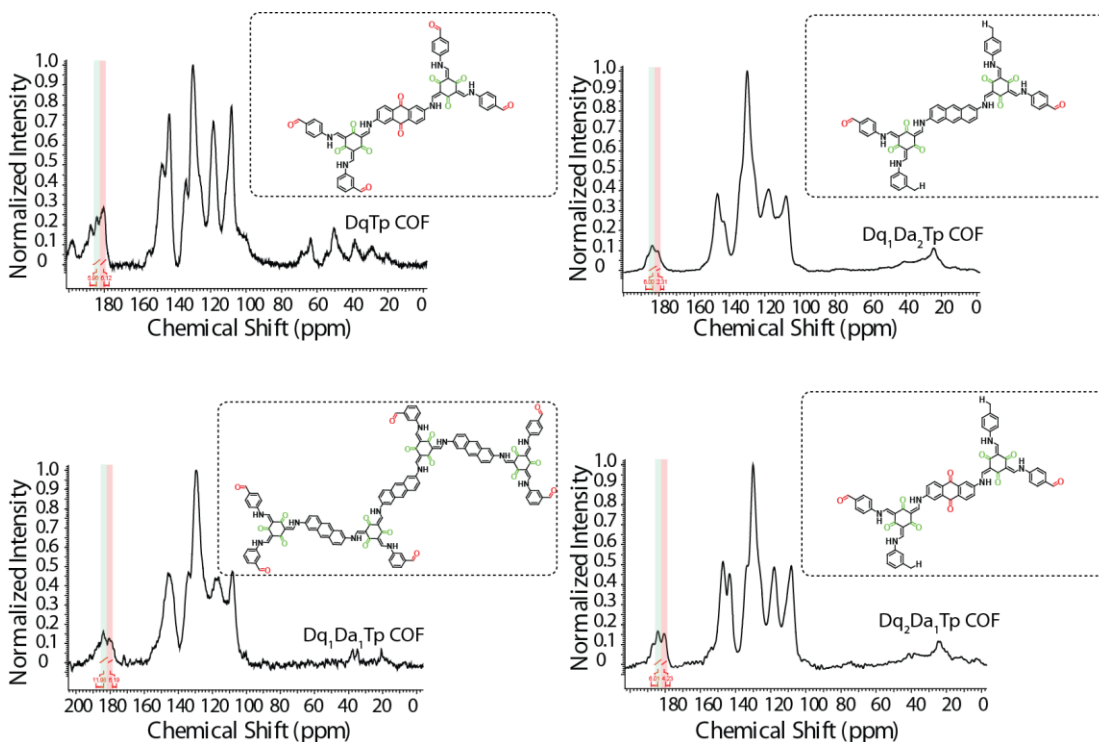


Figure 3.7: ¹³C CP MAS Solid-state quantitative integrations of all COFs.

keto-enol tautomeric C=O peak (183-185 ppm) and anthraquinone C=O peak (179-182 ppm).

The quantification of anthraquinone (Dq) and anthracene (Da) linkers in COFs:

To quantify the number **Dq** and **Da** moieties in COF, we have adopted a single layer of unit cell as a representation for the whole framework of each COFs (**Figure 3.7**). In ¹³C solid-state NMR, we have chosen the carbon from keto group of β -ketoenamine (**Tp** C=O) structure as a reference to integrate the number of carbons from C=O of **Dq** moiety (red colour). In this way, we could calculate the number of **Dq** appeared in each synthesized COFs. As a result, the number of **Da** moieties is also derived from the above calculation.

In order to ensure the validity of this method, we have derived the number of **Dq** from the **DqTp** in which the exact number of **Dq** linker in the unit cell of COF is already established (**Table 3.1**). As per the modeled single layer of unit cell of **DqTp**, it contains six number of C=O from three **Dq** (2×3) and six number of C=O from β -ketoenamine structure (3×2).

Notably, we could obtain the approximate integrated value of **Dq** C=O after the quantitative integration of ^{13}C NMR by taking **Tp** C=O as a reference. Similarly, we have applied the above method of calculation for the integration of **Dq** C=O of the convergent COFs too.

COFs	Theoretical values		From ^{13}C NMR					
	No. of C=O from two Tp moieties	No. of C=O units from Dq linkers	No. of C=O from two Tp moieties	No. of C=O units from Dq linkers	Total no. of linker s in a single layer of the unit cell	No. of Dq linkers in a unit cell $\frac{\text{Total number of C=O from anthraquinone}}{2}$	No. of Da in the unit cell = total number of linkers in unit cell - total number of Dq	Ratio of Dq:Da
DqTp	6	6	5.96 = ~6	6.12 = ~6	3	3	0	1:0
Dq₁Da₂Tp	6	2	6	2.31 = ~2	3	1	2	1:2
Dq₁Da₁Tp	12	6	11.96 = ~12	6.19 = ~6	6	3	3	1:1
Dq₂Da₁Tp	6	4	6.01 = ~6	4.23 = ~4	3	2	1	2:1

Table 3.1: The quantitative integration of ^{13}C CP MAS solid-state NMR for all COFs

3.2.4 Properties of COF thin sheets

Gas adsorption:

The synthesized single and hetero-linked COFs perform excellent thermal stability up to 430 °C, which has been done by thermo gravimetric analysis (TGA) (**Figure 3.8**). The well organization of nanopores in COFs have been confirmed by The N_2 adsorption isotherms at 77K (**Figure 3.9a**). It provides a type IV adsorption isotherm for each COFs which further signifies the micro-porous character of the material (Figure 2b). The single-linker **DqTp** and **DaTp** COFs show BET (Brunner Emmet Teller) surface area of 940 and 577 m^2g^{-1}

respectively. Similarly, the hetero-linked **Dq₁Da₂Tp**, **Dq₁Da₁Tp**, and **Dq₂Da₁Tp** COFs exhibit the surface area of 1400, 804 and 1004 m²g⁻¹ respectively. It is worth mentioning that even after the inclusion of two different linkers into the framework; it maintains the regular stacking of the building blocks and finally results a desired microporous feature. Moreover, the NLDFT (non-local density functional theorem) describes the pore size distribution of all COFs ranging from 2-2.3 nm (**Figure 3.9b**).

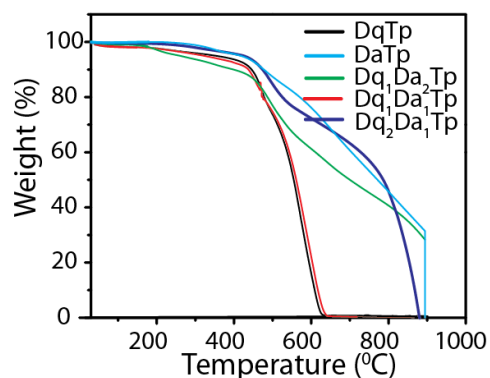


Figure 3.8: TGA of all COFs

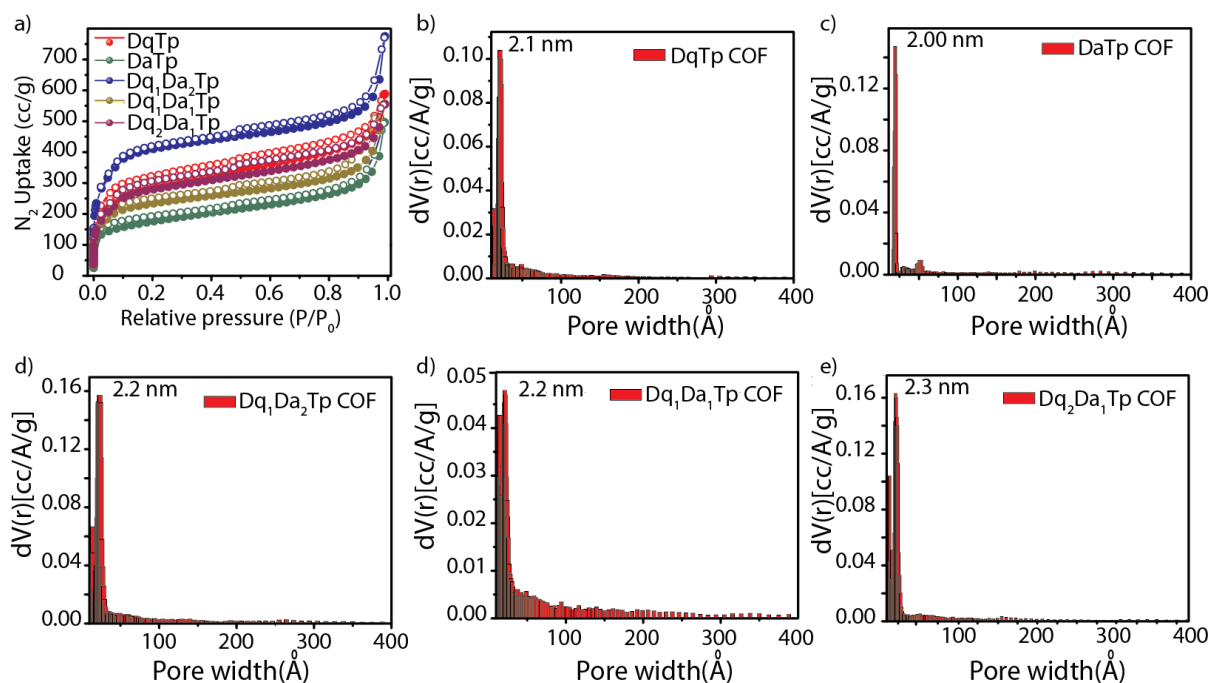


Figure 3.9: a) N₂ adsorption analysis of all COF thin sheets. b-e) NLDFT pore size distribution of COFs.

Mechanical strength:

The fabrication of free-standing COFs could be the same mechanism of interlocked tile arrangement in the graphene oxide (GO) thin-sheet formation. We have attempted to solve the issue of mutual exclusive nature of flexibility and good crystallinity in 2D macroscopic materials by controlling the electronic environment in COF crystallites. Herein, we believe the interlocked crystallite-crystallite assembly could be responsible for the mechanical

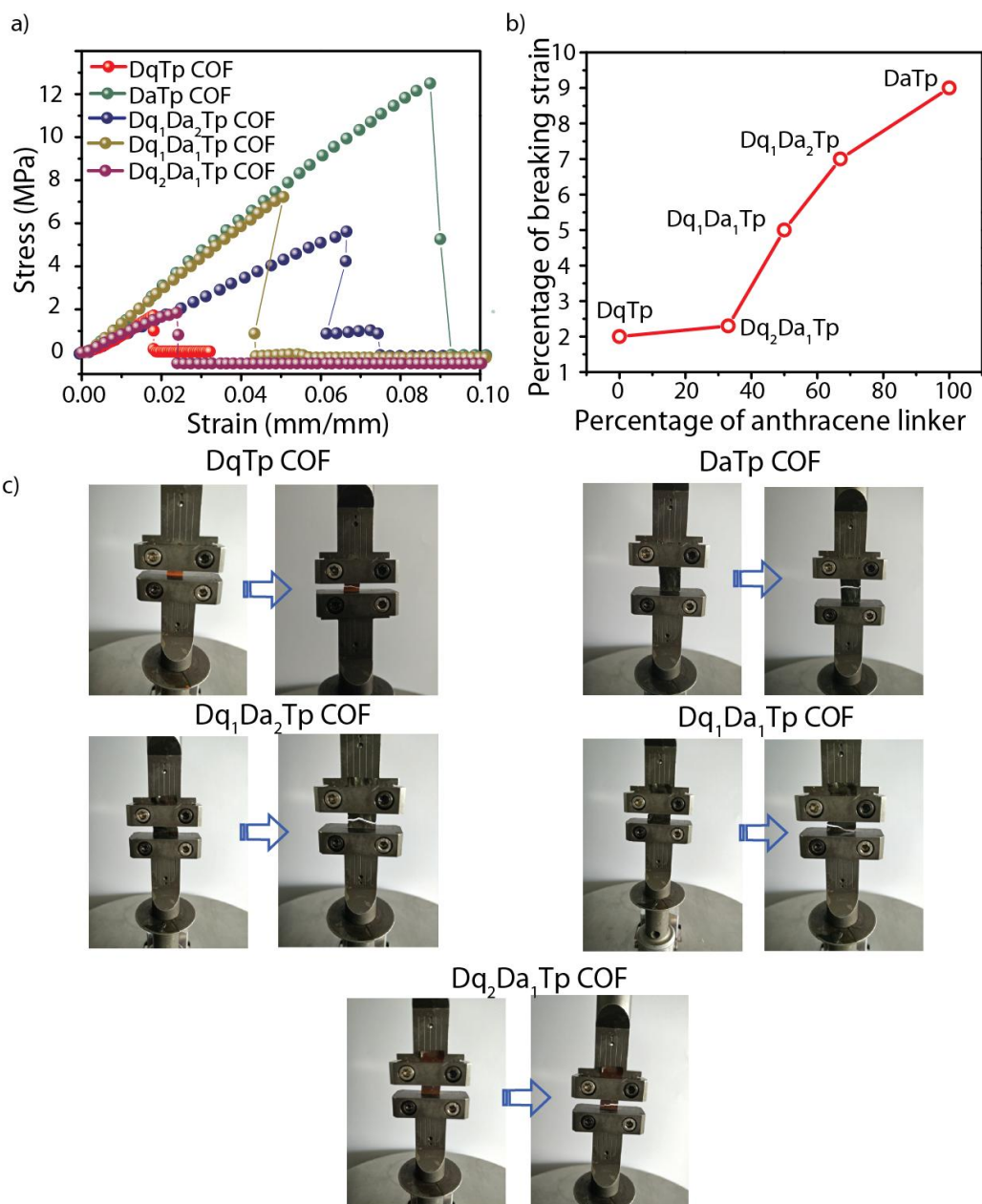


Figure 3.10: a) DMA of all COF thin sheets. b) The plot percentage of linker Vs percentage of breaking strain. c) Digital photographs of mechanical strength studies of all COFs.

robustness of the thin-sheets of COFs. Additionally, more non-covalent interaction sites in the interlocked crystallites create higher mechanical strength for the convergent COFs. On this ground, we surmise, anthracene linker can enhance the effectiveness of the crystallite packing through the efficient π - π interaction [3.8]. The mechanical robustness of COF thin sheets could be highly beneficial for novel flexible electrode energy storage devices in terms of easy

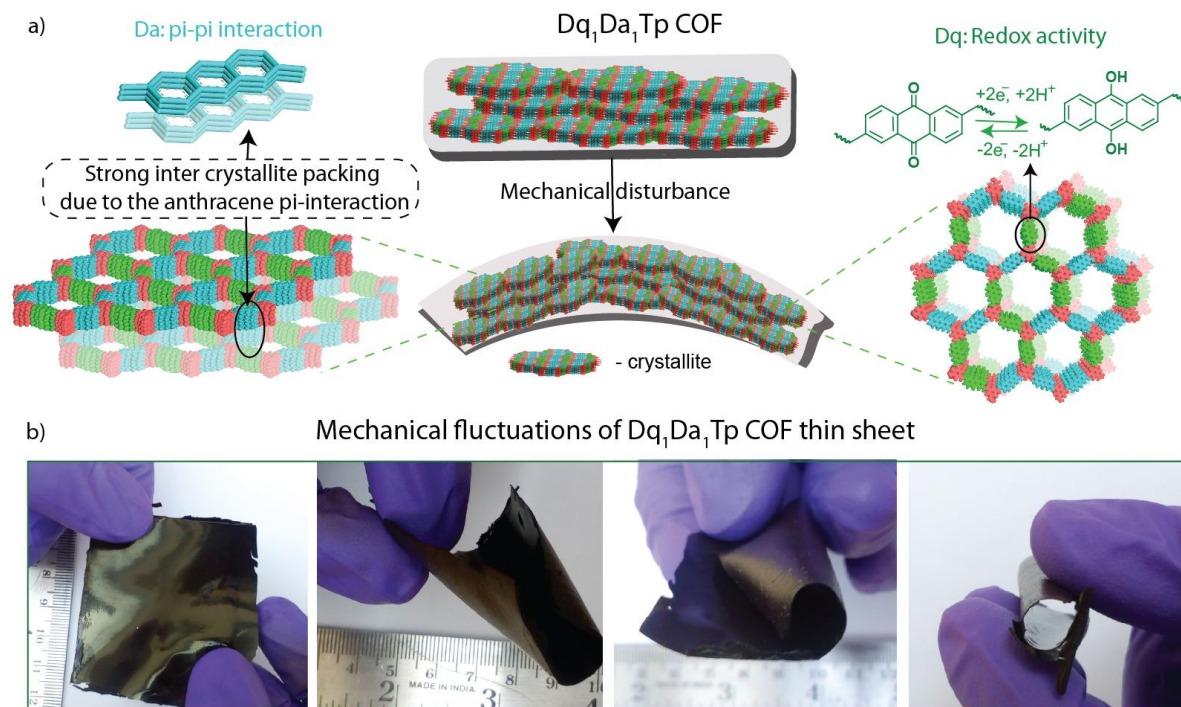


Figure 3.11: a) Convergent nature of **Dq₁Da₁Tp** COF. b) Digital photographs of mechanical fluctuation of **Dq₁Da₁Tp** COF thin sheet.

fabrication, smooth handling and the elevated durability. To figure out the mechanical properties of the COF thin sheets, we have characterized all COFs with the dynamic mechanic analyzer (DMA) instrument (**Figure 3.10**). In DMA, the free-standing COF thin sheets were subjected for applying a controlled physical stress at both ends of the sheets and subsequently measuring the strain developed inside it. The thin sheets are elastically brittle due to their crystalline porous nature. In this regard, the mechanical deformation can't be longer to a large extent like amorphous polymers. In the DMA, **DqTp** COF (**Da**=0%) shows only 2% of the breaking strain. At the same time, the higher breaking strain (9%) of **DaTp** (**Da**=100%) exhibits remarkable breaking strain (9%) compares to **DqTp** and it could be due to the robust π - π interaction of the inter-crystallites. The hetero-linked **Dq₁Da₁Tp**

(**Da**=50%), and **Dq₁Da₂Tp** (**Da**=67%) COF thin-sheets display enhanced breaking strain of 5 and 7% respectively when compared to **DqTp**. Moreover, the DMA of **Dq₂Da₁Tp** (**Da**=33%) exhibits the breaking strain of 2.3% only. These results indicate the incorporation of anthracene linkers into the COF matrix enhances the mechanical robustness of sheets and it is unable to break the **Da** rich COFs by simple stretching or bending (**Figure 3.11**). Meanwhile, the **DqTp** COF thin sheet can be broken by a small mechanical force or disturbances. It could be due to the insufficient non-covalent interactions in the COF matrix.

3.2.5 Morphology COF thin sheets

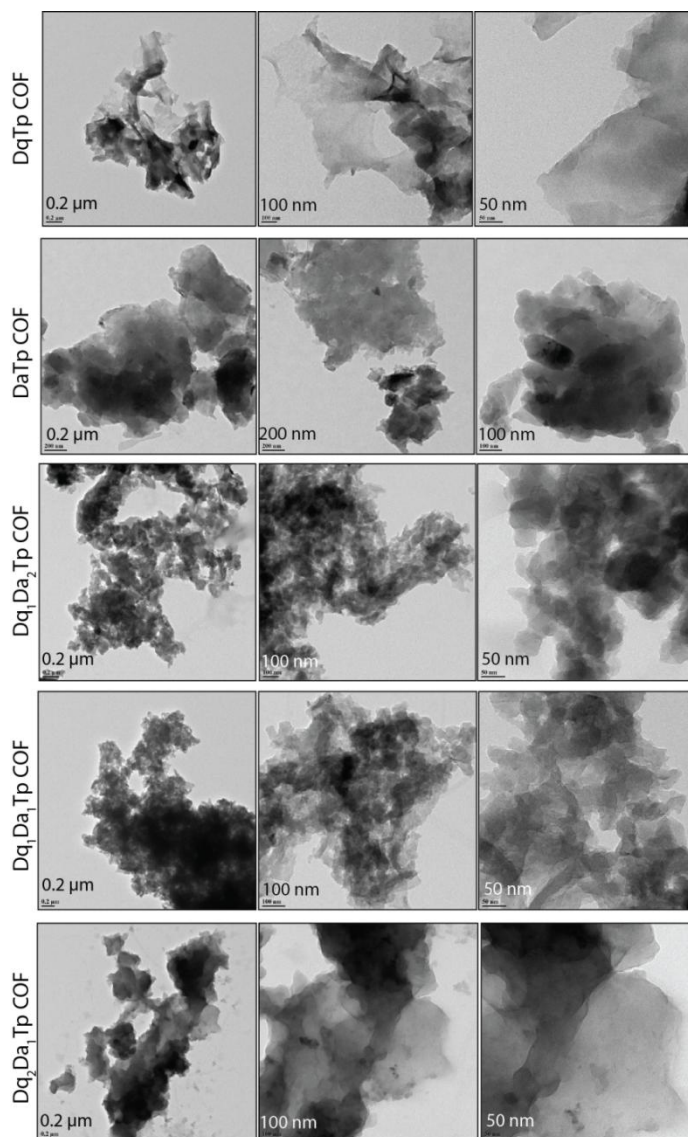


Figure 3.12: TEM images of COF thin sheets.

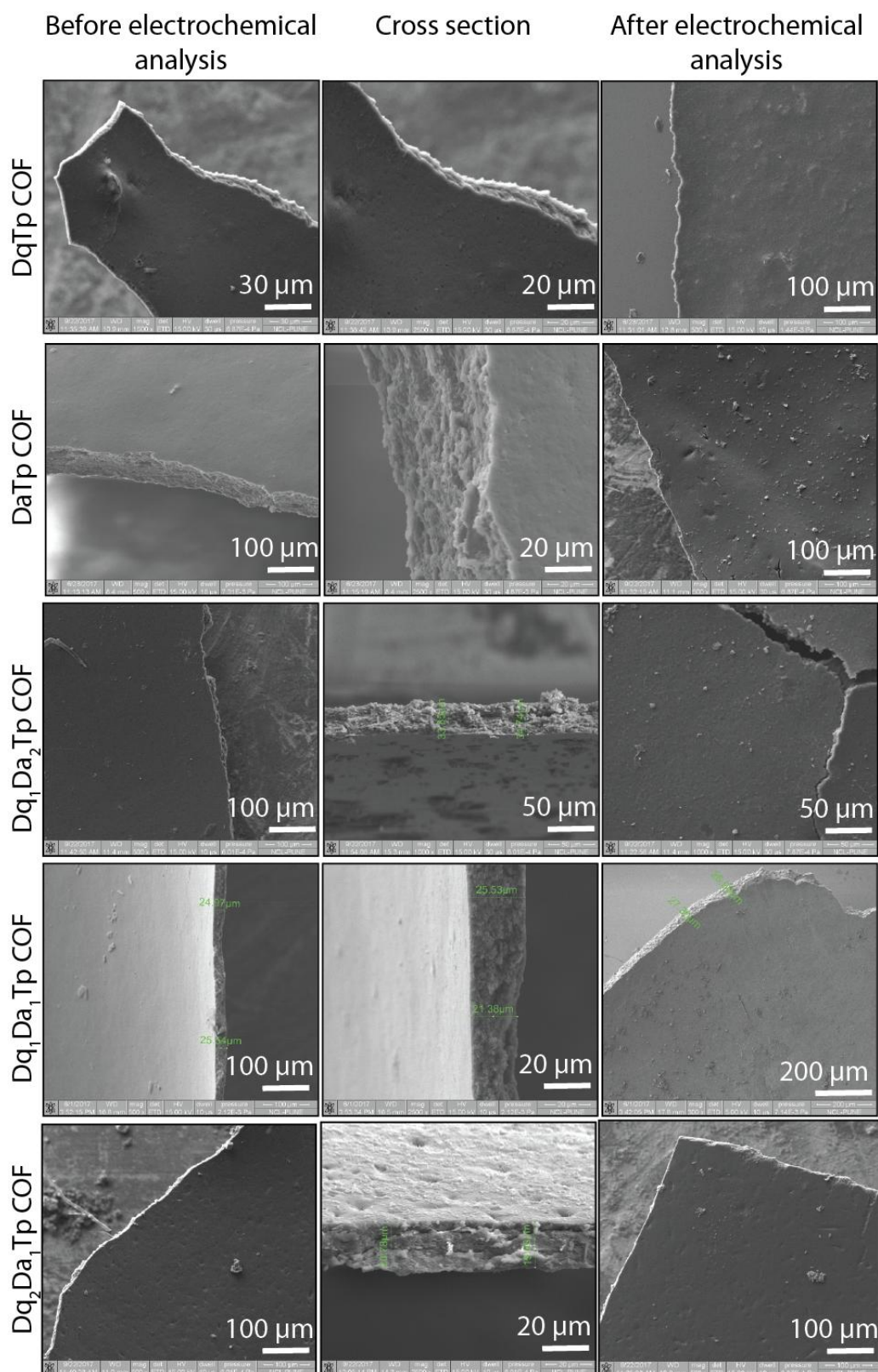


Figure 3.13: SEM images of COF thin sheets.

The morphology of COF thin sheets was investigated by scanning electron microscopy (SEM) and transmission electron microscopy (TEM). The SEM images provide the uniform, crack-free and continuous nature of the COF thin-sheets (**Figure 3.12**). It is noteworthy to mention the dense packing of the crystallites which has been inspected through the SEM cross-sectional imaging may be a possible factor of the free-standing character of the thin sheets. Also, the thickness of the sheets ranging within 25-100 μm along with an areal scalability of $\geq 15 \text{ cm}^2$ has been observed (Figure 3b, c & d). The TEM samples of COF thin sheets were prepared by acetonitrile dispersion of crushed and fine ground thin sheets. The TEM images display the nano-level morphology of the COFs (**Figure 3.13**). **DqTp**, **DaTp** and **Dq₂Da₁Tp** COFs have been noted with the agglomerated sheet-like morphology, meanwhile, a ribbon-like morphology has been displayed for both **Dq₁Da₂Tp** and **Dq₁Da₁Tp** COFs.

3.2.3 Electrochemical analysis of COF thin sheets

The fabrication of working for three-electrode experiment:

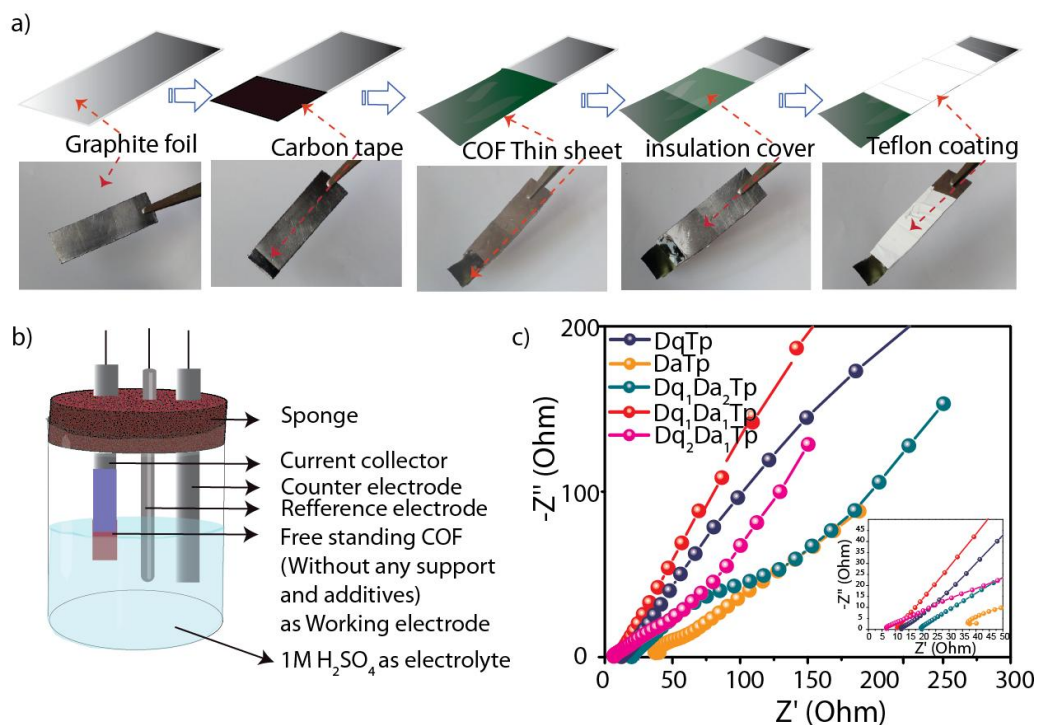


Figure 3.14: a) The graphical representation and photographs of working electrode fabrication. b) The graphical representation of three-electrode assembly. c) The impedance analysis of all COF thin sheets.

The working electrode for three-electrode configuration has been fabricated from COF thin sheets with the area of 0.16 cm^2 and the thickness $\sim 25 \text{ }\mu\text{m}$ (**Figure 3.14**). An electronic screw gauge is used for measuring the thickness for the COF electrode in every case. Then we have calculated the weight of each COF thin sheet electrodes in a micro-weighing balance instrument. Consequently, the COF electrodes were dipped in 1M H_2SO_4 acid solution for the activation pores prior to the electrochemical analysis. The soaking of electrode in electrolyte is an important requirement for the effective contact electrode-electrolyte surface in the energy storage systems like supercapacitors. Afterwards, the partially dried COF electrodes were assembled in three electrode system as a working electrode. We have pasted the COF electrode on a grafoil current collector which is aided by an adhesive carbon tape. Importantly, most of COF electrode portion were hanged on the electrolyte solution. Furthermore, $\text{Hg}/\text{Hg}_2\text{SO}_4$ and Pt mesh were taken as reference and counter electrodes, respectively. Cyclic voltammetry (CV) analysis were investigated in a range of scan rate from 10 to 500 mV s^{-1} by optimizing a potential window of 1 V (-0.3 to 0.7V). Additionally, the galvanostatic charge–discharge (GCD) experiments were analyzed at different current densities of 1.56, 3.12 and 6.25 mAcm^{-2} .

Specific capacitance from GCD experiment:

$$C = \frac{(I \times \Delta t)}{\Delta V * M} \dots \dots \dots \text{Equation (1)}$$

Where,

C= Specific capacitance (mFg^{-1})

I = Constant current used for charging and discharging (mA)

Δt = Discharge time (sec)

ΔV = Potential window (V)

M = Weight of COF thin-sheet (g)

The electrochemical analysis of three-electrode assembly:

The cumulative resistance of three-electrode assembly with COF as working electrode has been obtained from the Impedance analysis(**Figure 3.14c**). It provides a low ESR value of

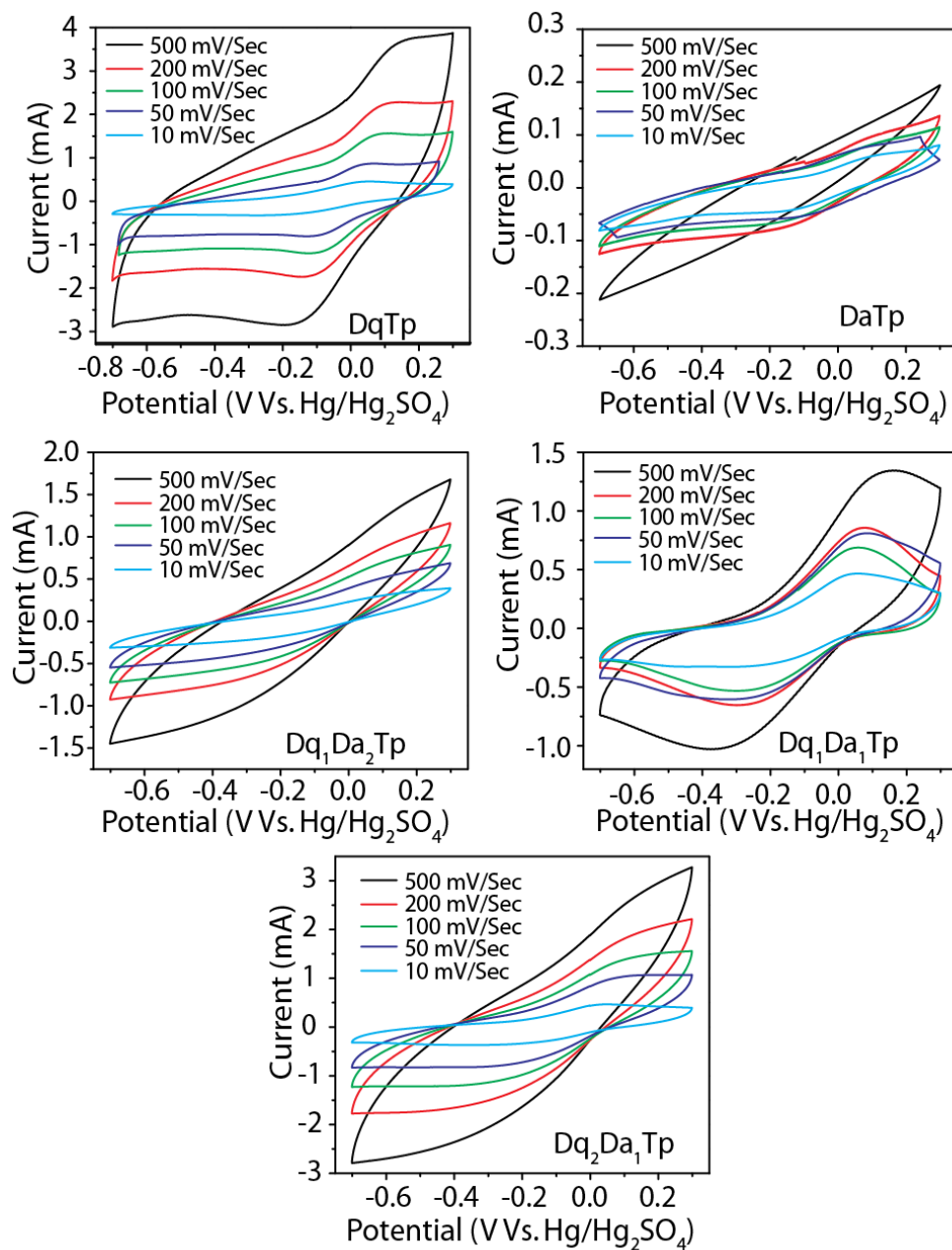


Figure 3.15: The cyclic voltammetry of COF thin sheets in three-electrode assembly.

the systems and suggest a feasible electrochemical energy storage, especially for the **Dq** rich COFs. Furthermore, we have measured the CV of each of COF electrodes to understand the response in the current by applying a potential window (-0.3 V to 0.7 V) (**Figure 3.15**). The CV profiles of the hetero-linked **Dq₁Da₁Tp** and **Dq₂Da₁Tp** COFs display a pair of reversible redox peaks and which could be attributed from the electrochemical redox reaction of **Dq** linker. It is noteworthy that the reversible redox peaks in the CV profile of **DqTp** COF

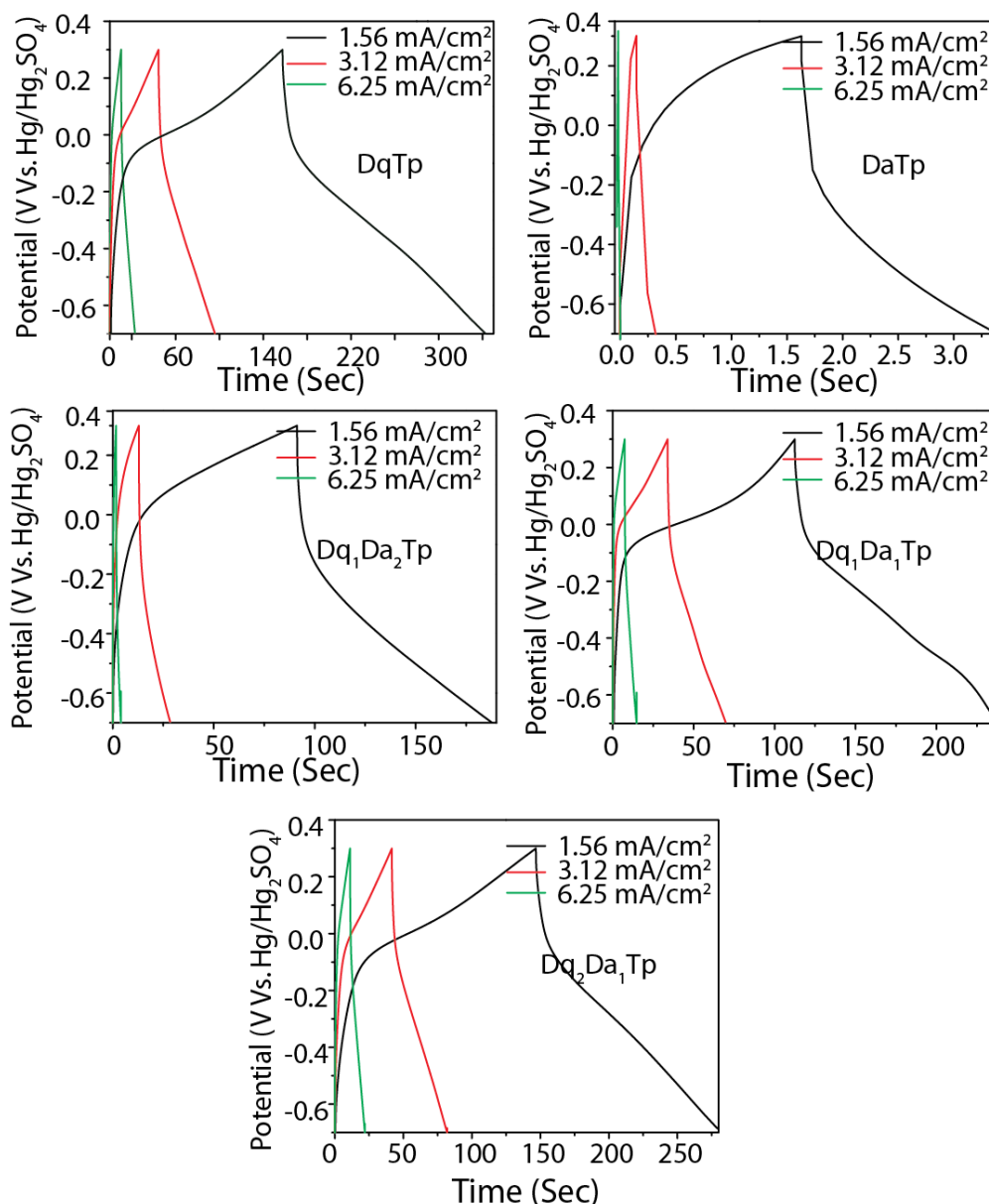


Figure 3.16: The galvanostatic charge-discharge curves of all COF electrodes.

electrode further supports the above observation on anthraquinone redox reactions. Meanwhile, the **Dq₁Da₂Tp** COF exhibits a modest redox activity in the CV experiment and it could be due to the insufficient number of anthraquinone in the respective framework. Moreover, the scanning rate ranging from 10 to 500 mVSec⁻¹ for all COF electrodes showcase the increasing of current in the I-V profile. The galvanostatic charge-discharge experiment (GCDC) provide the specific capacitance values of each COF thin sheets which were measured at the potential window of -0.7 to 0.3V in different current densities (1.56 to

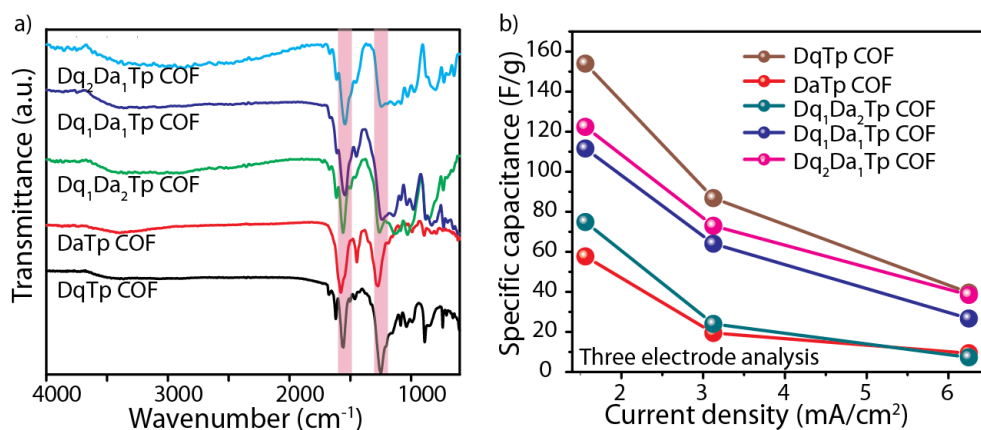


Figure 3.17: a) The FT-IR spectra of COF thin sheet electrodes after the electrochemical analysis. b) The plot of Current density Vs Specific capacitance of all COFs.

6.25 mAcm⁻²) (**Figure 3.16**). The hetero-linked **Dq₂Da₁Tp** (**Dq** = 67%) delivered the specific capacitance of 122 Fg⁻¹ at the current density of 1.56 mAcm⁻² which is comparable to the capacitance of **DqTp** (154 Fg⁻¹) at the same current density. Meanwhile, mechanically robust **Dq₁Da₁Tp** displays the specific capacitance value of 111 Fg⁻¹ at the same conditions. However, the poor capacitive performance of **DaTp** COF could be due to the insufficient redox active linkers in the framework. The IR spectra of COFs after the electrochemical experiments validates the stable nature of C=O and C–N bonds (from β -ketoenamine) in the framework (**Figure 3.17**). Obviously, the SEM images of all COF thin sheets were verified as continuous, uniform and crack-free nature even after the electrochemical analysis (**Figure 3.13**).

Device fabrication for two electrode experiment:

To fabricate a flexible quasi solid-state supercapacitor, we have used grafoil peeled adhesive carbon tape as a current collector (**Figure 3.18**). In this current collector, a layer of graphite is coated during the peeling process of carbon tape on a surface the graphite sheet. It could act as an enhanced electrically conductive flexible current collector in the supercapacitor device. Again, two COF electrodes were dipped in 1M H₂SO₄ acid solution for 1 hour for the activation pores prior to the electrochemical analysis. Then the partially dried COF electrodes (geometrical area-0.64 cm²) were pressed on the carbon tape current collector, and subsequently we have applied a thin coating of PVA- H₂SO₄ gel electrolyte on the surface of the COF thin sheets. We have fabricated two such electrodes which were act

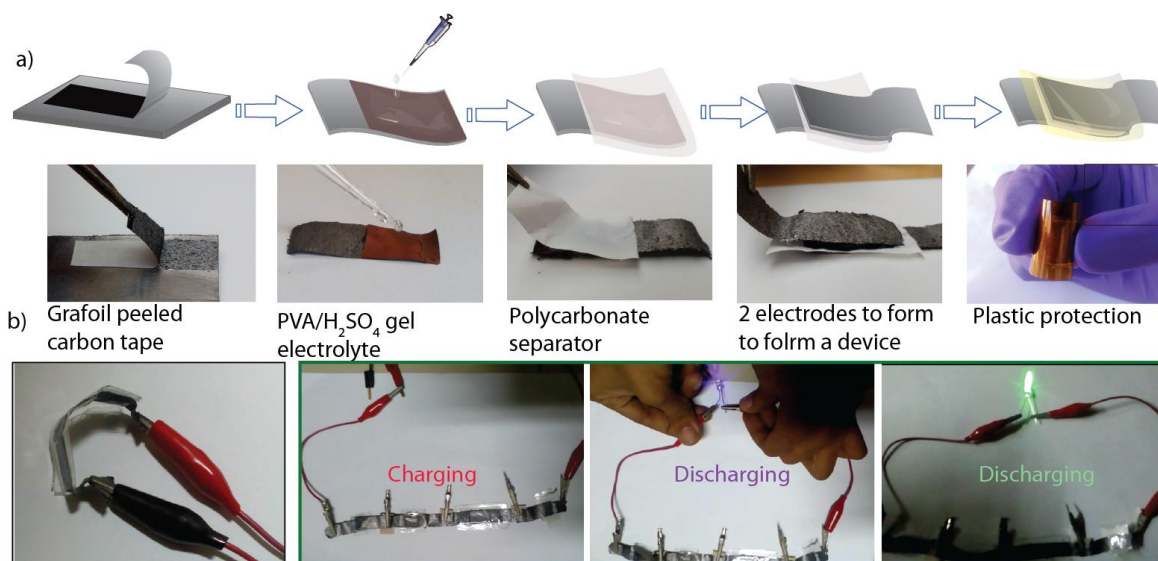


Figure 3.18: a) The diagrammatic and photographic representation of device fabrication. b) The flexible COF supercapacitor has been used for power LEDs.

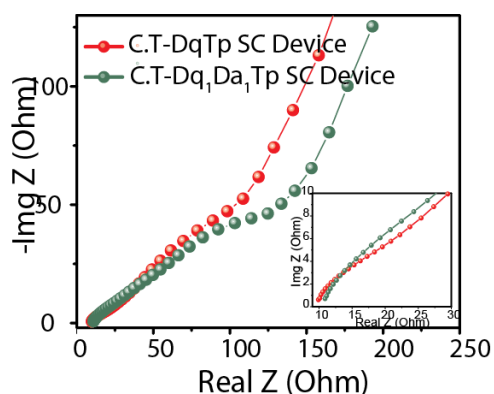


Figure 3.19: The impedance analysis of COF based supercapacitor devices

as positive and negative electrodes in symmetric supercapacitor device. Again, a polycarbonate porous separator was kept in between these two electrodes and the whole device coated with an insulation cover. Then the assembled flexible devices were subjected to the further electrochemical analysis. Herein, CV analysis were investigated in a range of scan rate from 10 to 500 mV s⁻¹. Moreover, the GCD experiments were analyzed at different current densities of 0.39, 0.78 and 1 mAcm⁻².

Specific capacitance, energy and power density calculation from GCD experiment:

The single electrode areal capacitance of the supercapacitor device,

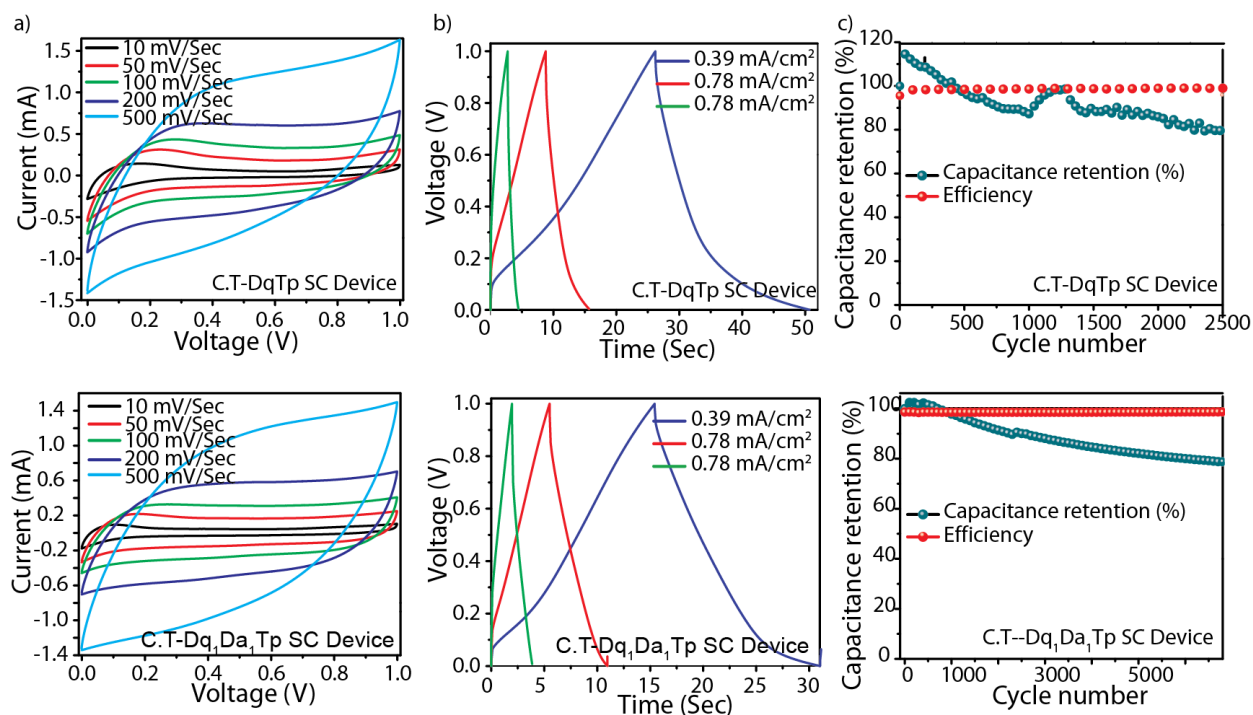


Figure 3.20: a) The CV; b) GCD; c) The long –term cyclic stability test of **C.T-DqTp** and **C.T-Dq₁Da₁Tp** supercapacitor devices.

$$C_a = \frac{2 \times (I \times \Delta t)}{\Delta V \times a} \dots \dots \dots \text{Equation (2)}$$

Where,

Ca = The areal capacitance (mFcm⁻²)

I = Constant current used for charging and discharging (mA)

Δt = Discharge time (Sec)

ΔV = Potential window (V)

a = Geometrical area of COF thin sheet in one electrode (cm²)

The energy density and power density of the electrode were calculated by the equations

Energy density (E_d) (mWhcm⁻²) =

$$\frac{C_a}{8 \times 3.6} V^2 \dots \dots \dots \text{Equation (3)}$$

Where,

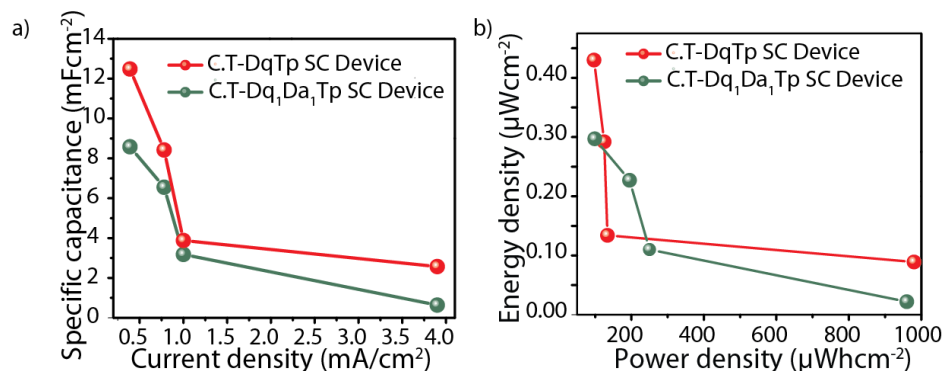


Figure 3.21: a) The plot of Current density Vs Specific capacitance and b) the Ragone plot of COF based supercapacitors.

‘Ca’ is the areal capacitance calculated by the charge-discharge (mFcm⁻²) method and ‘V’ is the voltage window.

Power density (P_d) (mWcm⁻²) =

$$\frac{Ed}{t} \dots \dots \dots \text{Equation (4)}$$

Where, ‘E_d’ is the energy density from **Equation (3)** and ‘t’ is the discharge time in hour calculated from the discharge curve.

The electrochemical performance COF supercapacitors:

The convergent **Dq₁Da₁Tp** COF thin sheet has been strategically selected as the electrode in the supercapacitor device (C.T-**Dq₁Da₁Tp**) based on the good mechanical strength as well as the redox-activity compared to the other two hetero-linked COFs. Additionally, we have also assembled a supercapacitor device with **DqTp** as electrode for checking relative performance (C.T-**DqTp** COF) in the energy storage. However, the electrode is mechanically poor compared to the convergent COF electrode. Then we have investigated the CV analysis of these devices in the potential window of 1 V and it suggest that charge storage property of

Active Material	Specific capacitance	Physical appearance	Use of binders or conducting additives	Specific surface area (m^2g^{-1})	Light-weight nature	Mechanical strength	Reference
1. Dq, Da, Tp COF	111 Fg^{-1} at 1.56 mAcm^{-2} (For three electrode) 8.5 mFcm^{-2} at 0.39 mAcm^{-2} (For two electrode)	Free-standing thin sheet	No	804	Yes	5% of breaking strain	This Work
2. DqTp COF	154 Fg^{-1} at 1.56 mAcm^{-2} (For three electrode) 12 mFcm^{-2} at 0.39 mAcm^{-2} (For two electrode)	✓	✓	940	✓	2% of breaking strain	
Triazatruxene conjugated microporous polymer (TAT-CMP-1)	141 Fg^{-1} at 1 Ag^{-1}	Powder ✗	Yes ✗	88 ✓	Yes ✓	Not reported ✗	Chem.Sci, 2017, 8, 2959
Activated carbon	140 Fg^{-1}	Powder ✗	Yes ✗	2000 ✓	Yes ✓	Not reported ✗	Science, 2006, 313, 1760
Chemically reduced graphene	150 Fg^{-1} at 0.8 Ag^{-1}	Powder ✗	Yes ✗	3100 ✓	Yes ✓	Not reported ✗	Science, 2011, 332, 1537
PANI/CNT	332 Fg^{-1} at 1 Ag^{-1} two electrode	Thin film ✓	Yes ✗	Not reported ✗	Yes ✓	Not reported ✗	Nano.Lett, 2010, 10, 4025
Graphite	1 mFcm^{-2} at 1 Vsec^{-1} for two electrode	Powder ✗	No ✓	Not reported ✗	No ✗	Not reported ✗	J. Power sources, 2011, 196, 8855
DAAQ-TFP COF	48 ± 10 Fg^{-1} at 10 mVSec^{-1}	Powder ✗	Yes ✗	1200 ✓	Yes ✓	Not reported ✗	J. Am. Chem. Soc. 2013, 135, 16821
DAAQ-TFP COF thin film	3.0 mFcm^{-2} at 0.4 mAcm^{-2} mAcm^{-2}	Thin film on gold support ✗	No ✓	Not reported ✗	Yes ✓	Not reported ✗	ACS Nano, 2015, 9, 3178
Nitrogen doped graphene nanosheet	219 Fg^{-1} at 1 Ag^{-1}	Powder ✗	Yes ✗	1040 ✓	Yes ✓	Not reported ✗	ACS Appl. Mater. Interfaces, 2014, 6, 1563
MOF/PANI	35 mFcm^{-2} at 0.05 mAcm^{-2} for two electrode	Thin film coated on carbon cloth ✗	Yes ✗	73 ✓	No ✗	Not reported ✗	J. Am. Chem. Soc., 2015, 137, 4920
RGO-SSC	118 Fg^{-1} at 1 Ag^{-1} two electrode	Thin film ✓	Yes ✗	Not reported ✗	Yes ✓	30.1 GPa of Young's Modulus with 5% Nafion loading	ACS Nano, 2011, 5, 7205
MnO_2 coated ZnO nanowire	2.0 mFcm^{-2} at 100 mVSec^{-1}	Nanowires on plastic support ✗	Yes ✗	Not reported ✗	No ✗	Not reported ✗	Angew. Chem. Int. Ed., 2011, 50, 1683
CNT Yarn	3.53 mFcm^{-2} at 1.67 Ag^{-1}	Fiber ✓	No ✓	Not reported ✗	Yes ✓	Not reported ✗	Adv. Mater., 2013, 25, 1155
CNT/PANI composite yarn	38 mFcm^{-2}	Yarn with PVA support ✗	No ✓	Not reported ✗	Yes ✓	CNT Yarn 500-800 MPa	Adv. Mater., 2013, 25, 1494
Laser scribed Graphene	3.67 mFcm^{-2} at 1 Ag^{-1} for two electrode	Thin film on a flexible substrate ✗	No ✓	1520 ✓	Yes ✓	Not reported ✗	Science, 2012, 335, 1326
[TEMPO]100% -NiP-COF	113 Fg^{-1} at 2 Ag^{-1}	Powder ✗	Yes ✗	975 ✓	Yes ✓	Not reported ✗	Angew. Chem. Int. Ed., 2015, 54, 6814

Table 3.2: The state-of-the-art-of the COF based supercapacitors.

the COF electrodes (**Figure 3.20a**). Furthermore, the areal capacitances of the devices have been calculated from the GCD experiment for the single electrode of C.T- **Dq₁Da₁Tp** and C.T-**DqTp** supercapacitor devices (8.5 mFcm⁻² and 12 mFcm⁻² respectively at 0.39 mAcm⁻²) (**Figure 3.20b**). Additionally, the Ragone plot provides the energy and power densities as high as of 0.43 μWhcm⁻² and 980 μWcm⁻² respectively for the C.T-**DqTp** supercapacitor device. Meanwhile, C.T-**Dq₁Da₁Tp** COF displays the energy density of 0.30 μWhcm⁻² and power density of 960 μWcm⁻² (Figure X). Furthermore, the C.T-**Dq₁Da₁Tp** supercapacitor device has been subjected to the long-term cyclic stability test for more than 7000 continuous charge-discharge cycles (**Figure 3.20c**). After 2500 cycles, it shows the retention of 90% capacitance and then maintain 78% of the capacitance retention at the last cycle (7000th). Meanwhile, we could observe 80% of the capacitance retention after 2500 continuous charge-discharge cycle of C.T-**DqTp** supercapacitor device (**Figure 3.20a**). Finally, we have present the practical usage of the constructed supercapacitor devices for light-up one LED. Herein, we have assembled four C.T-**Dq₁Da₁Tp** supercapacitor devices in series connection to give the power for a LED by charging for 20 sec and then lighted for ~15 seconds which indicates the real-life utility of COF based energy storage devices. We have detailed the state-of-the-art of the COF based supercapacitors in **Table 3.2**.

3.3 Conclusion

In summary, we have demonstrated a convergent strategy for the fabrication of a mechanically robust and redox active COF in a macroscopic 2D thin sheet form. In this synthetic method pi electron rich anthracene linker boosts the mechanical strength of the thin sheet through the enhancement of non-covalent interaction between the crystallites of COF matrix. Meanwhile, the anthraquinone linkers in the framework promote the electrochemical redox activity of the material. Importantly, the convergent synthesis upholds the crystallinity and porosity of the COFs along with the uniform and crack-free nature of the thin sheets. Finally, a mechanically robust flexible quasi-solid-state supercapacitor devices have been assembled and then further utilized for light-up a 3.5 V LED. We believe this unique convergent method has the potential relevance for the rational designing of the redox-active material used in flexible supercapacitor devices.

3.4 Experimental procedures

3.4.1 Materials

1, 3, 5-triformylphloroglucinol (**Tp**) and 2, 6-diaminoanthracene were synthesized from phloroglucinol and 2, 6-diaminianthraquinone respectively by the reference of reported articles [3.14 and 3.15]. Where 2, 6-diaminianthraquinone was purchased from TCI Chemicals.

3.4.2 Synthesis of **DqTp** COF thin sheet:

We have synthesized **DqTp** COF through the solid-state mixing (SSM) of amine and aldehyde linkers in the presence of *p*-Toluenesulphonic acid (PTSA) as a catalyst for imine condensation reaction. Herein, we have taken the amine linker **Dq** (0.3 mmol) and five equivalent of the catalyst PTSA (1.5 mmol) together and then it has been mixed with 50 μ l of water. Consequently, we have added 1, 3, 5-triformylphloroglucinol (**Tp**, 0.2 mmol) to the precursor mixture and again thoroughly mixed for the next 10 minutes. We have observed a brown colored paste has been formed and which is further coated on a glass slide as thin sheet form ($2.5 \times 8 \text{ cm}^2$) and then thermally treated (120°C) in a closed condition for 24 hours (The thickness has been controlled by varying the area of the glass plate. It is possible to fabricate 25-40 μm thick sheets by the applying the same amount COF mentioned above on the three number $2.5 \times 8 \text{ cm}^2$ glass slide). The thermal treatment of COF precursor paste allows the β -ketoenamine framework formation and the thin sheet stacked on the glass surface was peeled by dipping the glass slides in distilled water. Afterwards, the free-standing COF thin sheet was thoroughly washed with water, DMA and acetone to remove the precursor impurities and PTSA from the material. (Isolated yield: 90%).

3.4.3 Synthesis of **DaTp** COF thin sheet:

We have synthesized **DaTp** COF through the solid-state mixing (SSM) of amine and aldehyde linkers in the presence of *p*-Toluenesulphonic acid (PTSA) as a catalyst for imine condensation reaction. Herein, we have taken the amine linker **Da** (0.3 mmol) and five equivalent of the catalyst PTSA (1.5 mmol) together and then it has been mixed with 50 μ l of water. Consequently, we have added 1, 3, 5-triformylphloroglucinol (**Tp**, 0.2 mmol) to the precursor mixture and again thoroughly mixed for the next 10 minutes. We have observed a dark brown colored paste has been formed and which is further coated on a glass slide as thin

sheet form ($2.5 \times 8 \text{ cm}^2$) and then thermally treated (120°C) in a closed condition for 8 hours (The thickness has been controlled by varying the area of the glass plate. It is possible to fabricate 25-40 μm thick sheets by the applying the same amount COF mentioned above on the three number $2.5 \times 8 \text{ cm}^2$ glass slide). The thermal treatment of COF precursor paste allows the β -ketoenamine framework formation and the thin sheet stacked on the glass surface was peeled by dipping the glass slides in distilled water. Afterwards, the free-standing COF thin sheet was thoroughly washed with water, DMA and acetone to remove the precursor impurities and PTSA from the material. (Isolated yield: 90%)

3.4.4 Synthesis of convergent COF thin sheets:

We have synthesized convergent COFs through the solid-state mixing (SSM) of amines and aldehyde linkers in the presence of *p*-Toluenesulphonic acid (PTSA) as a catalyst for imine condensation reaction. Herein, we have taken the amine linkers **Dq** & **Da** (0.3 mmol) in various molar ratios (1:2; 1:1 and 2:1) and five equivalent of the catalyst PTSA (1.5 mmol) together and then it has been mixed with 50 μl of water. Consequently, we have added 1, 3, 5-triformylphloroglucinol (**Tp**, 0.2 mmol) to the precursor mixture and again thoroughly mixed for the next 10 minutes. We have observed a brown colored paste has been formed and which is further coated on a glass slide as thin sheet form ($2.5 \times 8 \text{ cm}^2$) and then thermally treated (120°C) in a closed condition for 24 hours (The thickness has been controlled by varying the area of the glass plate. It is possible to fabricate 25-40 μm thick sheets by the applying the same amount COF mentioned above on the three number $2.5 \times 8 \text{ cm}^2$ glass slide). The thermal treatment of COF precursor paste allows the β -ketoenamine framework formation and the thin sheet stacked on the glass surface was peeled by dipping the glass slides in distilled water. Afterwards, the free-standing COF thin sheet was thoroughly washed with water, DMA and acetone to remove the precursor impurities and PTSA from the material. (Isolated yield: 85-90%)

3.4.5 General methods for characterization

(a) Powder X-Ray Diffraction (PXRD): The PXRD data were investigated on a Phillips PANalytical diffractometer using a $\text{Cu K}\alpha$ radiation ($\lambda = 1.5406 \text{ \AA}$), with a scan rate of 2° min^{-1} . The tube current and voltage were optimized at 30 mA and 40 kV respectively. The

COF powder was taken in an Aluminium holder and then scanned between 2 and 40° 2 θ (step size of 0.02°).

(b) Thermogravimetric Analysis (TGA): TGA was investigated on SDT Q 600 TG-DTA analyzer instrument. 2 mg of the COF sample was placed in an aluminium crucible and heated from 25 to 900 °C under N₂ atmosphere at heating rate of 20 °C min⁻¹.

(c) IR Spectroscopy: The Fourier transform infrared spectra (FTIR) of the COFs were recorded on a *PERKIN ELMER FT-IR SPECTRUM* (Nicolet) spectrometer in ATR mode.

The FTIR profiles were investigated within the range of 4000-600 cm⁻¹.

(d) Gas Adsorption: The N₂ gas adsorption experiments of COF samples were analyzed in an *Autosorb* automatic volumetric instrument (*Quantachrome*) (up to 1 bar). COFs were degassed under vacuum at 120°C for 12 hours prior to the gas adsorption analysis.

(e) SEM: SEM images were recorded with a Zeiss DSM 950 scanning electron microscope and FEI, QUANTA 200 3D Scanning Electron Microscope with tungsten filament as electron source operated at 10 kV. The COF thin sheets were directly mounted vertically and horizontally to SEM sample holder with the carbon adhesive tape. The COF samples were sputtered with Au (nano-sized film) prior to imaging by a SCD 040 Balzers Union.

(f) TEM: TEM images were investigated by using FEI Tecnai G2 F20 X-TWIN TEM at an accelerating voltage of 200 kV. To prepare the TEM sample for the analysis, The crushed and ground COF thin sheet samples were dispersed in acetonitrile solvent and drop cast on copper grids TEM Window (TED PELLA, INC. 200 mesh).

(g) ¹³C CP MAS Solid-state NMR: We have used a Bruker 300 MHz NMR spectrometer, and for quantitative analysis ¹³C CP MAS decoupled solid state NMR was taken in Jeol 400 with scanning rate 849 and Ligand NMR data were taken in Bruker 200 MHz NMR spectrometer.

(h) Electrochemical analysis: We have carried out every electrochemical measurements like CV and impedance (Electrochemical Impedance Spectroscopic [EIS]) analysis recorded from 10⁶ to 0.01 Hz frequency against the open circuit potential (OCP) with a sinus amplitude of 10 mV [V_{rms} = 7.07mV] and galvanostatic charge/discharge analysis (GCD) were

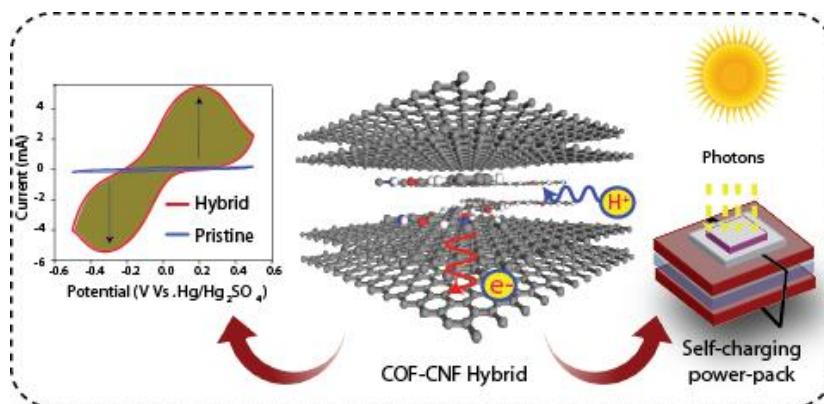
conducted by using a Bio-LogicSP-300 PG Stat instrument. Electrochemical data were analyzed in EC-Lab software **V10.19**

(i) Dynamic Mechanical Analysis: The mechanical strength of the COF thin sheets was performed by the measurement of the Tensile strength on a TA Instruments dynamic mechanical analyzer (DMA, RSA- III). Herein, we have conducted the stretching investigations by using the rectangular tension geometry for the COF thin-sheets. We have prepared the COF thin sheets in rectangular shapes and then vertically clamped in the DMA instrument. Afterwards, the stretching experiment has been performed with constant rate of 0.1 mm/s. All the DMA were conducted at room temperature (298K). We have calculated the stress-strain plot from the obtained results. Stress – strain Calculation: i.e., the engineering stress (σ_E) has been found by the stretching force (F) divided by initial cross-sectional area (A) ($\sigma_E = \frac{F}{A}$). Again, the engineering strain has been calculated by using this equation: $\varepsilon_E = \frac{l - l_0}{l_0}$, where, l is the final length and l_0 is the initial length.

NOTE: The experimental observations and results in this chapter have been already published in *ACS Appl. Mater. Interfaces*, 2018, 10, 33, 28139-28146; entitled: “*Convergent Covalent Organic Framework Thin Sheets as Flexible Supercapacitor Electrodes*”. The major contribution of this publication was done by the Dr. Rahul Banerjee and his student Abdul Khayum M from *CSIR National Chemical Laboratory, Pune*. The electrochemical analysis was investigated by the collaboration with Dr. Sreekumar Kurungot and his student Vidyanand Vijayakumar from *CSIR National Chemical Laboratory, Pune*.

Weak Intermolecular Interactions in Covalent Organic Framework-Carbon Nanofiber Hybrids for the Efficient Energy Storage

Abstract: The macroscopic two-dimensional (2D) form of covalent organic frameworks (COFs) face the challenge of modest performance in energy storage devices. It could



be due to the indigent electrical conductivity of COFs in micro as well as macro levels. Taking in this to account, in this chapter, we have presented a novel COF-CNF hybrid materials in 2D macroscopic thin sheet form as an excellent energy storage platform. In these COF-CNF hybrids, the efficient interlayer interaction between COF and CNF provide a pure blended matrix with high electrical conductivity compared to the pristine COFs. Additionally, they possess inherent crystalline and porous nature. Notably, the excellent energy storage performance of COF-CNF hybrids in supercapacitor electrodes indicates the prospect of the macro-architecture of COFs in a futuristic direction. Moreover, we have fabricated a self-charging power-pack for light energy harvesting and consequent storage as electrical energy with a decent performance.

4.1 Introduction

Covalent organic frameworks are the extended two-or three-dimensional (2D/3D) ordered network constructed from organic building blocks [4.1]. The structural regulation of the framework with redox-active backbone and the high surface area can be spectacted as outstanding electrochemical charge storage, especially in supercapacitor devices [4.2]. But, the commercialization of COF as real-life electrochemical energy storage devices are greatly dispirited due to the enormous difficulties to couple the most desired macroscopic free-standing thin sheet nature of the material with the high capacitive performance. The major drawback behind the substandard performance of the COFs are the modest inter & intra phase electron transfer in the framework matrix which owing to their insignificant conductivity, and the insufficient utilization of redox-active moieties and the active surface area for energy storage [4.2d & e]. The numerous grain boundaries and defects in nanocrystalline COFs obstruct the lucid movement of electrons through the polymeric network. So far a few attempts have been made to enhance the electrical conductivity of COFs. However, all of them ultimately results in the drastic mitigation in surface area with the production of unappealed granular form of the material [4.3]. Again, the resulted material was devoid of any profitable electrochemical performance. Furthermore, the granular nature of the material obtained *via* this process will be a road-block for the fabrication of the flexible supercapacitors [4.4]. Notably, Dichtel *et al.* developed an *in situ* PEDOT polymerisation in COF thin films for enhancing the electrical conductivity of the COF based electrode and hence a high capacitance [4.5]. However, this method face needs a highly expensive gold support for the fabrication of COF thin films. Once again, the aforementioned method is not scalable for the commercial purpose. Therefore, the further advances in this field could be the development of COF based free-standing thin-sheet with the electrically conducting nature, which has not been explored so far. Again, the fabrication of thin structured free-standing electrode (50-100 μm) is highly desirable in the commercial aspects [4.6]. Hence, to address all such obstacles, a facile synthetic route for the fabrication of porous, crystalline, free-standing COF thin sheet with profitable electrical conductivity has to be developed.

The enhancement of capacitance through weak intermolecular interactions:

In the charge storage system, the generated electrons during the electrochemical redox reaction should be carried through the entire electrode for the excellent capacitance performance. However, most of the redox active platforms are usually electrically resistive and retard the overall capacitance. In contrast, the electrical conductive platforms like graphene, CNT etc. exhibit poor capacitance due to the lack charge storage centers. In this regard, it is wise to make a hybrid of both materials to perform as a good electrode in the charge storage systems. However, these hybrids should possess robust significant interaction for the easy transfer of electrons from one system to another. In this aspect, weak intermolecular interactions between the constituents could be a powerful technique to make a hybrid charge storage system. Interestingly, the DFT calculations and experimental observations suggest the existence of weak π - π intermolecular interaction between the COF and the graphene layers of CNF [4.7a-b]. Such weak intermolecular interactions aid the tight binding of COF and CNF together and exhibit as a hybrid system. The similar kind of approach has been successfully done with small molecule with carbon nanotube. Herein, they have taken redox-active anthraquinone molecule and clubbed with CNT through a solvothermal reaction [4.8]. The resulted powder exhibits higher supercapacitance compared to the pristine molecule and CNT. Likewise, the intermolecular interaction of COFs with CNT is also reported for the lithium and potassium ion batteries [4.9]. However, all these materials are generally granular in nature and the fabrication of a hybrid system into free-standing thin sheet is a difficult task.

To attempt on this line, in this chapter, we have demonstrated a novel synthetic method consisted of in-situ solid state inclusion of electrically conducting carbon nanofiber (CNF) [4.10] into the COF precursor matrix using facile mechano-mixing deposition technique [4.11]. The obtained COF thin sheets, after the thermal treatment, exhibit excellent electrical conductivity in contrast to the insulated nature of the pristine COFs. It should be noted that the crystalline and porous nature of COF thin-sheets is well maintained even after the incorporation of the CNF within COF matrix. The synthesized COF-CNF hybrids are crystalline and porous even in a free-standing and flexible thin sheet form (~50 μm

thickness). We have studied these hybrids with different techniques like PXRD, XPS for analysing the interaction between the components. Additionally, we have also performed a possible structural analysis of COF-CNF system by investigating COF and graphene layers interactions. These COF-CNF hybrids show an excellent electrical conductivity ($0.25 \times 10^{-3} \text{ Scm}^{-1}$) as well as outstanding capacitance (464 mFcm^{-2}) compared to the pristine COFs (38 mFcm^{-2}). Herein, the electronic movement along through long channels is highly feasible due to the significant intermolecular interactions between the COF and CNF layers. Notably, the CNF facilitates the electron transport through sp^2 C=C framework. Therefore, higher electronic movement subsequently enhances the efficient utilization of redox-active centres which in turn reflects an excellent electrochemical energy storage performance in the hybrids. Additionally, we have fabricated a solar cell-supercapacitor integrated self-charging device for the direct harvesting of light energy to be stored as electrical energy [4.12].

4.2 Result and Discussion

4.2.1 Synthesis and characterization

Herein, we have synthesized two different β -ketoenamine based COF-CNF (anthraquinone-based single linker **DqTp-CNF** and anthracene-anthraquinone based hetero-linked **DqDaTp-CNF**) hybrids through the *p*-toluenesulphonic acid assisted solid-state synthesis (**Figure 4.1**). These hybrids possess good crystallinity as well as high porosity (472 and $532 \text{ m}^2\text{g}^{-1}$ for **DqTp-CNF** and **DqDaTp-CNF** respectively). Notably, the **DqDaTp-CNF** hybrid exhibits excellent mechanical robustness (5.8% of breaking strain) compared to the single linker **DqTp-CNF** hybrid (1.2% of breaking strain) due to the availability of electronically

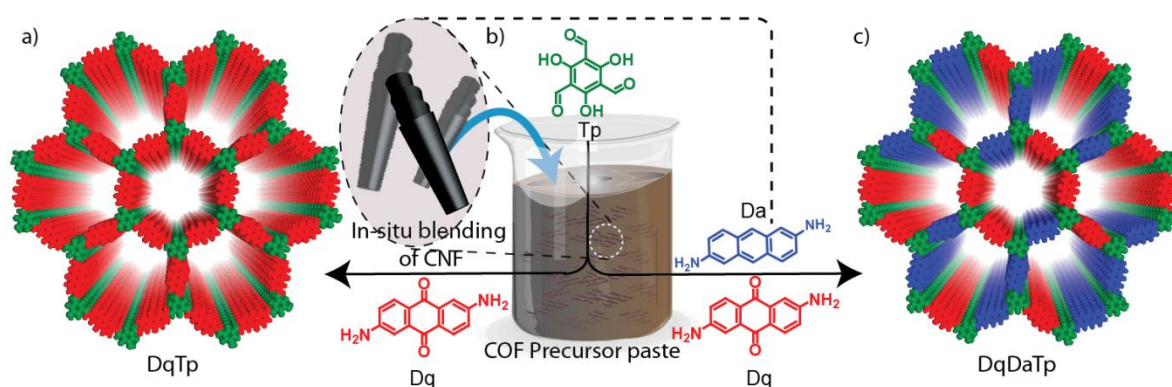


Figure 4.1: The diagrammatic representation of the COF-CNF hybrids.

conjugated anthracene moieties [4.13]. The as-synthesized COF-CNF hybrids were found to exhibit excellent electrochemical energy storage performance with high areal capacitance (464 and 364 mFcm^{-2} for **DqTp-CNF** and **DaDaTp-CNF** respectively) which is almost 10 times greater than the pristine COFs (38 and 28 mFcm^{-2} for **DqTp** and **DqDaTp** respectively). Additionally, we could fabricate a flexible supercapacitor device using the mechanically strong **DqDaTp-CNF** hybrid as the electrode where it could showcase a high capacitance performance of 167 mFcm^{-2} (at 0.5 mAcm^{-2}) and an excellent energy density of 5.5 μWhcm^{-2} . These findings greatly influence us to further integrate a photo-voltaic charged supercapacitor-solar cell device, for its further implementation towards concurrent harvest and storage of light energy in the form of electrical energy. Notably, the fabricated self-charging power-pack delivered an areal capacitance of 42 mFcm^{-2} at 0.25 mAcm^{-2} for 300 seconds photo charging.

2.2.2 The structural characterizations

The PXRD has been used to deduce the structural information of COF-CNF hybrids (**Figure 4.2**). The **DqTp-CNF** hybrid exhibits a crystalline profile with a sharp [100] and a broad [001] peaks at the 2θ of 3.6° and $26\text{-}27^\circ$ respectively. Likewise, the crystalline PXRD profile of **DqDaTp-CNF** hybrid shows a crystalline pattern with [100] and [001] peaks at the 2θ of

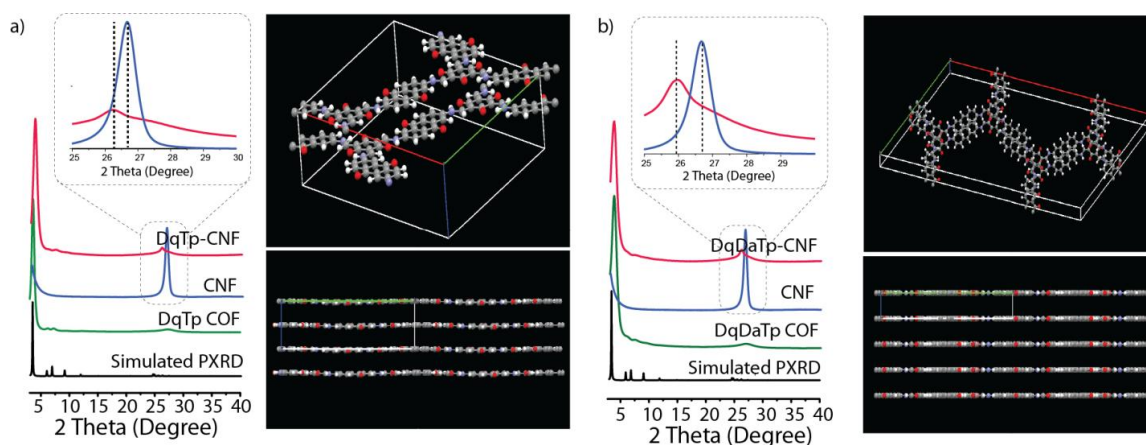


Figure 4.2: a) The PXR D comparison of *DqTp*-CNF with *DqTp* COF, CNF and simulated PXR D in eclipsed form. b) The PXR D comparison of *DqDaTp*-CNF with *DqDaTp* COF, CNF and simulated PXR D in eclipsed form.

3.4° and $\sim 27^\circ$ respectively. Moreover, the eclipsed honeycom 2D lattice modelling of both COFs agree with the obtained experimental PXR Ds of the corresponding COFs. Moreover, a sharp 002 peak has been noted at the angle of 2θ 26-27 $^\circ$ in the PXR D profiles COF-CNF hybrids which arised from the 002 planes of the in-situ added carbon nanofibers (CNF).

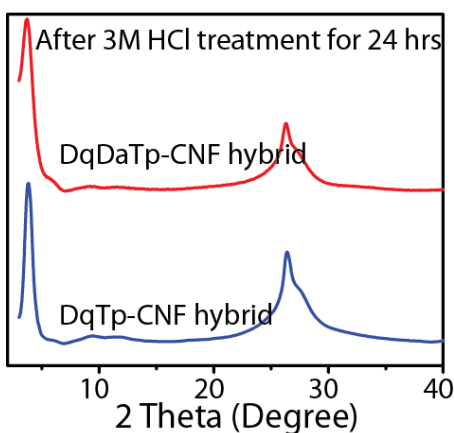


Figure 4.3: The PXR D of COF-CNF hybrids after the 3M HCl acid treatment for 24 hours.

However, a lower angle reflection of the 002 planes of CNF in the COF-CNF hybrids compared to pristine CNF may indicate that the interplanar widening of the graphene planes of the CNF after the pi interaction with COF. The special structural characters of the herringbone/cup-stacked hollow CNF with a fibre axial angle of 30° helps to the growth of the COF from its monomers on the surface of inside (the open aperture of CNF is ~ 100 nm with a central core diameter of 70-80 nm) and outside (the large lateral dimension of the CNF

makes a negligible curvature for the graphene layers) walls. In this way, the in-situ solid state inclusion of CNF allows the deposition of COF crystallites effectively on the CNF graphene

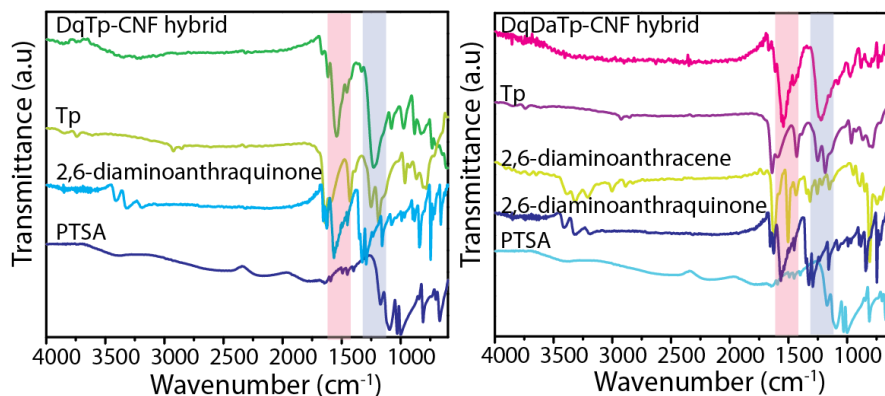


Figure 4.4: The FT-IR profiles of **DqTp-CNF** and **DqDaTp-CNF** hybrids and their starting materials.

layers. However, we could not observe a similar growth of COF on CNT with the diameter (~20 nm) due to the cylindrical curvature of the graphene layers, hence the $\Pi\cdots\Pi$ interaction of CNT and COF becomes very poor. Furthermore, the lack of efficient interaction between the units of composites makes free-standing thin sheet into more fragile.

4.2.3 Chemical characterization

The chemical bonding of the β -ketoenamine framework of COF-CNF hybrids (**DqTp-CNF** and **DqDaTp-CNF**) has been confirmed from stretching vibrations [C–N (1225 & 1216 cm^{-1}) and C=O bonds (1663 & 1667 cm^{-1})] in the corresponding FT-IR profiles (**Figure 4.4**). Similarly, the presence of anthraquinone displays a stretching vibration at 1663 and 1667 cm^{-1} for **DqTp-CNF** and **DqDaTp-CNF** hybrids respectively. Furthermore, the ^{13}C CP MAS solid-state NMR spectroscopy provides the details of the chemical environment of carbon in the molecular structure of the COFs. The β -ketoenamine C=O resonance at 183 - 184 ppm for both COF-CNF hybrids. Meanwhile, the enamine carbon(C=C-N) features at 147 (**DqTp-CNF**) and 145 ppm (**DqDaTp-CNF**) (**Figure 4.4**).

The binding energy shifts of COF-CNF hybrids compared to the pristine COFs and CNF were investigated by the X-Ray photoelectron spectroscopy (XPS) (**Figure 4.6a**) [4.14]. The XPS profile displays the binding energy shifts of C1s of the pristine CNF and **DqDaTp** positioned at 284.5 and 284.8 eV respectively (**Figure 4.6b**). Whereas, the C1s binding energy of **DqDaTp-CNF** hybrid is shifted to the higher energy of 285.9 eV. It could be due to

the interlayer $\pi\cdots\pi$ interaction between the COF and the CNF. Again, the peak of C1s profile of **DqTp**-

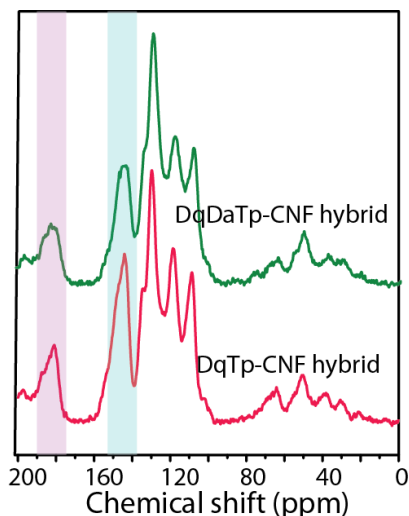


Figure 4.5: The ^{13}C CP MAS solid-state NMR profiles of -CNF and **DqDaTp**-CNF hybrids.

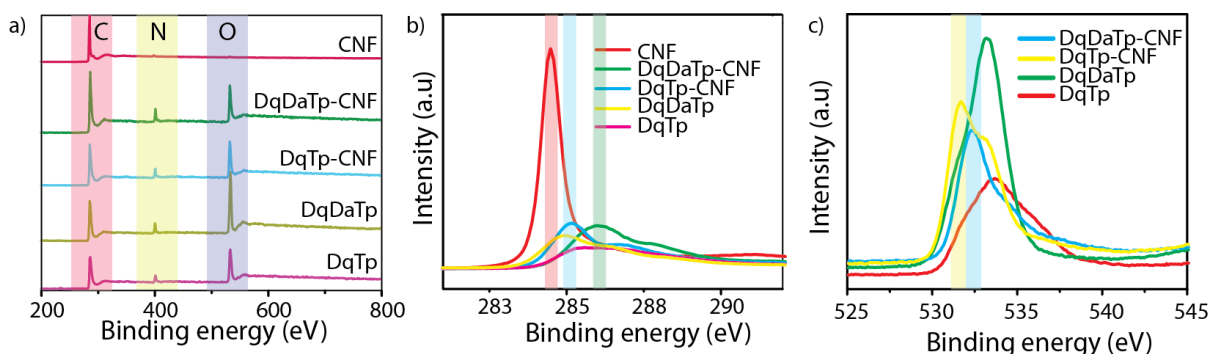


Figure 4.6: The XPS profiles of all COF-CNF hybrids, COFs and CNF. b) The XPS profile of C1s. c) The XPS profile of O1s.

CNF hybrid shows at the binding energy of ~ 285.1 eV. Herein, it has been noted that the binding energy of **DqTp**-CNF is higher than the pristine CNF (284.5 eV). However, this hybrid exhibits an energy shift to the lower binding energy compared to the pristine **DqTp** (285.4 eV). Again, this can be explained as the presence of the more number of electrophilic **Dq** moieties in **DqTp** compared to the **DqDaTp** COF. In **DqDaTp**-CNF, the **Da** (π electron rich, which can donate electrons), **Dq** (electron deficient, which can accept electron) and graphene layer (graphenes are amenable to accept or donate or partially share their π -electrons, depending on the electronic property of the neighbouring counter molecules) make the higher binding energy shift

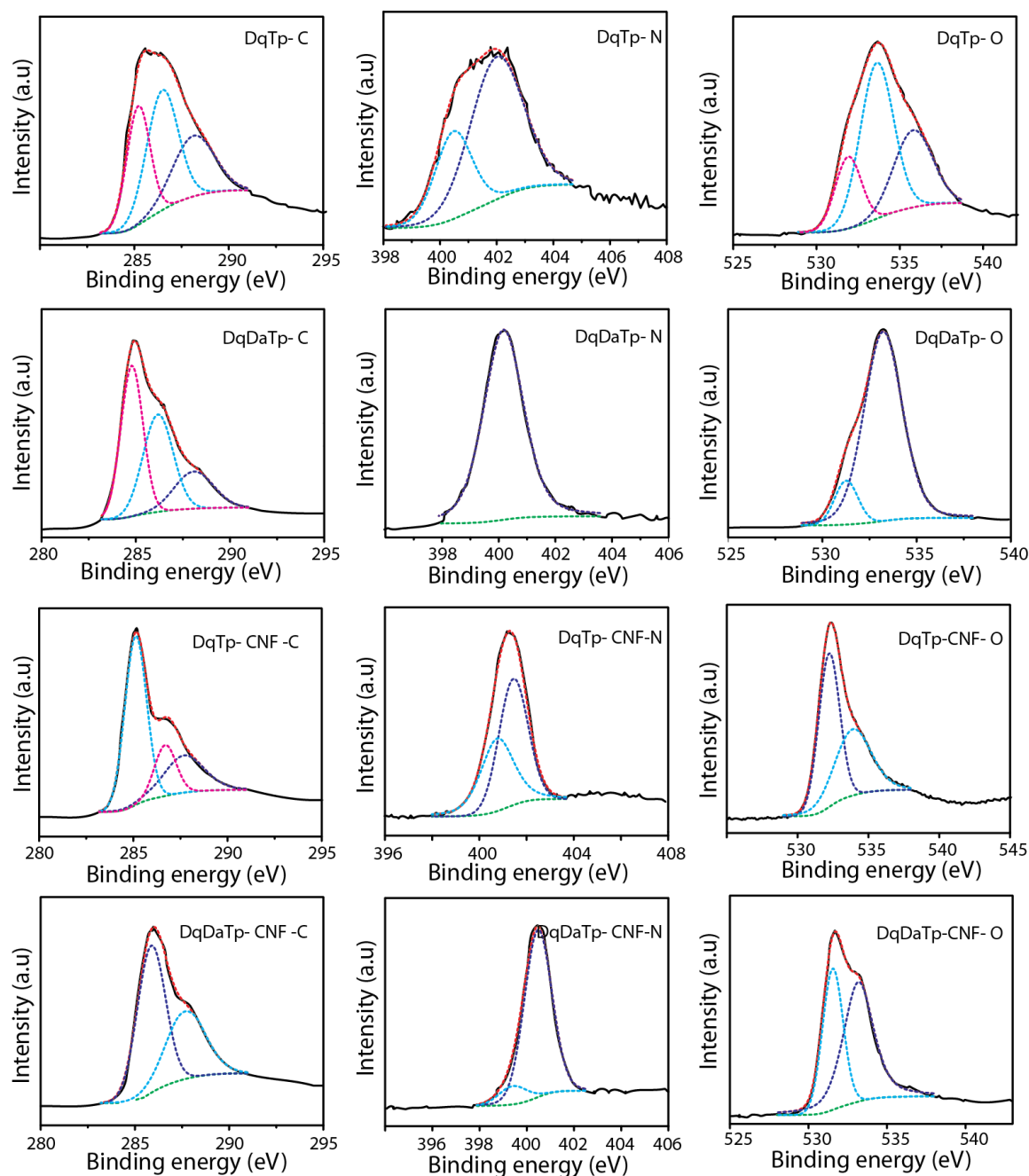


Figure 4.7: The XPS profiles of all hybrids and COFs after deconvolution.

in XPS. Meanwhile, in **DqTp**, the more number of **Dq** moieties make the COF is willing to accept electron from graphene, hence a mid-positioned binding energy compared to the pristine units. Furthermore, the broad peak at the binding energy of ~ 287.7 eV (**DqDaTp-CNF**) and 286.0 eV (**DqTp-CNF**) originates from the C 1s of the C=O linkages. Additionally, it was noted to be the binding energy shifts in the XPS

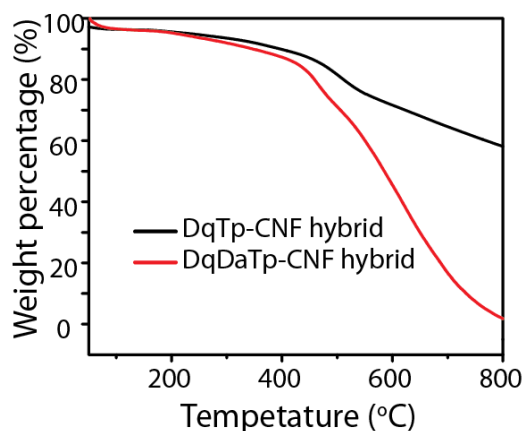


Figure 4.8: The TGA curves of COF-CNF hybrids.

profile of N1s of the COF-CNF hybrid compared to the pristine COFs (**Figure 4.7**). The N1s binding energy is shifted from 400.0 eV (pristine) to 400.5 eV (in the hybrid) for **DqDaTp**. Moreover, a tiny shift towards the higher binding energy is observable for the pristine **DqTp COF** (400.5 eV) to **DqTp-CNF hybrid** (400.7 eV). Whereas, the lowering binding energy shift has been observed for all COF-CNF hybrids in the O1s XPS profile of hybrids [**DqTp CNF** (532.2) and **DqDaTp-CNF** (531.5 eV)] compared to the pristine [**DqTp** (533.7) and **DqDaTp** (533.2 eV)] (**Figure 4.6c**).

4.2.4 Properties of COF-CNF hybrid thin sheets

Porosity:

The TGA profiles display good thermal stability of COF-CNF hybrids up to 430°C (**Figure 4.7**). However, we could notice a slight loss in the weight percentage of both hybrids in the temperature range 200-400° C. It could be due to the thermal decomposition of the oligomers were trapped in the hybrid matrix. It should be noted that the in-situ carbon nano fibre blended COFs preserve the well porous nature unlike many other COF composites [4.15]. The N₂ adsorption analysis of COF- CNF hybrids provides the BET surface areas of 472 (**DqTp-CNF**) and 532 m²g⁻¹ (**DqDaTp-CNF**). (Supporting Information, Figure S18). It is noteworthy that the surface of hybrids exhibits higher than CNF alone (96 m²g⁻¹). The non-local density theorem (NLDF), provided 2-2.2 nm pore diameter for both COF-CNF hybrids suggest that the well-organized pore size distribution of the frameworks.

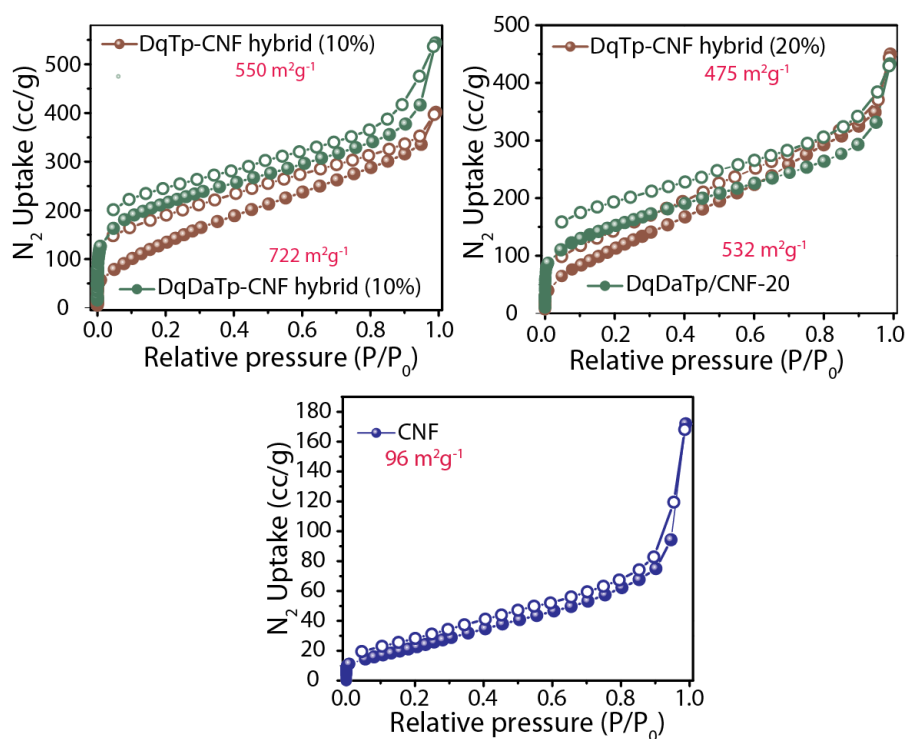


Figure 4.9: The N_2 gas adsorption of COF-CNF hybrids and CNF.

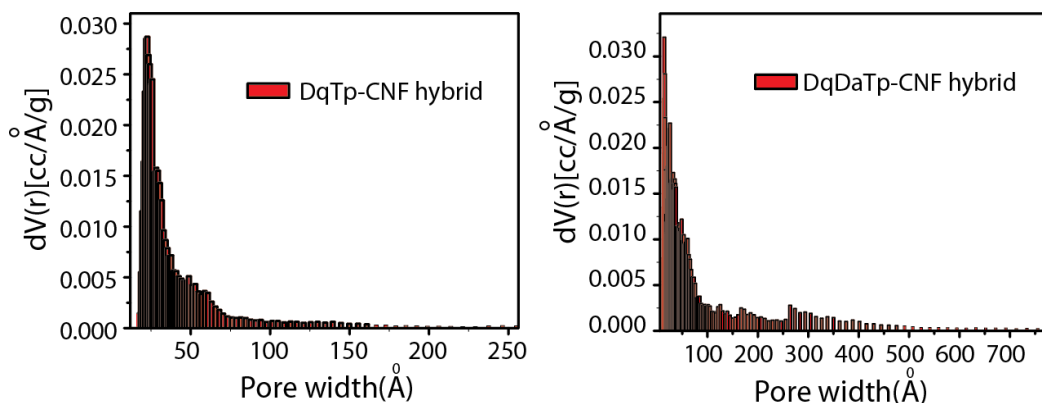


Figure 4.10: The NLDFT pore size distribution of COF-CNF hybrids.

Electrical conductivity:

The presence of CNF aids to amplify the electrical conductivity of the COF-CNF hybrid thin sheets. To measure the conductivity, the hybrids as well as the pristine **DqTp** and **DqDaTp** were subjected to current-voltage characteristics (I-V characteristics) (**Figure 4.11a**). We have taken $0.5 \times 0.5 \text{ cm}^2$ COF-CNF hybrid thin sheets sandwiched by two grafoil plates.

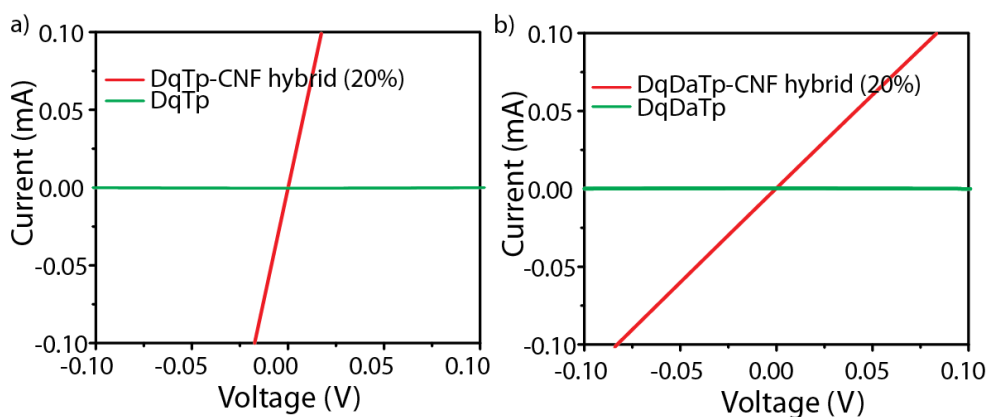


Figure 4.11: The I-V plot of a) **DqTp** COF and **DqTp-CNF** hybrid and b) **DqDaTp** COF and **DqDaTp-CNF** hybrid.

Particularly, the edges of grafoils were completely insulated for avoiding the direct contact between them. Then the assembled set was carried to a Swagelok cell for investigating the current-voltage measurements (-0.1V to +0.1V). Notably, **DqTp-CNF** exhibits an excellent electrical conductivity of $2.5 \times 10^{-4} \text{ Scm}^{-1}$. At the same time, **DqDaTp-CNF** evince the enhanced electrical conductivity of $5.2 \times 10^{-5} \text{ Scm}^{-2}$ respectively. Whereas, the pristine COFs perform with very high electrical resistance ($>10^{-14} \text{ Scm}^{-1}$) in the I-V plot and the current increment is almost parallel to the voltage axis. It signifies even the low percentage of CNF doping enhances the conductivity of COF thin sheet to a large extent ($>10^9$). We assumed the redox active COF matrix with a good flow of electrons may function as an excellent charge storage electrode in the electrochemical reaction.

4.2.5 DFTB optimization of COF-CNF interactions

To get the information about the interlayer COF-CNF graphene layer interaction of the hybrids, we have studied the possible models through the tight-binding density functional theory (DFTB). We have optimized the models of COF- planar graphene in vacuum and non-vacuum mode by considering the slightly curved graphene layers of the herringbone cup/stacked CNF. Due to the large asymmetric unit of **DqDaTp** in 1:1 ratio, instead of it, we have focused on hetero-linked **Dq₁Da₂Tp** (1:2) and **Dq₂Da₁Tp** (2:1) for DFTB studies (**Figure 4.12**). Notably, we have built up the multilayer optimizations like 2-2-2 [2 graphene layers -2 COF layers -2 graphene layers] and 3-3-3 [3 graphene layers -3 COF layers -3 graphene layers] models to estimate the interlayer interactions of the COF-CNF hybrids (**Figure 14-16**). Firstly, we

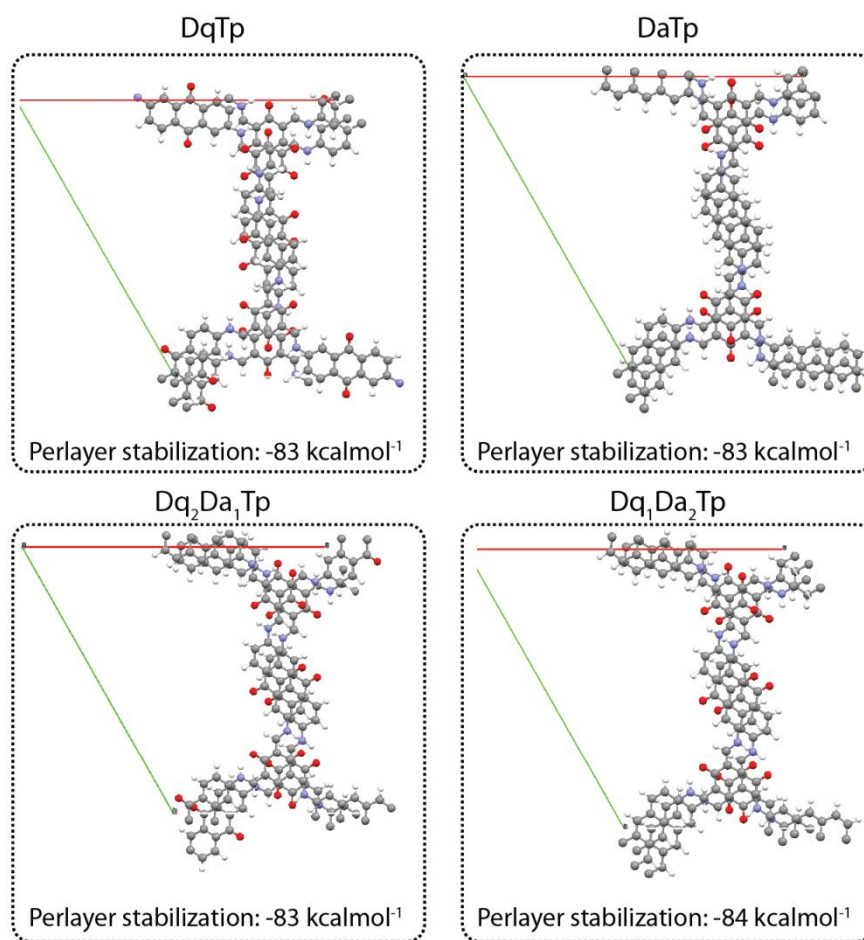


Figure 4.12: The DFTB optimized unit cells of *DqTp*, *DaTp*, *Dq₂Da₁Tp* and *Dq₁Da₂Tp* COFs for the interlayer interaction studies.

have optimized the structure of COF-graphene monolayer which displays the single layer of COF stacks with a slight shift corresponding to 002 plane of the single layer of graphene (**Figure 13**). Moreover, the DFTB results suggest the perlayer stabilization of the COF-planar graphene has been enhanced by 3-fold times compared to the pristine COFs. The perlayer stabilization of each model of COF-planar graphene is given below in **Table 4.1**. Importantly, the DFTB outcomes of COF-planar graphene models suggest a shortening of the interlayer distances in the COF-COF (3.36 Å to 3.31-3.21 Å) and COF-graphene (3.21 Å) [4.7a-b]. The investigations on the DFTB results of interlayer distances reflect the significant interaction between COF and graphene layers. It was found to be the interlayer distance of graphene is increased to ~3.41 Å whereas pristine graphene model exhibits only 3.36 Å, which signifies the cut down of the $\Pi \cdots \Pi$ interaction between the graphene layers. We have

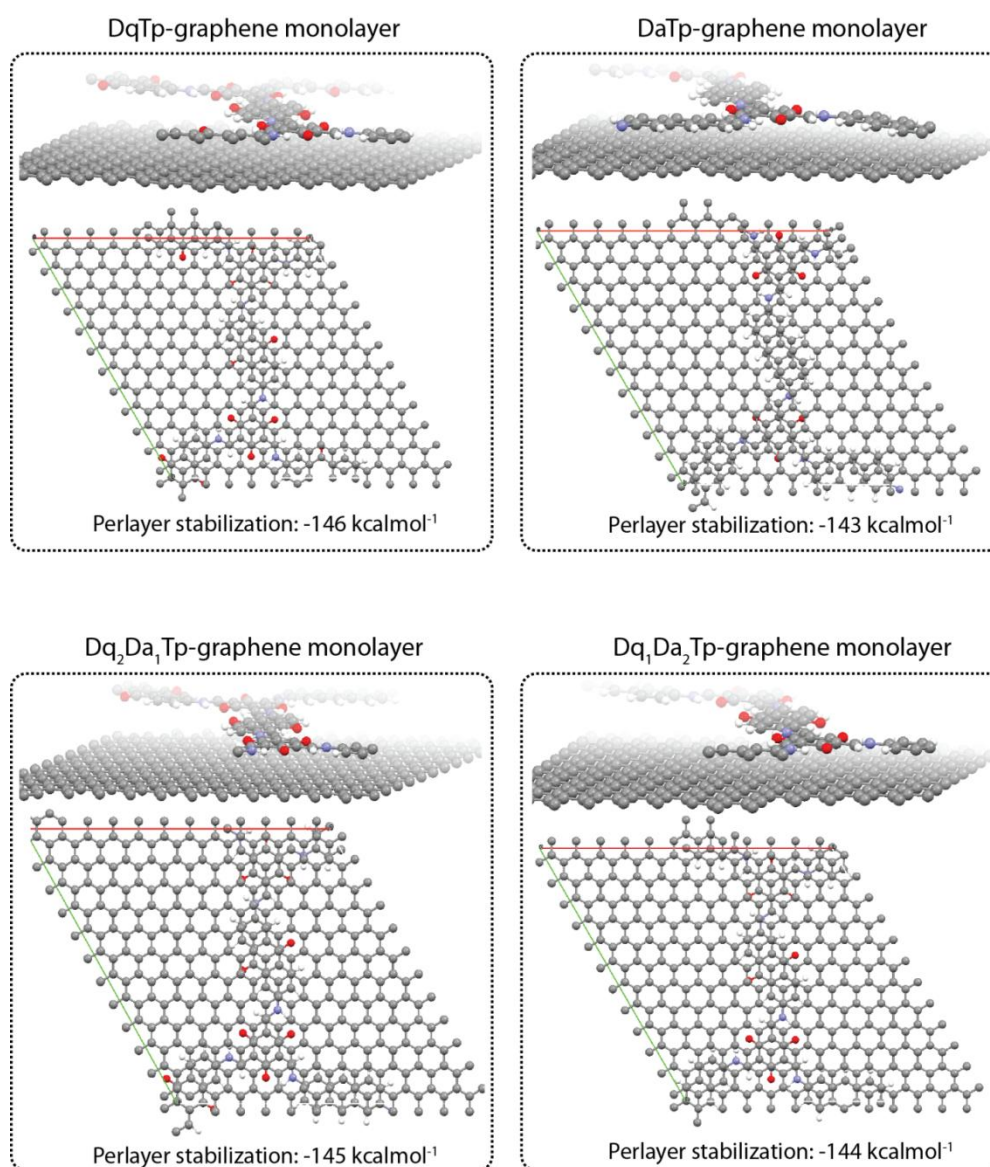


Figure 4.13: The DFTB optimized monolayer COF-graphene systems.

also modelled COF-curved graphene system in armchair the (AC) configuration for understanding the interaction COF layers with vertical graphene edges. (**Figure 4.16**). A slight enhancement in the perlayer stabilization energy ($\sim 105 \text{ kcalmol}^{-1}\text{layer}^{-1}$) has been observed when compared to the pristine COFs ($80\text{-}84 \text{ kcalmol}^{-1}\text{layer}^{-1}$). We believe, both

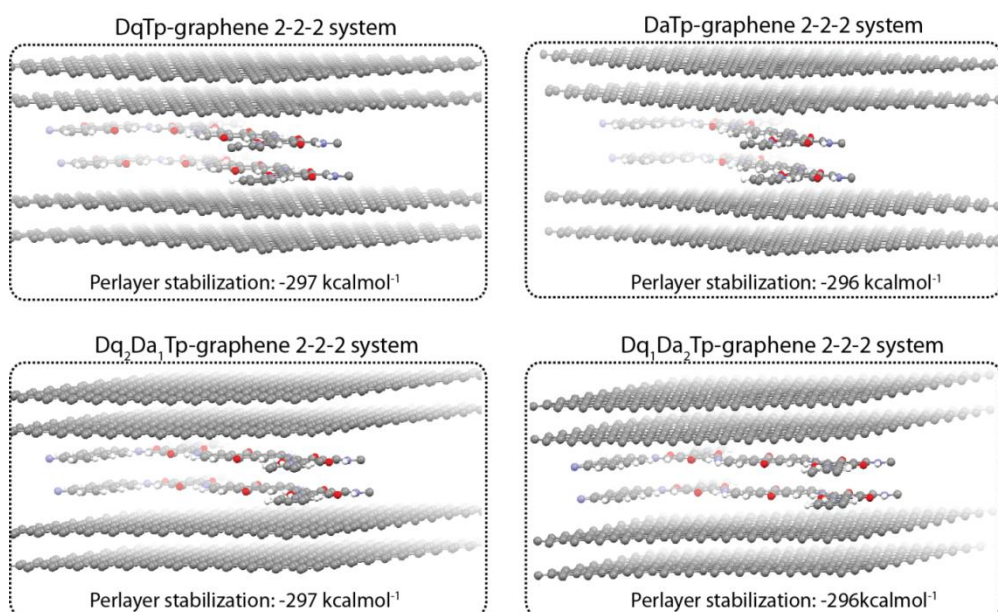


Figure 4.14: The DFTB optimized 2-2-2 COF-graphene systems.

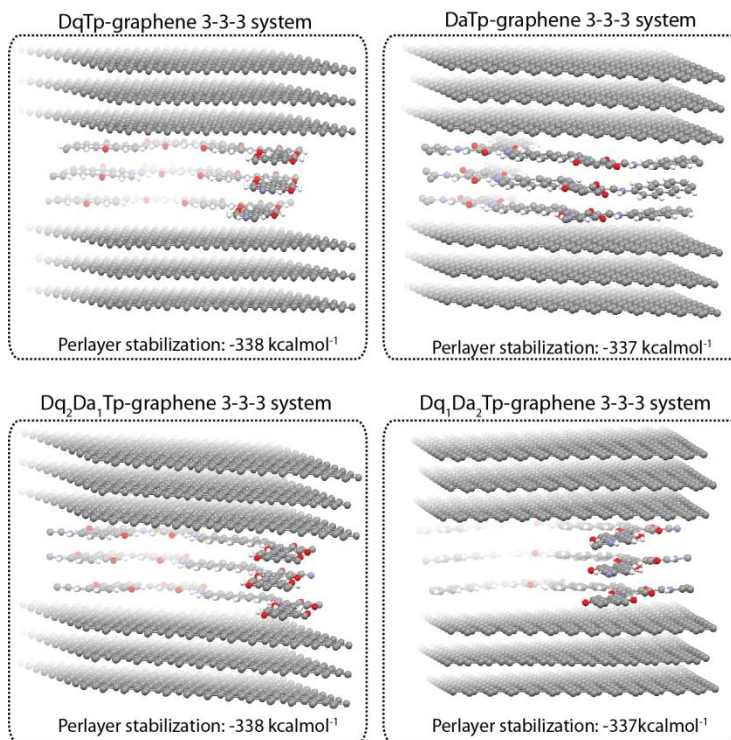


Figure 4.15: The DFTB optimized 3-3-3 COF-graphene systems.

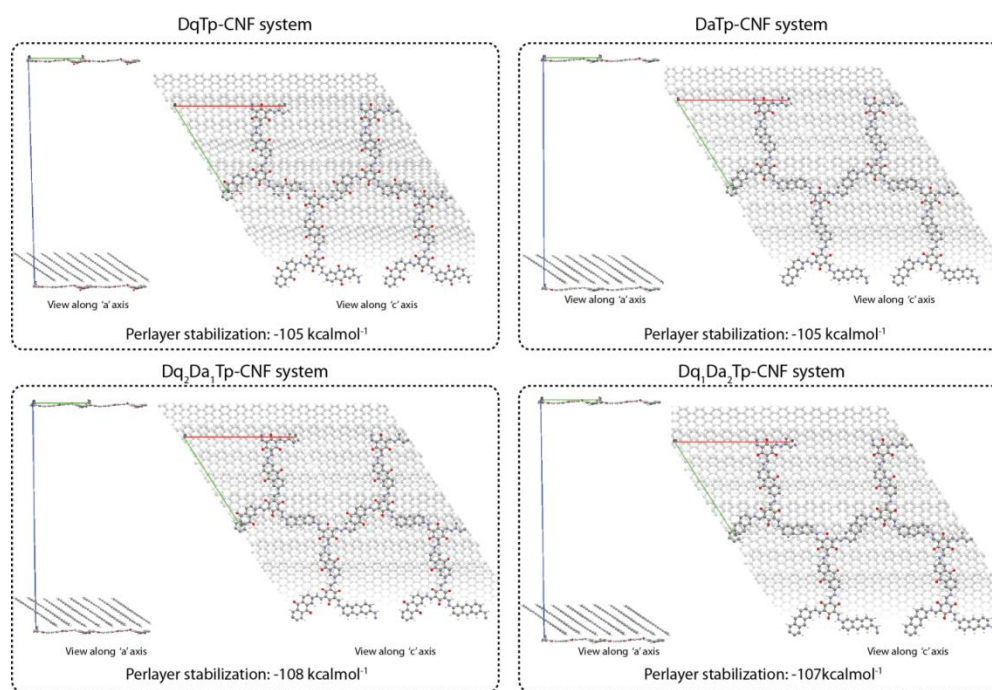


Figure 4.16: The DFTB optimized models of vertically stacked COF on a slightly curved graphene.

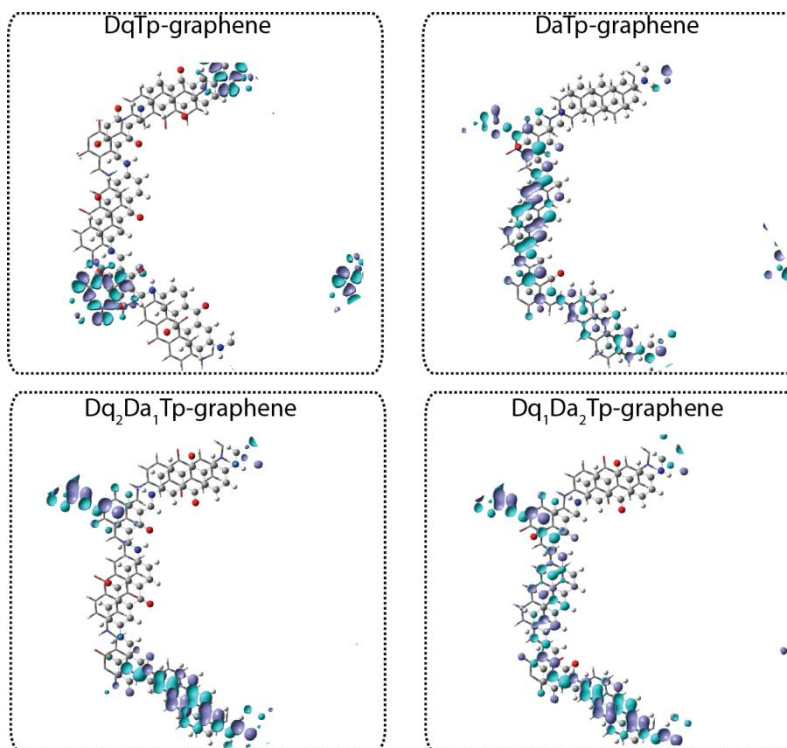


Figure 4.17: The DFTB optimization of HOMO/LUMO of COFs.

COFs	Pristine		COF-Graphene monolayer		COF-Graphene 2-2-2		COF-Graphene 3-3		COF-graphene 3-3-3 (No vacuum)		COF-CNF Arm chair	
	Per layer stabilization energy	HO MO-LU MO gap	Per layer stabilization energy	HO MO-LU MO gap	Per layer stabilization energy	HOMO-LUMO gap	Per layer stabilization energy	HO MO-LU MO gap	Per layer stabilization energy	HO MO-LU MO gap	Per layer stabilization energy	HO MO-LU MO gap
DqTp	-83.47	1.76	-145.92	1.79	-297.45	1.80	-337.97	1.75	-421.74	1.76	-105.44	0.80
DaTp	-82.77	1.63	-142.68	1.71	-295.82	1.64	-336.65	1.55	-420.29	1.60	-104.81	0.82
Dq ₂ D a ₁ Tp	-83.67	1.54	-144.83	1.57	-296.88	1.56	-337.50	1.51	-421.11	1.47	-107.80	0.81
Dq ₁ D a ₂ Tp	-83.23	1.58	-143.99	1.55	-296.38	1.54	-337.28	1.52	-419.63	1.50	-106.99	0.81

Table 4.1: DFTB data of COF-CNF hybrids (Perlayer stabilization in kcalmol⁻¹ and band gap in eV).

COF-planar graphene and curved graphene model could suggest the possible interaction happen in the COF-CNF hybrids.

4.2.6 Morphology COF-CNF hybrid thin sheets

The nano-level morphologies of **DqTp-CNF** and **DqDaTp-CNF** hybrids were inspected through the TEM analysis which displayed the COF crystallites associated with an aggregated planar ribbon-like morphology which is stacked on the surface of 70-80 nm febrile CNF (**Figure 4.18**). It could possible that the larger diameter of the CNF can accommodate the COF crystallites on the inner and the outer walls. We believe, due to the $\Pi\cdots\Pi$ interactions, covalent linkage formation of the framework starts on the surface of the CNF graphene layers.

Whereas, the TEM images of the physical mixture of COF and CNF show both entities are distinctly separate each other (**Figure 4.19**). It signifies the importance of the in-situ solid state inclusion of the CNF in the COF matrix. Moreover, the TEM analysis of COF-CNT hybrids suggest the poor interaction of COF crystallites with the surface of small radii carbon nanotubes (CNT) (**Figure 4.20**). It could be due to the failure of COF growth on the surface of CNT with higher curvature nature. Additionally, the vertical cross-section and horizontal imaging of both COF-CNF hybrids have been scanned by the SEM. It shows a uniform thickness (~50 μm) for both of the hybrid thin sheet with a crack-free nature (**Figure 4.21**). In the cross-sectional SEM image of the hybrid thin sheet, the embedded CNFs in COF matrix are clearly visible with a fibrillar morphology (Figure 4a&b).

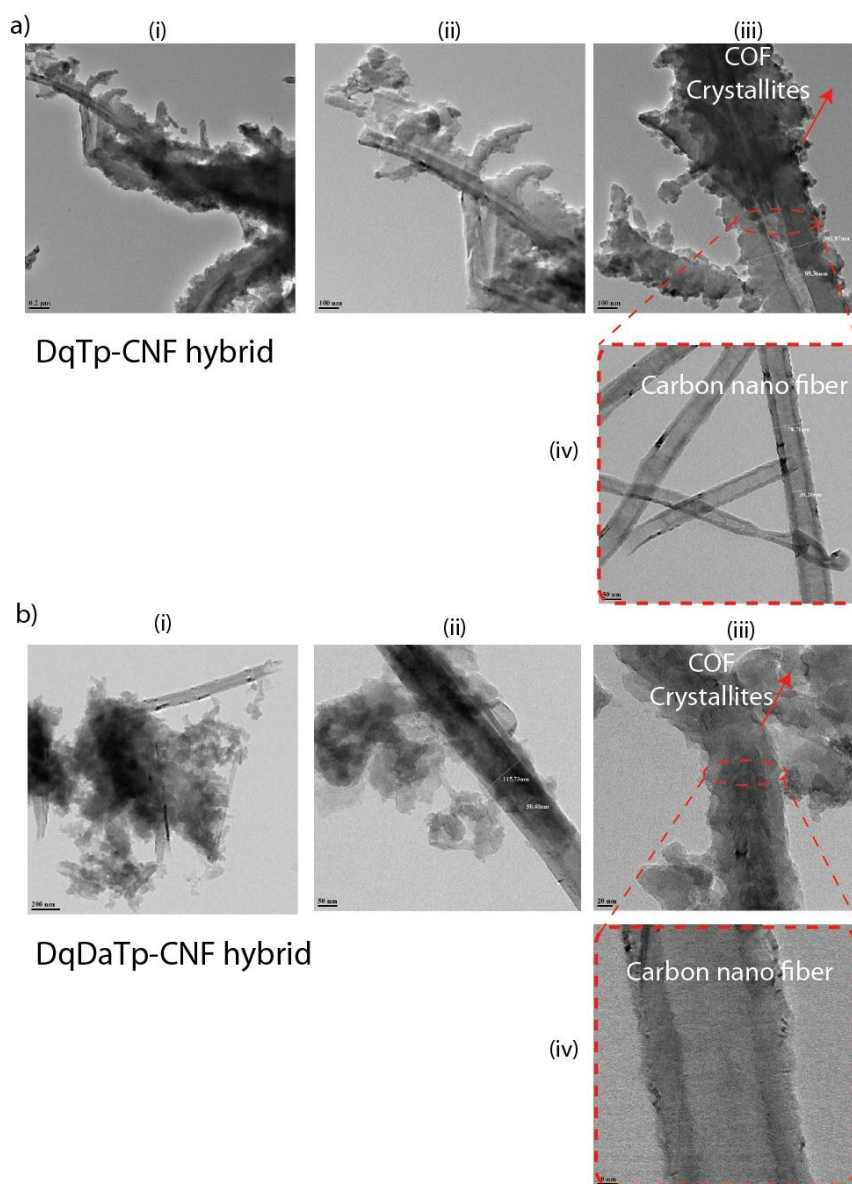


Figure 4.18: The TEM images of COF-CNF hybrid thin sheets.

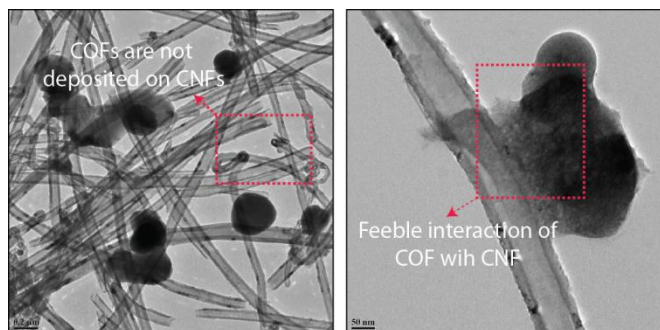


Figure 4.19: The TEM images of the physical mixture of COF and CNF.

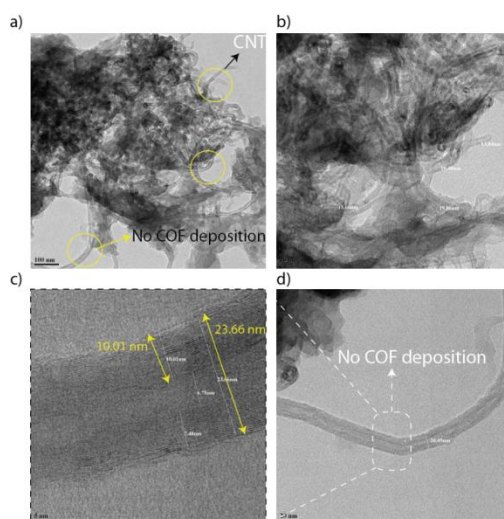


Figure 4.20: The TEM images of the COF-CNT hybrids. The scale bar represents a) 100 nm; b) 50 nm; c) 5 nm; and d) 20 nm.

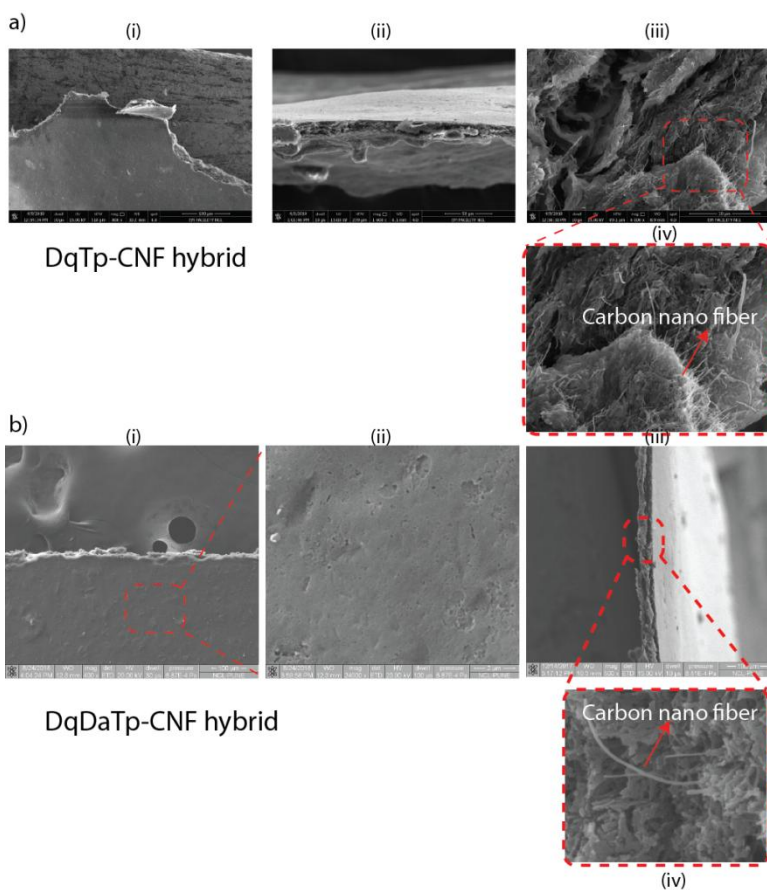


Figure 4.21: The SEM images of COF-CNF hybrid thin sheets. a) (i)-(iv) **DqTp-CNF** hybrid and b) (i)-(iv) **DqDaTp-CNF** hybrid. It shows the surface and vertical cross-section of the thin sheet. Again, the CNFs are clearly visible in the zoomed image of vertical cross-section.

The synthetic strategy of COF-CNF hybrids advances the smooth surface and large areal fabrication ($>16 \text{ cm}^2$) which are evident from the SEM imaging. It is noteworthy to mention, the weak, but significant interactions of COF and CNF promote the structural integrity for

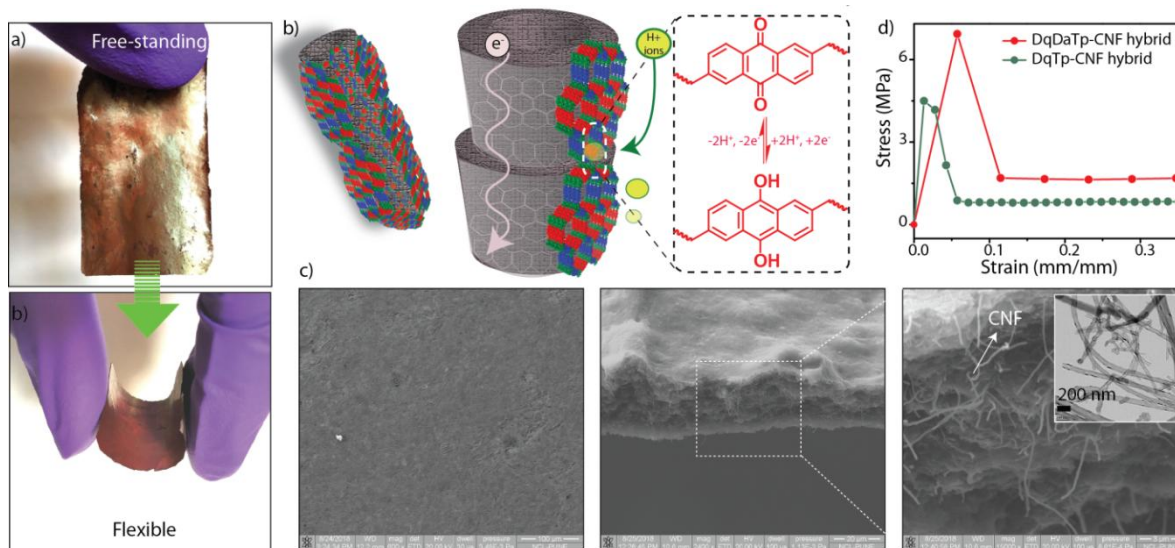


Figure 4.22: a) Free-standing and flexible *DqDaTp*-CNF hybrid. b) The graphical representation of COF on the surface of CNF. d) The DMA of both COF-CNF hybrids. e) The SEM images of *DqDaTp*-CNF hybrid thin sheet.

the hybrid thin sheet even under continuous ultrasonication and thermal treatment in solvents with high polarity.

4.2.7 Electrochemical analysis of COF-CNF hybrid thin sheets

Three-electrode analysis:

We have set a three-electrode assembly of COF-CNF hybrids as pure working electrode (without any current collector support) for the analysis of electrochemical performance. Herein, we have taken the electrodes with a large area of 1 cm^2 considering the real-life aspects of energy storage devices. Notably, the large current response of the COF-CNF hybrids compared to pristine COFs has been evidently shown in the cyclic voltammetry (CV, -0.5V to 0.5V) profile (**Figure 4.23 a & b**). It could be due to the lucid electron movement in the COF-CNF hybrid matrix compared to poor electrical conductive pristine COFs. The electronic movement through the COF matrix enhances the efficiency of the charge storage and exhibits excellent capacitance. Again, the increasing scan rate displays the large

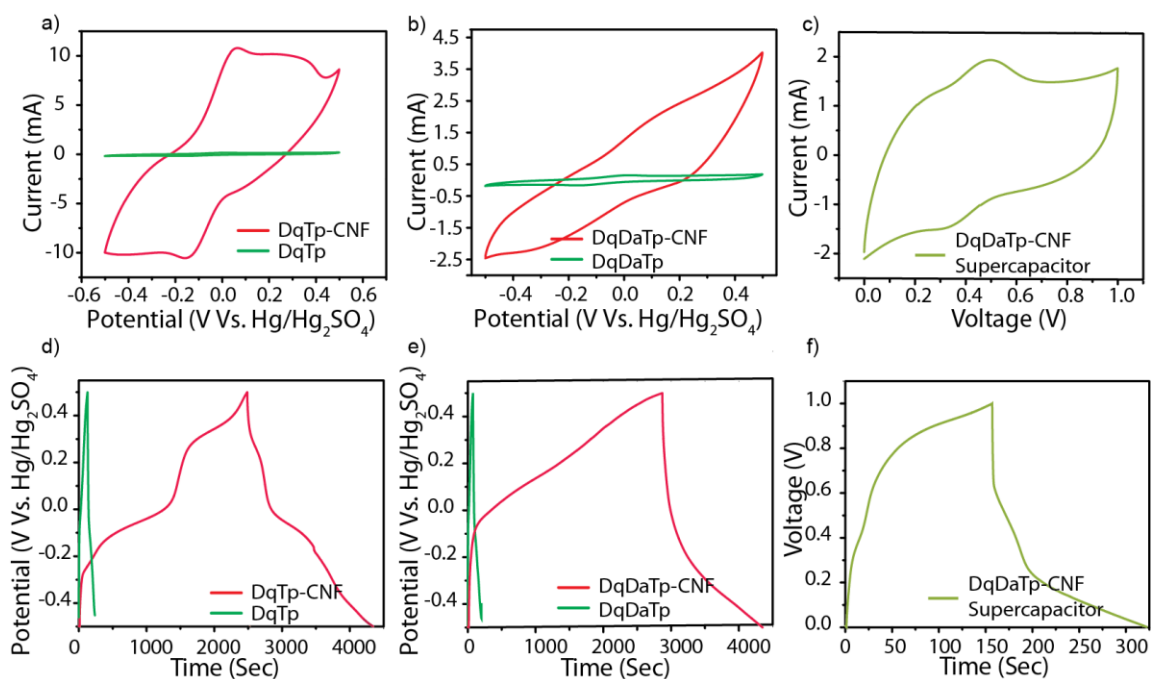


Figure 4.23: a) The CV profile of **DqTp-CNF** hybrid and **DqTp** COF at 50 mVsec^{-1} . b) a) The CV profile of **DqDaTp-CNF** hybrid and **DqDaTp** COF at 50 mVsec^{-1} . c) a) The CV profile of **DqDaTp-CNF** hybrid and **DqDaTp** Supercapacitor at 50 mVsec^{-1} . d) The GCD curves of **DqTp-CNF** hybrid and **DqTp** COF at 0.25 mA g^{-1} . e) The GCD curves of **DqDaTp-CNF** hybrid and **DqDaTp** COF at 0.25 mA g^{-1} . f) The GCD curves of **DqDaTp-CNF** hybrid and **DqDaTp** Supercapacitor at 0.50 mA g^{-1} .

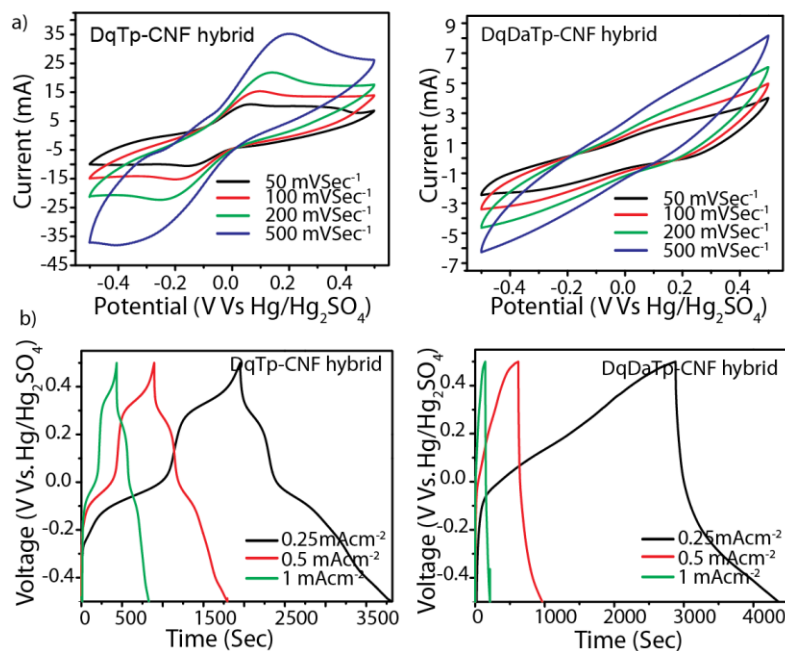


Figure 4.24: a) CV and b) GCD profiles of **DqTp-CNF** & **DqDaTp-CNF** hybrids.

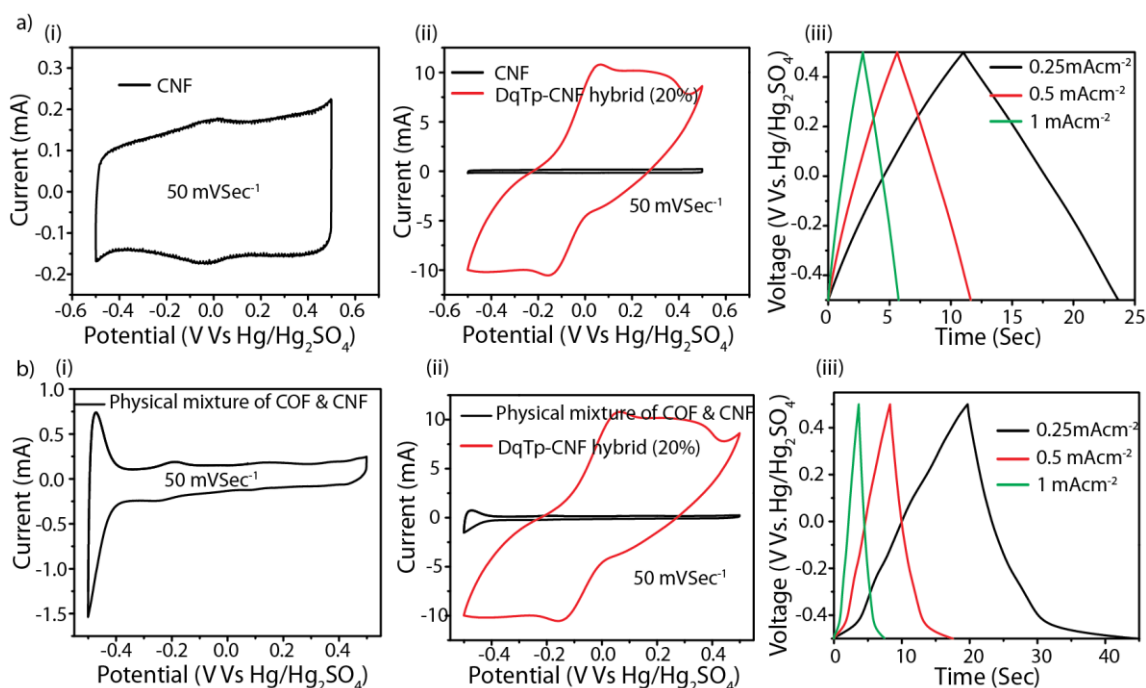


Figure 4.25: a) CV profile of CNF at 50 mVsec^{-1} ; (ii) Comparison of CV profiles of **DqTp-CNF** hybrid with CNF at 50 mVsec^{-1} ; (iii) The GCD curve of CNF at different current densities. b) a) CV profile of physical mixture COF and CNF at 50 mVsec^{-1} ; (ii) Comparison of CV profiles of **DqTp-CNF** hybrid with physical mixture at 50 mVsec^{-1} ; (iii) The GCD curve of CNF at different current densities.

enhancement in the current response in the CV measurements of COF-CNF hybrids (**Figure 4.24a**). Furthermore, the galvanostatic charge-discharge experiments (GCDC) provided the areal capacitances of the hybrids [**DqTp-CNF** (464 mFcm^{-2}), and **DqDaTp-CNF** (364 mFcm^{-2}) at a current density of 0.25 mAcm^{-2}] (**Figure 4.23 d & e**). Whereas, the pristine COFs displayed comparatively poor areal capacitance values of 38 (for **DqTp**) and 28 mFcm^{-2} (for **DqDaTp**) only. However, it has been observed that an insignificant capacitive performance capacitance of CNF (3 mFcm^{-2} at 0.25 mAcm^{-2} ; **Figure 4.25a**) in the GCDC experiment 1 mgcm^{-2} coated on a carbon paper. The poor and excellent performance of pristine and hybrids point out: 1) CNF is only responsible for carrying the electrons in the hybrid matrix; 2) pristine COFs are almost inert towards the electrochemical condition if it is in a direct connection to the circuit and 3) the excellent performance of hybrid is due to the concurrent functioning of redox activity and ease of electron movement. Moreover, the physical mixture of **DqTp** and CNF shows a negligible capacitance of 6.25 mFcm^{-2} at 0.25

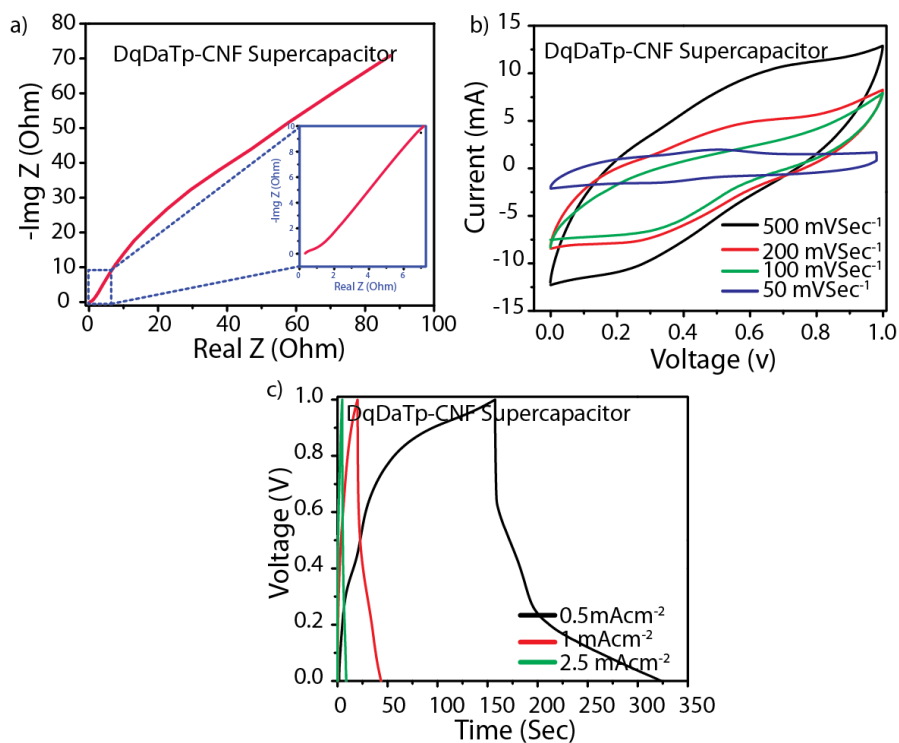


Figure 4.26: a) The CV and b) GCD analysis of *DqDaTp-CNF* supercapacitor.

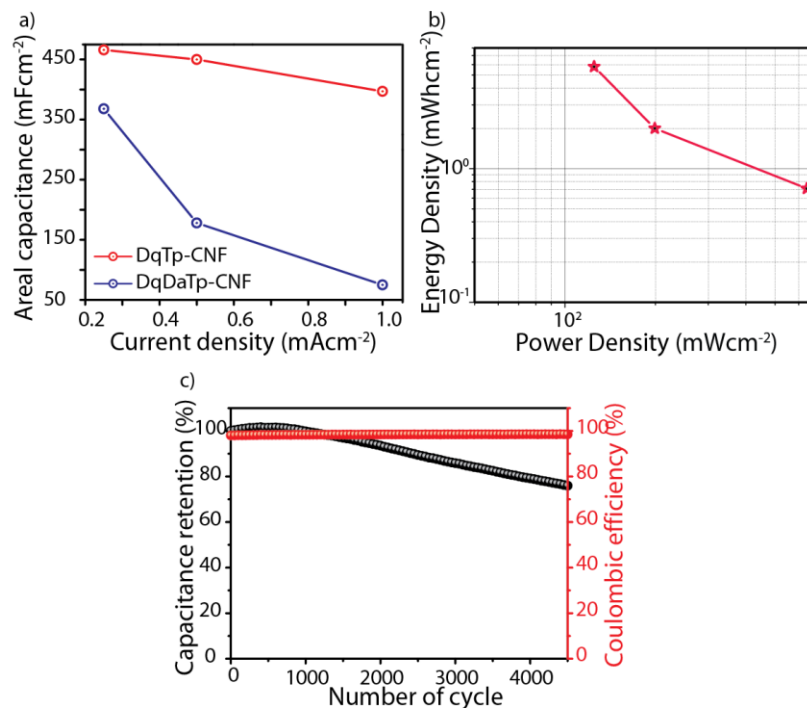


Figure 4.27: a) The plot of current density Vs areal capacitance. b) Ragone plot of power density Vs energy density. c) The long-term cyclic stability of *DqDaTp-CNF* supercapacitor.

Active material	Supercapacitor Capacitance	Nature of the electrode	Reference
DqDaTp-CNF hybrid	167 mFcm ⁻² at 0.5 mAcm ⁻²	Flexible and free-standing thin sheet (Thickness- ~50 μm)	This work
MOF-PANI	35 mFcm ⁻² at 0.05 mAcm ⁻²	MOF thin film deposited on carbon cloth	L. Wang et al., <i>J. Am. Chem. Soc.</i> 2015, 137, 4920–4923
Pen Ink nanoparticles	11.9–19.5 mFcm ⁻² at 0.083 to 16.7 mA cm ⁻²	21 μm thick ink film	<i>Y. Fu et al., Adv. Mater.</i> 2012, 24 (42), 5713–5718.
rGO sheets	6.49 mFcm ⁻²	30 μm thick rGO on a gold wire	Y. R. Li et al., <i>Chem. Commun.</i> 2013, 49, 291–293.
DqTp COF	12 mFcm ⁻² at 0.39 mAcm ⁻²	Flexible and free-standing thin sheet (Thickness- ~25 μm)	A. K. M et al., <i>ACS Appl. Mater. Interfaces</i> , 2018, 10, 33, 28139–28146.
CNT/AC	39.67 mFcm ⁻² (For device)	A carbon composite fiber	J. Ren et al., <i>Adv. Mater.</i> 2013, 25, 5965–5970
TpOMe-DAQ	84 mFcm ⁻²	Flexible and free-standing thin sheet (Thickness- ~200 μm)	A. Halder et al., <i>J. Am. Chem. Soc.</i> 2018, 140, 10941-10945.
CNT-PEDOT	73 mFcm ⁻²	20 μm diameter yarn	J. A. Lee et al., <i>Nat. Commun.</i> 2013, 4, 1970
Porous graphene foam-based supercapacitor (GFSC)	38 mFcm ⁻² at 0.67 mAcm ⁻²	Sheet thickness ~550 μm	L. Manjakkal et al., <i>Nano Energy</i> 2018, 51, 604–612.

CNT	50 mFcm ⁻² at 1.4 mA cm ⁻² (for three electrode)	Free-standing film	Y. Chen et al., 2015, 287, 68-74
Graphite nanosheets/PANI	77.8 mFcm ⁻²	Paper based electrode	B. Yao et al., <i>Nano Energy</i> , 2013, 2, 1071–1078.
CNT/PPy	280 mFcm ⁻² (for three electrode) 4.9 F/cm ³ at 0.05 A/cm ³ (for device)	Free-standing film (Thickness 50 μm) with 16 MPa tensile strength	Y. Chen et al., 2015, 287, 68-74
CNT/TiO ₂ /ionomer	85 at 5 mV S ⁻¹	Electrode thickness 110 μm.	C. Huang et al., <i>J. Mater. Chem. A</i> 2014, 2, 11022–11028.

Table 4. 2: Areal capacitance of the supercapacitors reported previously. The areal capacitances from the three-electrode analysis were specified.

mAcm⁻² due to the inefficient interactions with each other (**Figure 4.25b**). Although pristine COFs contain ordered nanopores which enhance the electrode-electrolyte interaction, the hindered electronic movement causes the mitigation in the capacitive performance. Whereas, the lucid electronic movement through the *sp*² C=C framework of the graphene layers of CNF enhance the efficiency of charge storage where the COF and CNF interact with each other.

4.2.8 Supercapacitor studies:

Although the **DqTp-CNF** hybrid has been proved for its good capacitive performance, the further fabrication of the electrode into flexible devices is not recommendable due to the poor mechanical strength of the thin sheet (the breaking is only 1.2% as evaluated from the stress-

strain DMA plot; **Figure 4.22d**). Meanwhile, the **DqDaTp-CNF** displays good mechanical strength of the breaking strain 5.8% due to the existence of anthracene linkers in the framework [4.15]. By taking the advantages of the significant mechanical strength and the energy storage performance of **DqDaTp-CNF** hybrid electrode, we have assembled a symmetric quasi-solid state super-capacitor with hybrid as electrodes and PVA/H₂SO₄ as electrolyte gel. From the Nyquist plot, it is noted that a low cumulative resistance value, i.e., the ESR of 0.2 Ω (**Figure 4.25a**). The redox waves in the CV profile (potential window of 1V) of the device clearly indicate the charge storage behaviour of anthraquinone moiety (**Figure 4.25b**). The areal capacitance had been calculated from the GCDC experiment (160 mFcm⁻² at 0.5 mAcm⁻²) (**Figure 4.25c**). Moreover, we have investigated the long-life cyclic stability of the device for 4500 charge-discharge cycles at a current density of 5 mAcm⁻² which performs the retention of 76% of initial capacitance. (**Figure 4.26c**). The **DqDaTp-CNF** supercapacitor device displays an excellent areal energy density (**Ea**) of 5.8 μWhcm^{-2} and areal power density (**Pa**) of 125.0 μWcm^{-2} at 0.5 mAcm⁻².

4.2.9 Self-charging power-pack

In addition, to step the next level of the advanced flexible mobile electronic systems, we have integrated a supercapacitor-solar cell device, called as self charging power-pack, for the concurrent harvest and storage of energy (**Figure 4.26**). These photovoltaically self-charging (PSC) power-packs have great scientific and technological relevance due to their efficient effective storage of green energy and the miniaturization of electronic equipment. The X-ray tomography of the fabricated self charging power-pack device clearly shows the close packing of the interfaces of supercapacitor electrodes and solar cell (**Figure 4.28**). In this PSC power-pack, the **DqDaTp-CNF** supercapacitor has been assembled with a perovskite solar cell (the power conversion efficiency of 16.7%) (**Figure 4.29a**). The solar cell converts the light energy to the electrical energy under the solar simulator illumination (0.88Sun), which

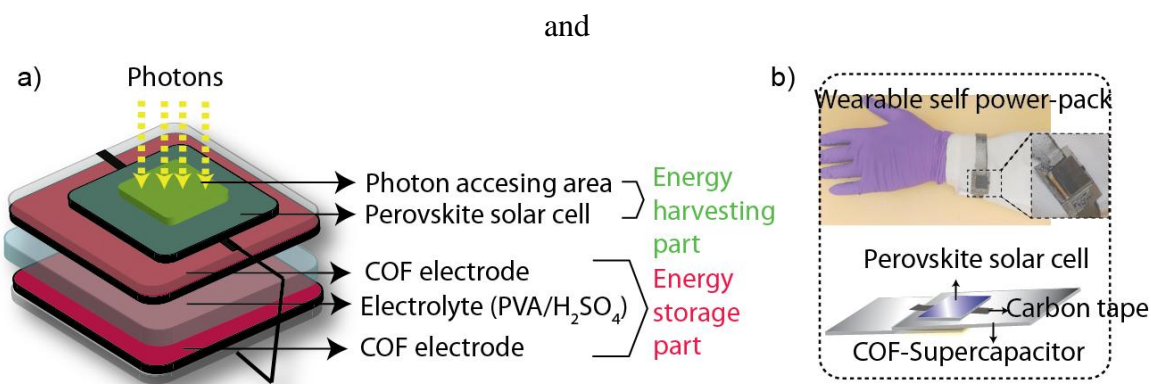


Figure 4.28: a) The diagrammatic representation of self-charging power-pack. b) Digital photograph of the self power-pack device.

in turn, charged (0.8 V within 100 seconds) the supercapacitor device bearing with a geometrical active area of 1.0 cm². Herein, we have analyzed the galvanostatic discharging time of photovoltaically charged the PSC device for 100, 200 and 300 seconds. (**Figure 4.29 b-d**). We could note that a proportional increase discharge time with photovoltaic charging time of the PSC device which indicates the relevance of the device in real-life as wearable

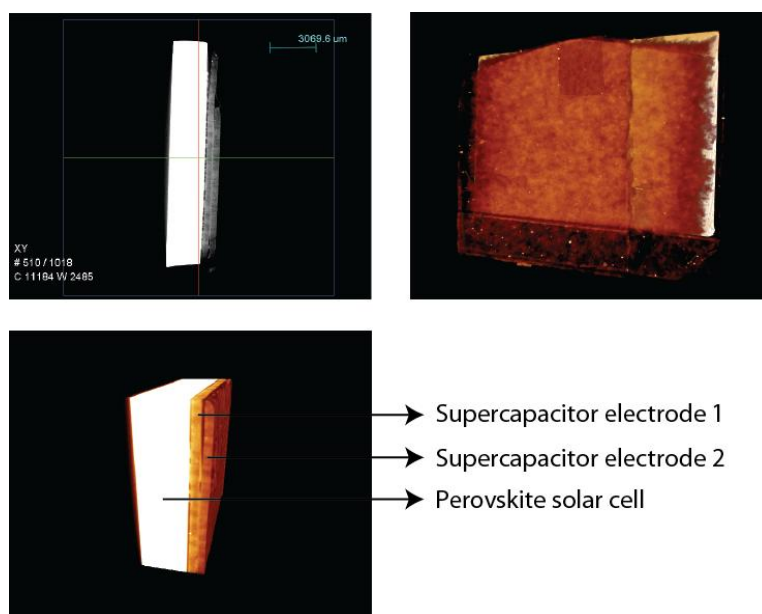


Figure 4.29: The X-ray tomography of self-charging power-pack device.

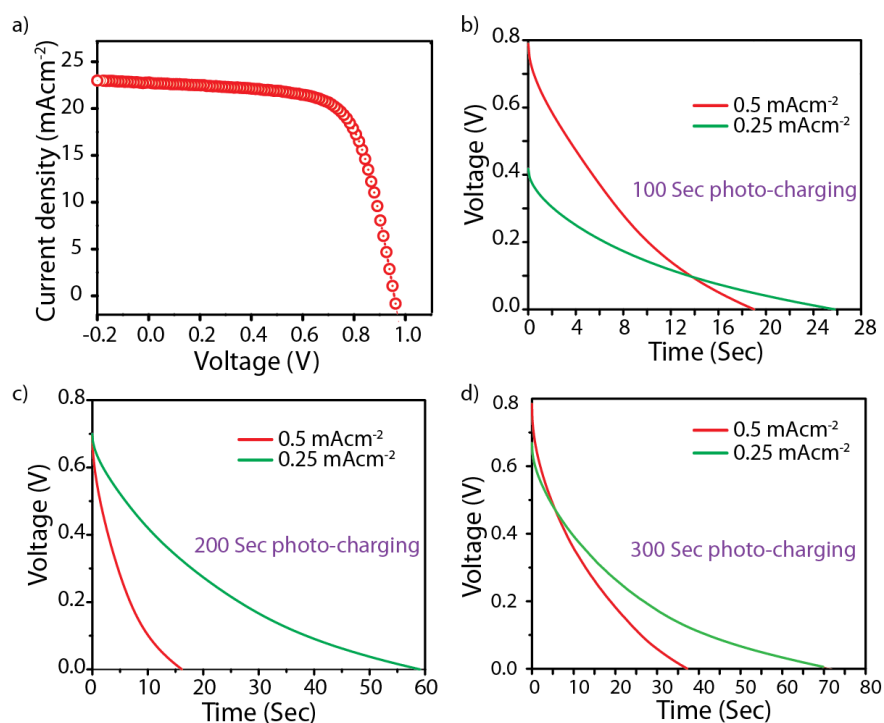


Figure 4.30: a) Voltage-current density curve of the perovskite solar cell. b-d) The discharging curves of supercapacitor in self-charging power-pack in different time photo charging.

electronics. We have also investigated at different current densities (0.25 and 0.5 mAcm⁻²) to calculate the areal capacitance of the supercapacitor device in PSC (42.0 mFcm⁻² areal capacitance at the current density of 0.25 mAcm⁻² for the photo-charging of 300 seconds).

4.3 Conclusion

Herein, we have enhanced the electrochemical performance of 2D macroscopic forms of COF by integrating the CNF into a hybrid matrix through in-situ inclusion. We could observe with the support of DFTB, a significant interaction between COF and graphene layers present in CNF. The synthesized COF-CNF hybrid macroscopic thin sheets were displayed as continuous and crack-free nature with a large areal scalability. Additionally, the COF-CNF hybrids maintain the crystalline and porous nature along with excellent enhancement of electrical conductivity. Taking these into account, the fabricated COF-CNF hybrid supercapacitor exhibits high performance in the capacitance (167 mFcm⁻²). Notably, it has been further ingrated as a self-charging power-pack for the concurrent harvest and storage of energy from light to electrical power.

4.4 Experimental procedures

4.4.1 Materials

1, 3, 5-triformylphloroglucinol (**Tp**) and 2, 6-diaminoanthracene were synthesized from phloroglucinol and 2, 6-diaminanthraquinone respectively by the reference of reported articles [3.14 and 3.15]. Where 2, 6-diaminanthraquinone was purchased from TCI Chemicals.

4.4.2 Synthesis of **DqTp**-CNF hybrid thin sheet:

We have synthesized **DqTp**-CNF hybrid through the solid-state mixing (SSM) of amine and aldehyde linkers in the presence of *p*-Toluenesulphonic acid (PTSA) as a catalyst for imine condensation reaction. Herein, we have taken the amine linker **Dq** (0.6 mmol) and five equivalent of the catalyst PTSA (1.5 mmol) together and then it has been mixed with 50 μ l of water. Consequently, we have added 1,3,5-triformylphloroglucinol (**Tp**, 0.4 mmol) to the precursor mixture and again thoroughly mixed for the next 10 minutes. At last, 20% (the weight percentage of amine and aldehyde were taken for the reaction) of CNF has been added and mixed thoroughly until a black colored paste is formed in the reaction vessel. We have observed a brown colored paste has been formed and which is further coated on a glass slide as thin sheet form ($2.5 \times 8 \text{ cm}^2$) and then thermally treated (120°C) in a closed condition for 24 hours (The thickness has been controlled by varying the area of the glass plate). The thermal treatment of COF precursor paste allows the β -ketoenamine framework formation and the thin sheet stacked on the glass surface was peeled by dipping the glass slides in distilled water. Afterwards, the free-standing COF thin sheet was thoroughly washed with water, DMA and acetone to remove the precursor impurities and PTSA from the material. (Isolated yield: 90%).

4.4.3 Synthesis of **DqDaTp**-CNF hybrid thin sheet:

We have synthesized **DqTp**-CNF hybrid through the solid-state mixing (SSM) of amines and aldehyde linkers in the presence of *p*-Toluenesulphonic acid (PTSA) as a catalyst for imine condensation reaction. Herein, we have taken both amine linkers **Dq & Da** in 0.6 mmol in 1:1 ratio (0.3 mmol each) and five equivalent of the catalyst PTSA (1.5 mmol) together and then it has been mixed with 50 μ l of water. Consequently, we have added 1,3,5-triformylphloroglucinol (**Tp**, 0.4 mmol) to the precursor mixture and again thoroughly mixed for next 10 minutes. At last, 20% (the weight percentage of amine and aldehyde were taken

for the reaction) of CNF has been added and mixed thoroughly until a black colored paste is formed in the reaction vessel. We have observed a brown colored paste has been formed and which is further coated on a glass slide as thin sheet form ($2.5 \times 8 \text{ cm}^2$) and then thermally treated (120°C) in a closed condition for 24 hours (The thickness has been controlled by varying the area of the glass plate). The thermal treatment of COF precursor paste allows the β -ketoenamine framework formation and the thin sheet stacked on the glass surface was peeled by dipping the glass slides in distilled water. Afterwards, the free-standing COF thin sheet was thoroughly washed with water, DMA and acetone to remove the precursor impurities and PTSA from the material. (Isolated yield: 90%).

4.4.4 Three-electrode assembly:

The working electrode for three-electrode configuration has been fabricated from COF-CNF hybrid thin sheets with the area of 1 cm^2 and the thickness $\sim 50 \mu\text{m}$. An electronic screw gauge is used for measuring the thickness for the COF-CNF electrode in every case. Consequently, the COF-CNF electrodes were dipped in 1M H_2SO_4 acid solution for the activation pores prior to the electrochemical analysis. Afterwards, the partially dried COF electrodes were assembled in three electrode system as a working electrode. Herein, we have directly attached the COF-CNF electrode to the crocodile clip of the electrical wire which is aided with a small piece of grafoil for the better electrical contact. Furthermore, $\text{Hg}/\text{Hg}_2\text{SO}_4$ and Pt mesh were taken as reference and counter electrodes, respectively. Cyclic voltammetry (CV) analysis were investigated in a range of scan rate from 10 to 500 mV s^{-1} by optimizing a potential window of 1 V (-0.5 to 0.5V). Additionally, the galvanostatic charge–discharge (GCD) experiments were analyzed at different current densities of 0.25, 0.50 and 1.0 mAcm^{-2} .

Specific capacitance from GCD experiment:

$$C_a = \frac{(I \times \Delta t)}{\Delta V * a} \dots\dots\dots\text{Equation (1)}$$

Where,

C_a = Areal capacitance (mFcm^{-2})

I = Constant current used for charging and discharging (mA)

Δt = Discharge time (sec)

ΔV = Potential window (V)

a = Geometrical area of COF-CNF hybrid thin-sheet (cm^2)

4.4.5 Device fabrication for two electrode experiment:

To fabricate a flexible quasi solid-state supercapacitor, we have used grafoil sheet as a current collector. Two COF-CNF electrodes were dipped in 1M H_2SO_4 acid solution for 1 hour for the activation pores prior to the electrochemical analysis. Then the partially dried COF electrodes (geometrical area-1 cm^2) were pressed on the grafoil sheet and subsequently we have applied a thin coating of PVA- H_2SO_4 gel electrolyte on the surface of the COF-CNF thin sheets. We have fabricated two such electrodes which were act as positive and negative electrodes in symmetric supercapacitor device. Again, a polypropylene porous separator was kept in between these two electrodes and the whole device coated with an insulation cover. Then the assembled flexible devices were subjected to the further electrochemical analysis. Herein, CV analysis were investigated in a range of scan rate from 10 to 500 mV s^{-1} . Moreover, the GCD experiments were analyzed at different current densities of 0.5, 1.0 and 2.50 mA cm^{-2} .

Specific capacitance, energy and power density calculation from GCD experiment:

The single electrode areal capacitance of the supercapacitor device,

$$C_a = \frac{2 \times (I \times \Delta t)}{\Delta V \times a} \dots\dots\dots\text{Equation (2)}$$

Where,

C_a = The areal capacitance (mF cm^{-2})

I = Constant current used for charging and discharging (mA)

Δt = Discharge time (Sec)

ΔV = Potential window (V)

a = Geometrical area of COF thin sheet in one electrode (cm^2)

The energy density and power density of the electrode were calculated by the equations

Energy density (E_d) (mWh cm^{-2}) =

$$\frac{C_a}{8 \times 3.6} V^2$$

.....Equation (3)

Where,

‘Ca’ is the areal capacitance calculated by the charge-discharge (mFcm⁻²) method and ‘V’ is the voltage window.

$$\text{Power density (P}_d\text{) (mWcm}^{-2}\text{)} = \frac{Ed}{t} \text{Equation (4)}$$

Where, ‘E_d’ is the energy density from **Equation (3)** and ‘t’ is the discharge time in hour calculated from the discharge curve.

Calculation of electrical conductivity:

$$\text{Resistance (R)} = \frac{\rho l}{A} \text{Equation (5)}$$

Where, R = Resistance (Ω)

l = Thickness (cm)

A = Area of the COF-CNF hybrid thin sheet (cm²)

ρ = Electrical resistivity (Ω.cm)

$$\text{Conductivity} = \sigma = \frac{1}{\rho} \text{Equation (6)}$$

Where, σ = conductivity (Scm⁻¹)

4.4.6 General methods for characterization

(a) Powder X-Ray Diffraction (PXRD): The PXRD data were investigated on a Phillips PANalytical diffractometer using a Cu Kα radiation (λ = 1.5406 Å), with a scan rate of 2° min⁻¹. The tube current and voltage were optimized at 30 mA and 40 kV respectively. The COF powder was taken in an Aluminium holder and then scanned between 2 and 40° 2θ (step size of 0.02°).

(b) Thermogravimetric Analysis (TGA): TGA was investigated on SDT Q 600 TG-DTA analyzer instrument. 2 mg of the COF sample was placed in an aluminium crucible and heated from 25 to 900 °C under N₂ atmosphere at heating rate of 20 °C min⁻¹.

(c) IR Spectroscopy: The Fourier transform infrared spectra (FTIR) of the COFs were recorded on a *PERKIN ELMER FT-IR SPECTRUM* (Nicolet) spectrometer in ATR mode.

The FTIR profiles were investigated within the range of 4000-600 cm^{-1} .

(d) Gas Adsorption: The N_2 gas adsorption experiments of COF samples were analyzed in an *Autosorb* automatic volumetric instrument (*Quantachrome*) (up to 1 bar). COFs were degassed under vacuum at 120°C for 12 hours prior to the gas adsorption analysis.

(e) SEM: SEM images were recorded with a Zeiss DSM 950 scanning electron microscope and FEI, QUANTA 200 3D Scanning Electron Microscope with tungsten filament as electron source operated at 10 kV. The COF thin sheets were directly mounted vertically and horizontally to SEM sample holder with the carbon adhesive tape. The COF samples were sputtered with Au (nano sized film) prior to imaging by a SCD 040 Balzers Union.

(f) TEM: TEM images were investigated by using FEI Tecnai G2 F20 X-TWIN TEM at an accelerating voltage of 200 kV. To prepare the TEM sample for the analysis, The crushed and ground COF thin sheet samples were dispersed in acetonitrile solvent and drop cast on copper grids TEM Window (TED PELLA, INC. 200 mesh).

(g) ^{13}C CP MAS Solid-state NMR: We have used a Bruker 300 MHz NMR spectrometer, and for quantitative analysis ^{13}C CP MAS decoupled solid state NMR was taken in Jeol 400 with scanning rate 849 and Ligand NMR data were taken in Bruker 200 MHz NMR spectrometer.

(h) Electrochemical analysis: We have carried out every electrochemical measurements like CV and impedance (Electrochemical Impedance Spectroscopic [EIS]) analysis recorded from 10^6 to 0.01 Hz frequency against the open circuit potential (OCP) with a sinus amplitude of 10 mV [$V_{\text{rms}} = 7.07\text{mV}$] and galvanostatic charge/discharge analysis (GCD) were conducted by using a Bio-LogicSP-300 PG Stat instrument. Electrochemical data were analyzed in EC-Lab software **V10.19**

(i) Dynamic Mechanical Analysis: The mechanical strength of the COF thin sheets was performed by the measurement of the Tensile strength on a TA Instruments dynamic mechanical analyzer (DMA, RSA- III). Herein, we have conducted the stretching

investigations by using the rectangular tension geometry for the COF thin-sheets. We have prepared the COF thin sheets in rectangular shapes and then vertically clamped in the DMA instrument. Afterwards, the stretching experiment has been performed with constant rate of 0.1 mm/s. All the DMA were conducted at room temperature (298K). We have calculated the stress-strain plot from the obtained results. Stress – strain Calculation: i.e., the engineering stress (σ_E) has been found by the stretching force (F) divided by initial cross-sectional area (A) ($\sigma_E = \frac{F}{A}$). Again, the engineering strain has been calculated by using this equation: $\epsilon_E = \frac{l - l_0}{l_0}$, where, l is the final length and l_0 is the initial length.

(j) X-ray tomography: 3D X-ray imaging of photovoltaic self-charging power-pack device is investigated by non-invasive X-ray microtomography using Xradia Versa 510 Microscope (Zeiss X-ray Microscopy, Pleasanton, CA, USA).

(k) Solar simulator: The I–V analysis of the perovskites solar cell were investigated by using a Newport solar simulator (with AM1.5G filter) having light intensity of 0.88 sun (calibrated through the Silicon reference cell provided by Newport) connected to the Keithley 2420 I–V measurement system.

NOTE: The experimental observations and results in this chapter have been already published in *ACS Appl. Mater. Interfaces* 2019, 11, 34, 30828–30837; entitled: “*Weak Intermolecular Interactions in Covalent Organic Framework-Carbon Nanofiber based Crystalline, Yet Flexible Devices Organic Framework-Carbon Nanofiber Hybrids for the Efficient Energy Storage.*” The major contribution of this publication was done by the Dr. Rahul Banerjee and his student Abdul Khayum M from *CSIR National Chemical Laboratory, Pune*. The electrochemical analysis were investigated by the collaboration with Dr. Sreekumar Kurungot and his students Vidyanand Vijayakumar and Meena Ghosh from *CSIR National Chemical Laboratory, Pune*.

CHAPTER 5

3D-Printable Covalent Organic Framework Aerogels for Water Purification

Abstract: *The software controlled three dimensional (3D) macro-architecture of functional porous materials gains tremendous scientific and technological attention towards the molecular uptake. Meanwhile, the exceptional intrinsic porous features*



of covalent organic frameworks (COFs) shows excellent molecular uptake through the adsorptive interactions. However, the molecular pollutant uptake from water requires a high exposure of the intrinsic pores towards the external environments for the lucid diffusion of water through the internal porous matrix. In this regard, we have demonstrated the integration of crystalline and porous COFs into template-free 3D printable objects with intrinsic micro- and extrinsic macro porosity. The interconnected 3D openings in these COF aerogels further enhances the rapid and efficient uptake of organic and inorganic pollutants from water (>95% of removal within 1 minute).

5.1 Introduction

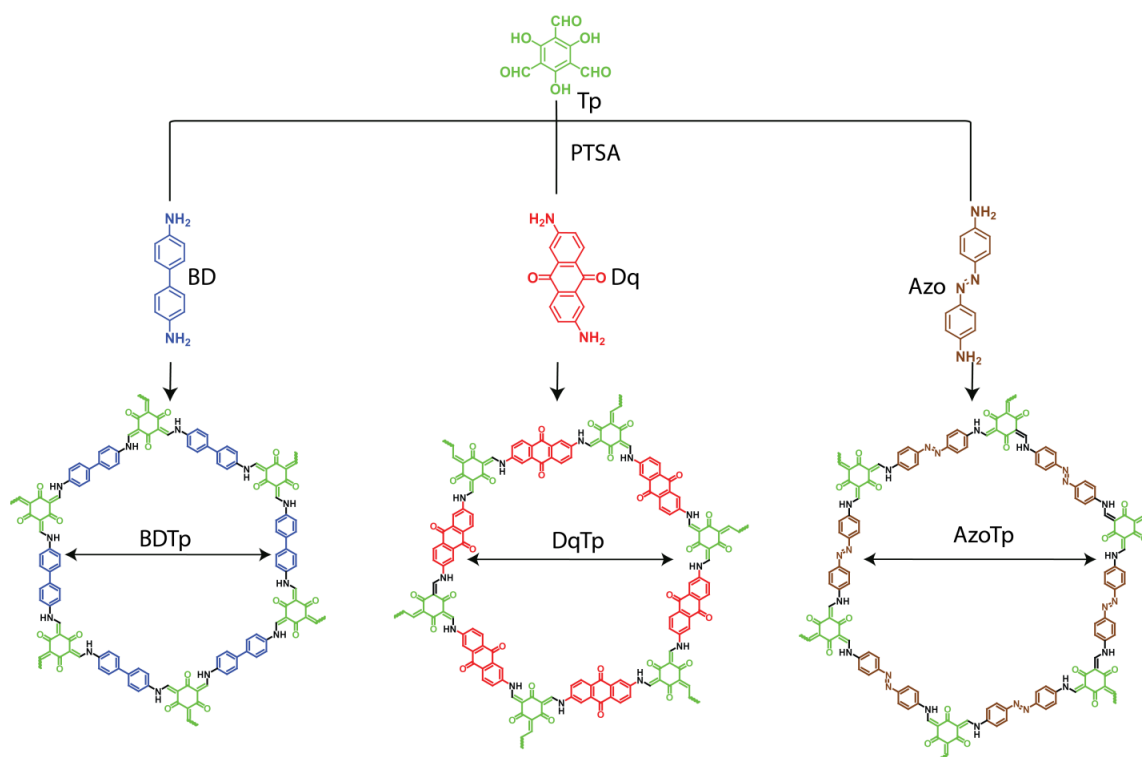
Covalent organic frameworks (COFs) with exceptional intrinsic micro or meso porosity, have been investigated for the successful removal of hazardous chemicals from water by considering both adsorption and separation methods [5.1]. Moreover, the water purification by using COFs is mostly confined either in its powdered form or more advance membrane-based technique [5.2]. However, membrane or thin film based separation techniques are restricted due to the difficulty to maintain the crack-free form, otherwise which resulted poor separation of toxic materials from water. In this regard, the adsorption technique is much more reliable, as a lucid diffusion of guest molecules through the adsorptive matrix can enhance the interaction and promote effective separation [5.3]. However, to facilitate the easy transportation of these big molecules throughout the framework matrix, the intrinsic pores should be interconnected by extrinsic macropores. In this regard, an air-filled macroscopic three-dimensional (3D) monolithic architecture, called aerogels, can be a potential and distinctive adsorbent material for the water purification [5.4]. Notably, graphene; supra-molecular and polymeric based aerogels are developed as benchmark adsorbents [5.5]. However, tunable functionalities; well-ordered nano-pores; and chemical and thermal stabilities into a single aerogel system still remain as an unbeatable challenge. In this perspective, two-dimensional (2D) COFs can be a potential candidate towards the construction 3D macroscopic architecture of crystalline and intrinsic-extrinsic porous aerogels.

Keeping this in mind, to induce the macropores inside bulk monolithic COF, we strategically doped graphene oxides as spacers into the water which contained precursor matrix of COFs. Thus, the obtained COF aerogels after the freeze-drying process exhibit well macroporous structure with a higher fraction of void volume compared to the pristine COFs. Moreover, to take the applicability of these aerogels to the advanced level, it is crucial to control the manipulation of the 3D patterning of the monoliths [5.6].

A brief account on 3D printing:

3D printing is an advanced technology to fabricate the prototypes of the material objects in a fast and low-cost method. Due to the additive manufacturing nature of the 3D printing, it has minimum loss of the precursors material compared to the mould depended object

fabrications. The industrial and academic interest on 3D printing technology leads to the advanced research on the fabrication of both micro and macro level structures. Notably, the applications of 3D printed objects extended to energy storage; various electronic equipments; biotechnology; micro-structuring; purifications; and different macro-structuring. It should be noted that, the progress in 3D printing technology directs the construction of the objects with precisely and incorporate smart functional behavior. Although software controlled 3D printing technology has been widely used for such additive manufacturing, it is mainly limited to the fabrication of graphene-based aerogels and polymers [5.6b]. Moreover, the 3D manufacturing of hierarchical intrinsic and extrinsic porous structures with desired functionalities can be facilitated advanced level applications.



Scheme 5.7: The Chem-Draw image of synthetic scheme of COFs.

In this regard, by taking the advantage of good shear thinning behaviour and controllable viscosity of the COF-GO precursor paste, we have 3D-printed self-supported COF aerogel on the desired shape and size. Again, these COF aerogels had further been used as excellent adsorbents for the rapid purification of water from different organic and inorganic chemicals (~95% removal within less than 1 min).

5.2 Result and Discussion

5.2.1 Synthesis and characterization

In the synthetic process, the COF precursor paste was synthesized from C₃ building units of 1, 3, 5-triformylphloroglucinols aldehyde (**Tp**: 0.2 mmol) and C₂ symmetric amine (**BD**-benzidine/ **Dq**-2,6-diaminoanthraquinone/ **Azo**-4,4'-Azodianiline: 0.3 mmol) in the presence of excess amount of PTSA as catalyst (4.5 mmol) and water (50 μ l) as green solvent (*Scheme 5.1*). It is noteworthy that, the solid-state synthesis of 2D-COFs although provides monolithic and free-standing macroscopic forms, the obtained high-density material suffers several disadvantageous like volume shrinking and subsequent blocking of internal pores. As

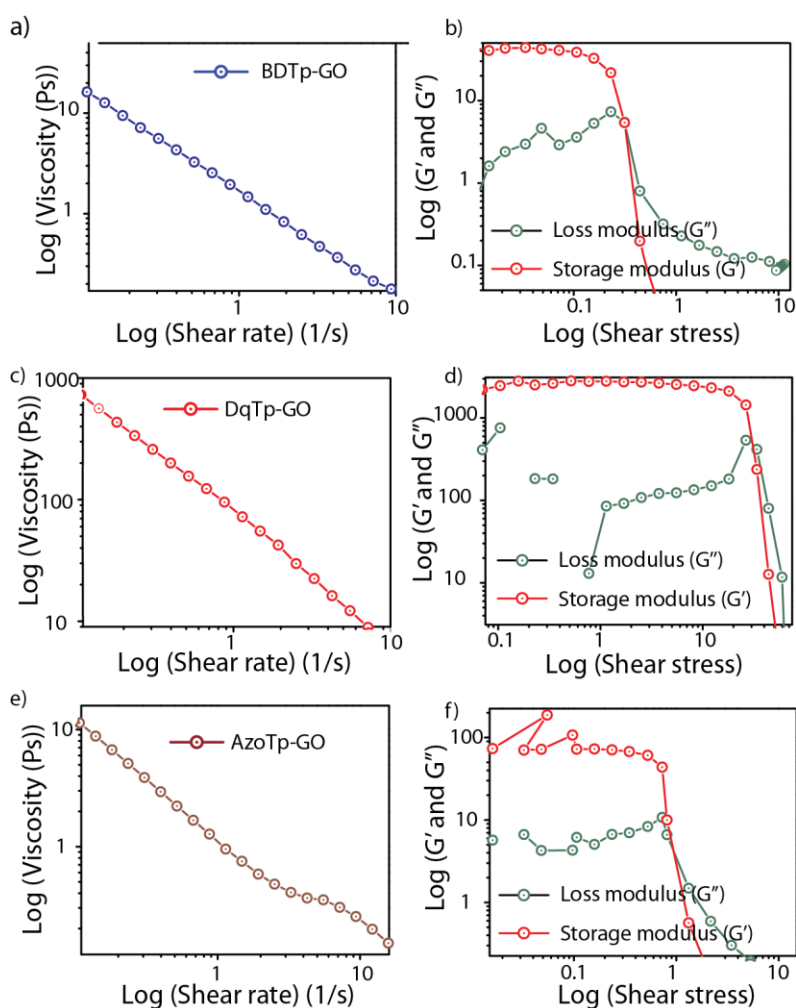


Figure 5.1: The rheology analysis of COF aerogel precursor paste.

To analyze the properties of COF-GO precursor paste as 3D print ink, we have performed the rheological studies of them in different conditions. We have measured the shear rate and then analyzed the viscosity of a flowing precursor paste. The rheological analysis suggests the good shear thinning and viscosity of the COF-GO precursor paste (**Figure 5.1**). In general, a good 3D-print ink should possess the physicochemical properties like suitable viscous

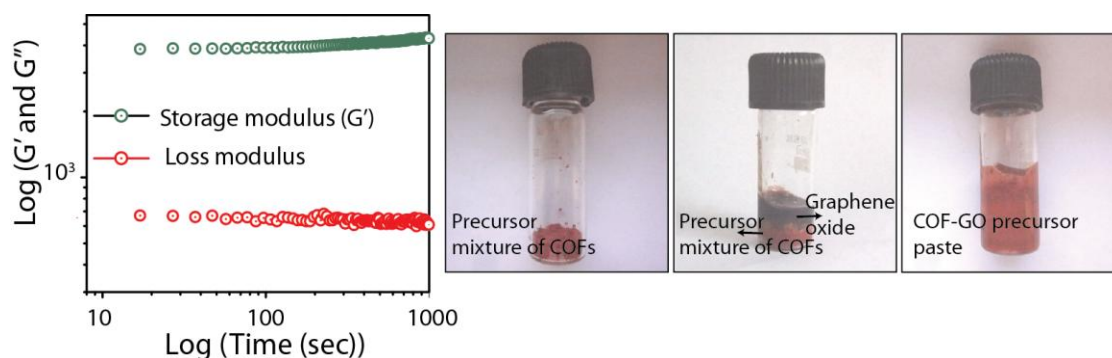


Figure 5.8: a) Rheology analysis of Time Vs Storage and Loss modulus; and b) COF precursor synthesis.

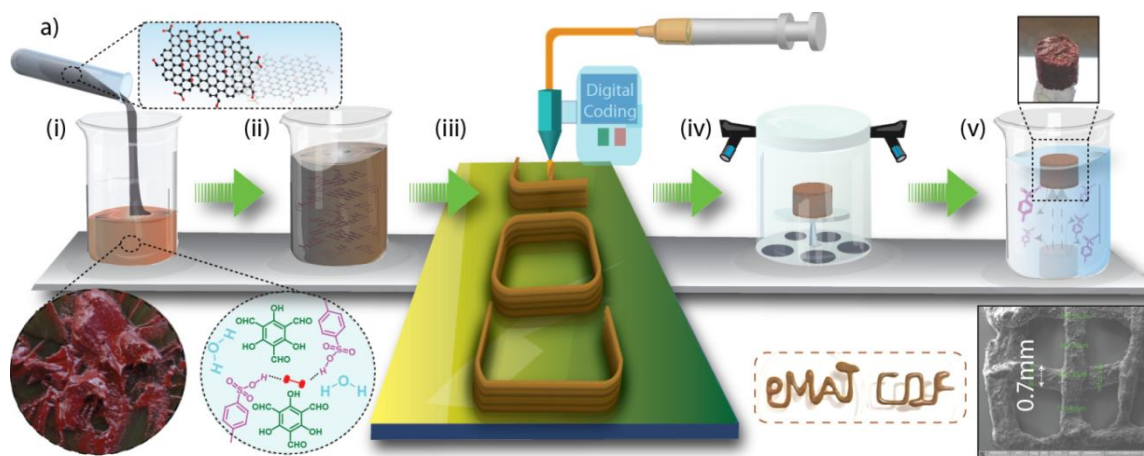


Figure 5.9: The fabrication 3D-printed COF aerogel.

behaviour for the easy flowing of the material under a stress along with good shear thinning nature for the precise printability [5.8]. The presence of graphene oxide aids to form a self-assembled hydrogel which features the inter-molecular hydrogen bonding between GO layers in water. Furthermore, we have investigated any transformation of physical properties like elasticity and viscosity of the precursor paste with time (**Figure 5.2**). The plot of the time (15 min) against storage modulus and loss modulus (G'') clearly indicates the little changes in the

physical property of the paste for a printable time of the concerned material. All these rheological results signify the physical character of the material is suitable for 3D-printing.

5.2.3 3D-Printing of COF aerogel

Keeping the advantageous of good shear thinning behaviour and controllable viscosity of the COF-GO precursor paste, herein, we have 3D-printed self-supported COF aerogel in different shapes includes grids; cubes; and letters by using widely-used software controlled

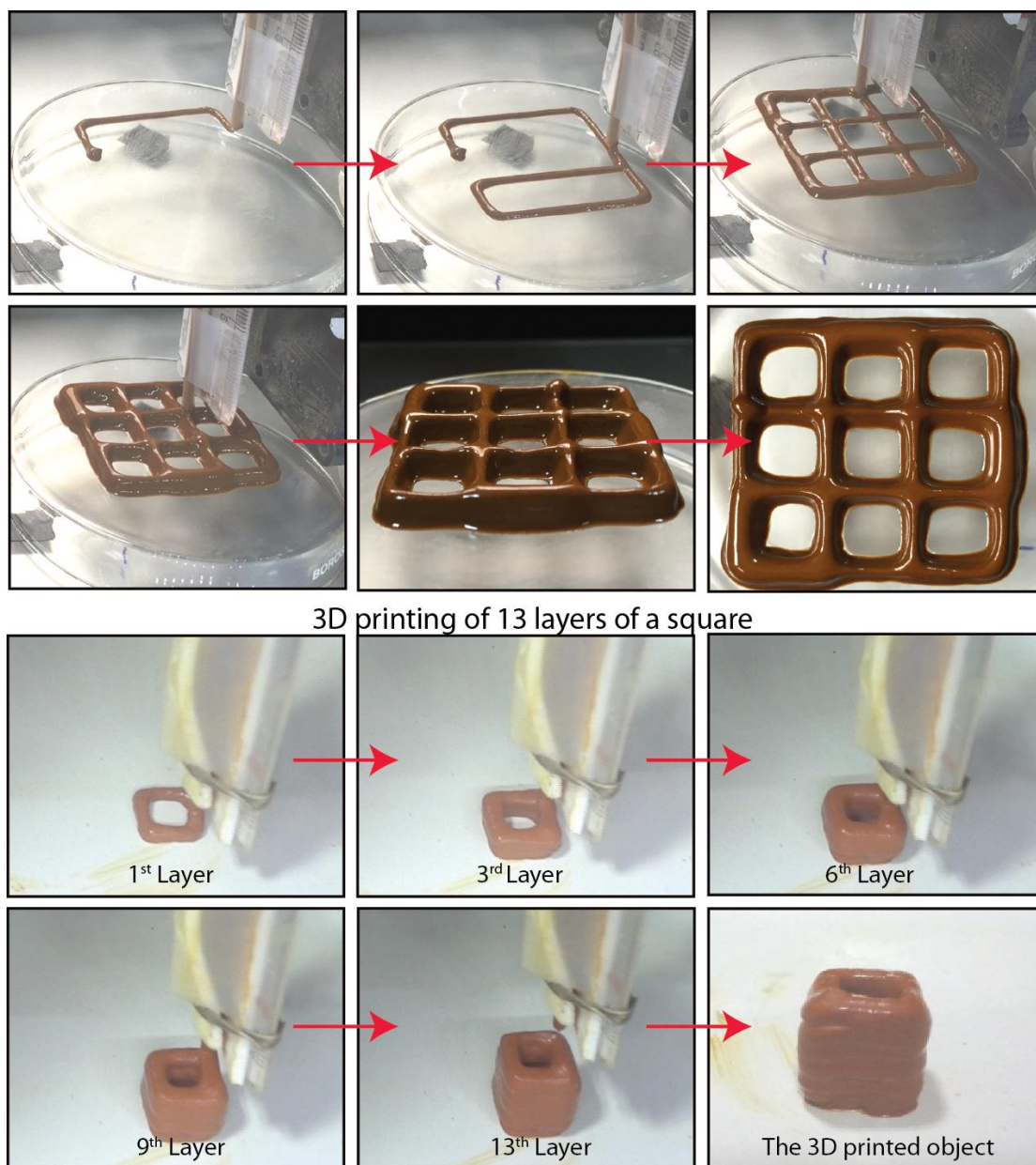


Figure 5.4: a) 3D printing of a nine numbered square grid; and b) 3D printing of 13 layers square object.

FDM 3D Printer (**Figure 5.3** & **Figure 5.4**). The assembly speed was set for 10 mmsec^{-1} to pump 1 ml per minute of the 3D print ink material. It is important to note that we could leverage the printing possibility of aerogel in a layer by layer mode up to 13 layers. Interestingly, it is noted that the structural maintenance of the printed object even after the 13th layer integration. Notably, this could offer the 3D architecting of COF into different shapes. Afterwards, the precursor kept at 90°C at the closed condition for 8-10 hours. During the thermal treatment, PTSA catalyzes the imine

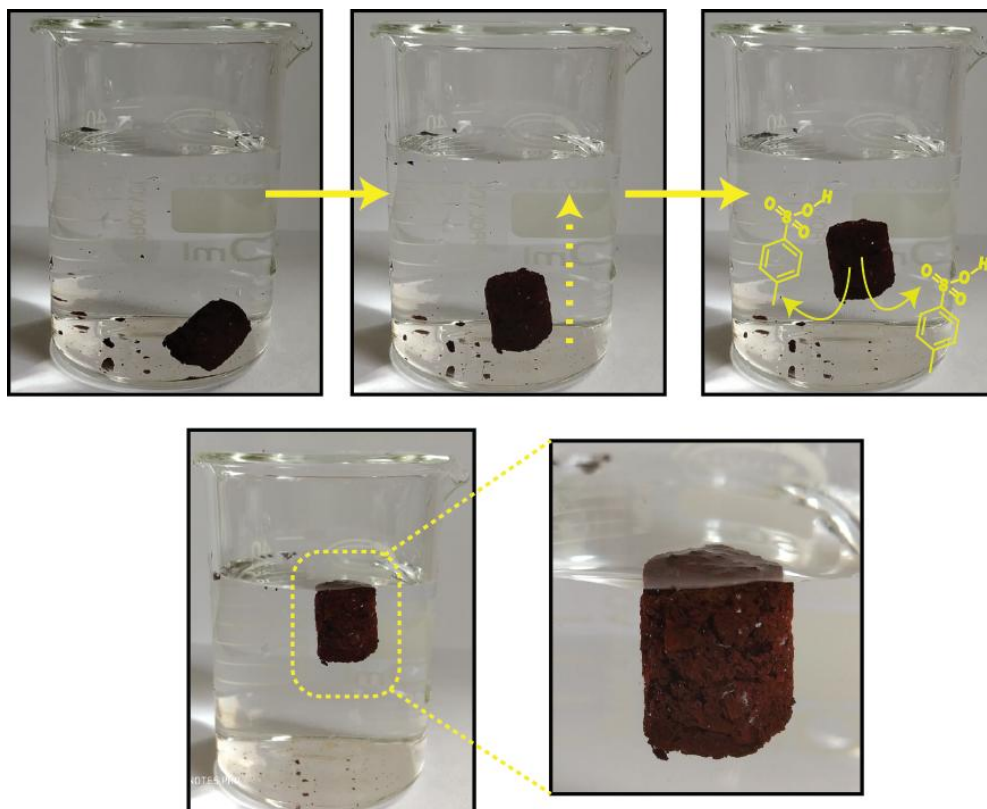


Figure 5.5: The COF aerogels are floating in water after the removal of PTSA.

bond formation between the organic building units and subsequent formation of β -ketoenamine COF after the π - π interaction of each framework layers [5.9]. The 3D network of GO maintains the volume of the aerogel matrix by providing enough intrinsic space for the growth of COF. After the thermal treatment, to remove water, the COF-GO hybrid is treated for freeze-drying process (**Figure 5.3**). The obtained dried monolith exhibits a physical nature of very hard and heavy in mass due to the excessive content of PTSA which is washed with water and again subjected to freeze-drying process. It is worth mentioning that once PTSA is getting removed, aerogel became light-weight and floated in water (**Figure 5.5**).

Additionally, after the freeze-drying, the COF aerogel becomes soft and light-weight in nature along with well maintain its porosity and crystallinity in 3D shapes.

5.2.3 The structural characterizations

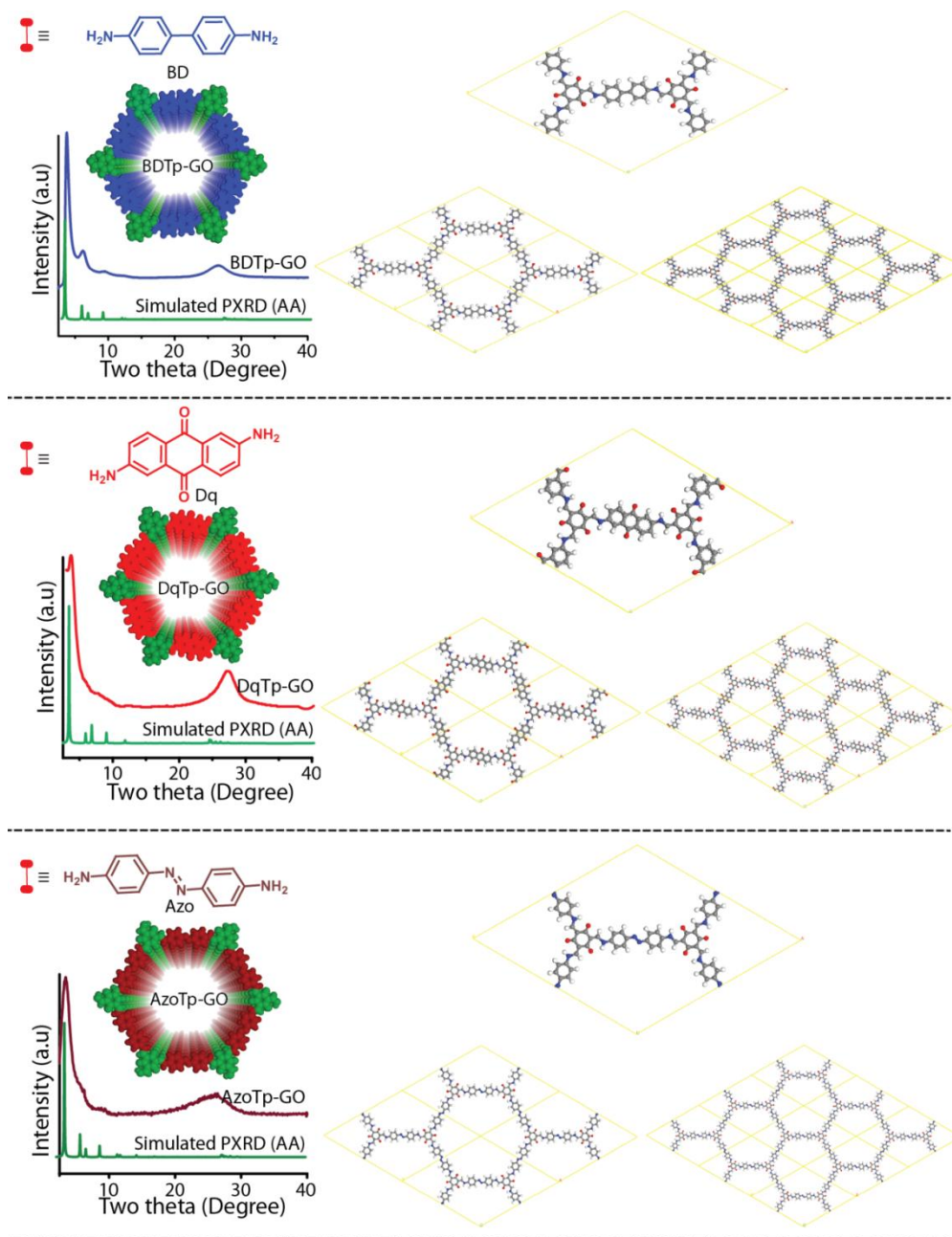


Figure 5.6: The comparison of the experimental PXRD of COF aerogel with simulated AA eclipsed PXRD and their corresponding models.

The crystallinity of COF aerogels was investigated by the PXRD analysis. The PXRD profiles of all COF aerogels exhibit a crystalline pattern and matched well with the simulated PXRD of pristine COFs thus indicating the formation of a regular π - π stacked framework

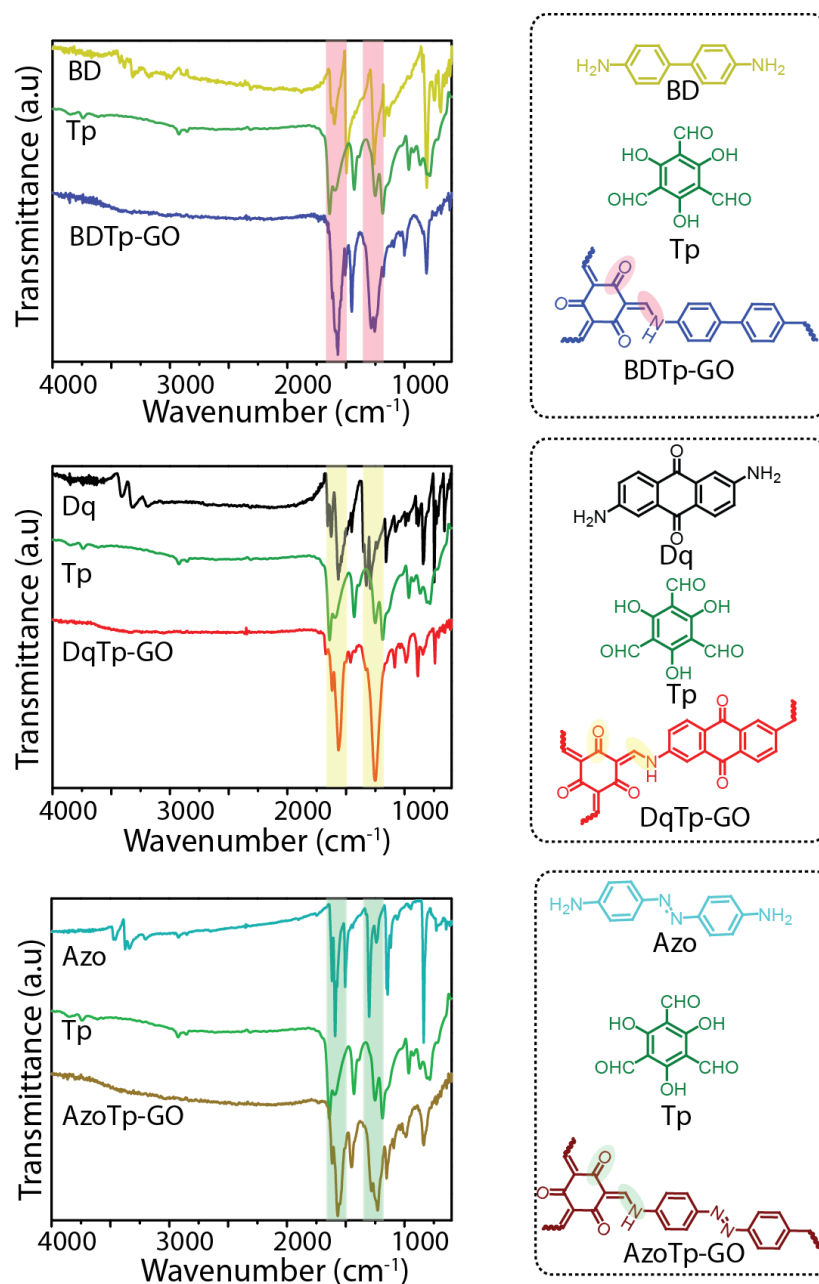


Figure 5.7: The IR spectra of COF aerogels with the monomers.

structure (**Figure 5.6**). The first intense peak originated from 100 planes diffracted at the 2θ angle 3.8° , 3.7° , 3.5° (2θ) correspond to the COFs **BDTp-GO**, **DqTp-GO**, and **AzoTp-GO** respectively. A weak and broad peak is visible at angle 26 - 27° (2θ) which signifies the π - π

stacking of hexagonal COF layers in the aerogel matrix. Again, a weak and merged peak is appeared at 2θ angle $5-6^\circ$ for each COF in PXRD profile. The FT-IR spectroscopy has been performed for checking the bond formation in the framework.

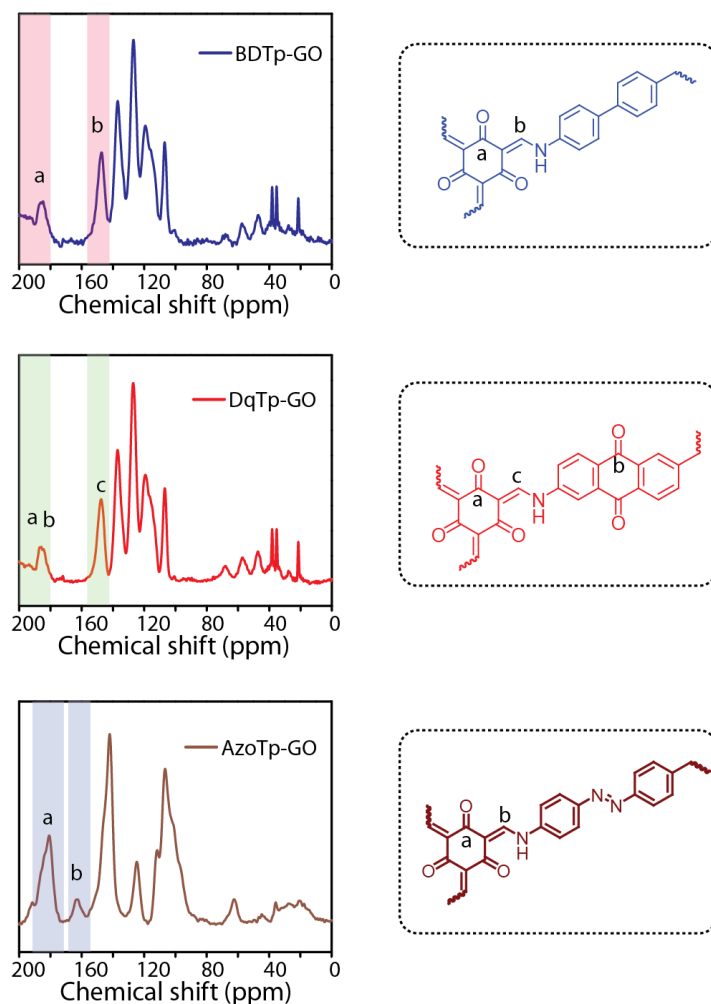


Figure 5.8: The ^{13}C CP MAS Solid-state NMR of COF aerogels.

It displays the formation of C=C ($1560-1570\text{ cm}^{-1}$); C=O ($1590-1620\text{ cm}^{-1}$); and C-N ($1220-1250\text{ cm}^{-1}$) stretching frequencies which are originated from β -ketoenamine framework of each COFs (**Figure 5.7**). Moreover, the FT-IR profiles of each COF aerogel suggest the materials are free from the presence of starting materials. Again, the atomic level constructions of COF aerogels were analyzed by ^{13}C solid-state NMR spectroscopy (**Figure 5.8**). A broad peak resonance at $183-186\text{ ppm}$ for all COF aerogels represents the carbon atom from C=O functionality originated during β -keto-enol tautomerism. Again, the COF

aerogels display the enamine and α -enamine carbon positioned at 146-147 and 107 ppm respectively.

5.2.4 Properties of COF aerogels

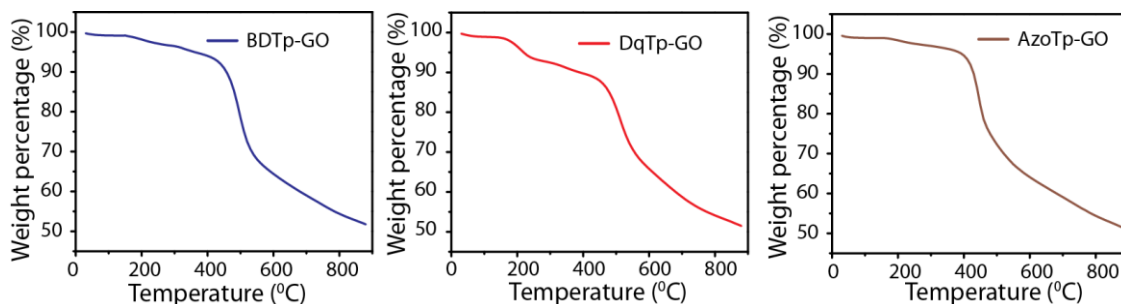


Figure 5.9: The TGA curves of COF aerogels.

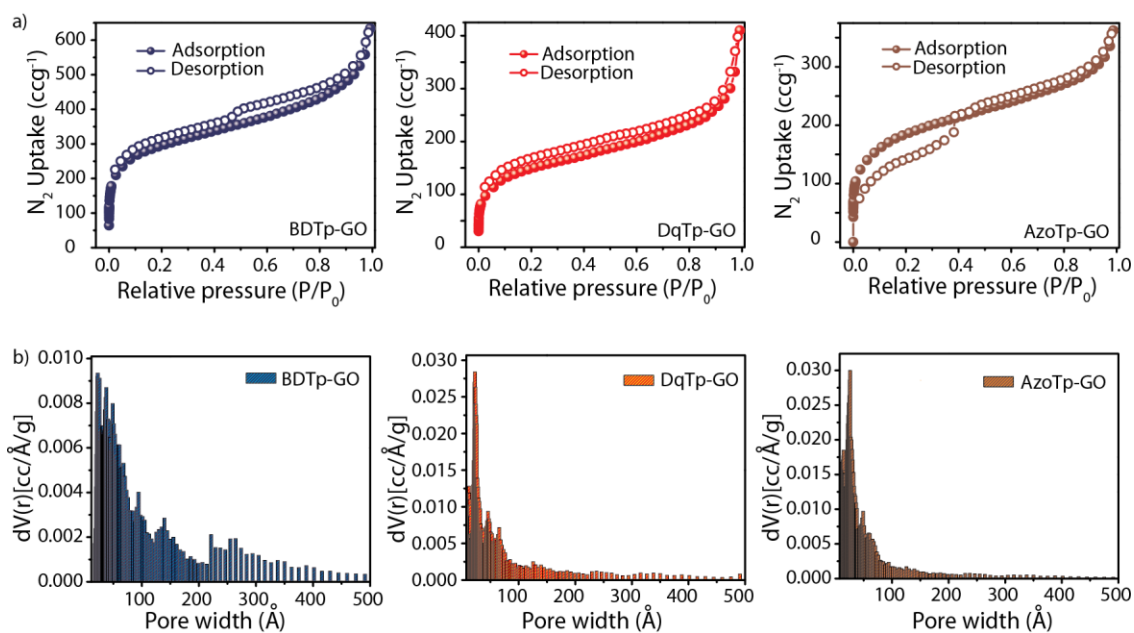


Figure 5.10: a) N_2 Gas adsorption analysis; and b) NLDFT pore size distribution of COF aerogels.

Additionally, the TGA analysis under N_2 atmosphere displayed thermal stability of COF aerogels up to 400°C with 90% of the retention of mass (**Figure 5.9**). The slight weight-loss from 200°C - 400°C of aerogels could be due to the thermal degradation of oligomers present inside of the COF matrix. To investigate the porosity and surface area of COF aerogels, we have analyzed N_2 adsorption isotherm at 77K after activating the samples at 130°C under vacuum. It showed a typical type II isotherm which represents the microporous nature of the COFs confined in aerogels. It has been noted with a typical type II isotherm represents the

microporous nature of the COFs in aerogels. **BDTp-GO**; **DqTp-GO**; and **AzoTp-GO** show the BET surface area of 971; 500 and 624 m^2g^{-1} respectively. Furthermore, the pore size distribution (~ 2 nm) of COF aerogels have been detailed in the NLDFT profiles. Whereas, the small hysteresis loop in each isotherm could be an indication of the extrinsic mesoporous nature of the typical 3D-architected aerogels.

5.2.5 The Morphology of COF aerogels

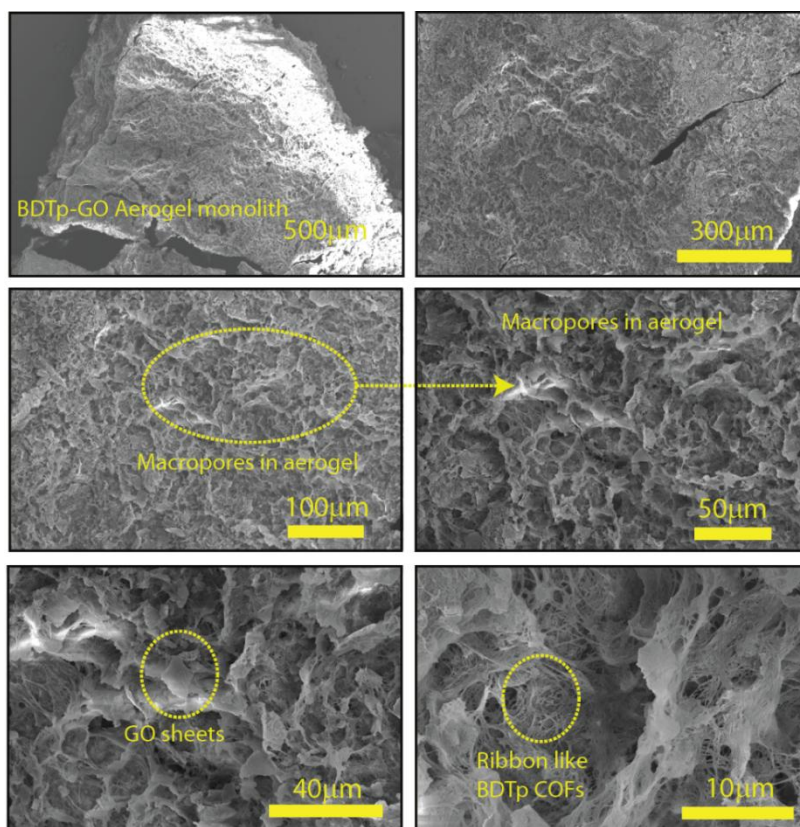


Figure 5.11: The SEM images of **BDTp-GO** aerogel.

The tailored micro and nano level assembly of all COF aerogels have been revealed through scanning electron microscopy (SEM) and transmission electron microscopy (TEM). The 3D construction of macropores is clearly visible in the SEM images of **BDTp-GO** aerogel (**Figure 5.11**). Additionally, a diligent observation of the SEM images clearly displays the presence of several macropores ranging from 5-100 μm which is believed to originate from the doped graphene oxide flakes confined within the aerogel matrix. Along with the GO which has a sheet-like morphology, the inside of the macropores have been occupied with the nanometer-sized ribbon like **BDTp** COFs. Whereas, the COF crystallites present in the

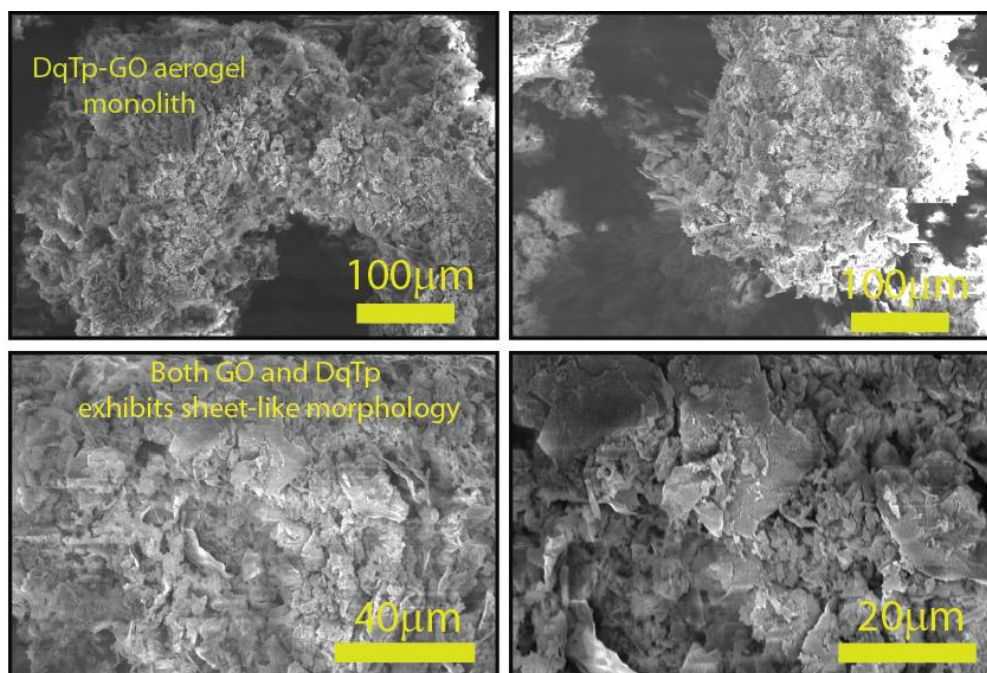


Figure 5.12: The SEM images of **DqTp-GO** aerogel.

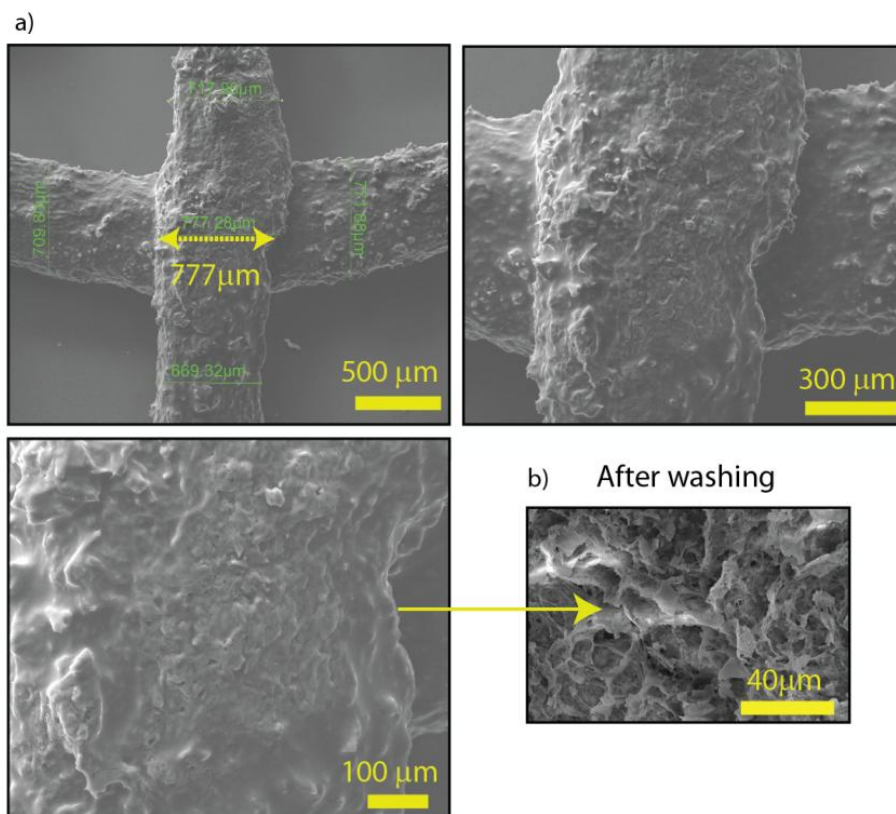


Figure 5.13: The SEM images of **BDTp-GO** before and after washing with water.

DqTp-GO aerogel matrix exhibit a sheet-like morphology with macropores ranging between 5-100 μm (**Figure 5.12**). However, the lateral size of the COF nanoflakes are much shorter (1-2 μm) compared to several tens of micrometer-sized graphene oxide. Furthermore, we have 3D printed a small grid of **BDTp-GO** on the top of a glass surface to analyze the resolution of the printed material. We have performed the SEM image of the four square grid sample without washing and found to be the maximum resolution of $\sim 700 \mu\text{m}$ thickness (**Figure 5.13**). To get the insight of the nano-level construction of aerogel, we have also recorded the TEM images (**Figure 5.14**). To prepare the sample, we have dispersed the aerogels in acetonitrile solvent and then drop cast on Cu TEM grid. TEM images display the

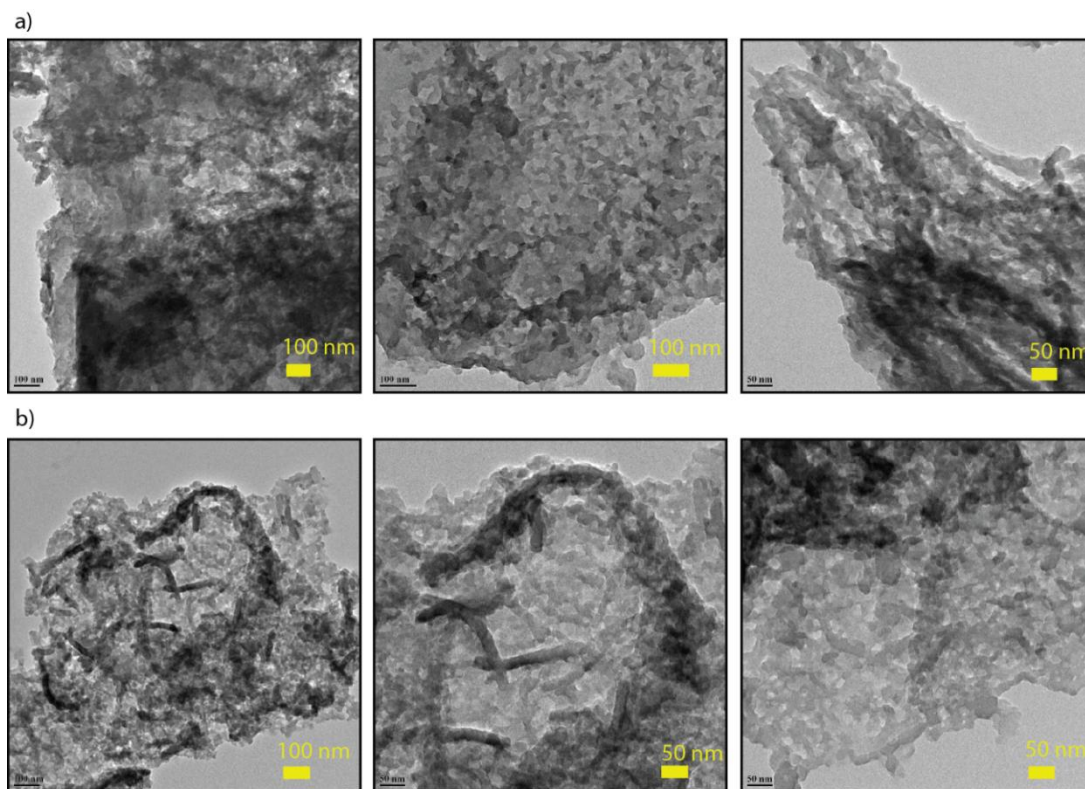


Figure 5.14: The TEM images of a) **BDTp-GO**; and **DqTp-GO**.

morphological features of COF along with the GO layers with large lateral sizes. Notably, due to the inter disconnection of the particles, it seems difficult to visualizing the macropores inside the aerogel matrix. However, it has been observed that the mesopores are well arranged from 2-50 nm associated with the self-assembling of the COF crystallites. Again, the confocal microscopic images display the well-interconnected porous crystallites of aerogel with respect to a non-porous self-assembly structure associated with the pristine

COFs. Herein, we have performed the confocal fluorescent microscopic 3D imaging of COF aerogels for substantiating the porous features of the synthesized materials. The observation of **BDTp-GO** and **DqTp-GO** powder aerogels after staining with fluorescent Rhodamine B (RhB) solution suggests a scattered particle morphology of both materials which contains many micrometer sized pores. Specifically, in **BDTp-GO**, the particles size is too small compared to **DqTp-GO**. Meanwhile, the particles in the pristine COFs are more closely packed compared to the aerogels. The numbers of bigger pores present in the pristine COFs are very less, especially for close-packed sheet morphology of **DqTp**.

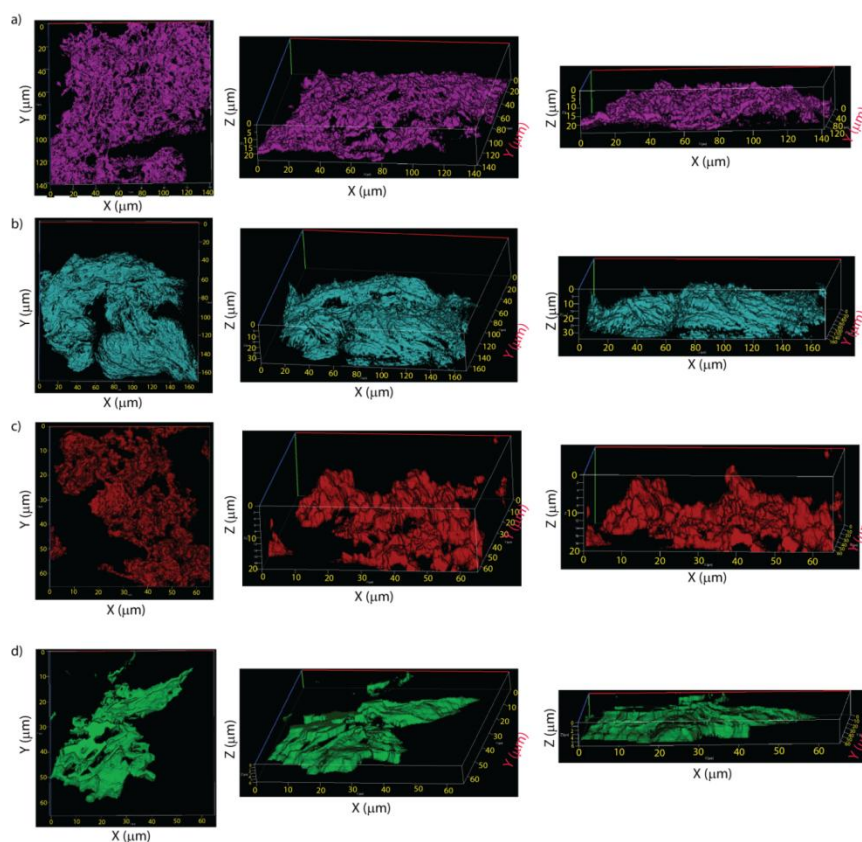


Figure 5.15: Fluorescent microscopic images of COF aerogels and pristine COFs: a) **BDTp-GO**; b) **BDTp**; c) **DqTp-GO**; and d) **DqTp**.

Furthermore, to get the true 3D image of the monolith aerogels, we have analyzed the concerned monoliths in X-ray micro tomography instrument (**Figure 5.17**). As expected, it provides the three-dimensional morphology of the aerogel mostly exhibited in the micrometer range. **BDTp-GO** and **DqTp-GO** were considered as illustrative examples for the tomographical analysis. Notably, it distinctively proved the 3D interconnected macropores inside aerogel matrix. The vertical and horizontal cross-sectional view of the 3D image

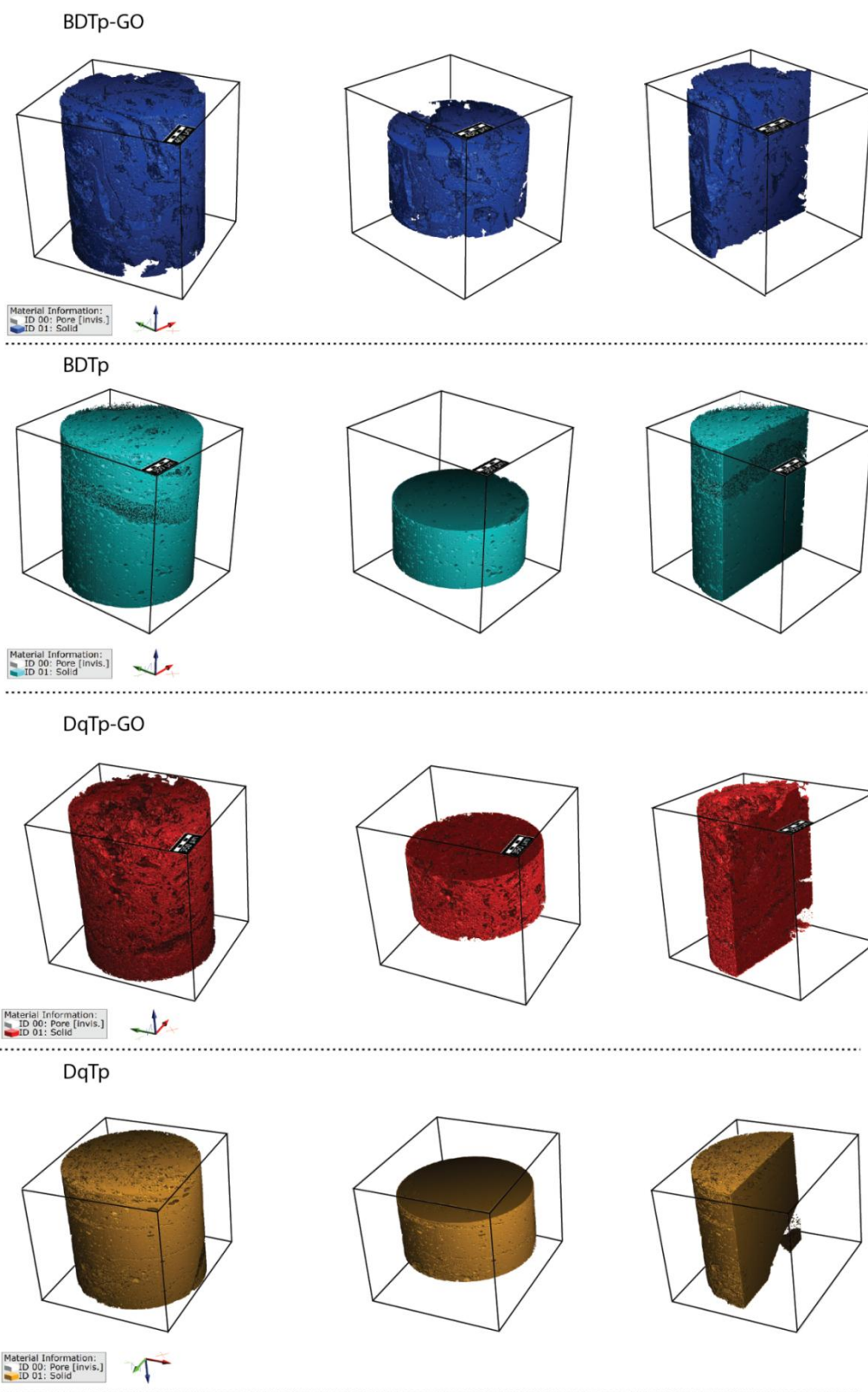


Figure 5.16: The X-ray tomographic 3D images of COF aerogel and pristine COFs.

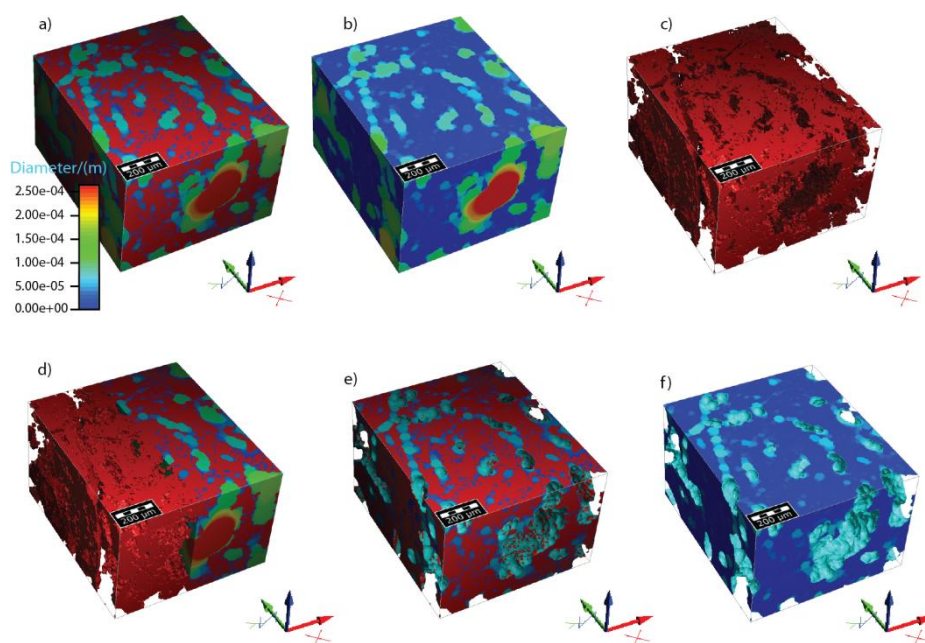


Figure 5.17: The X-ray tomographic 3D images of macroporous structure of **BDTp-GO** aerogel.

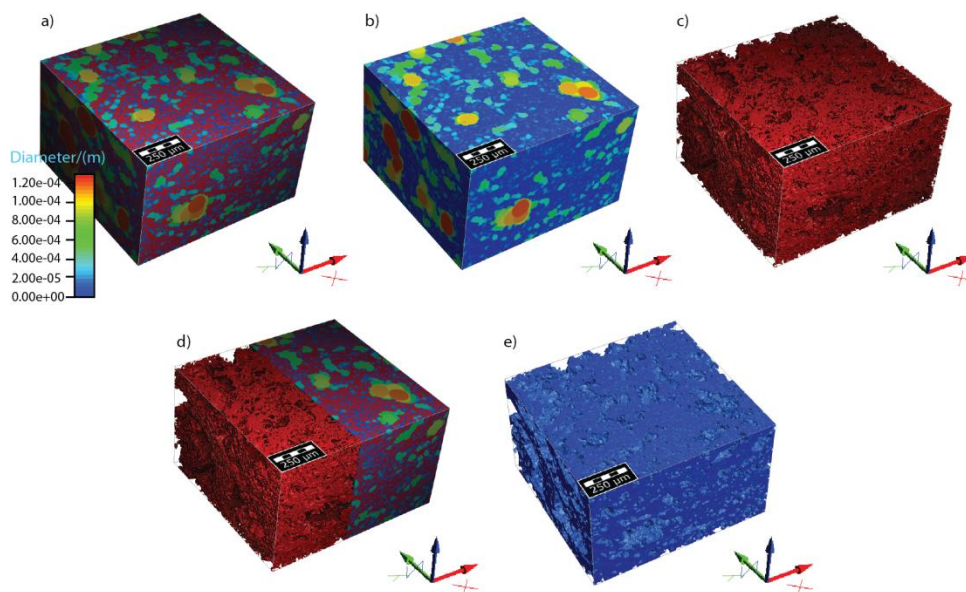


Figure 5.18: The X-ray tomographic 3D images of macroporous structure of **DqTp-GO** aerogel.

of the aerogels displays the presence of macropores not only on the surface but also in the entire aerogel matrix. Moreover, the **DqTp-GO** is associated with more number of smaller size such as 20% of the pores with a diameter of 9-11 μm pores outside as well as inside of the matrix compared to **BDTp-GO** which exhibit only 7% of the pores with a diameter of 9-

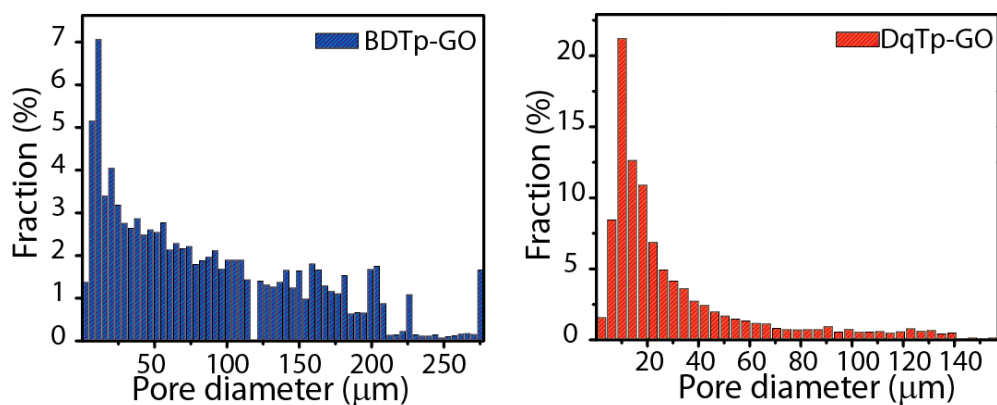


Figure 5.19: The X-ray tomographic calculation of pore size distribution of COF aerogels in the μm range.

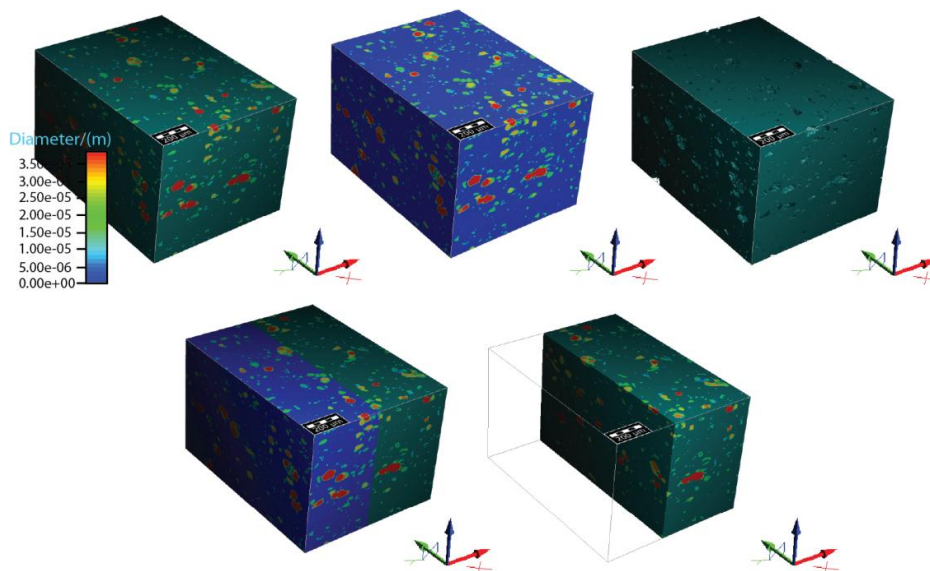


Figure 5.20: The X-ray tomographic 3D images of macroporous structure of pristine **BDTp** COF.

11 μm (**Figure 5.18** & **Figure 5.20**). Additionally, we have performed the tomographical analysis for the pristine COF monoliths to validate the potential structural importance associated to COF aerogels. Notably, the 3D tomographic image of pristine COF display nonporous solid structures and the inter-connected macropores were not visible in the pristine COF matrix (**Figure 5.21**). Therefore, it proves the simple solid-state synthesis of COF majorly provides a non-macroporous dense structure associated with only the intrinsic microporosity.

In order to get the deep understanding of the inter-connected macroporous character of the aerogel, we have analyzed the pore size distribution of the matrix. The calculation of pore

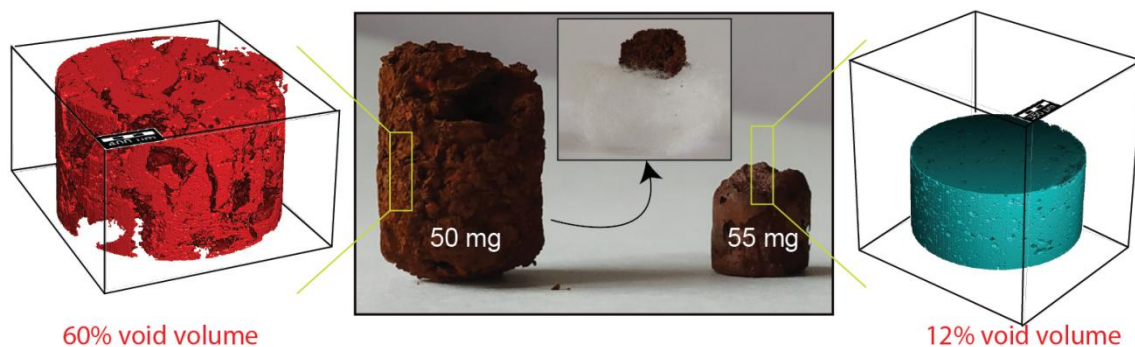


Figure 5.21: The macroscopic features COF aerogel and pristine COF.

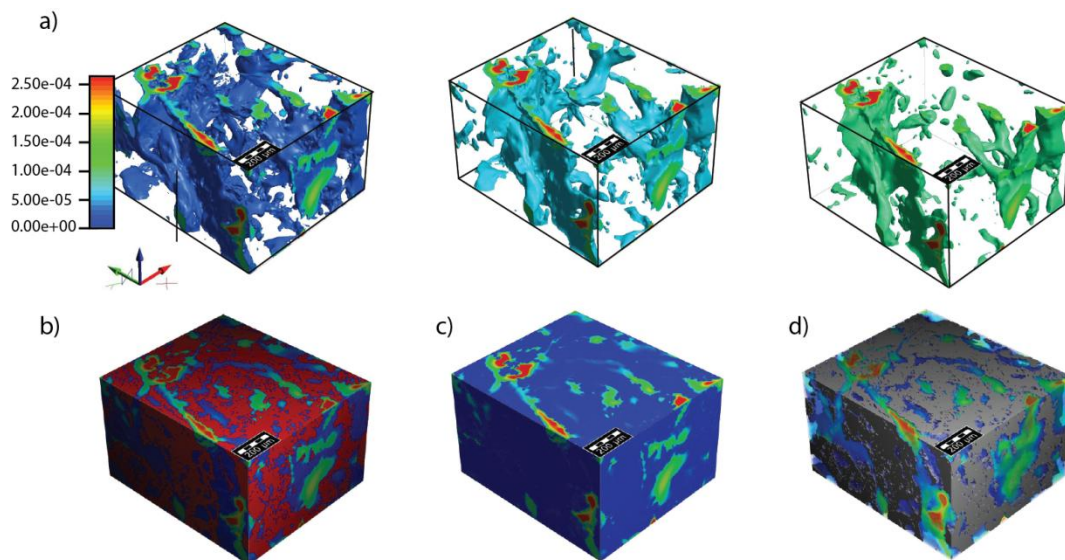


Figure 5.22: The X-ray tomographic water flow analysis of **BDTp-GO**.

size is done by considering the pores as spheres which are fitting into the empty volume of the aerogel (**Figure 5.19**) The **BDTp-GO** aerogel exhibits 55% of macroporous volume in the entire matrix which very larger than the corresponding **BDTp COF** (11% of the macroporous volume). In addition, the 90% of the macropores are less than 188 μm in diameter. Wide range diameters (30-180 μm) of 3D interconnected macro-pores are present in the **BDTp-GO** aerogel. Meanwhile, the 90% of the pristine COF contains only the macropores up to 37 μm in diameter. Furthermore, **DqTp-GO** aerogel provides 74% of the macro-porous

volume of the entire matrix. Out of this porous volume fraction, 90% of the macropores are in the diameter up to 80 μm . The strategic incorporation of the higher fraction of the macroporous volume in the COF aerogel aid the effective access of the adsorbent active sites

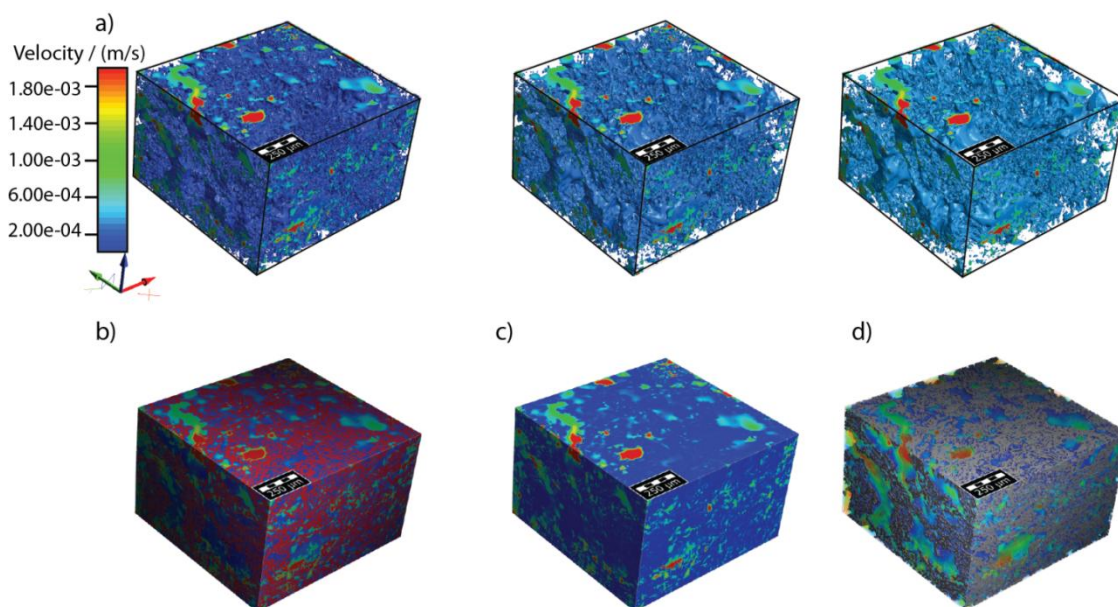


Figure 5.23: The X-ray tomographic water flow analysis of **DqTp-GO**.

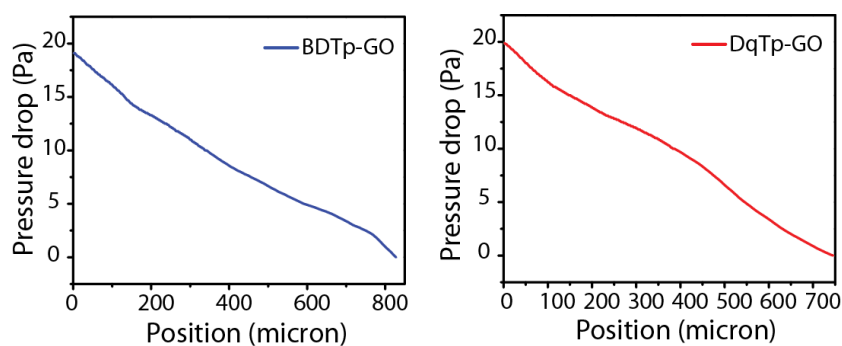


Figure 5.24: The X-ray tomographic water flow analysis plot of 'Position Vs Pressure drop' of COF aerogels.

in the COF crystallites. Whereas, from the pore size distribution analysis of pristine COF suggests the fewer number of macropores in the monolith blocks the passage of solvent and the most possible way is the meso and ordered micro-pores inside the aerogel. The **figure 5.22** explains how the induced void volume inside COF matrix helps for increasing the size of the macroscopic object. The X-ray tomography suggests the void volume of **BDTp-GO**

aerogel is 60% to the total volume of the material. Whereas, in the pristine, the void volume is only up to 12% only. The fraction of this void is reflected in the size of 50-55 mg of the aerogel and their corresponding COF.

5.2.6 COF aerogel for micropollutants removal

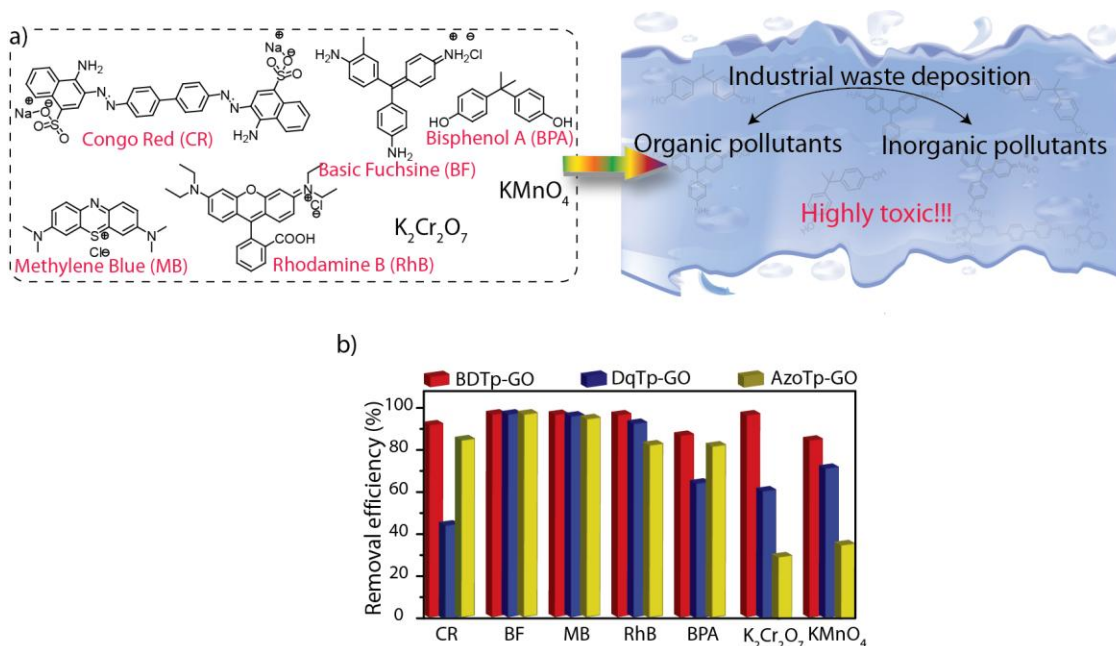


Figure 5.25: a) The organic and inorganic micropollutants; and b) The bar diagram of the efficiency of the removal each micropollutants by using COF aerogels.

The porous aerogel matrix has further been used as the adsorbents of inorganic and organic chemicals from water. The COF aerogel gets into the interaction with adsorbate molecules during the water (containing different pollutants) flow through the entire porous matrix. As a result, we could observe a rapid adsorption (>90% in less than 1 min time) of seven different pollutant chemicals from water into the COF-GO aerogels (**Figure 5.26** & **Figure 5.27**). We have introduced herein all three different COF aerogels (**BDTp-GO**, **DqTp-GO**, and **AZOTp-GO**) for the adsorption of methylene blue (MB); congo red (CR); Rhodamine B (RhB); Basic Fuschin (BF); Bisphenol-A; $KMnO_4$; and $K_2Cr_2O_7$ as different chemical pollutants. The **BDTp-GO** performs rapid uptake of >80 % all these chemicals within 1 min. It should be noted that **BDTp-GO** adsorbs 95% of the organic dye MB from the water just in 5 seconds, which indicates the rapid diffusion and subsequent adsorption of MB in the COF matrix. We have noted the similar for other dyes too, especially a highly toxic organic

pollutant BF which has been removed >99% in 30 seconds time of adsorption. At the same time, **DqTp-GO** adsorbs BF; MB; and RhB >90% from the water. The similar removal efficiency of BF, and MB was also observed for **AzoTp-GO** aerogel as adsorbent. Again, very high uptake of 196 mgg^{-1} has been observed for BDTp-GO aerogel as adsorbent even in high concentration

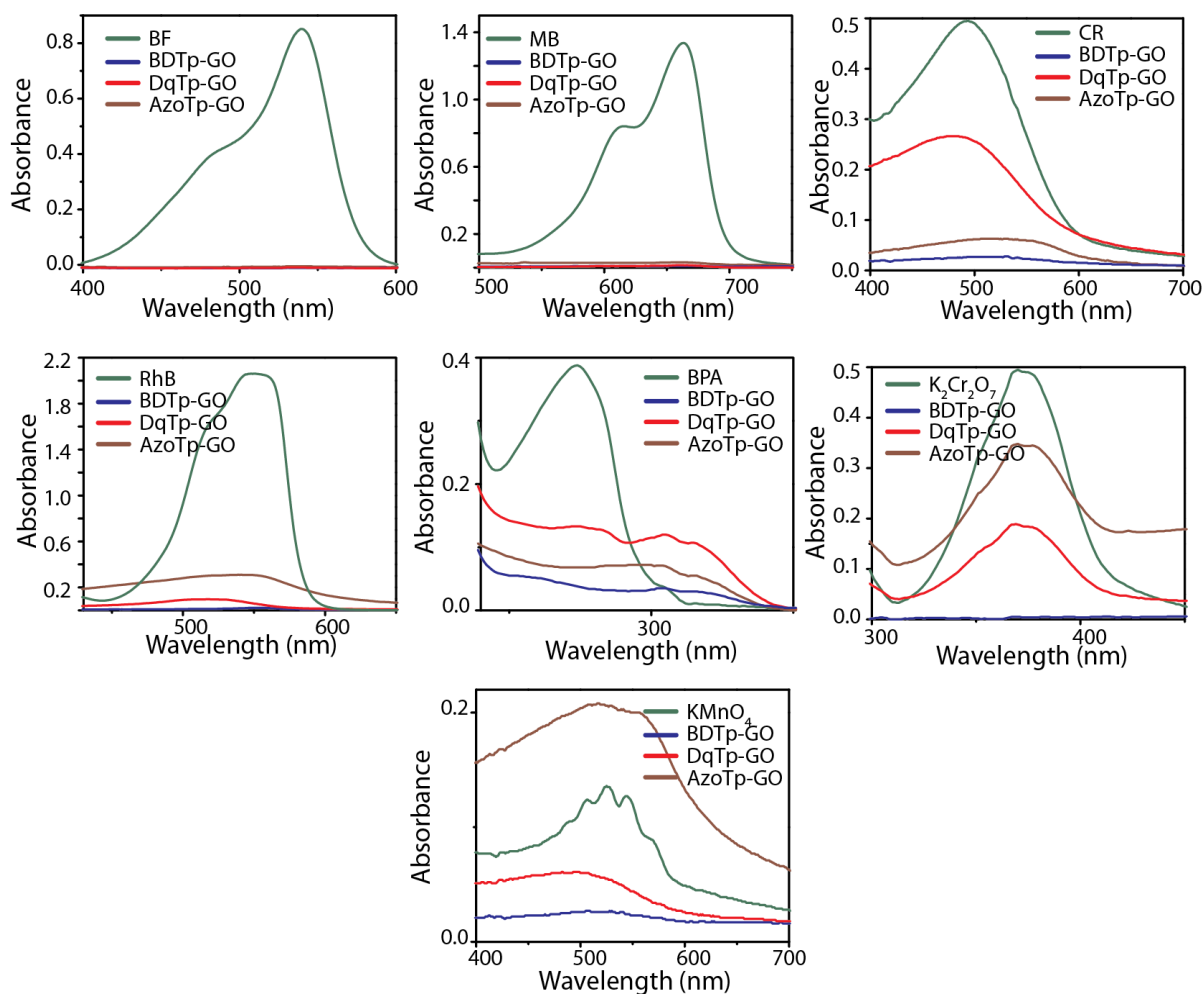


Figure 5.26: The UV spectroscopic characterizations the adsorption properties of COF aerogels.

solution of MB ($1000 \mu\text{m}$) with the removal efficiency as high as 65%. We have also performed the uptake study of dangerous plastic pollutant such as BPA in water [5.10]. Notably, **BDTp-GO** aerogel performs an excellent uptake of 156 mgg^{-1} of BPA with the removal efficiency exceeds 85%. The rapid and efficient removal of various organic and inorganic pollutants in water signifies the macroporous matrix decorated with intrinsic micropores of COF aerogels enhances the potential adsorptive capacity. The water flow

analysis in Flow-Dict software provides the velocity distribution of water in COF-GO aerogel under a pressure drop (**Figure 5.24 & Figure 5.25**). The water accessibility into the inner core of the aerogel matrix suggests the maximum possible solid (COF-GO)-pollutant solution interaction.

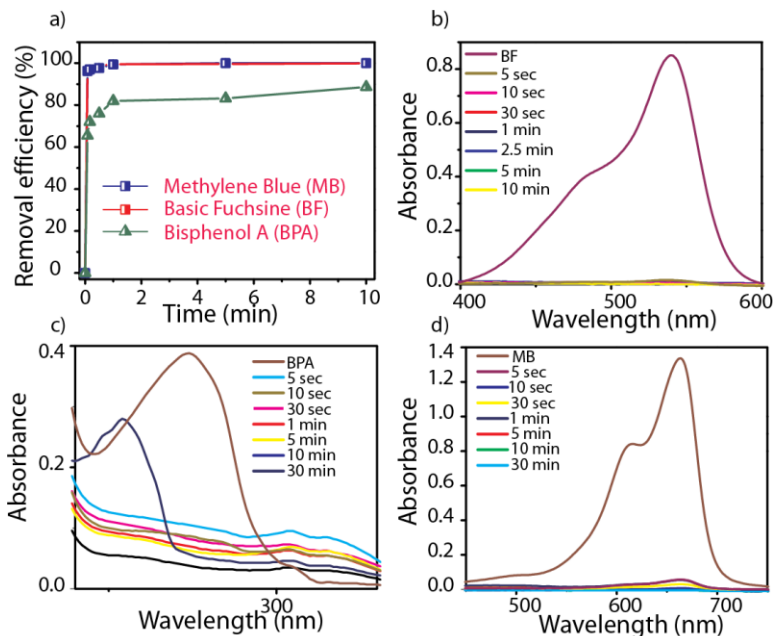


Figure 5.27: The Kinetic study of micropollutant removal from water.

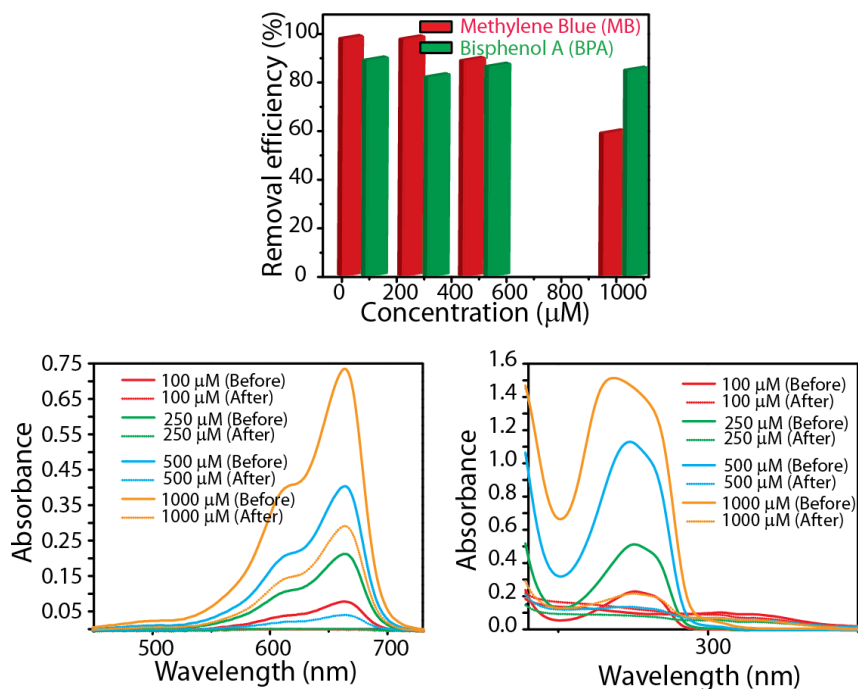


Figure 5.28: The concentration study of micropollutant removal from water.

We have performed the kinetic study of the adsorption of three different organic micro pollutants (MB; BF and BPA) in water by using **BDTp-GO** aerogel (*Figure 5.28*). It suggests the uptake of >95% of pollutants within 5 seconds. Whereas, the **BDTP-GO** adsorbed 65% of the BPA within 5 seconds. Again, we have tested the adsorption capacity of

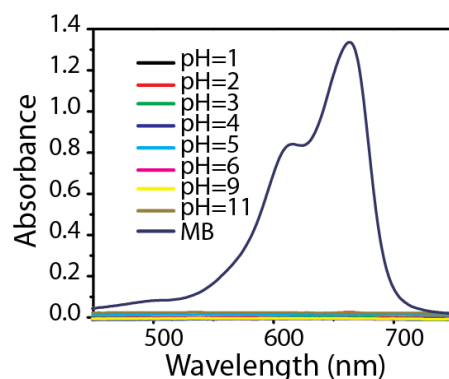


Figure 5.29: The pH study of micropollutant removal from water.

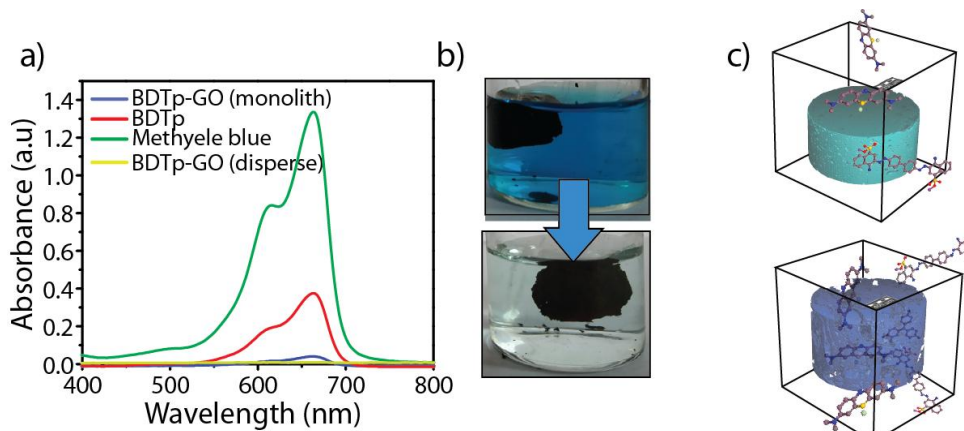


Figure 5.30: a) The UV spectra of COF aerogel adsorption; b) The digital photograph of COF aerogel adsorption of MB; and c) The diagrammatic representation of the interaction of micropollutant with the 3D tomographic images of COF aerogel and pristine.

BDTP-GO towards MB and BPA pollutants (*Figure 5.29*). We have taken 100; 250; 500; and 1000 μm concentration of pollutants in water. Notably, the **BDTp-GO** has adsorbed ~99% of lower concentration (100 and 250 μm) and 90% uptake at 500 μm concentration. Similarly, for BPA, we could observe more than 85% of uptake even at high concentrations. Furthermore, the adsorption analysis of BDTp-GO aerogel of MB at various pH (calculated

from 1 to 13) display an excellent rapid and efficient uptake (>99% in less than a minute) signifies the potential utility of material under real-life conditions (**Figure 5.30**). Again, the excellent recyclability (5 times) of **BDTp-GO** aerogel for MB dye indicates the pollutants are only physically adsorbed and they can be desorbed back from the surface of aerogel upon treatment with an organic polar solvent. As a proof of concept, we have used the 3D printed monolith of **BDTp-GO** aerogel for the adsorption of MB from water. The COF aerogel could take 99% of the MB from water within 10 hours. Whereas the pristine COF monolith exhibits only 40% of the uptake after 10 hours which indicates the potential applicability of monolithic COF aerogel for water purification in a simple dipping method. Additionally, it can avoid any the tedious separation process of the adsorbents dispersed in water.

5.3 Conclusion

In summary, the strategic inclusion of macro-pores by means of GO as spacers in a COF matrix creates crystalline and porous aerogel. The good shear-thinning and optimum viscosity of the precursor paste allow us to perform the software controlled 3d printing of the concerned material in different shapes and multiple layers. Moreover, the interconnected macroporous matrix decorated with intrinsic micropores shows an excellent adsorption capability of pollutants from water. We believe, the blending of advanced 3D printing of aerogel can pave as a leading water purification material in the industrial level in future.

5.4 Experimental procedures

5.4.1 Materials

1, 3, 5-triformylphloroglucinol (**Tp**) was synthesized from phloroglucinol and all other chemical were purchased from *sigma-aldrich* and *TCI chemicals*.

5.4.2 Synthesis of COF aerogels

We have prepared the precursor paste of **COF** aerogels through the solid-state mixing (SSM) of amine and aldehyde linkers in the presence of *p*-Toluenesulphonic acid (PTSA) as a catalyst for imine condensation reaction. Herein, we have taken the amine linker (**BD**; **Dq**; and **Azo**: 0.6 mmol) and 15 equivalent of the catalyst PTSA (9 mmol) together and then it has been mixed with 50 μ l of water. Afterwards, we have added 1,3,5-triformylphloroglucinol (**Tp**, 0.4 mmol) to the precursor mixture and again thoroughly mixed

for next 10 minutes. Again, 15% (We have dispersed 120 mg of GO in 7.5 ml water and the 15% of weight percentage of amine and aldehyde were taken for the reaction) of graphene oxide dispersion in water has been added and mixed thoroughly until a brown colored hydrogel is formed in the vessel. This precursor paste has been used for 3D printing process. After the 3D printing, the material was subjected for thermal treatment at 60° C for 8-12 hours under closed condition. Again, the obtained material is undergone for freeze-drying process in lyophilization instrument. After freeze-drying, the COF was observed as very hard and brittle due to the presence of PTSA. We have dipped the COF in water and removed PTSA from the material. During PTSA was come out from the COF and dissolving water, COF was floated in water layer. Again, the COF was subjected to freeze-drying process and the obtained material was low-weight aerogel (Isolated yield: 80-90%).

5.4.3 Water purification

We have taken pollutants in 5 ml of water with different concentration (50 μM ; 100 μM ; 250 μM ; 500 μM ; and 100 μM) and 5 mg of COF aerogel was used for the adsorption studies. We have dispersed the aerogel into pollutant solution and separated through a filter paper which is separating COF only. The filtered solutions were subjected to UV spectroscopy analysis to find percentage of dye removal from water.

To study the kinetics, we have analyzed the adsorption of 50 μM concentration of pollutants with 5 mg of COF aerogel in water. In order to perform this, we have prepared 100 μM pollutant in 5 ml water. Then, we have added 2.5 ml of this prepared solution into 2.5 ml of water which contained 5 mg of aerogel. Then we have stirred the solution and perform the experiment by using a stop watch.

The pH variation analysis has been by taking 50 μM concentration of MB solution and 5 mg COF in different concentration of HCl. We have prepared pH = 1; 2; 3; 4; 5; and 6 by varying the concentration HCl in 5 ml of water. Again, pH = 9; and 11 have been made by varying the concentration of NaOH in 5 ml of water. Then, 50 μM concentration of MB was added. Afterwards, we have performed the adsorption studies.

To understand the adsorption properties of aerogel monolith; we have directly dipped the 50 mg of COF aerogel monolith into the 50 μM MB in 5 ml water. Afterwards, we have simply removed the aerogel from water and rest solution was carried for further UV analysis.

5.4.4 General methods for characterization

(a) Powder X-Ray Diffraction (PXRD): The PXRD data were investigated on a Phillips PANalytical diffractometer using a Cu K α radiation ($\lambda = 1.5406 \text{ \AA}$), with a scan rate of 2° min^{-1} . The tube current and voltage were optimized at 30 mA and 40 kV respectively. The COF powder was taken in an Aluminium holder and then scanned between 2 and 40° 2θ (step size of 0.02°).

(b) Thermogravimetric Analysis (TGA): TGA was investigated on SDT Q 600 TG-DTA analyzer instrument. 2 mg of the COF sample was placed in an aluminum crucible and heated from 25 to 900°C under N_2 atmosphere at heating rate of $20^\circ \text{C min}^{-1}$.

(c) IR Spectroscopy: The Fourier transform infrared spectra (FTIR) of the COFs were recorded on a PERKIN ELMER FT-IR SPECTRUM (Nicolet) spectrometer in ATR mode.

The FTIR profiles were investigated within the range of $4000\text{-}600 \text{ cm}^{-1}$.

(d) Gas Adsorption: The N_2 gas adsorption experiments of COF samples were analyzed in an Autosorb automatic volumetric instrument (*Quantachrome*) (up to 1 bar). COFs were degassed under vacuum at 120°C for 12 hours prior to the gas adsorption analysis.

(e) SEM: SEM images were recorded with a Zeiss DSM 950 scanning electron microscope and FEI, QUANTA 200 3D Scanning Electron Microscope with tungsten filament as electron source operated at 10 kV. The COF samples were sputtered with Au (nano sized film) prior to imaging by a SCD 040 Balzers Union.

(f) TEM: TEM images were investigated by using FEI Tecnai G2 F20 X-TWIN TEM at an accelerating voltage of 200 kV. To prepare the TEM sample for the analysis, The COF Samples were dispersed in acetonitrile solvent and drop cast on copper grids TEM Window (TED PELLA, INC. 200 mesh).

(g) ^{13}C CP MAS Solid-state NMR: We have used a Bruker 300 MHz NMR spectrometer, and for quantitative analysis ^{13}C CP MAS decoupled solid state NMR was taken in Jeol 400 with scanning rate 849 and Ligand NMR data were taken in Bruker 200 MHz NMR spectrometer.

(h) 3D Printer: 3D printing is an additive manufacturing technique wherein the material is deposited layer by layer to create the desired shape object. We have used the Fused Deposition Modeling (FDM) printer for the printing of COF aerogels. Upon thermal treatment, the aerogel solidifies and maintains the shape given. In this work, we customized the widely-used FDM 3D printer to meet our requirements. An external syringe pump (HOLMARC Syringe Pump HO-SPLF-2) was used to pump the material till the printer bed for printing. The pump was connected to the printer assembly head through a commercially available flexible silicon tube. The final print resolution is governed mainly by the diameter of the tube. In this work, we used a tube with an internal diameter of 1.5 mm. The pumping flow rate and the assembly movement speed are the critical parameters for the best print. The optimum values of pumping rate and assembly speed should be maintained. Higher material pumping rate compared to the assembly movement leads to local accumulation of material which is undesirable. Also, higher assembly speed relative to the material flow leaves unfilled spaces in the object. The material was pumped at 1 ml/min and the assembly speed was set at 5 mm/s for good synchronization. Another critical parameter that governs the smooth printing process is the viscosity of the material. Very high viscosity of the material leads to high pressure drop in the flow channel leading to undesirable rupture of the tube at the weakest joint. Too low viscosity leads to spreading of the material after deposition on the bed or on previous layers which affects the spatial resolution of the object.

(h) Confocal laser scanning microscope: (CLSM) (Zeiss, Oberkochen, Germany Model LSM 710) has been used for background-free high resolution images of COF aerogels and pristine COFs. The instrument has EC Epiplan-APOCHROMAT objective of 50X magnification and a numerical aperture of 0.9. Fluorescence from the sample was excited with the 488-nm line of an Argon laser. The fluorescence was separated from the excitation light by band pass sliders (493 nm-619 nm) in front of spectral detectors. The microscope objective has been attached to an opto-electronically coded focus z-driver to scan the objective along the vertical z direction and produce three dimensional images. A pinhole was used to reject the out-of-plane light for background rejection hence better signal to noise ratio. We typically acquired 150–200 sliced stacks of 512 X 512 pixel images in the horizontal x–y plain separated by 0.25 μm in the z direction. The length of the full-sized field of view is approximately 283 μm and a depth approximately 40 μm . The images were

processed using the Zen software (Zeiss, Oberkochen). Images of each plain were converted to 2.5 dimensional (2.5D) images to understand the absorbed dye intensity profile on the S5 surface and internal microspores (graphical illustration of intensities per pixel for each plain using grayscale).

(h) X-ray tomography: We have characterized the 3D images COF aerogels by using X-ray microtomography of Xradia Versa 510 X-ray Microscope (Zeiss X-ray Microscopy, Pleasanton, CA, USA). The aerogels were directly placed to the sample holder for the analysis which is in between the X-ray source and detector assembly. Detector assembly consists of a scintillator, objective lens and a CCD camera. X-ray source is ramped up to 80 kV and 7 W. The tomographic image acquisitions were completed by acquiring 3201 projections over 360° of rotation with a pixel size of 2.25 microns. In addition, projections without the samples in the beam (reference images) were also collected and averaged. Filtered back-projection algorithm is used for the reconstruction of the projections to generate two-dimensional (2D) virtual cross-sections of the specimens. Image processing software, Dragonfly Pro (Version 3.1) is used to generate volume-rendered three dimensional (3D) image of specimens.

NOTE: The experimental observations and results in this chapter have not been published in any medium. The major contribution of this work was done by the Dr. Rahul Banerjee and his student Abdul Khayum M from *CSIR National Chemical Laboratory, Pune*.

CHAPTER 6

Conclusion and Future Directive

6.1 Conclusions

In this thesis work, we have dealt about the macroscopic architecture of COFs for energy storage and water purification from micropollutants. In this regard, we have described the potential features of COFs in the 1st Chapter of thesis for introducing the importance among other porous materials. Again, apart from the properties, this chapter explained the synthetic strategies; chemistry of the framework formations; and the applications of the material. In the later section of the chapter narrated the paramount importance of the macroscopic architecture of functional materials and significance of buildup of COFs into different macroscopic forms like thin films; thin sheets; and 3D monoliths.

Keeping these in perspective, we have introduced a facile strategy to fabricate free-standing films of COFs in nanometer thickness in the 2nd Chapter. Herein, we have approached a Diels-Alder reaction based chemical exfoliation of an anthracene linked β -ketoenamine COF into N-hexylmaleimide functionalized CONs. Consequently, the planar anthracene is bent to an angle of 107° which result in the breaking Π - Π stacking between the interlayers of COF and bring out the chemical exfoliation of the COF layers. Notably, the **DaTp CONs** exhibit good dispersion nature in the various polar organic solvents due to the presence of long alkyl chains. Considering this, we have fabricated centimeter scale free-standing CON thin film through the layer by layer self-assembly at the air-water interface. The fabricated **DaTp CON** thin film displays a defect-free and continuous nature.

To introduce the macroscopic form of COFs in real-life applications like energy storage, in the 3rd Chapter, we have fabricated mechanically strong and redox-active COF thin sheet through convergent solid-state mixing strategy. In this synthetic method Π electron rich anthracene linker enhances the mechanical strength of the thin sheet through the better non-covalent interaction between the crystallites of COF matrix. At the same time, the **Dq** linkers

in the framework bring out the electrochemical charge storage of the material. Importantly, the convergent synthesis maintains the crystallinity and porosity of the COFs along with the uniform and crack-free nature of the thin sheets. Finally, a mechanically robust flexible quasi-solid-state supercapacitor devices have been integrated and then further utilized for giving power to 3.5 V LED. We believe this unique convergent method has the potential relevance for the rational designing of the redox-active material used in flexible supercapacitor devices.

However, the flexible supercapacitors made of the pristine COFs exhibit poor areal capacitance (8-12.5 mFcm⁻²). It could be due to the high electric resistance of COF which restricts the smooth of electrons through entire matrix of COF. Keeping this in mind, in the 4th Chapter, we have presented the enhancement of electrochemical energy storage of 2D macroscopic forms of COF by integrating the CNF into a hybrid matrix through the *in situ* inclusion. We could observe a predominant weak interaction between COF and graphene layers present in CNF with the support of DFTB. The COF-CNF hybrid macroscopic thin sheets were observed as continuous and crack-free nature with a large areal scalability. Moreover, the COF-CNF hybrids could uphold the porous-crystalline nature with excellent electrical conductivity. Notably, the fabricated COF-CNF hybrid supercapacitor exhibits high performance in the capacitance (167 mFcm⁻²). Again, it has been further ingrated as a self-charging power-pack for the concurrent harvest and storage of energy from light to electrical power.

The 5th Chapter recounted the 3D macroarchitere of COFs for water purification applications. Herein, the strategic inclusion of macropores by means of GO as spacers in a COF matrix creates crystalline and porous aerogel. The good shear-thinning and optimum viscosity of the precursor paste allow us to perform the software controlled 3d printing of the concerned material in different shapes and multiple layers. Moreover, the interconnected macroporous matrix decorated with intrinsic micropores shows rapid and efficient adsorption capability of molecular pollutants from water. We believe, the blending of advanced 3D printing possibilities of the aerogel can be delivered fruitful industrial level water purification in future.

6.2 *Future directive*

Developing the macroscopic forms of COF as the smart responsive materials

6.2.1 *Introduction*

The technological advancement to create an intelligent environment requires properly placed stimuli-responsive smart materials. In this regard, the research on responsive materials gets wide scientific and technological attention considering to their ongoing and futuristic relevance [6.1]. In most cases, smart materials are functional molecular integrated polymers which responsive towards the stimuli like light; heat; mechanical pressure etc [6.2]. Herein, light responsive materials are widely researched due to their importance in light controlled drug delivery applications; various sensors; morphological transformations; etc. Considering to their exceptional features, the fabrication of smart responsive COF into the macroscopic form can have a potential future in the commercial level applications. The presence of intrinsic micropores with controllable size and geometry as well as decorated tunable functional molecules can deliver excellent properties for COFs in the macroscopic form. Moreover, the controlling of properties of COF by triggering light or any other external stimuli is very interesting in the scientific and technological aspects.

6.2.1 *The synthesis light responsive macroscopic forms of COF*

Azobenzenes are light responsive molecules which will form trans configuration in visible light and cis configuration in UV light [6.3]. Taking this into consideration, it is possible to fabricate 3D COF aerogel (TpBD(NO₂) COF) decorated with azobenzenes inside the pores for the controlled molecular uptake in various conditions.

The nitro benzene linker of the aerogel can be reduced and functionalized with azobenzenes through a post-modification reaction. As a result, it is expected that intrinsic micropores will be closed at the normal visible light condition, whereas, the UV light can trigger the pore opening for molecular uptake from the environment or release to the environment (**Figure 6.2**). This could be useful for the light triggered water purification by using COF aerogel or membrane in industry where the automotive controlled systems are highly required. We surmise, it can assist the size selective separation of molecules from a mixture and drug

loading of drug molecules. Herein, we need to develop COF with varying pore-size for the different molecular separations.

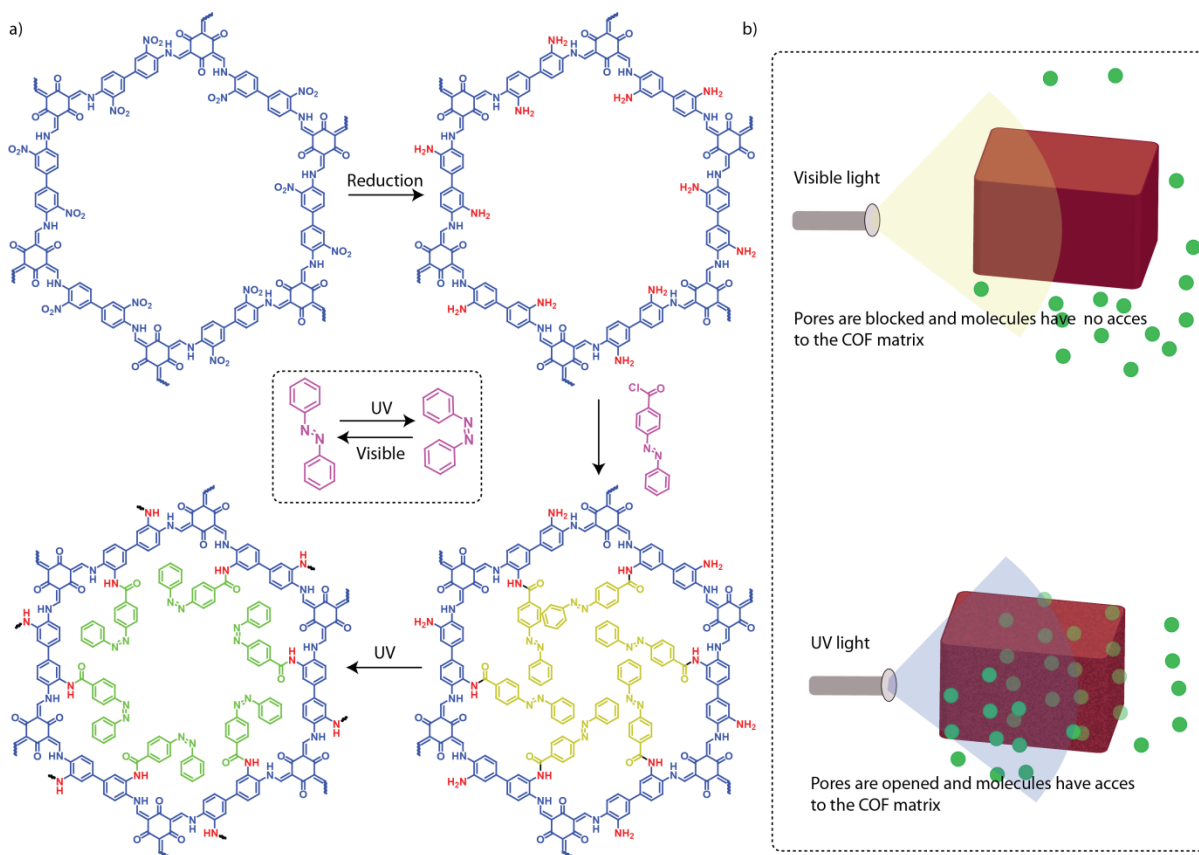


Figure 6.1: a) The schematic representation of the post modification of COF into azobenzene decorated pores. b) The diagrammatic representation of COF aerogel activity towards molecular uptake under visible or UV light condition.

REFERENCES

CHAPTER 1

- [1.1] (a) D. Wu, F. Xu, B. Sun, R. Fu, H. He, K. Matyjaszewski, *Chem. Rev.***2012**, *112*, 3959. (b) G. M. Whitesides, E. E. Simanek, J. P. Mathias, C. T. Seto, D. Chin, M. Mammen, D. M. Gordon, *Acc. Chem. Res.*, **1995**, *28*, 37. (c) J. D. Wuest, *Chem. Commun.*, **2005**, *47*, 5830. (d) J. M. Zayed, N. Nouvel, U. Rauwald and O. A. Scherman, *Chem. Soc. Rev.*, **2010**, *39*, 2806. (e) S. J. Rowan, S. J. Cantrill, G. R. L. Cousins, J. K. M. Sanders, J. F. Stoddart, *Angew. Chem., Int. Ed.*,**2002**, *41*, 898.
- [1.2] K. Ishizaki, S. Komarneni, M. Nanko. *Porous Materials: Process, technology and applications*. Kluwer Academic, **1998**.
- [1.3] (a) Y. Yang, K. Chiang, N. Burke, *Catal. Today*, **2011**, *178*, 197–205; (b) F. Schuth, K. S. W. Sing, J. Weitkamp, editors. *Handbook of Porous Solids*. Wiley-VCH Verlag GmbH, **2002**.
- [1.4] (a) J. Lee, J. Kim, T. Hyeon. *Adv. Mater.***2006**, *18*, 2073. (b) M. C. Orilall, U. Wiesner. *Chem. Soc. Rev.* **2011**, *40*, 520. (c) Y. Zhou, Y. Kim, C. Jo, J. Lee, C. W. Lee, S. Yoon. *Chem. Commun.* **2011**, *47*, 4944. (d) Y. Ishii, Y. Kanamori, T. Kawashita, I. Mukhopadhyay, S. Kawasaki. *J. Phys. Chem. Solids*, **2010**, *71*, 511. (e) L. Fu, H. Liu, H. Zhang, C. Li, T. Zhang, Y. Wu, H. Wu. *J. Power Sources*,**2006**, *159*, 219. (f) D.-H. Lee, J. -G. Park, K. Jin Choi, H. -J. Choi, D.-W. Kim, *Eur. J. Inorg. Chem.* **2008**, *2008*, 878.
- [1.5] (a) M. Eddaoudi, D. B. Moler, H. Li, B. Chen, T. M. Reinecke, M. O’Keeffe, O. M. Yaghi, *Acc. Chem. Res.* **2001**, *34*, 319. (b) C. Janiak, *Angew. Chem., Int. Ed. Engl.*,**1997**,*36*, 1431. (c) A. J. Blake, N. R. Champness, P. Hubberstey, W.-S. Li, M. A. Withersby, M. Schroder, *Coord. Chem. Rev.*,**1999**,*183*, 117. (d) O. M. Yaghi, G. Li, H. Li, *Nature*, **1995**, *378*, 703. (e) S. Kitagawa, R. Kitaura, S. -I. Noro, *Angew. Chem., Int. Ed.*,**2004**, *43*, 2334. (f) G. Ferey, *Chem. Soc. Rev.***2008**, *37*, 191. (g) B. Chen, S. Xiang, G. Qian, *Acc. Chem. Res.*,**2010**, *43*, 1115. (h) L. Ma, C. Abney, W. Lin, *Chem. Soc. Rev.*,**2009**, *38*, 124. (i) Z. G. Gu, Y. P. Cai, H. C. Fang, Z. Y. Zhou, P. K. Thallapally, J. A.

-
- Tian, J. Liu, G. J. Exarhos, *Chem. Commun.*, **2010**, *46*, 5373. (j) B. Chen, M. Eddaoudi, S. T. Hyde, M. O’Keeffe, O. M. Yaghi, *Science*, **2001**, *291*, 1021. (k) P. Pachfule, Y. Chen, J. Jiang, R. Banerjee *J. Mater. Chem.*, **2011**, *21*, 17737. (l) J. W. Yoon, S. H. Jung, Y. K. Hwang, S. M. Humphrey, P. T. Wood, J. -S. Chang, *Adv. Mater.* **2007**, *19*, 1830. (m) K. L. Mulfort, O. K. Farha, C. D. Malliakas, M. G. Kanatzidis, J. T. Hupp, *Chem. Eur. J.*, **2010**, *16*, 276. (n) H. -S. Choi, M. P. Suh, *Angew. Chem.* **2009**, *121*, 6997. (o) X. Gu, Z.-H. Lu, Q. Xu, *Chem. Commun* **2010**, *46*, 7400. (p) S. -T. Zheng, J. T. Bu, Y. Li, T. Wu, F. Zuo, P. Feng, X. Bu. *J. Am. Chem. Soc.* **2010**, *132*, 17062. (q) J. An, N. L. Rosi, *J. Am. Chem. Soc.* **2010**, *132*, 5578. (r) A. G. Wong-Foy, O. Lebel, A. J. Matzger, *J. Am. Chem. Soc.* **2007**, *129*, 15740. (s) H. Chun, D. N. Dybtsev, H. Kim, K. Kim, *Chem. Eur. J.* **2005**, *11*, 3521. (t) J. Rowsell, A. Millward, K. Park, O. Yaghi *J. Am. Chem. Soc.* **2004**, *126*, 5666.
- [1.6] (a) Y. Li, R. T. Yang, *AIChE J.* **2008**, *54*, 269. (b) Z. Liang, M. Marshall, A. L. Chaffee, *Energy Fuels* **2009**, *23*, 2785. (c) F. Gul-E-Noor, B. Jee, A. Poppl, M. Hartmann, D. Himsl, M. Bertmer, *Phys. Chem. Chem. Phys.* **2011**, *13*, 7783. (d) N. C. Burtch, H. Jasuja, K. S. Walton, *Chem. Rev.*, **2014**, *114*, 10575.
- [1.7] A. P. Cote, A. I. Benin, N. W. Ockwig, M. O’Keeffe, A. J. Matzger, O. M. Yaghi, *Science*, **2005**, *310*, 1166.
- [1.8] X. Feng, X. Ding, D. Jiang, *Chem. Soc. Rev.* **2012**, *41*, 6010-6022.
- [1.9] S. Karak, K. Dey, A. Torris, A. Halder, S. Bera, F. Kanheerampockil, Rahul Banerjee, *J. Am. Chem. Soc.* **2019**, *141*, 18, 7572-7581.
- [1.10] (a) C. J. Brinker, *Curr. Opin. Solid State Mater. Sci.* **1996**, *1*, 798-805; (b) H. Zheng, F. Gao, V. Valtchev, *J. Mater. Chem. A*, 2016, *4*, 16756.
- [1.11] (a) Y. Cui, H. Xu, Y. Yue, Z. Guo, J. Yu, Z. Chen, J. Gao, Y. Yang, G. Qian, B. Chen, *J. Am. Chem. Soc.* **2012**, *134*, 3979. (b) A. M. Shultz, O. K. Farha, J. T. Hupp, S. T. Nguyen, *J. Am. Chem. Soc.* **2009**, *131*, 4204. (c) V. Stavila, R. K. Bhakta, T. M. Alam, E. H. Majzoub, M. D. Allendorf, *ACS Nano* **2012**, *6*, 9807.
- [1.12] (a) Y. Lee, J. Kim, W. Ahn, *Korean J. Chem. Eng.* **2013**, *30*, 1667. (b) A. Schneemann, V. Bon, I. Schwedler, I. Senkowska, S. Kaskel, R. A. Fischer

-
- Chem. Soc. Rev.*, **2014**, *43*, 6062. (c) F. X. Coudert, *Chem. Mater.*, **2015**, *27* (6), 1905.
- [1.13] (a) M. J. Allen, V. C. Tung, R. B. Kaner, *Chem. Rev.* **2010**, *110*, 1, 132-145; (b) W. Choi, I. Lahiri, R. Seelaboyina and Y. S. Kang, *Crit. Rev. Solid State Mater. Sci.*, 2010, *35*, 52–71.
- [1.14] (a) G. Cheng, T. Hasell, A. Trewin, D. J. Adams, A. I. Cooper, *Angew. Chem., Int. Ed.*, **2012**, *51*, 12727. (b) L. Chen, Y. Honsho, S. Seki, D. Jiang, *J. Am. Chem. Soc.*, **2010**, *132*, 6742. (c) J. X. Jiang, F. B. Su, A. Trewin, C. D. Wood, N. L. Campbell, H. J. Niu, C. Dickinson, A. Y. Ganin, M. J. Rosseinsky, Y. Z. Khimiyak, A. I. Cooper, *Angew. Chem., Int. Ed.*, **2007**, *46*, 8574. (d) J. X. Jiang, A. Trewin, D. J. Adams, A. I. Cooper, *Chem. Sci.*, **2011**, *2*, 1777. (e) Y. H. Xu, L. Chen, Z. Q. Guo, A. Nagai, D. Jiang, *J. Am. Chem. Soc.*, **2011**, *133*, 17622. (f) S. W. Yuan, B. Dorney, D. White, S. Kirklin, P. Zapol, L. P. Yu, D. J. Liu, *Chem. Commun.*, **2010**, *46*, 4547. (g) A. Li, R. F. Lu, Y. Wang, X. Wang, K. L. Han, W. Q. Deng, *Angew. Chem., Int. Ed.*, **2010**, *49*, 3330. (h) A. Li, H. X. Sun, D. Z. Tan, W. J. Fan, S. H. Wen, X. J. Qing, G. X. Li, S. Y. Li, W. Q. Deng, *Energy Environ. Sci.*, **2011**, *4*, 2062. (i) Q. Chen, J. X. Wang, F. Yang, D. Zhou, N. Bian, X. J. Zhang, C. G. Yan, B. H. Han, *J. Mater. Chem.*, **2011**, *21*, 13554. (j) Y. Kou, Y. Xu, Z. Guo, D. Jiang, *Angew. Chem., Int. Ed.*, **2011**, *50*, 8753. (k) A. I. Cooper, *Advanced Materials*, **2009**, *21*, 1291. (l) J.-X. Jiang, F. Su, A. Trewin, C. D. Wood, H. Niu, J. T. Jones, Y. Z. Khimiyak, A. I. Cooper, *J. Am. Chem. Soc.*, **2008**, *130*, 7710.
- [1.15] (a) R.-B. Lin, Y. He, P. Li, H. Wang, W. Zhou, B. Chen, *Chem. Soc. Rev.* **2019**, *48*, 1362 – 1389; (b) J. Luo, J.-W. Wang, J.-H. Zhang, S. Lai, D.-C. Zhong, *Cryst Eng Comm.* **2018**, *20*, 5884 – 5898; (c) K. E. Maly, E. Gagnon, T. Maris, J. D. Wuest, *J. Am. Chem. Soc.* **2007**, *129*, 14, 4306-4322.
- [1.16] (a) Y. Luo, B. Li, W. Wang, K. Wu, B. Tan, *Advanced Materials*, **2012**, *24*, 5703. (b) T. Ben, S. L. Qiu, *Cryst Eng Comm*, **2013**, *15*, 17. (c) T. Ben, H. Ren, S. Q. Ma, D. P. Cao, J. H. Lan, X. F. Jing, W. C. Wang, J. Xu, F. Deng, J. M. Simmons, S. L. Qiu, G. S. Zhu, *Angew. Chem., Int. Ed.*, **2009**, *48*, 9457. (d) S. Y. Ding, W. Wang, *Chem. Soc. Rev.*, **2013**, *42*, 548. (e) P. M. Budd, B. S. Ghanem, S. Makhseed, N. B. McKeown, K. J. Msayib, C. E. Tattershall,

-
- Chem. Commun.*, **2004**, 230. (f) X. Feng, X. Ding, D. Jiang, *Chem. Soc. Rev.*, **2012**, *41*, 6010.
- [1.17] Y. Jin, C. Yu, R. J. Denmana, W. Zhang, *Chem. Soc. Rev.*, **2013**, *42*, 6634-6654.
- [1.18] H. M. El-Kaderi, J. R. Hunt, J. L. Mendoza-Cortes, A. P. Cote, R. E. Taylor, M. O’Keeffe, O. M. Yaghi, *Science*, **2007**, *316*, 268.
- [1.19] (a) M. S. Lohse, T. Bein, *Adv. Funct. Mater.* **2018**, *28*, 1705553; (b) A. P. Co[^]te’, H. M. El-Kaderi, H. Furukawa, J.R. Hunt, O. M. Yaghi, *J. Am. Chem. Soc.* **2007**, *129*, 12914-12915.
- [1.20] (a) F. J. Uribe-Romo, J. R. Hunt, H. Furukawa, C. Klock, M. O’Keeffe, O. M. Yaghi, *J. Am. Chem. Soc.*, **2009**, *131*, 4570. (b) S.-Y. Ding, J. Gao, Q. Wang, Y. Zhang, W.-G. Song, C.-Y. Su, W. Wang, *J. Am. Chem. Soc.*, **2011**, *133*, 19816. (c) S. Wan, F. Gandara, A. Asano, H. Furukawa, A. Saeki, S. K. Dey, L. Liao, M. W. Ambrogio, Y. Y. Botros, X. Duan, S. Seki, J. F. Stoddart, O. M. Yaghi, *Chem. Mater.*, **2011**, *23*, 4094.
- [1.21] S. Kandambeth, A. Mallick, B. Lukose, M. V. Mane, T. Heine, R. Banerjee, *J. Am. Chem. Soc.* **2012**, *134*, 19524.
- [1.22] (a) F. J. Uribe-Romo, C. J. Doonan, H. Furukawa, K. Oisaki, O. M. Yaghi, *J. Am. Chem. Soc.*, **2011**, *133*, 11478; (b) S. Dalapati, S. Jin, J. Gao, Y. Xu, A. Nagai, D. Jiang, *J. Am. Chem. Soc.* **2013**, *135*, 17310.
- [1.23] P. Kuhn, M. Antonietti, A. Thomas, *Angew. Chem., Int. Ed.*, **2008**, *47*, 3450. (b) M. J. Bojdys, J. Jeromenok, A. Thomas, M. Antonietti, *Adv. Mater.*, **2010**, *22*, 2202.
- [1.24] X. Zhuang, W. Zhao, F. Zhang, Y. Cao, F. Liu, S. Bi, X. Feng, *Polym. Chem.* **2016**, *7*, 4176.
- [1.25] N. L. Campbell, R. Clowes, L. K. Ritchie, A. I. Cooper, *Chem. Mater.*, **2009**, *21*, 204.
- [1.26] (a) D. D. Medina, J. M. Rotter, Y. H. Hu, M. Dogru, V. Werner, F. Auras, J. T. Markiewicz, P. Knochel, T. Bein, *J. Am. Chem. Soc.*, **2015**, *137*, 1016; (b) K. Dey, M. Pal, K. C. Rout, S. Kunjattu, H. A. Das, R. Mukherjee, U. K. Kharul, R. Banerjee, *J. Am. Chem. Soc.* **2017**, *139*, 13083–13091; (c) D. R. S.

-
- Miguel, A. Abrishamkar, J. A. R. Navarro, R. R. Trujillo, D. B. Amabilino, R. M. Ballesté, F. Zamora, J. P. Luis, *Chem. Commun.*, **2016**, 52, 9212.
- [1.27] (a) B. P. Biswal, S. Chandra, S. Kandambeth, B. Lukose, T. Heine, R. Banerjee, *J. Am. Chem. Soc.*, **2013**, 135, 5328; (b) S. Kandambeth, B. P. Biswal, H. D. Chaudhari, K. C. Rout, H. S. Kunjattu, S. Mitra, S. Karak, A. Das, R. Mukherjee, U. K. Kharul, R. Banerjee, *Adv. Mater.* **2017**, 29, 1603945; (c) S. Karak, S. Kandambeth, B. P. Biswal, H. S. Sasmal, S. Kumar, P. Pachfule, R. Banerjee, *J. Am. Chem. Soc.* **2017**, 139, 1856.
- [1.28] S. J. Lyle, P. J. Waller, O. M. Yaghi, *Trends in Chemistry* 2019, 1 (2), 172–184.
- [1.29] N. Huang, L. Zhai, D. E. Coupry, M. A. Addicoat, K. Okushita, K. Nishimura, T. Heine and D. Jiang, *Nat. Commun.*, 2016, 7, 12325.
- [1.30] (a) A. M. Evans, L. R. Parent, N. C. Flanders, R. P. Bisbey, E. Vitaku, M. S. Kirschner, R. D. Schaller, L. X. Chen, N. C. Gianneschi, W. R. Dichtel, *Science*, **2018**, 361, eaar7883; (b) T. Ma, E. A. Kapustin, S. X. Yin, L. Liang, Z. Zhou, J. Niu, L. H. Li, Y. Wang, J. Su, J. Li, X. Wang, W. D. Wang, W. Wang, J. Sun and O. M. Yaghi, *Science*, **2018**, 361, 48.
- [1.31] (a) L. M. Lanni, R. W. Tilford, M. Bharathy, J. J. Lavigne, *J. Am. Chem. Soc.*, **2011**, 133, 13975; (b) H. Xu, J. Gao, D. Jiang, *Nat. Chem.* **2015**, 7, 905; A. Halder, S. Karak, M. Addicoat, S. Bera, A. Chakraborty, S. H. Kunjattu, P. Pachfule, T. Heine, R. Banerjee, *Angew. Chem. Int. Ed.* **2018**, 57, 5797–5802.
- [1.32] (a) M. P. Suh, H. J. Park, T. K. Prasad, D.-W. Lim, *Chem. Rev.*, **2012**, 112, 782. (b) W. Huang, Y. Jiang, X. Li, X. Li, J. Wang, Q. Wu, X. Liu, *ACS Appl. Mater. Interfaces*, **2013**, 5, 8845. (c) X. W. Lou, L. A. Archer, Z. C. Yang, *Adv. Mater.* **2008**, 20, 3987.
- [1.33] H. Furukawa, O. M. Yaghi, *J. Am. Chem. Soc.*, **2009**, 131, 8875.
- [1.34] Y. J. Choi, J. H. Choi, K. M. Choi, J. K. Kang, *J. Mater. Chem.*, **2011**, 21, 1073.
- [1.35] C. J. Doonan, D. J. Tranchemontagne, T. G. Glover, J. R. Hunt, O. M. Yaghi, *Nat. Chem.*, **2010**, 2, 235.
- [1.36] (a) S. Y. Ding, J. Gao, Q. Wang, Y. Zhang, W. G. Song, C. Y. Su, W. Wang, *J. Am. Chem. Soc.*, **2011**, 133, 19816. (b) D. B. Shinde, S. Kandambeth, P.

-
- Pachfule, R. R. Kumar R. Banerjee, *Chem. Commun.*, **2015**, *51*, 310. (c) P. Pachfule, S. Kandambeth, A. Mallick, R. Banerjee, *Chem. Commun.*, **2015**, *51*, 11717. (d) P. Pachfule, S. Kandambeth, D. Diaz Diaz, R. Banerjee, *Chem. Commun.*, **2014**, *50*, 3169; (e) M. Bhadra, S. Kandambeth, M. K. Sahoo, M. Addicoat, E. Balaraman, R. Banerjee, *J. Am. Chem. Soc.* **2019**, *141*, 15, 6152-6156; (f) M. Bhadra, H. S. Sasmal, A. Basu, S. P. Midya, S. Kandambeth, P. Pachfule, E. Balaraman, R. Banerjee, *ACS Appl. Mater. Interfaces*, **2017**, *9*, 13785–13792; (g) H. Xu, J. Gao, D. Jiang, *Nat. Chem.*, **2015**, *7*, 905–912; (h) H. Hu, Q. Yan, R. Ge, Y. Gao, *Chin. J. Catal.*, **2018**, *39*, 1167.
- [1.37] (a) Y. He, W. Chen, X. Li, Z. Zhang, J. Fu, C. Zhao, E. Xie, *ACS Nano*, **2013**, *7*, 174; (b) C. Meng, C. Liu, L. Chen, C. Hu, S. Fan, *Nano Lett.* **2010**, *10*, 4025; (c) J. Chen, A. I. Minett, Y. Liu, C. Lynam, P. Sherrell, C. Wang, G. G. Wallace, *Adv. Mater.* **2008**, *20*, 566; (d) L. Dong, C. Xu, Y. Li, Z. -H. Huang, F. Kang, Q.-H. Yanga, X. Zhaod, *J. Mater. Chem. A*, **2016**, *4*, 4659; (e) V. Vijayakumar, B. Anothumakkool, A.T.A. T, S. B. Nair, M. V. Badiger, S. Kurungot, *J. Mater. Chem. A* **2017**, *5*, 8461; (f) R. Soni, A. Raveendran, S. Kurungot, *Nanoscale*, **2017**, *9*, 3593.
- [1.38] (a) C. R. DeBlase, K. E. Silberstein, T. T. Truong, H. D. Abruna, W. R. Dichtel, *J. Am. Chem. Soc.*, **2013**, *135*, 16821. (b) C. R. DeBlase, K. Hernandez-Burgos, K. E. Silberstein, G. G. Rodriguez-Calero, R. P. Bisbey, H. D. Abruna, W. R. Dichtel, *ACS Nano*, **2015**, *9*, 3178. (c) F. Xu, H. Xu, D. Wu, Y. Wu, H. Liu, C. Gu, R. Fu, D. Jiang Chen, *Angew. Chem Int. Ed.* **2015**, *54*, 6814; (d) J. Zhou, B. Wang, *Chem. Soc. Rev.* **2017**, *46*, 6927; (e) S. Wang, Q. Wang, P. Shao, Y. Han, X. Gao, L. Ma, S. Yuan, X. Ma, J. Zhou, X. Feng, B. Wang, *J. Am. Chem. Soc.* **2017**, *139*, 4258-4261; (f) S. Gu, S. Wu, L. Cao, M. Li, N. Qin, J. Zhu, Z. Wang, Y. Li, Z. Li, J. Chen, Z. Lu, *J. Am. Chem. Soc.* **2019**, *141*, 24, 9623-9628; (g) S. Chandra, D. R. Chowdhury, M. Addicoat, T. Heine, A. Paul, Rahul Banerjee, *Chem. Mater.* **2017**, *29*, 5, 2074-2080.
- [1.39] (a) S. Wan, J. Guo, J. Kim, H. Ihee, D. Jiang, *Angew. Chem., Int. Ed.*, **2009**, *48*, 5439. (b) S. Wan, J. Guo, J. Kim, H. Ihee, D. Jiang, *Angew. Chem., Int. Ed.*, **2008**, *47*, 8826. (c) X. Feng, L. Liu, Y. Honsho, A. Saeki, S. Seki, S. Irle,

-
- Y. Dong, A. Nagai, D. Jiang, *Angew. Chem., Int. Ed.*, **2012**, *51*, 2618. (d) X. S. Ding, J. Guo, X. Feng, Y. Honsho, J. D. Guo, S. Seki, P. Maitarad, A. Saeki, S. Nagase, D. Jiang, *Angew. Chem., Int. Ed.*, **2011**, *50*, 1289. (e) X. Feng, L. Chen, Y. Honsho, O. Saengsawang, L. Liu, L. Wang, A. Saeki, S. Irle, S. Seki, Y. Dong, D. Jiang, *Adv.Mater.*, **2012**, *24*, 3026.
- [1.40] (a) X. Zhu, S. An, Y. Liu, J. Hu, H. Liu, C. Tian, S. Dai, X. Yang, H. Wang, C. W. Abney, S. Dai, *AICHE J.* **2017**, *63*, 3470; (b) N. Huang, L. Zhai, H. Xu, D. Jiang, *J. Am. Chem. Soc.* **2017**, *139*, 2428; (c) Q. Sun, B. Aguila, J. Perman, L. D. Earl, C. W. Abney, Y. Cheng, H. Wei, N. Nguyen, L. Wojtas, S. Ma, *J. Am. Chem. Soc.* **2017**, *139*, 2786; (d) H. Lu, C. Wang, J. Chen, R. Ge, W. Leng, B. Dong, J. Huang, Y. Gao, *Chem. Commun.* **2015**, *51*, 15562.
- [1.41] (a) Q. Fang, J. Wang, S. Gu, R. B. Kaspar, Z. Zhuang, J. Zheng, H. Guo, S. Qiu, Y. Yan, *J. Am. Chem. Soc.*, **2015**, *137*, 8352; (b) S. Kandambeth, V. Venkatesh, D. B. Shinde, S. Kumari, A. Halder, S. Verma, R. Banerjee, *Nat. Commun.* **2015**, *6*, Article No. 6786.
- [1.42] (a) T. Shang, Z. Lin, C. Qi, X. Liu, P. Li, Y. Tao, Z. Wu, D. Li, P. Simon, Q.-H. Yang, *Adv. Funct. Mater.* 2019, 1903960; (b) T. M. Gü, *Energy Environ. Sci.*, **2018**, *11*, 2696-2767; (c) B. Lee, S. Lee, M. Lee, D.H. Jeong, Y. Baek, J. Yoonc, Y. H. Kim, *Nanoscale*, **2015**, *7*, 6782-6789; (d) W. Wan, R. Zhang, W. Li, H. Liu, Y. Lin, L. Li, Y. Zhou, *Environ. Sci.: Nano*, **2016**, *3*, 107-113.
- [1.43] (a) B. Khorshidi, I. Biswas, T. Ghosh, T. Thundat, M. Sadrzadeh, *Sci.Rep*, **2018**, *8*, 1–10; (b) M.K. Patil, S. Shaikh, I. Ganesh, *Current Nanosci.* **2015**, *11*, 271-285; (c) D. Lee, M. F. Rubner, R. E. Cohen, *Nano Lett.* **2006**, *6*, 10, 2305-231.
- [1.44] (a) F. Ishiwari, Y. Shoji, T. Fukushima, *Chem. Sci.*, **2018**, *9*, 2028; (b) J. Wang, X. Zhang, *ACS Nano*, **2015**, *9*, 11, 11389-11397; (c) N. M. Sangeetha, U. Maitra, *Chem. Soc. Rev.*, **2005**, *34*, 821-836; (d) A.R. Hirst, B. Escuder, J. F. Miravet, D. K. Smith, *Angew. Chem. Int. Ed.* 2008, *47*, 8002 – 8018
- [1.45] (a) O. C. Compton, S. T. Nguyen, *Small* **2010**, *6*, 71; (b) R. K. L. Tan, S. P. Reeves, N. Hashemi, D. G. Thomas, E. Kavak, R. Montazami and N. N. Hashemi, *J. Mater. Chem. A*, **2017**, *5*, 17777–17803.

-
- [1.46] (a) D. A. Dikin, S. Stankovich, E. J. Zimney, R. D. Piner, G. H. B. Dommett, G. Evmenenko, S. T. Nguyen, R. S. Ruoff, *Nature* **2007**, *448*, 457–460; (b) K. Bramhaiah and N. S. John, *Adv. Nat. Sci.: Nanosci. Nanotechnol.*, **2012**, *3*, 045002 (c) K. Chen, S. Zhang, A. Li, X. Tang, L. Li, L. Guo, *ACS Nano* **2018**, *12*, 54, 269–4279; (d) Q. Zhang, F. Zhang, S. P. Medarametla, H. Li, C. Zhou, Dong Lin, *small* **2016**, *12*, 13, 1702–1708; (e) V. Chabot, D. Higgins, A. Yu, X. Xiao, Z. Chena, J. Zhang, *Energy Environ. Sci.*, 2014, *7*, 1564–1596.
- [1.47] (a) A. Bétard, A. Fischer, *Chem. Rev.* **2012**, *112*, 2, 1055–1083; (b) G. J. H. Lim, Y. Wu, B. B. Shah, J. J. Koh, C. K. Liu, D. Zhao, A. K. Cheetham, J. Wang, J. Ding, *ACS Materials Lett.* **2019**, *1*, 147–153.
- [1.48] (a) J. W. Colson, A. R. Woll, A. Mukherjee, M. P. Levendorf, E. L. Spitler, V. B. Shields, M. G. Spencer, J. Park, W. R. Dichtel, *Science*, **2011**, *332*, 228; (b) H. Wang, Z. Zeng, P. Xu, L. Li, G. Zeng, R. Xiao, Z. Tang, D. Huang, L. Tang, C. Lai, D. Jiang, Y. Liu, H. Yi, L. Qin, S. Ye, X. Ren and W. Tang, *Chem. Soc. Rev.*, **2019**, *48*, 488–516.
- [1.49] a) I. Berlanga, M. L. Ruiz-Gonzalez, J. M. Gonzalez-Calbet, J. L. G. Fierro, R. Mas-Balleste, F. Zamora, *Small* **2011**, *7*, 1211; b) S. Chandra, S. Kandambeth, B. P. Biswal, B. Lukose, S. M. Kunjir, M. Chaudhary, R. Babarao, T. Heine, R. Banerjee, *J. Am. Chem. Soc.* **2013**, *135*, 17853 – 17861; (c) D. N. Bunck, W. R. Dichtel, *J. Am. Chem. Soc.* **2013**, *135*, 14952 – 14955; (d) S. Mitra, S. Kandambeth, B. P. Biswal, M. A. Khayum, C. K. Choudhury, M. Mehta, G. Kaur, S. Banerjee, A. Prabhune, S. Verma, S. Roy, U. K. Kharul, R. Banerjee, *J. Am. Chem. Soc.* **2016**, *138*, 2823 – 2828.
- [1.50] C. R. DeBlase, K. Hernandez-Burgos, K. E. Silberstein, G. G. Rodriguez-Calero, R. P. Bisbey, H. D. Abruna, W. R. Dichtel, *ACS Nano* **2015**, *9*, 3178–3183.
- [1.51] (a) D. D. Medina, V. Werner, F. Auras, R. Tautz, M. Dogru, J. Schuster, S. Linke, M. Dobliger, J. Feldmann, P. Knochel, T. Bein, *ACS Nano*, **2014**, *8*, 4042–4052; (b) X. H. Gou, Q. Zhang, Y. L. Wu, Y. J. Zhao, X. F. Shi, X. Fan, L. Z. Huang, G. Lu, *RSC Adv.*, **2016**, *6*, 39198–39203.

-
- [1.52] J. I. Feldblyum, C. H. McCreery, S. C. Andrews, T. Kurosawa, E. J. G. Santos, V. Duong, L. Fang, A. L. Ayzner, Z. N. Bao, *Chem. Commun.*, **2015**, 51, 13894–13897.
- [1.53] W. Y. Dai, F. Shao, J. Szczerbinski, R. McCaffrey, R. Zenobi, Y. H. Jin, A. D. Schluter, W. Zhang, *Angew. Chem.Int. Ed.*, **2016**, 55, 213–217.
- [1.54] (a) C. R. Mulzer, L. Shen, R. P. Bisbey, J. R. McKone, N. Zhang, H. D. Abruña, W. R. Dichtel, *ACS Cent. Sci.* **2016**, 2, 667–673; (b) S. Wang, Q. Wang, P. Shao, Y. Han, X. Gao, L. Ma, S. Yuan, X. Ma, J. Zhou, X. Feng, B. Wang, *J. Am. Chem. Soc.* **2017**, 139, 4258–4261.
- [1.55] (a) C. Montoro, D. Rodriguez-San-Miguel, E. Polo, R. Escudero-Cid, M. L. Ruiz-Gonzalez, J. A. R. Navarro, P. Ocon, F. Zamora, *J. Am. Chem. Soc.*, **2017**, 139, 10079–10086; (b) H. S. Sasmal, H. B. Aiyappa, S. N. Bhange, S. Karak, A. Halder, S. Kurungot, R. Banerjee, *Angew. Chem., Int. Ed.*, **2018**, 57, 10894–10898.
- [1.56] S. L. Cai, Y. B. Zhang, A. B. Pun, B. He, J. H. Yang, F. M. Toma, I. D. Sharp, O. M. Yaghi, J. Fan, S. R. Zheng, W. G. Zhang, Y. Liu, *Chem. Sci.*, **2014**, 5, 4693–4700.
- [1.57] M. Matsumoto, L. Valentino, G. M. Stiehl, H. B. Balch, A. R. Corcos, F. Wang, D. C. Ralph, B. J. Marinas, W. R. Dichtel, *Chem*, **2018**, 4, 308–317.
- [1.58] (a) H. W. Fan, J. H. Gu, H. Meng, A. Knebel, J. Caro, *Angew. Chem., Int. Ed.*, **2018**, 57, 4083–4087; (b) G. Li, K. Zhang, T. Tsuru, *ACS Appl. Mater. Interfaces*, **2017**, 9, 8433–8436; (c) Z. X. Kang, Y. W. Peng, Y. H. Qian, D. Q. Yuan, M. A. Addicoat, T. Heine, Z. G. Hu, L. Tee, Z. G. Guo, D. Zhao, *Chem. Mater.*, **2016**, 28, 1277–1285.

CHAPTER 2

- [2.1] (a) A. P. Côté, A. I. Benin, N. W. Ockwig, A. J. Matzger, M. O' Keeffe, O. M. Yaghi, *Science*. **2005**, 310, 1166–1170; (b) D. N. Bunck, W. R. Dichtel, *Angew. Chem. Int. Ed.* **2012**, 51, 1885–1889; (c) N. Huang, X. Ding, J. Kim, H. Ihee, D. Jiang, *Angew. Chem. Int. Ed.* **2015**, 54, 8704–8707; (d) L. Ascherl,

-
- T. Sick, J. T. Margraf, S. H. Lapidus, M. Calik, C. Hettstedt, K. Karaghiosoff, M. Döblinger, T. Clark, K. W. Chapman, F. Auras, T. Bein, *Nat. Chem.* **2016**, *8*, 310-316; (e) X. H. Liu, C. Z. Guan, S. Y. Ding, W. Wang, H. J. Yan, D. Wang, L. J. Wan, *J. Am. Chem. Soc.* **2013**, *135*, 10470-10474; (f) L. Stegbauer, K. Schwinghammer, B. V. Lotsch, *Chem. Sci.* **2014**, *5*, 2789-2793.
- [2.2] (a) L. Stegbauer, K. Schwinghammer, B. V. Lotsch, *Chem. Sci.* **2014**, *5*, 2789. (b) L. Ascherl, T. Sick, J. T. Margraf, S. H. Lapidus, M. Calik, C. Hettstedt, K. Karaghiosoff, M. Döblinger, T. Clark, K. W. Chapman, F. Auras, T. Bein, *Nat. Chem.* **2016**, *8*, 310. (c) S. Y. Ding, J. Gao, Q. Wang, Y. Zhang, W. G. Song, C. Y. Su, W. Wang, *J. Am. Chem. Soc.* **2011**, *133*, 19816. (d) C. J. Doonan, D. J. Tranchemontagne, T. G. Glover, J. R. Hunt, O. M. Yaghi, *Nat. Chem.* **2010**, *2*, 235. (e) L. Jiao, Y. Hu, H. Ju, C. Wang, M. R. Gao, Q. Yang, J. Zhu, S. H. Yu, H. L. Jiang, *J. Mater. Chem. A*, **2017**, *5*, 23170. (f) W. Yang, J. Wang, H. Wang, Z. Bao, J. Zhao, B. Chen, *Cryst. Growth Des.*, **2017**, *17*, 6132.
- [2.3] (a) J. W. Colson, A. R. Woll, A. Mukherjee, M. P. Levendorf, E. L. Spitler, V. B. Shields, M. G. Spencer, J. Park, W. R. Dichtel, *Science*, **2011**, *332*, 228; (b) H. Wang, Z. Zeng, P. Xu, L. Li, G. Zeng, R. Xiao, Z. Tang, D. Huang, L. Tang, C. Lai, D. Jiang, Y. Liu, H. Yi, L. Qin, S. Ye, X. Ren and W. Tang, *Chem. Soc. Rev.*, **2019**, *48*, 488–516.
- [2.4] I. Berlanga, M. L. Ruiz-Gonzalez, J. M. Gonzalez-Calbet, J. L. G. Fierro, R. Mas-Balleste, F. Zamora, *Small* **2011**, *7*, 1211.
- [2.5] S. Chandra, S. Kandambeth, B. P. Biswal, B. Lukose, S. M. Kunjir, M. Chaudhary, R. Babarao, T. Heine, R. Banerjee, *J. Am. Chem. Soc.* **2013**, *135*, 17853 – 17861.
- [2.6] D. N. Bunck, W. R. Dichtel, *J. Am. Chem. Soc.* **2013**, *135*, 14952 – 14955
- [2.7] S. Mitra, S. Kandambeth, B. P. Biswal, M. A. Khayum, C. K. Choudhury, M. Mehta, G. Kaur, S. Banerjee, A. Prabhune, S. Verma, S. Roy, U. K. Kharul, R. Banerjee, *J. Am. Chem. Soc.* **2016**, *138*, 2823 – 2828.
- [2.8] E. R. Thapaliya, B. Captain, F. M. Raymo, *J. Org. Chem.* **2014**, *79*, 3973-3981.

-
- [2.9] S. Huang, X. Cen, H. Peng, S. Guo, W. Wang, T. Liu, *J. Phys. Chem. B.* **2009**, *113*, 15225-15230.
- [2.10] S. Kandambeth, A. Mallick, B. Lukose, M. V. Mane, T. Heine, R. Banerjee, *J. Am. Chem. Soc.* **2012**, *134*, 19524-19527.
- [2.11] C. A. Hunter, J. K. M. Sanders, *J. Am. Chem. Soc.* **1990**, *112*, 5525.
- [2.12] (a) J. Zou and F. Kim, *ACS Nano*, **2012**, *6*, 10606-10613; (b) L.J. Cote, F. Kim, J. Huang, *J. Am. Chem. Soc.* **2009**, *131*, 1043-1049; (c) L. Ji, G. Guo, H. Sheng, S. Qin, B. Wang, D. Han, T. Li, D. Yang, and A. Dong, *Chem. Mater.* **2016**, *28*, 3823-3830.
- [2.13] (a) J. Borges, and J. F. Mano, *Chem. Rev.* **2014**, *114*, 8883-8942; (b) L. Yang, C. Adam, G.S. Nichol and S. L. Cockroft, *Nat. Chem.* **2013**, *5*, 1006-1010.

CHAPTER 3

- [3.1] (a) K. Dey, M. Pal, K. C. Rout, S. Kunjattu, H. A. Das, R. Mukherjee, U. K. Kharul, R. Banerjee, *J. Am. Chem. Soc.* **2017**, *139*, 13083-13091; (b) S. Kandambeth, B. P. Biswal, H. D. Chaudhari, K. C. Rout, H. S. Kunjattu, S. Mitra, S. Karak, A. Das, R. Mukherjee, U. K. Kharul, R. Banerjee, *Adv. Mater.* **2017**, *29*, 1603945; (c) C. R. DeBlase, K. Hernandez-Burgos, K. E. Silberstein, G. G. Rodriguez-Calero, R. P. Bisbey, H. D. Abruna, W. R. Dichtel, *ACS Nano* **2015**, *9*, 3178-3183.
- [3.2] S. Yuan, X. Li, J. Zhu, G. Zhang, P. V. Puyveldeb, B. V. Bruggen, *Chem. Soc. Rev.* **2019**, *48*, 2665-2681.
- [3.3] (a) J. Zhou, B. Wang, *Chem. Soc. Rev.* **2017**, *46*, 6927; (b) C. R. DeBlase, K. E. Silberstein, T. T. Truong, H. D. Abruna, W. R. Dichtel, *J. Am. Chem. Soc.* **2013**, *135*, 16821. (c) F. Wang, X. Wu, X. Yuan, Z. Liu, Y. Zhang, L. Fu, Y. Zhu, Q. Zhou, Y. Wu, W. Huang, *Chem. Soc. Rev.* **2017**, *46*, 6816.
- [3.4] (a) F. Xu, H. Xu, D. Wu, Y. Wu, H. Liu, C. Gu, R. Fu, D. Jiang Chen, *Angew. Chem Int. Ed.* **2015**, *54*, 6814; (b) J. Zhou, B. Wang, *Chem. Soc. Rev.* **2017**, *46*, 6927; (c) S. Wang, Q. Wang, P. Shao, Y. Han, X. Gao, L. Ma, S. Yuan, X. Ma, J. Zhou, X. Feng, B. Wang, *J. Am. Chem. Soc.* **2017**, *139*, 4258-

-
- 4261; (d) S. Gu, S. Wu, L. Cao, M. Li, N. Qin, J. Zhu, Z. Wang, Y. Li, Z. Li, J. Chen, Z. Lu, *J. Am. Chem. Soc.* **2019**, *141*, 24, 9623-9628.
- [3.5] (a) Y. He, W. Chen, X. Li, Z. Zhang, J. Fu, C. Zhao, E. Xie, *ACS Nano*, **2013**, *7*, 174; (b) C. Meng, C. Liu, L. Chen, C. Hu, S. Fan, *Nano Lett.* **2010**, *10*, 4025; (c) J. Chen, A. I. Minett, Y. Liu, C. Lynam, P. Sherrell, C. Wang, G. G. Wallace, *Adv. Mater.* **2008**, *20*, 566; (d) L. Dong, C. Xu, Y. Li, Z. -H. Huang, F. Kang, Q.-H. Yang, X. Zhao, *J. Mater. Chem. A*, **2016**, *4*, 4659; (e) V. Vijayakumar, B. Anothumakkool, A.T.A. T, S. B. Nair, M. V. Badiger, S. Kurungot, *J. Mater. Chem. A* **2017**, *5*, 8461; (f) R. Soni, A. Raveendran, S. Kurungot, *Nanoscale*, **2017**, *9*, 3593.
- [3.6] U. Gulzar, S. Goriparti, E. Miele, T. Li, G. Maidecchi, A. Toma, F. D. Angelis, C. Capiglia, R. P. Zaccaria, *J. Mater. Chem. A*, **2016**, 16771.
- [3.7] (a) Q. Xue, J. Sun, Y. Huang, M. Zhu, Z. Pei, H. Li, Y. Wang, N. Li, H. Zhang, C. Zhi, *Small* **2017**, *13*, 1701827; (b) Y. Cheng, S. Lu, H. Zhang, C. V. Varanasi, J. Liu, *Nano Lett.* **2012**, *12*, 4206.
- [3.8] (a) C. A. Hunter, J. K. M. Sanders, *J. Am. Chem. Soc.* **1990**, *112*, 5525; (b) K. Müller-Dethlefs, P. Hobza, *Chem. Rev.* **2000**, *100*, 143; (c) E. M. Perez, N. Martin, *Chem. Soc. Rev.* **2015**, *44*, 6425.
- [3.9] (a) V. Georgakilas, J. N. Tiwari, K. C. Kemp, J. A. Perman, A. B. Bourlinos, K. S. Kim, R. Zboril, *Chem. Rev.* **2016**, *116*, 5464; (b) D. Chen, H. Feng, J. Li, *Chem. Rev.* **2012**, *112*, 6027; (c) S. Stankovich, D. A. Dikin, G. H. B. Dommett, K. M. Kohlhaas, E. J. Zimney, E. A. Stach, R. D. Piner, S. T. Nguyen, R. S. Ruoff, *Nature* **2006**, *442*, 282.
- [3.10] (a) M. K. Cyranski, *Chem. Rev.*, **2005**, *105*, 3773; (b) D. A. M. Egbe, S. Türk, S. Rathgeber, F. Kühnlenz, R. Jadhav, A. Wild, E. Birckner, G. Adam, A. Pivrikas, V. Cimrova, G. n. Knör, N. S. Sariciftci, H. Hoppe, *Macromolecules* **2010**, *43*, 1261; (c) M. A. Khayum, S. Kandambeth, S. Mitra, S. B. Nair, A. Das, S. S. Nagane, R. Mukherjee, Banerjee, R. *Angew. Chem., Int. Ed.* **2016**, *55*, 15604.
- [3.11] (a) X. Chen, M. Addicoat, S. Irle, A. Nagai, D. Jiang, *J. Am. Chem. Soc.* **2013**, *135*, 546; (b) W. Leng, Y. Peng, J. Zhang, H. Lu, X. Feng, R. Ge, B. Dong, B. Wang, X. Hu, Y. Gao, *Chem. Eur. J.* **2016**, *22*, 9087; (c) S. F. Pang, S. Q. Xu,

T. Y. Zhou, R. R. Liang, T. G. Zhan, X. Zhao, *J. Am. Chem. Soc.* **2016**, *138*, 4710.

- [3.12] (a) S. Kandambeth, A. Mallick, B. Lukose, M.V. Mane, T. Heine, R. Banerjee, *J. Am. Chem. Soc.* **2012**, *134*, 19524; (b) S. Karak, S. Kandambeth, B.P. Biswal, H. S. Sasmal, S. Kumar, P. Pachfule, R. Banerjee, *J. Am. Chem. Soc.* **2017**, *139*, 1856.

CHAPTER 4

- [4.1] X. Feng, X. Ding, D. Jiang, *Chem. Soc. Rev.* **2012**, *41*, 6010-6022.
- [4.2] (a) C. R. DeBlase, K. E. Silberstein, T. T. Truong, H. D. Abruna, W. R. Dichtel, *J. Am. Chem. Soc.* **2013**, *135*, 16821-16824; (b) C. R. DeBlase, K. Hernandez-Burgos, K. E. Silberstein, G. G. Rodriguez-Calero, R. P. Bisbey, H. D. Abruna, W. R. Dichtel, *ACS Nano* **2015**, *9*, 3178-3183; (d) J. Zhou, B. Wang, *Chem. Soc. Rev.* **2017**, *46*, 6927; (e) F. Wang, X. Wu, X. Yuan, Z. Liu, Y. Zhang, L. Fu, Y. Zhu, Q. Zhou, Y. Wu, W. Huang, *Chem. Soc. Rev.* **2017**, *46*, 6816.
- [4.3] Z. Zha, L. Xu, Z. Wang, X. Li, Q. Pan, P. Hu, S. Lei, *ACS Appl. Mater. Interfaces* **2015**, *7*, 17837-17843.
- [4.4] (a) Y. He, W. Chen, X. Li, Z. Zhang, J. Fu, C. Zhao, E. Xie, *ACS Nano*, **2013**, *7*, 174; (b) C. Meng, C. Liu, L. Chen, C. Hu, S. Fan, *Nano Lett.* **2010**, *10*, 4025; (c) J. Chen, A. I. Minett, Y. Liu, C. Lynam, P. Sherrell, C. Wang, G. G. Wallace, *Adv. Mater.* **2008**, *20*, 566; (d) L. Dong, C. Xu, Y. Li, Z. -H. Huang, F. Kang, Q.-H. Yanga, X. Zhaod, *J. Mater. Chem. A*, **2016**, *4*, 4659; (e) V. Vijayakumar, B. Anothumakkool, A.T.A. T, S. B. Nair, M. V. Badiger, S. Kurungot, *J. Mater. Chem.A* **2017**, *5*, 8461; (f) R. Soni, A. Raveendran, S. Kurungot, *Nanoscale*, **2017**, *9*, 3593.
- [4.5] C. R. Mulzer, L. Shen, R. P. Bisbey, J. R. McKone, N. Zhang, H. D. Abruña, W. R. Dichtel, *ACS Cent. Sci.* **2016**, *2*, 667-673.
- [4.6] (a) Y. Gogotsi, P. Simon, *Science* **2011**, *334*, 917-918; (b) Y. Xia, T. S. Mathis, M.-Q. Zhao, B. Anasori, A. Dang, Z. Zhou, H. Cho, Y. Gogotsi, S. Yang, *Nature* **2018**, *557*, 409-412.

-
- [4.7] (a) R. N. Gunasinghe, D. G. Reuven, K. Suggs, X. -Q. Wang, *J. Phys. Chem. Lett.* **2012**, *3*, 3048–3052; (b) L. Xu, X. Zhou, W. Q. Tian, T. Gao, Y. F. Zhang, S. Lei, Z. F. Liu, *Angew. Chem. Int. Ed.* **2014**, *53*, 9564–9568; (c) C. A. Hunter, J. K. M. Sanders, *J. Am. Chem. Soc.* **1990**, *112*, 5525-5534; (b) K. Müller-Dethlefs, P. Hobza, *Chem. Rev.* **2000**, *100*, 143; (d) E. M. Perez, N. Martin, *Chem. Soc. Rev.* **2015**, *44*, 6425; (e) G. R. Desiraju, *Acc. Chem. Res.* **1996**, *29*, 441-449; (f) T. Steiner, G. R. Desiraju, *Chem. Commun.* **1998**, *0*, 891-892; (g) W. Wang, Y. Zhang, B. Wang, *J. Chem. Phys.* **2014**, *140*, 094302.
- [4.8] X. Chen, H. Wang, H. Yi, X. Wang, *J. Phys. Chem. C* **2014**, *118*, 8262–8270
- [4.9] (a) Z. Lei, Q. Yang, Y. Xu, S. Guo, W. Sun, H. Liu, L.-P. Lv, Y. Zhang, ; Y. Wang, *Nat. Commun.* **2018**, *9*, 576; (b) X. Chen, H. Zhang, C. Ci, W. Sun, Y. Wang, *ACS Nano* **2019**, *13*, 3600–3607.
- [4.10] L. Feng, N. Xie, J. Zhong, *Materials* **2014**, *7*, 3919–3945.
- [4.11] S. Karak, S. Kandambeth, B. P. Biswal, H. S. Sasmal, S. Kumar, P. Pachfule, R. Banerjee, *J. Am. Chem. Soc.* **2017**, *139*, 1856-1862.
- [4.12] (a) W. X. Guo, X. Y. Xue, S. H. Wang, C. J. Lin, Z. L. Wang, *Nano Lett.* **2012**, *12*, 2520-2523; (b) Z. Zhang, X. Chen, P. Chen, G. Guan, L. Qiu, H. Lin, Z. Yang, W. Bai, Y. Luo, H. Peng, *Adv. Mater.* **2014**, *26*, 466-470; (c) X. Xu, S. Li, H. Zhang, Y. Shen, S. M. Zakeeruddin, M. Graetzel, Y.-B. Cheng, M. A. Wang, *ACS Nano* **2015**, *9*, 1782–1787; (d) J. Kim, S. M. Lee, Y.-H. Hwang, S. Lee, B. Park, J.-H. Jangac, K. Lee, *J. Mater. Chem. A*, **2017**, *5*, 1906-1912.
- [4.13] A. K. M, V. Vijayakumar. S. Karak, S. Kandambeth, M. Bhadra, K. Suresh, N. Acharambath, S. Kurungot, R. Banerjee, *ACS Appl. Mater. Interfaces*, **2018**, *10*, 28139–28146.
- [4.14] (a) D. Usachov, O. Vilkov, A. Gruneis, D. Haberer, A. Fedorov, V. K. Adamchuk, A. B. Preobrajenski, P. Dudin, A. Barinov, M. Oehzelt, C. Laubschat, D. V. Vyalikh, *Nano Lett.* **2011**, *11*, 5401–5407; (b) J. Guo, C.-Y. Lin, Z. Xia, Z. Xiang, *Angew. Chem. Int. Ed.*, **2018**, *57*, 1–7. (c) S. Kabir, K. Artyushkova, A. Serov, B. Kiefer, P. Atanassov, *Surf. Interface Anal.* **2016**,

48, 293–300. (d) K. Artyushkova, B. Kiefer, B. Halevi, A. Knop-Gericke, R. Schlogl, P. Atanassov, *Chem. Commun.* **2013**, 49, 2539–2541.

- [4.15] (a) V. Georgakilas, J. N. Tiwari, K. C. Kemp, J. A. Perman, A. B. Bourlinos, K. S. Kim, R. Zboril, *Chem. Rev.* **2016**, 116, 5464-5519; (b) D. Chen, H. Feng, J. Li, *Chem. Rev.* **2012**, 112, 6027-6053; (c) S. Stankovich, D. A. Dikin, G. H. B. Dommett, K. M. Kohlhaas, E. J. Zimney, E. A. Stach, R. D. Piner, S. T. Nguyen, R. S. Ruoff, *Nature* **2006**, 442, 282-286.

CHAPTER 5

- [5.1] (a) X. Zhu, S. An, Y. Liu, J. Hu, H. Liu, C. Tian, S. Dai, X. Yang, H. Wang, C. W. Abney, S. Dai, *AIChE J.* **2017**, 63, 3470; (b) N. Huang, L. Zhai, H. Xu, D. Jiang, *J. Am. Chem. Soc.* **2017**, 139, 2428; (c) Q. Sun, B. Aguila, J. Perman, L. D. Earl, C. W. Abney, Y. Cheng, H. Wei, N. Nguyen, L. Wojtas, S. Ma, *J. Am. Chem. Soc.* **2017**, 139, 2786; (d) H. Lu, C. Wang, J. Chen, R. Ge, W. Leng, B. Dong, J. Huang, Y. Gao, *Chem. Commun.* **2015**, 51, 15562; (e) Karak, K. Dey, A. Torris, A. Halder, S. Bera, F. Kanheerampockil, Rahul Banerjee, *J. Am. Chem. Soc.* **2019**, 141, 18, 7572-7581.
- [5.2] (a) K. Dey, M. Pal, K. C. Rout, S. Kunjattu, H. A. Das, R. Mukherjee, U. K. Kharul, R. Banerjee, *J. Am. Chem. Soc.* **2017**, 139, 13083–13091; (b) S. Kandambeth, B. P. Biswal, H. D. Chaudhari, K. C. Rout, H. S. Kunjattu, S. Mitra, S. Karak, A. Das, R. Mukherjee, U. K. Kharul, R. Banerjee, *Adv. Mater.* **2017**, 29, 1603945.
- [5.3] (a) K. Jie, M. Liu, Y. Zhou, M. A. Little, A. Pulido, S. Y. Chong, A. Stephenson, A. R. Hughes, F. Sakakibara, T. Ogoshi, F. Blanc, G. M. Day, F. Huang, A. I. Cooper, *J. Am. Chem. Soc.* **2018**, 140, 6921–6930; (b) H. Y. Yang, Z. J. Han, S. F. Yu, K. L. Pey, K. Ostrikov, R. Karnik, *Nat. Commun.*, **2013**, 4, 2220.
- [5.4] (a) B. Lee, S. Lee, M. Lee, D.H. Jeong, Y. Baek, J. Yoon, Y. H. Kim, *Nanoscale*, **2015**, 7, 6782-6789; (b) W. Wan, R. Zhang, W. Li, H. Liu, Y. Lin, L. Li, Y. Zhou, *Environ. Sci.: Nano*, **2016**, 3, 107-113.

-
- [5.5] (a) C. Stubenrauch, A. Menner, A. Bismarck, W. Drenckhan, *Angew. Chem. Int. Ed.* **2018**, *57*, 10024 – 10032; (b) C. Cheng, Y. Cai, G. Guan, L. Yeo, Dayang Wang, *Angew. Chem. Int. Ed.* **2018**, *57*, 1 – 6; (c) G. Zu, T. Shimizu, K. Kanamori, Y. Zhu, A. Maeno, H. Kaji, J. Shen, K. Nakanishi, *ACS Nano*, **2018**, *12*, 1, 521-532.
- [5.6] (a) G.J. H. Lim, Y. Wu, B. B. Shah, J. J.Koh, C. K. Liu, D. Zhao, A. K. Cheetham, J. Wang, J. Ding, *ACS Materials Lett.* **2019**, *1*, 147–153; (b) Q. Zhang, F. Zhang, S. P. Medarametla, H. Li, C. Zhou, Dong Lin, *small* **2016**, *12*, 13, 1702–1708; (c) K. Fu, Y. Yao, J. Dai, L. Hu, *Adv. Mater.* **2017**, *29*, 1603486; (d) D. J. Wales, Q. Cao, K. Kastner, E. Karjalainen, G. N. Newton, Victor Sans, *Adv. Mater.* **2018**, *30*, 1800159.
- [5.7] (a) H. Huang, P. Chen, X. Zhang, Y. Lu, W. Zhan, *small* **2013**, *9*, 8, 1397–1404; (b) N. V. Medhekar, A. Ramasubramaniam, R. S. Ruoff and V. B. Shenoy, *ACS Nano*, **2010**, *4*, 2300–2306.
- [5.8] X. Wang, M. Jiang, Z. W. Zhou, J. H. Gou, D. Hui, *Compos. Pt. B-Eng.* **2017**, *110*, 442.
- [5.9] S. Kandambeth, A. Mallick, B. Lukose, M. V. Mane, T. Heine, R. Banerjee, *J. Am. Chem. Soc.* **2012**, *134*, 19524.
- [5.10] (a) A. Alsaiee, B. J. Smith, L. Xiao, Y. Ling, D. E. Helbling and W. R. Dichtel, *Nature*, 2015, 529, 190; (b) L. N. Vandenberg, R. Hauser, M. Marcus, N. Olea, W. V. Welshons, *Reprod. Toxicol.* **2007**, *24*, 139–177

CHAPTER 6

- [6.1] (a) K. Dutta, S. De, *J. Mater. Chem. A*, **2017**, *5*, 22095–22112; (b) F. Guo and Z. Guo, *RSC Adv.*, **2016**, *6*, 36623; (c) F. D. Jochum and P. Theato, *Chem. Soc. Rev.*, **2013**, *42*, 7468; (d) M. A. C. Stuart, W. T. S. Huck, J. Genzer, M. Müller, C. Ober, M. Stamm, G. B. Sukhorukov, I. Szleifer, V. V. Tsukruk, M. Urban, F. Winnik, S. Zauscher, I. Luzinov, S. Minko, *Nat. Mater.*, **2010**, *9*, 101.
- [6.2] (a) D. Roy, J. N. Cambre and B. S. Sumerlin, *Prog. Polym. Sci.*, **2010**, *35*, 278. (b) H. Ma, B. Liu, B. Li, L. Zhang, Y. G. Li, H. Tan, H. Zang and G. Zhu, *J. Am. Chem. Soc.*, **2016**, *138*, 5897; (c) C. Zhao, S. Nie, M. Tang and S. Sun, *Prog. Polym. Sci.*, **2011**, *36*, 1499; (d) T. Ito, T. Hioki, T. Yamaguchi, T.

Shinbo, S.-i. Nakao, S. Kimura, *J. Am. Chem. Soc.*, **2002**, *124*, 7840; (e) F. P. Nicoletta, D. Cupelli, P. Formoso, G. De Filpo, V. Colella and A. Gugliuzza, *Membranes*, **2012**, *2*, 134.

- [6.3] Z. Mahimwalla, K. G. Yager, J.-i. Mamiya, A. Shishido, A. Priimagi, C. J. Barrett, *Polym. Bull.* **2012**, *69*, 967–1006.

ABOUT THE AUTHOR



Mr. Abdul Khayum M, son of Mohammed A S F and Hafsa Muhammed, was born in Puthucode village of Palakkad district, Kerala, India, in 1991. He did his schooling (2007) from Sarvajana High School, Puthucode. He has completed his higher secondary (2009) in science stream from A.S.M.M, Alathur and B.Sc. in Chemistry (2012) from the St. Thomas' College, Trichur. After qualifying Common Admission Test to M.Sc. (CAT) he moved to Department of Applied Chemistry, Cochin to pursue his M.Sc. in Chemistry (2012-2014). Again, after qualifying all India joint CSIR-UGC National Eligibility Test (NET-JRF) examination, he moved to Physical and Materials Chemistry Division, CSIR-National Chemical Laboratory, Pune, India to pursue his Ph.D. degree in July 2015 under the guidance of Prof. Dr. Rahul Banerjee. Later, he has worked in Polymer Science and Engineering Division, NCL, Pune under the guidance of Dr. Ulhas K Kharul and co-guidance of Dr. Rahul Banerjee. He has received the research fellowship (JRF and SRF) from University Grants Commission (UGC), New Delhi, India for the period of July 2015 - July 2020 to carry out the Ph.D. thesis work.

LIST OF PUBLICATIONS

1. **Abdul Khayum M**, Sharath Kandambeth, Shouvik Mitra, Sanoop B Nair, Anuja Das, Samadhan S Nagane, Rabibrata Mukherjee, Rahul Banerjee. Chemically Delaminated Free-Standing Ultrathin Covalent Organic Nanosheets.
Angew. Chem. Int. Ed. **2016**, *55*, 15604 – 15608.
2. Shouvik Mitra, Sharath Kandambeth, Bishnu P. Biswal, **Abdul Khayum M**, Chandan Kumar Choudhury, Mihir Mehta, Gagandeep Kaur, Subhrashis Banerjee, Asmita A. Prabhune, Sandeep Verma, Sudip Roy, Ulhas K. Kharul, Rahul Banerjee. Self-Exfoliated Guanidinium-Based Ionic Covalent Organic Nanosheets (iCONs).
J. Am. Chem. Soc., **2016**, *138*, 2823-2828.
3. Arindam Mal, Rakesh K. Mishra, Vakayil K. Praveen, **Abdul Khayum M**, Rahul Banerjee, Ayyappanpillain Ajayaghosh. Supramolecular Reassembly of Self-Exfoliated Ionic Covalent Organic Nanosheets for Label-Free Detection of dsDNA.
Angew. Chem. Int. Ed. **2018**, DOI: 10.1002/anie.201801352.
4. **Abdul Khayum M**, Vidyanand Vijayakumar, Suwendu Karak, Sharath Kandambeth, Mohitosh Bhadra, Karthika Suresh, Nikhil Acharambath, Sreekumar Kurungot, and Rahul Banerjee. Convergent Covalent Organic Framework Thin Sheets as Flexible Supercapacitor Electrodes.
ACS Appl. Mater. Interfaces **2018**, *10*, 33, 28139–28146.
5. Arjun Halder, Meena Ghosh, **Abdul Khayum M**, Saibal Bera, Matthew Addicoat, Himadri Sekhar Sasmal, Suwendu Karak, Sreekumar Kurungot, and Rahul Banerjee. Interlayer Hydrogen-Bonded Covalent Organic Frameworks as High-Performance Supercapacitors.
J. Am. Chem. Soc. **2018**, *140*, 35, 10941-10945.
6. **Abdul Khayum M**, Meena Ghosh, Vidyanand Vijayakumar, Arjun Halder, Maryam Nurhuda, Sushil Kumar, Matthew Addicoat, Himadri Sreekumar Kurungot, and Rahul Banerjee. Zinc Ion Interaction in a Two-Dimensional Covalent Organic Framework Based Aqueous Zinc Ion Battery.

7. **Abdul Khayum M**, Vidyanand Vijayakumar, Meena Ghosh, Arjun Halder, Matthew Addicoat, Umesh Bansode, Sreekumar Kurungot, and Rahul Banerjee.
Weak Intermolecular Interactions in Covalent Organic Framework-Carbon Nanofiber Based Crystalline yet Flexible Devices.
ACS Appl. Mater. Interfaces **2019**, *11*, 34, 30828–30837.

CONFERENCES AND PRESENTATIONS

1. National seminar “CITRIC-2014”, CUSAT, India
Presented oral in “24th Congress and General Assembly of the International Union of Crystallography (IUCr) conference”, **2017**, Hyderabad, India

